

Important Notice

This copy may be used only for the purposes of research and private study, and any use of the copy for a purpose other than research or private study may require the authorization of the copyright owner of the work in question. Responsibility regarding questions of copyright that may arise in the use of this copy is assumed by the recipient.

THE UNIVERSITY OF CALGARY

Seismic Properties of Thin Beds

by

Hai-Man Chung

A DISSERTATION

SUBMITTED TO THE FACULTY OF GRADUATE STUDIES

IN PARTIAL FULFILLMENT OF THE REQUIREMENTS FOR THE

DEGREE OF DOCTOR OF PHILOSOPHY

DEPARTMENT OF GEOLOGY AND GEOPHYSICS

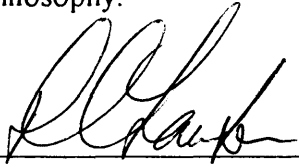
CALGARY, ALBERTA

SEPTEMBER, 1994

© Hai-Man Chung 1994

FACULTY OF GRADUATE STUDIES

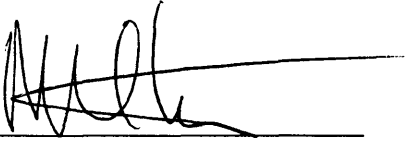
The undersigned certify that they have read, and recommend to the Faculty of Graduate Studies for acceptance, a dissertation entitled "Seismic Properties of Thin Beds" submitted by Hai-Man Chung in partial fulfillment of the requirements for the degree of Doctor of Philosophy.



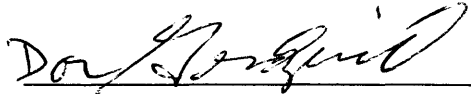
Supervisor, Dr. D.C. Lawton
Department of Geology and Geophysics



Dr. L.V. Hills
Department of Geology and Geophysics



Dr. R.R. Stewart
Department of Geology and Geophysics



External Examiner, Dr. D.J. Gendzwill
The University of Saskatchewan



Dr. R.J. Brown
Department of Geology and Geophysics



Dr. H. Laue
Department of Physics and Astronomy

NOVEMBER 24, 1994

Date

Abstract

In this dissertation, the seismic properties of thin layers are studied. The normal-incidence properties of one layer and two layers are studied in terms of amplitude, frequency, and complex attributes of the composite wavelet. The offset-dependent properties of one layer are also studied.

The amplitude results for one-layer models indicate that, as the thickness increases from zero to the $(1/8)\lambda_d$ value, the amplitude changes quadratically. However, if the two reflection coefficients have equal magnitudes and opposite polarities, the amplitude increases linearly. At $(1/4)\lambda_d$ thickness, all four models show tuning effect.

The amplitude results for two-layered models show that the amplitude changes quadratically as the thickness of one of the two layers increases from zero to the $(1/8)\lambda_d$ value, with tuning effect occurring at close to the $(1/4)\lambda_d$ thickness. However, the model with alternating polarities for the three reflection coefficients exhibits a minimum at approximately the $(1/16)\lambda_d$ thickness, and a maximum at close to the $(1/4)\lambda_d$ thickness. These properties do not change appreciably as the thickness of one of the two layers increases within a range of five fold.

In the frequency study, the results indicate that, as the thickness increases, the peak frequencies of the composite reflections decrease slowly. However, for the one-layered model whose reflection coefficients have unequal magnitude and opposite polarities and the two-layered model whose reflection coefficients have alternating polarities, the peak frequencies increase as the thickness increases from zero to the $(1/16)\lambda_d$ value, and then decrease as the thickness increases further.

The complex attributes study indicates that the instantaneous frequency is useful for studying wavelet interference. Amplitude tuning effect combined with frequency

tuning effect appears to be a good indicator of the existence of thin layers. However, the use of complex attributes remains largely empirical and a pattern recognition tool.

The results of the offset-dependent study show that tuning effect can change drastically the effect of lateral changes in Poisson's ratio in terms of amplitude, peak frequency, and complex attributes. To interpret AVO effect properly in thin-bed interpretation, the effect of offset-dependent tuning must be accounted for.

Acknowledgments

Many people have contributed to this dissertation. Dr. Lawton has made many valuable and useful suggestions to this dissertation, and provided the computer program for solving Zoeppritz equations. The Crewes project has offered me an unique opportunity to pursue my interest in the properties of thin beds. Alberta Energy Company provided the seismic data used in both case studies. Steve Popadynetz helped me with the programming of the equations, and Amy Wong assisted me in preparing the final script. Daniel Hampson has allowed me to use his software for generating complex attributes and hardware for plotting them. I express my sincere and deep gratitude to all these people who have made my work possible.

Above all, I want to thank my wife, Catherine, and my son, Justin, who have been very patient with me for the last six years.

Table of Content

Approval Page	ii
Abstract	iii
Acknowledgments	v
Table of Contents	vi
List of Tables	x
List of Figures	xv

CHAPTER ONE: INTRODUCTION

1.1 Background	1
1.2 Dissertation objectives	2
1.3 The seismic responses of thin beds.....	4
1.4 Amplitude variation with offset (AVO)	8
1.5 Review of complex attributes	12
1.6 Dissertation structure.....	14
1.7 Hardware and software used	15

CHAPTER TWO: AMPLITUDE CHARACTERISTICS OF SEISMIC REFLECTIONS FROM THIN BEDS

2.1 Introduction.....	16
2.2 Theory	17
2.2.1 Sinusoidal approximation	17
2.2.2 Ricker zero-phase wavelet	24
2.3 Normal incidence, single-layer model	31
2.3.1 Type I reflectivity.....	34
2.3.2 Type II reflectivity	37
2.3.3 Type III reflectivity	39
2.3.4 Type IV reflectivity.....	42
2.4 Normal incidence, two-layer model	43
2.4.1 Sinusoidal approximation	43
2.4.2 Type V reflectivity	47
2.4.3 Type VI reflectivity.....	51

2.4.4 Type VII reflectivity.....	55
2.5 Discussion	56

CHAPTER THREE: FREQUENCY CHARACTERISTICS OF SEISMIC REFLECTIONS FROM THIN BEDS

3.1 Introduction	64
3.2 Theory	66
3.2.1 Single-layer model	66
3.2.2 Two-layer model.....	72
3.3 Normal incidence, single-layer model.....	75
3.3.1 Type I reflectivity.....	75
3.3.2 Type II reflectivity	76
3.3.3 Type III reflectivity	78
3.3.4 Type IV reflectivity.....	78
3.4 Normal incidence, two-layer model.....	80
3.4.1 Modelling comparison of Types V, VI, and VII reflectivity series.....	80
3.4.2 Frequency dependence of Types V, VI, and VII reflectivity series	82
3.5 Discussion.....	86

CHAPTER FOUR: COMPLEX ATTRIBUTES OF THIN BEDS

4.1 Introduction	89
4.2 Properties of complex attributes	90
4.2.1 Instantaneous amplitude.....	90
4.2.2 Instantaneous phase	94
4.2.3 Instantaneous frequency.....	97
4.3 Normal incidence, single-layer model.....	99
4.3.1 Instantaneous amplitude.....	99
4.3.2 Instantaneous phase	100
4.3.3 Instantaneous frequency.....	104
4.4 Normal incidence, two-layer model.....	110
4.4.1 Instantaneous amplitude.....	111
4.4.2 Instantaneous phase	113
4.4.3 Instantaneous frequency.....	114
4.5 Discussion.....	118

CHAPTER FIVE: OFFSET-DEPENDENT SEISMIC PROPERTIES

5.1	Offset-dependent properties of thin beds	121
5.2	Amplitude versus offset for a thin layer	122
5.2.1	Type I reflectivity	127
5.2.2	Type IA reflectivity	132
5.2.3	Type II reflectivity	136
5.2.4	Type IIA reflectivity	140
5.3	Offset-dependent peak frequency analysis	143
5.3.1	Type I reflectivity	144
5.3.2	Type IA reflectivity	148
5.3.3	Type II reflectivity	150
5.3.4	Type IIA reflectivity	153
5.4	Offset-dependent properties of complex attributes	158
5.4.1	Instantaneous amplitude	159
5.4.2	Instantaneous phase	160
5.4.3	Instantaneous frequency	162
5.5	Discussion	168

CHAPTER SIX: CASE STUDIES

6.1	Introduction	172
6.2	Sandbar example	172
6.2.1	Geological background	173
6.2.2	Geophysical background	175
6.2.3	Amplitude variation with offset analysis	178
6.2.4	Complex attributes	188
6.2.4a	Instantaneous amplitude	188
6.2.4b	Instantaneous phase	188
6.2.4c	Instantaneous frequency	191
6.2.5	Discussion	193
6.3	Sheet sand example	195
6.3.1	Geological background	195
6.3.2	Geophysical background	196
6.3.3	Amplitude analysis	197
6.3.4	Frequency interpretation	202

6.3.5 Complex attributes.....	207
6.3.6 Discussion	210

CHAPTER SEVEN: DISSERTATION SUMMARY

7.1 Summary.....	212
7.2 Future research.....	214

REFERENCES	215
-------------------------	------------

APPENDIX A	221
-------------------------	------------

APPENDIX B	241
-------------------------	------------

APPENDIX C	247
-------------------------	------------

List of Tables

Table 2.1	Lithologies, layer velocities, layer densities, and reflection coefficients for four models.....	32
Table 2.2a	Comparison of modelling data with Ricker and sinusoidal approximations for Type I reflectivity at 18-Hz peak frequency ($\lambda_d = 130.26$ m).....	221
Table 2.2b	Comparison of modelling data with Ricker and sinusoidal approximations for Type I reflectivity at 31-Hz peak frequency ($\lambda_d = 75.63$ m).....	222
Table 2.2c	Comparison of modelling data with Ricker and sinusoidal approximations for Type I reflectivity at 50-Hz peak frequency ($\lambda_d = 46.89$ m).....	222
Table 2.3a	Comparison of modelling data with Ricker and sinusoidal approximations for Type II reflectivity at 18-Hz peak frequency ($\lambda_d = 152.14$ m).....	223
Table 2.3b	Comparison of modelling data with Ricker and sinusoidal approximations for Type II reflectivity at 31-Hz peak frequency ($\lambda_d = 88.34$ m).....	224
Table 2.3c	Comparison of modelling data with Ricker and sinusoidal approximations for Type II reflectivity at 50-Hz peak frequency ($\lambda_d = 54.77$ m).....	224
Table 2.4	Comparison of modelling data with Ricker and sinusoidal approximations for Type III reflectivity at 31-Hz peak frequency ($\lambda_d = 75.63$ m).....	225
Table 2.5	Comparison of modelling data with Ricker and sinusoidal approximations for Type IV reflectivity at 31-Hz peak frequency ($\lambda_d = 83.20$ m).....	225
Table 2.6	Lithologies, layer velocities, layer densities and reflection coefficients for the Type V, VI and VII reflectivity.....	48
Table 2.7a	Comparison of modelling data with the sinusoidal and pseudo-Ricker approximations for Type V ($\overline{\tau}^{\text{II}}$) reflectivity with a 2-m underlying thin layer ($\lambda_{d_1} = 75.63$ m, $\lambda_{d_2} = 94.29$ m).....	226
Table 2.7b	Comparison of modelling data with the sinusoidal and pseudo-Ricker approximations for Type V ($\overline{\tau}^{\text{II}}$) reflectivity with a 4-m underlying thin layer ($\lambda_{d_1} = 75.63$ m, $\lambda_{d_2} = 94.29$ m).....	227
Table 2.7c	Comparison of modelling data with the sinusoidal and pseudo-Ricker approximations for Type V ($\overline{\tau}^{\text{II}}$) reflectivity with a 6-m underlying thin layer ($\lambda_{d_1} = 75.63$ m, $\lambda_{d_2} = 94.29$ m).....	228

Table 2.7d	Comparison of modelling data with the sinusoidal and pseudo-Ricker approximations for Type V ($\overline{\text{T}}\text{---}$) reflectivity with a 8-m underlying thin layer ($\lambda_{d_1} = 75.63$ m, $\lambda_{d_2} = 94.29$ m)	229
Table 2.7e	Comparison of modelling data with the sinusoidal and pseudo-Ricker approximations for Type V ($\overline{\text{T}}\text{---}$) reflectivity with a 10-m underlying thin layer ($\lambda_{d_1} = 75.63$ m, $\lambda_{d_2} = 94.29$ m)	230
Table 2.8a	Comparison of modelling data with the sinusoidal and pseudo-Ricker approximations for Type VI ($\overline{\text{T}}\text{---}$) reflectivity with a 2-m underlying thin layer ($\lambda_{d_1} = 75.63$ m, $\lambda_{d_2} = 94.29$ m)	231
Table 2.8b	Comparison of modelling data with the sinusoidal and pseudo-Ricker approximations for Type VI ($\overline{\text{T}}\text{---}$) reflectivity with a 4-m underlying thin layer ($\lambda_{d_1} = 75.63$ m, $\lambda_{d_2} = 94.29$ m)	232
Table 2.8c	Comparison of modelling data with the sinusoidal and pseudo-Ricker approximations for Type VI ($\overline{\text{T}}\text{---}$) reflectivity with a 6-m underlying thin layer ($\lambda_{d_1} = 75.63$ m, $\lambda_{d_2} = 94.29$ m)	233
Table 2.8d	Comparison of modelling data with the sinusoidal and pseudo-Ricker approximations for Type VI ($\overline{\text{T}}\text{---}$) reflectivity with a 8-m underlying thin layer ($\lambda_{d_1} = 75.63$ m, $\lambda_{d_2} = 94.29$ m)	234
Table 2.8e	Comparison of modelling data with the sinusoidal and pseudo-Ricker approximations for Type VI ($\overline{\text{T}}\text{---}$) reflectivity with a 10-m underlying thin layer ($\lambda_{d_1} = 75.63$ m, $\lambda_{d_2} = 94.29$ m)	235
Table 2.9a	Comparison of modelling data with the sinusoidal and pseudo-Ricker approximations for Type VII ($\overline{\text{T}}\text{---}$) reflectivity with a 2-m underlying thin layer ($\lambda_{d_1} = 83.20$ m, $\lambda_{d_2} = 94.29$ m)	236
Table 2.9b	Comparison of modelling data with the sinusoidal and pseudo-Ricker approximations for Type VII ($\overline{\text{T}}\text{---}$) reflectivity with a 4-m underlying thin layer ($\lambda_{d_1} = 83.20$ m, $\lambda_{d_2} = 94.29$ m)	237
Table 2.9c	Comparison of modelling data with the sinusoidal and pseudo-Ricker approximations for Type VII ($\overline{\text{T}}\text{---}$) reflectivity with a 6-m underlying thin layer ($\lambda_{d_1} = 83.20$ m, $\lambda_{d_2} = 94.29$ m)	238

Table 2.9d	Comparison of modelling data with the sinusoidal and pseudo-Ricker approximations for Type VII ($\perp\perp\perp$) reflectivity with a 8-m underlying thin layer ($\lambda_{d_1} = 83.20$ m, $\lambda_{d_2} = 94.29$ m)	239
Table 2.9e	Comparison of modelling data with the sinusoidal and pseudo-Ricker approximations for Type VII ($\perp\perp\perp$) reflectivity with a 10-m underlying thin layer ($\lambda_{d_1} = 83.20$ m, $\lambda_{d_2} = 94.29$ m)	240
Table 3.1	Theoretical and modelling peak frequency values for Type I (\top) reflectivity	241
Table 3.2	Theoretical, modelling, and thin-bed peak frequency values for Type II (\perp) reflectivity	242
Table 3.3	Theoretical, modelling, and thin-bed peak frequency values for Type III (\top) reflectivity	243
Table 3.4	Theoretical, modelling, and thin-bed peak frequency values for Type IV (\perp) reflectivity	243
Table 3.5	Peak frequency comparisons for Types V, VI, and VII reflectivities. λ_d is 75.63 m for Types V and VI, and is 83.2 m for Type VII	244
Table 3.6	Peak frequency values for Type V ($\top\perp$) reflectivity	245
Table 3.7	Peak frequency values for Type VI ($\top\top$) reflectivity	245
Table 3.8	Peak frequency values for Type VII ($\perp\perp$) reflectivity	246
Table 4.1	Peak frequencies and corresponding barycentral frequencies for Type I reflectivity as a function of the wedge thickness	108
Table 5.1	Layer lithologies, velocities, densities, and reflection coefficients for four models for AVO study. Layer 1, layer 2, and layer 3 correspond to the layers in Figure 5.1	125
Table 5.2a	Percentage change in maximum absolute amplitude of P -wave for Type I reflectivity as σ changes from 0.3 to 0.1 for the thin layer. Positive and negative signs represent amplitude increases and decreases respectively..	247
Table 5.2b	Percentage change in maximum absolute amplitude of PS -wave for Type I reflectivity as σ changes from 0.3 to 0.1 for the thin layer. Positive and negative signs represent amplitude increases and decreases respectively..	247
Table 5.3a	Percentage change in maximum absolute amplitude of P -wave for Type IA reflectivity as σ changes from 0.3 to 0.1 for the thin layer. Positive and negative signs represent amplitude increases and decreases respectively..	248

Table 5.3b	Percentage change in maximum absolute amplitude of <i>PS</i> -wave for Type IA reflectivity as σ changes from 0.3 to 0.1 for the thin layer. Positive and negative signs represent amplitude increases and decreases respectively..	248
Table 5.4a	Percentage change in maximum absolute amplitude of <i>P</i> -wave for Type II reflectivity as σ changes from 0.3 to 0.1 for the thin layer. Positive and negative signs represent amplitude increases and decreases respectively..	249
Table 5.4b	Percentage change in maximum absolute amplitude of <i>PS</i> -wave for Type II reflectivity as σ changes from 0.3 to 0.1 for the thin layer. Positive and negative signs represent amplitude increases and decreases respectively..	249
Table 5.5a	Percentage change in maximum absolute amplitude of <i>P</i> -wave for Type IIA reflectivity as σ changes from 0.3 to 0.1 for the thin layer. Positive and negative signs represent amplitude increases and decreases respectively..	250
Table 5.5b	Percentage change in maximum absolute amplitude of <i>PS</i> -wave for Type IIA reflectivity as σ changes from 0.3 to 0.1 for the thin layer. Positive and negative signs represent amplitude increases and decreases respectively..	250
Table 5.6a	Peak frequencies of reflected <i>P</i> -wave for Type I reflectivity as a function of the incident angle	251
Table 5.6b	Peak frequencies of reflected <i>PS</i> -wave for Type I reflectivity as a function of the incident angle	251
Table 5.7a	Peak frequencies of reflected <i>P</i> -wave for Type IA reflectivity as a function of the incident angle	252
Table 5.7b	Peak frequencies of reflected <i>PS</i> -wave for Type IA reflectivity as a function of the incident angle	252
Table 5.8a	Peak frequencies of reflected <i>P</i> -wave for Type II reflectivity as a function of the incident angle	253
Table 5.8b	Peak frequencies of reflected <i>PS</i> -wave for Type II reflectivity as a function of the incident angle	253
Table 5.9a	Peak frequencies of reflected <i>P</i> -wave for Type IIA reflectivity as a function of the incident angle	254
Table 5.9b	Peak frequencies of reflected <i>PS</i> -wave for Type IIA reflectivity as a function of the incident angle	254
Table 5.10a	Amplitude comparison between primary reflections only and primary reflections plus locally-converted shear waves for Type I reflectivity	255

Table 5.10b	Amplitude comparison between primary reflections only and primary reflections plus locally-converted shear waves for Type IA reflectivity.....	255
Table 5.10c	Amplitude comparison between primary reflections only and primary reflections plus locally-converted shear waves for Type II reflectivity	256
Table 5.10d	Amplitude comparison between primary reflections only and primary reflections plus locally-converted shear waves for Type IIA reflectivity ..	256
Table 5.11a	Peak frequency comparison between primary reflections only and primary reflections plus locally-converted shear waves for Type I reflectivity	257
Table 5.11b	Peak frequency comparison between primary reflections only and primary reflections plus locally-converted shear waves for Type IA reflectivity.....	257
Table 5.11c	Peak frequency comparison between primary reflections only and primary reflections plus locally-converted shear waves for Type II reflectivity	258
Table 5.11d	Peak frequency comparison between primary reflections only and primary reflections plus locally-converted shear waves for Type IIA reflectivity ..	258
Table 6.1	Processing steps for seismic template line	177

List of Figures

Figure 1.1	Waves generated at an interface by an incident <i>P</i> -wave 9
Figure 2.1	Sinusoidal and Ricker approximations for Type II ($\perp\perp$) reflectivity. (b) and (d) are schematic representatives of summations of the two curves in (a) and (c), respectively..... 22
Figure 2.2	Sinusoidal and Ricker approximations for Type I ($\top\perp$) reflectivity. (b) and (d) are summations of the two curves in (a) and (e) respectively. (c) shows the 90°- phase equivalent of (c)..... 22
Figure 2.3	Comparison between sinusoidal and Ricker approximations for Type II ($\perp\perp$) reflectivity..... 29
Figure 2.4	A wedge model..... 31
Figure 2.5	Synthetic seismograms for (a) Type I ($\top\perp$), (b) Type II ($\perp\perp$), (c) Type III ($\top\perp$), and (d) Type IV ($\perp\perp$) reflectivities. The source wavelet is a 31-Hz Ricker wavelet, and the arrows indicate the $(1/8)\lambda_d$ and $(1/4)\lambda_d$ locations. Timing lines are at 10-ms intervals 33
Figure 2.6a	The amplitude response for Type I reflectivity ($\top\perp$) with a Ricker 18-Hz source wavelet whose maximum amplitude is 1000. Modelling (0°) and modelling (90°) are modelling results with zero-phase and 90°-phase wavelets, respectively..... 36
Figure 2.6b	The amplitude response for Type I reflectivity ($\top\perp$) with a Ricker 31-Hz source wavelet whose maximum amplitude is 1000 36
Figure 2.6c	The amplitude response for Type I reflectivity ($\top\perp$) with a Ricker 50-Hz source wavelet whose maximum amplitude is 1000 37
Figure 2.7a	The amplitude response for Type II reflectivity ($\perp\perp$) with a Ricker 18-Hz source wavelet whose maximum amplitude is 1000 40
Figure 2.7b	The amplitude response for Type II reflectivity ($\perp\perp$) with a Ricker 31-Hz source wavelet whose maximum amplitude is 1000 40
Figure 2.7c	The amplitude response for Type II reflectivity ($\perp\perp$) with a Ricker 50-Hz source wavelet whose maximum amplitude is 1000 41
Figure 2.8	The amplitude response for Type III reflectivity ($\top\perp$) with a Ricker 31-Hz source wavelet whose maximum amplitude is 1000 42

Figure 2.9	The amplitude response for Type IV reflectivity ($\perp\perp$) with a Ricker 31-Hz source wavelet whose maximum amplitude is 1000	44
Figure 2.10	The wedge model for two-layer study	47
Figure 2.11	Synthetic seismograms for (a) Type V ($\top\perp\perp$) reflectivity, (b) Type VI ($\top\top\perp$) reflectivity, and (c) Type VII ($\perp\perp\perp$) reflectivity with underlying layer thicknesses 4-m and 8-m. The source wavelet is a Ricker 31-Hz wavelet. Timing lines are at 10-ms intervals.....	49
Figure 2.12a	Comparison of modelling data with the sinusoidal and pseudo-Ricker approximations for Type V reflectivity ($\top\perp\perp$) with an underlying thin layer 2-m thick	52
Figure 2.12b	Comparison of modelling data with the sinusoidal and pseudo-Ricker approximations for Type V reflectivity ($\top\perp\perp$) with an underlying thin layer 4-m thick	53
Figure 2.12c	Comparison of modelling data with the sinusoidal and pseudo-Ricker approximations for Type V reflectivity ($\top\perp\perp$) with an underlying thin layer 6-m thick	53
Figure 2.12d	Comparison of modelling data with the sinusoidal and pseudo-Ricker approximations for Type V reflectivity ($\top\perp\perp$) with an underlying thin layer 8-m thick	54
Figure 2.12e	Comparison of modelling data with the sinusoidal and pseudo-Ricker approximations for Type V reflectivity ($\top\perp\perp$) with an underlying thin layer 10-m thick	54
Figure 2.13a	Comparison of modelling data with the sinusoidal and pseudo-Ricker approximations for Type VI reflectivity ($\top\top\perp$) with an underlying thin layer 2-m thick	57
Figure 2.13b	Comparison of modelling data with the sinusoidal and pseudo-Ricker approximations for Type VI reflectivity ($\top\top\perp$) with an underlying thin layer 4-m thick	57
Figure 2.13c	Comparison of modelling data with the sinusoidal and pseudo-Ricker approximations for Type VI reflectivity ($\top\top\perp$) with an underlying thin layer 6-m thick	58

Figure 2.13d	Comparison of modelling data with the sinusoidal and pseudo-Ricker approximations for Type VI reflectivity ($\overline{\tau\tau}$) with an underlying thin layer 8-m thick	58
Figure 2.13e	Comparison of modelling data with the sinusoidal and pseudo-Ricker approximations for Type VI reflectivity ($\overline{\tau\tau}$) with an underlying thin layer 10-m thick	59
Figure 2.14a	Comparison of modelling data with the sinusoidal and pseudo-Ricker approximations for Type VII reflectivity ($\underline{\perp\perp}$) with an underlying thin layer 2-m thick	59
Figure 2.14b	Comparison of modelling data with the sinusoidal and pseudo-Ricker approximations for Type VII reflectivity ($\underline{\perp\perp}$) with an underlying thin layer 4-m thick	60
Figure 2.14c	Comparison of modelling data with the sinusoidal and pseudo-Ricker approximations for Type VII reflectivity ($\underline{\perp\perp}$) with an underlying thin layer 6-m thick	60
Figure 2.14d	Comparison of modelling data with the sinusoidal and pseudo-Ricker approximations for Type VII reflectivity ($\underline{\perp\perp}$) with an underlying thin layer 8-m thick	61
Figure 2.14e	Comparison of modelling data with the sinusoidal and pseudo-Ricker approximations for Type VII reflectivity ($\underline{\perp\perp}$) with an underlying thin layer 10-m thick	61
Figure 3.1	A simple thin layer model	66
Figure 3.2	Two thin layers embedded in two thick layers	72
Figure 3.3	Peak frequency values vs. thickness for Type I reflectivity ($\overline{\tau^\perp}$)	76
Figure 3.4	Peak frequency values vs. thickness for Type II reflectivity ($\underline{\perp\perp}$)	77
Figure 3.5	Peak frequency values vs. thickness for Type III reflectivity ($\overline{\tau^\perp}$)	79
Figure 3.6	Peak frequency values vs. thickness for Type IV reflectivity ($\underline{\perp\perp}$)	79
Figure 3.7	Peak frequency comparison between equation (3.8) and modelling for Type V reflectivity ($\overline{\tau\perp}$). The source wavelet is a 31-Hz Ricker wavelet, and the underlying layer is 2-m thick	81

Figure 3.8	Peak frequency comparison between equation (3.8) and modelling for Type VI reflectivity ($\tau\tau\tau$). The source wavelet is a 31-Hz Ricker wavelet, and the underlying layer is 4-m thick.....	82
Figure 3.9	Peak frequency comparison between equation (3.8) and modelling for Type VII reflectivity ($\perp\perp\perp$). The source wavelet is a 31-Hz Ricker wavelet, and the underlying layer is 6-m thick.....	83
Figure 3.10	Peak frequency values from equation (3.8) for Type V reflectivity ($\tau\perp\perp$).....	85
Figure 3.11	Peak frequency values from equation (3.8) for Type VI reflectivity ($\tau\tau\tau$).....	85
Figure 3.12	Peak frequency values from equation (3.8) for Type VII reflectivity ($\perp\perp\perp$).....	86
Figure 4.1	Phasor representation of instantaneous amplitude and instantaneous phase. The rate of rotation is the instantaneous frequency.....	95
Figure 4.2	Phasor representation of a portion of a seismic trace (from White, 1991)	96
Figure 4.3	Comparison of weighted and unweighted instantaneous frequencies (White, 1991).....	96
Figure 4.4	Instantaneous amplitudes for (a) Type I ($\tau\perp$), (b) Type II ($\perp\perp$), (c) Type III ($\tau\perp$), and (d) Type IV ($\perp\perp$) reflectivities. The source wavelet is a 31-Hz Ricker wavelet, and the arrows indicate the $(1/8)\lambda_d$ and $(1/4)\lambda_d$ locations. Timing lines are at 10-ms intervals.....	101
Figure 4.5	Instantaneous phases for (a) Type I ($\tau\perp$), (b) Type II ($\perp\perp$), (c) Type III ($\tau\perp$), and (d) Type IV ($\perp\perp$) reflectivities. The source wavelet is a 31-Hz Ricker wavelet, and the arrows indicate the $(1/8)\lambda_d$ and $(1/4)\lambda_d$ locations. Timing lines are at 10-ms intervals.....	103
Figure 4.6	Instantaneous frequencies for (a) Type I ($\tau\perp$), (b) Type II ($\perp\perp$), (c) Type III ($\tau\perp$), and (d) Type IV ($\perp\perp$) reflectivities. The source wavelet is a 31-Hz Ricker wavelet, and the arrows indicate the $(1/8)\lambda_d$ and $(1/4)\lambda_d$ locations. Timing lines are at 10-ms intervals.....	106
Figure 4.7	Instantaneous amplitudes for Types V ($\tau\perp\perp$), VI ($\tau\tau\tau$), and VII ($\perp\perp\perp$) reflectivities with underlying layer thicknesses 4-m and 8-m. The source wavelet is a Ricker 31-Hz wavelet. Timing lines are at 10-ms intervals..	112

Figure 4.8	Instantaneous phases for Types V ($\overline{\text{T}}\perp\perp$), VI ($\overline{\text{T}}\overline{\text{T}}\perp$), and VII ($\perp\perp\perp$) reflectivities with underlying layer thicknesses 4-m and 8-m. The source wavelet is a Ricker 31-Hz wavelet. Timing lines are at 10-ms intervals.. 115
Figure 4.9	Instantaneous frequencies for Types V ($\overline{\text{T}}\perp\perp$), VI ($\overline{\text{T}}\overline{\text{T}}\perp$), and VII ($\perp\perp\perp$) reflectivities with underlying layer thicknesses 4-m and 8-m. The source wavelet is a Ricker 31-Hz wavelet. Timing lines are at 10-ms intervals. Colour legend A is for Type V reflectivity, colour legend B is for Types VI and VII reflectivity..... 116
Figure 5.1	Thin-layer model with lateral change in Poisson's ratio. Zones A and B have different <i>P</i> -wave velocities and densities. <i>S</i> -wave velocities in the two zones are equal..... 123
Figure 5.2	A single thin layer model for AVO study. Geophone group spacing is 50 m with the near-offset at 50 m..... 124
Figure 5.3	Comparison between the primary reflections only (<i>PP</i> and <i>PPP</i> for <i>P</i> -waves; <i>PS</i> and <i>PPSS</i> for <i>S</i> -waves) and primary reflections plus locally-converted waves (<i>PSPP</i> and <i>PPSP</i> for <i>P</i> -waves; <i>PPPS</i> , <i>PSPS</i> and <i>PSSS</i> for <i>S</i> -waves) for Type I reflectivity ($\overline{\text{T}}\perp$) for both <i>P</i> -waves and <i>S</i> -waves. 128
Figure 5.4	Shot gathers for Type I reflectivity at 5-m thickness:(a) <i>P</i> -wave, $\sigma = 0.3$; (b) <i>S</i> -wave, $\sigma = 0.3$; (c) <i>P</i> -wave, $\sigma = 0.1$; (d) <i>S</i> -wave, $\sigma = 0.1$. Timing lines are at 10-ms intervals..... 129
Figure 5.5a	Change in maximum absolute amplitude of <i>P</i> -wave event for Type I reflectivity for a change from $\sigma = 0.3$ to $\sigma = 0.1$ in layer 2..... 131
Figure 5.5b	Change in maximum absolute amplitude of <i>S</i> -wave event for Type I reflectivity for a change from $\sigma = 0.3$ to $\sigma = 0.1$ in layer 2..... 131
Figure 5.6	Shot gathers for Type IA reflectivity at 5-m thickness:(a) <i>P</i> -wave, $\sigma = 0.3$; (b) <i>S</i> -wave, $\sigma = 0.3$; (c) <i>P</i> -wave, $\sigma = 0.1$; (d) <i>S</i> -wave, $\sigma = 0.1$. Timing lines are at 10-ms intervals..... 134
Figure 5.7a	Change in maximum absolute amplitude of <i>P</i> -wave event for Type IA reflectivity for a change from $\sigma = 0.3$ to $\sigma = 0.1$ in layer 2 135
Figure 5.7b	Change in maximum absolute amplitude of <i>S</i> -wave event for Type IA reflectivity for a change from $\sigma = 0.3$ to $\sigma = 0.1$ in layer 2 135

Figure 5.8	Shot gathers for Type II reflectivity at 5-m thickness:(a) <i>P</i> -wave, $\sigma = 0.3$; (b) <i>S</i> -wave, $\sigma = 0.3$; (c) <i>P</i> -wave, $\sigma = 0.1$; (d) <i>S</i> -wave, $\sigma = 0.1$. Timing lines are at 10-ms intervals	138
Figure 5.9a	Change in maximum absolute amplitude of <i>P</i> -wave event for Type II reflectivity for a change from $\sigma = 0.3$ to $\sigma = 0.1$ in layer 2	139
Figure 5.9b	Change in maximum absolute amplitude of <i>S</i> -wave event for Type II reflectivity for a change from $\sigma = 0.3$ to $\sigma = 0.1$ in layer 2	139
Figure 5.10	Shot gathers for Type IIA reflectivity at 5-m thickness:(a) <i>P</i> -wave, $\sigma = 0.3$; (b) <i>S</i> -wave, $\sigma = 0.3$; (c) <i>P</i> -wave, $\sigma = 0.1$; (d) <i>S</i> -wave, $\sigma = 0.1$. Timing lines are at 10-ms intervals	141
Figure 5.11a	Change in maximum absolute amplitude of <i>P</i> -wave event for Type IIA reflectivity for a change from $\sigma = 0.3$ to $\sigma = 0.1$ in layer 2	142
Figure 5.11b	Change in maximum absolute amplitude of <i>S</i> -wave event for Type IIA reflectivity for a change from $\sigma = 0.3$ to $\sigma = 0.1$ in layer 2	143
Figure 5.12a	Peak frequencies versus angle of incidence for layer 2 thicknesses of 1-m and 5-m for reflected <i>P</i> -waves of Type I reflectivity	146
Figure 5.12b	Peak frequencies versus angle of incidence for layer 2 thicknesses of 9-m and 13-m for reflected <i>P</i> -waves of Type I reflectivity	146
Figure 5.12c	Peak frequencies versus angle of incidence for layer 2 thicknesses of 1-m and 5-m for reflected <i>S</i> -waves of Type I reflectivity	147
Figure 5.12d	Peak frequencies versus angle of incidence for layer 2 thicknesses of 9-m and 13-m for reflected <i>S</i> -waves of Type I reflectivity	147
Figure 5.13a	Peak frequencies versus angle of incidence for layer 2 thicknesses of 1-m and 5-m for reflected <i>P</i> -waves of Type IA reflectivity	149
Figure 5.13b	Peak frequencies versus angle of incidence for layer 2 thicknesses of 9-m and 13-m for reflected <i>P</i> -waves of Type IA reflectivity	149
Figure 5.13c	Peak frequencies versus angle of incidence for layer 2 thicknesses of 1-m and 5-m for reflected <i>S</i> -waves of Type IA reflectivity	151
Figure 5.13d	Peak frequencies versus angle of incidence for layer 2 thicknesses of 9-m and 13-m for reflected <i>S</i> -waves of Type IA reflectivity	151
Figure 5.14a	Peak frequencies versus angle of incidence for layer 2 thicknesses of 1-m and 5-m for reflected <i>P</i> -waves of Type II reflectivity	153
Figure 5.14b	Peak frequencies versus angle of incidence for layer 2 thicknesses of 9-m and 13-m for reflected <i>P</i> -waves of Type II reflectivity	154

Figure 5.14c	Peak frequencies versus angle of incidence for layer 2 thicknesses of 1-m and 5-m for reflected <i>S</i> -waves of Type II reflectivity	154
Figure 5.14d	Peak frequencies versus angle of incidence for layer 2 thicknesses of 9-m and 13-m for reflected <i>S</i> -waves of Type II reflectivity	155
Figure 5.15a	Peak frequencies versus angle of incidence for layer 2 thicknesses of 1-m and 5-m for reflected <i>P</i> -waves of Type IIA reflectivity	155
Figure 5.15b	Peak frequencies versus angle of incidence for layer 2 thicknesses of 9-m and 13-m for reflected <i>P</i> -waves of Type IIA reflectivity	156
Figure 5.15c	Peak frequencies versus angle of incidence for layer 2 thicknesses of 1-m and 5-m for reflected <i>S</i> -waves of Type IIA reflectivity	157
Figure 5.15d	Peak frequencies versus angle of incidence for layer 2 thicknesses of 9-m and 13-m for reflected <i>S</i> -waves of Type IIA reflectivity	157
Figure 5.16	Instantaneous amplitudes for Type IA reflectivity at 5-m thickness: (a) <i>P</i> -wave, $\sigma = 0.3$; (b) <i>S</i> -wave, $\sigma = 0.3$; (c) <i>P</i> -wave, $\sigma = 0.1$; (d) <i>S</i> -wave, $\sigma = 0.1$. Timing lines are at 10-ms intervals.....	161
Figure 5.17	Instantaneous amplitudes for Type II reflectivity at 5-m thickness: (a) <i>P</i> -wave, $\sigma = 0.3$; (b) <i>S</i> -wave, $\sigma = 0.3$; (c) <i>P</i> -wave, $\sigma = 0.1$; (d) <i>S</i> -wave, $\sigma = 0.1$. Timing lines are at 10-ms intervals.....	163
Figure 5.18	Instantaneous phases for Type IA reflectivity at 5-m thickness: (a) <i>P</i> -wave, $\sigma = 0.3$; (b) <i>S</i> -wave, $\sigma = 0.3$; (c) <i>P</i> -wave, $\sigma = 0.1$; (d) <i>S</i> -wave, $\sigma = 0.1$. Timing lines are at 10-ms intervals.....	164
Figure 5.19	Instantaneous phases for Type II reflectivity at 5-m thickness: (a) <i>P</i> -wave, $\sigma = 0.3$; (b) <i>S</i> -wave, $\sigma = 0.3$; (c) <i>P</i> -wave, $\sigma = 0.1$; (d) <i>S</i> -wave, $\sigma = 0.1$. Timing lines are at 10-ms intervals.....	166
Figure 5.20	Instantaneous frequencies for Type IA reflectivity at 5-m thickness: (a) <i>P</i> -wave, $\sigma = 0.3$; (b) <i>S</i> -wave, $\sigma = 0.3$; (c) <i>P</i> -wave, $\sigma = 0.1$; (d) <i>S</i> -wave, $\sigma = 0.1$. Timing lines are at 10-ms intervals.....	167
Figure 5.21	Instantaneous frequencies for Type II reflectivity at 5-m thickness: (a) <i>P</i> -wave, $\sigma = 0.3$; (b) <i>S</i> -wave, $\sigma = 0.3$; (c) <i>P</i> -wave, $\sigma = 0.1$; (d) <i>S</i> -wave, $\sigma = 0.1$. Timing lines are at 10-ms intervals.....	169
Figure 6.1	Informal stratigraphic column for the study area modified after Glaister (1959) and Energy Resources Conservation Board (1978)	174
Figure 6.2	Interpreted Glauconitic channels in the subject area	174

Figure 6.3	Schematic structural cross-section A-A' (Figure 6.2). The logs (gamma on the left and sonic on the right) are generalized and are plotted for aesthetic purpose only	176
Figure 6.4	Final full-offset stack of the seismic line. The gas sandbar anomaly is indicated inside the rectangle. The Glauconitic reflection is a trough along the top of the sandbar and is a peak in off-sand bar areas.....	176
Figure 6.5	(a) Full-offset stack (21-fold) of seismic anomaly with normal polarity (<i>P</i> -wave velocity increases correspond to peaks). The offset covers a distance of 0 - 1600 m. (b) Near-offset stack (8-fold) of seismic anomaly with normal polarity. The offset covers a distance of 0 - 1050 m. (c) Far-offset stack (8-fold) of seismic anomaly with normal polarity. The offset covers a distance of 1050 - 1600 m	179
Figure 6.6	Ostrander gather, summing over 6 CDP locations and three-offset range with no trace-balancing	180
Figure 6.7	(a) Reflection coefficients versus offsets for the Glauconite Member in modified well B. The left-hand side shows the logs from the well with the Poisson's ratio equal to 0.1 for the Glauconitic Member and 0.25 for all other formations. (b) NMO-corrected synthetic seismogram, and (c) pseudo-zero-offset synthetic seismogram for well B	183
Figure 6.8	(a) Reflection coefficients versus offsets for the Glauconite Member in channel shale well C. The left-hand side shows the logs from the well with the Poisson's ratio equal to 0.25 for all formations. (b) NMO-corrected synthetic seismogram, and (c) pseudo-zero-offset synthetic seismogram for well C	184
Figure 6.9	(a) Reflection coefficients versus offsets for the Glauconitic Member in the regional well F. The left-hand side shows the logs from the well with the Poisson's ratio equal to 0.25 for all formations. (b) NMO-corrected synthetic seismogram, and (c) pseudo-zero-offset synthetic seismogram for well F.....	185
Figure 6.10	Near-offset stack (0 - 1050 m) with a band-pass filter of (a) 8-16/35-40 Hz, (b) 8-16/40-45, (c) 8-16/45-50 Hz and (d) 8-16/50-55 Hz	187
Figure 6.11	The instantaneous amplitude plot of the sandbar anomaly for the (a) full-offset stack (0 - 2100 m), (b) near-offset stack (0 - 1050 m), and (c) mid-offset stack (1050 - 1600 m)	189

Figure 6.12	The instantaneous phase plot of the sandbar anomaly for the (a) full-offset stack (0 - 1600 m), (b) near-offset stack (0 - 1050 m), and (c) mid-offset stack (1050 - 1600 m)	190
Figure 6.13	The instantaneous frequency plot of the sandbar anomaly for the (a) full-offset stack (0 - 1600 m), (b) near-offset stack (0 - 1050 m), and (c) mid-offset stack (1050 - 1600 m)	192
Figure 6.14	Informal stratigraphic column for the study area (Kohrs and Norman, 1988)	196
Figure 6.15	A map showing the locations of the seismic lines, the wells, and the graben trend	198
Figure 6.16	Synthetic seismogram for well A. Timing lines are at 10-ms interval	198
Figure 6.17	Seismic displays for line 1: (a) conventional display, (b) instantaneous amplitude, (c) instantaneous phase, (d) instantaneous frequency. Timing lines are at 10-ms intervals	199
Figure 6.18	Seismic displays for line 2: (a) conventional display, (b) instantaneous amplitude, (c) instantaneous phase, (d) instantaneous frequency. Timing lines are at 10-ms intervals	200
Figure 6.19	Seismic displays for line 3: (a) conventional display, (b) instantaneous amplitude, (c) instantaneous phase, (d) instantaneous frequency. Timing lines are at 10-ms intervals	201
Figure 6.20a	Absolute maximum amplitudes for the Halfway Formation event for line 1 ...	203
Figure 6.20b	Absolute maximum amplitudes for the Halfway Formation event for line 2 ...	203
Figure 6.20c	Absolute maximum amplitudes for the Halfway Formation event for line 3 ...	204
Figure 6.21	Absolute maximum amplitudes for the Halfway reflections as a function of the thickness. Maximum amplitudes corresponding to wells A, B, and C are also plotted	204
Figure 6.22a	Peak frequencies for the Halfway Formation event for line 1.....	206
Figure 6.22b	Peak frequencies for the Halfway Formation event for line 2.....	206
Figure 6.22c	Peak frequencies for the Halfway Formation event for line 3.....	207
Figure 6.23	Three frequency spectra for the Halfway reflections on line 4 at three seismic line intersections: (a) intersection with line 1, (b) intersection with line 2 and, (c) intersection with line 3. The amplitude is measured in db down.....	208
Figure 6.24	Peak frequencies for the Halfway reflections as a function of thickness. Peak frequencies corresponding to wells A, B, and C are also plotted.....	209

Chapter 1 - Introduction

1.1 Background

In the Western Canadian Sedimentary Basin, geological formations of the Lower Cretaceous and the Triassic periods have produced large quantity of hydrocarbons, and are continuing to do so. Lower Cretaceous formations alone probably contain nearly 50% of the total oil and gas reserves of western Canada (Masters, 1984). A more recent publication by Anderson *et al.* (1989) shows that the total remaining gas reserves for Lower Cretaceous formations in western Canada is approximately 726×10^9 cubic metres. Therefore, a great deal of exploration effort has been, and still is, devoted to delineating hydrocarbon reservoirs in these rocks. Most of these formations are clastic rocks in layers whose thicknesses are below the temporal resolution of seismic data with respect to the dominant frequencies commonly obtained in data from western Canada. Hence, one cannot resolve separate reflections from the tops and bottoms of such formations. Under such circumstances, stratigraphic interpretation is employed where waveform analysis is used to deduce information on the thickness and lithology of a formation (Neidell and Poggiagliolmi, 1977). For example, the presence of bright spots on seismic data often indicates the presence of thick porous sands. Recently, peak frequency information has also been considered in thin-layer stratigraphic interpretation (Lange and Almoghrabi, 1988), although their treatment is qualitative only.

Waveform analysis is not unambiguous, since waveform changes can be attributed to more than one cause. Jain (1985) discussed briefly some of the imperfections of stacked seismic data for stratigraphic interpretation. In the last decade, improvements in field data acquisitions technique have also enabled geophysicists to make use of AVO

(amplitude variation with offset) effects for interpretation. This, however, brings both advantages and disadvantages, since an AVO response can also be attributed to many causes, some of which are not geological (Neidell, 1986). However, what most complicates waveform interpretation of seismic data from thin geological formations are variable tuning effects due to changing layer thicknesses. Channels, pinchouts, and angular unconformities are typical geological features where the thicknesses of the targets can vary laterally. Tuning effects, for both normally incident and obliquely incident data, often create anomalies which might otherwise be interpreted as changes in lithology and therefore such effects must be accounted for in the interpretation of seismic data from thinly stratified media.

Most stratigraphic interpretations of seismic data focus on amplitude studies. The approach of this dissertation is to examine not only amplitude characteristics, but also frequency and phase of seismic events, since these are all equally important attributes of a wavelet. For frequency, the behaviour of the peak frequency will be studied; to study phase, which partially determines the shape of the wavelet, complex attributes will be used in lieu of the Fourier phase spectrum to study subtle waveform changes. This offers an opportunity to study the usefulness of a physical method which has been proposed but not widely used in exploration. Whenever possible, mathematical expressions will be developed.

1.2 Dissertation objectives

The main goals of the dissertation are to study the seismic properties of thin geological formations and to investigate how to make use of some of these properties to assist in seismic interpretation. These goals will be achieved through four approaches. The first component is to study the responses of a thin bed to normally incident plane

waves for the general case. There has been a considerable number of seismic studies of a thin bed embedded in an infinite homogeneous medium, almost exclusively dealing with the case where the reflection coefficients on either side of the thin bed are of opposite polarities and equal value. However, there is very little published literature on the general case, that is opposite and/or equal polarities, and equal and/or different values for these reflection coefficients.

The second component of the dissertation is to examine the responses to normally incident plane waves of two thin beds embedded in an infinite and homogeneous medium. Three models simulating three geological situations are studied. These responses are compared to that of a single layer with the purpose of determining to what extent theories developed for one thin layer can be applied to two thin layers. This comparison is important because most seismic reflections are from geological sequences involving more than one layer.

The third component is to evaluate the offset-dependent behaviour of P -wave (P - P) and converted shear wave (P - S) reflections from a single thin bed. These responses are compared to the responses of normally incident plane waves with the objective of determining how much effect the stacking process actually has on the reflected wavelet in terms of its amplitude, frequency, and phase. The final objective is to determine the usefulness of complex attributes in seismic exploration in basins containing thin beds. The approach is simply to apply existing theories of complex attributes and study the observed results for the thin-bed case. The emphasis is on using complex attributes in lieu of the phase spectrum to detect subtle waveform changes.

1.3 The seismic responses of thin beds

Historically, the definition of a thin bed is related intimately to the temporal or vertical resolving power of the seismic wavelet. Ricker (1953) studied the composite waveform as a function of the temporal separation of two equal-value reflection coefficients of equal polarity. He chose the limit of resolution to be the separation at which the composite waveform has a flat spot at its central maximum, and showed that it can be determined by differentiating the wavelet twice. Conversely, Widess (1973) studied the case of two equal-value reflection coefficients but with opposite polarities. He investigated the composite waveform obtained by convolving a zero-phase wavelet with the two coefficients, and observed that, as the separation between them decreases to about a value of $(1/8)\lambda_d$, where λ_d is the predominant wavelength of the input wavelet, the composite wavelet assumes the shape of the derivative of the input wavelet. Below $(1/8)\lambda_d$ separation, there was no further apparent change in the wavelet shape. Therefore, Widess established the $(1/8)\lambda_d$ separation as the limit of resolution of a thin bed.

Other authors (Meckel and Nath, 1977; Neidell and Poggiagliolmi, 1977) simply defined the limit of resolution of a thin layer to be the thickness equal to $(1/4)\lambda_d$ of the input wavelet. This thickness is also the tuning thickness of a thin layer, namely the thickness at which the amplitude of the reflected wavelet is a maximum if the two reflection coefficients are of opposite polarities, and is a minimum if they are of equal polarity. It should also be emphasized that, in terms of 2-way traveltime, $(1/4)\lambda_d$ is transformed into only half the corresponding 2-way traveltime between the two reflection coefficients. Taking both the criteria of Ricker (1953) and Widess (1973) for the limit of resolution, Kallweit and Wood (1982) generalized the limit of thin-bed resolution to be the separation between the inflection points on the central lobe of the convolved wavelet regardless of the polarities of the reflection coefficients. They also pointed out that the

composite wavelet described by Widess (1973) does not stabilize in shape at the bed thickness equal to $(1/8)\lambda_d$ as Widess concluded on a visual basis. Rather, the predominant wavelength keeps decreasing (peak frequency increasing) as the bed thins, and stabilizes only at the limit of zero separation.

A second approach to defining a thin bed is given by the linearity limit of the maximum amplitude of the composite wavelet as a function of the bed thickness. By approximating the amplitude behaviour of a wavelet near its peak with that of a monochromatic sine wave whose period is equal to the predominant period of the wavelet, Widess (1973) derived the expression:

$$A_d = \frac{4\pi A_i r b}{\lambda_d} \quad (1.1)$$

where A_d = maximum amplitude of the composite wavelet

A_i = mean amplitude of the maximum peak and trough of the input wavelet

r = magnitude of the reflection coefficients

b = thickness of the thin bed

λ_d = predominant wavelength in the thin bed

The above expression indicates that, for thin beds, the maximum amplitude of the reflection is approximately proportional to the thickness of the bed and inversely proportional to the predominant wavelength. Indirectly, Widess (1973) defined a thin bed as a bed whose thickness is such that the amplitude of a composite reflection obeys the above expression. Koefoed and de Voogd (1980) refined this definition and proposed that a bed is thin if the amplitude response, as a function of thickness, deviates less than 10%

from a linear relationship. Using an integral representation of a wavelet, de Voogd and den Rooijen (1983) derived the relationship:

$$b(x, t) = \frac{r\zeta}{1-r^2} a'(x, t) \quad (1.2)$$

where $b(x, t)$ = composite wavelet, x being the depth

$a'(x, t)$ = first derivative of the input wavelet $a(x, t)$ with respect to time

r = reflection coefficient

ζ = 2-way travelttime in the thin layer

They concluded that a layer is thin if the composite reflection has the shape of the first derivative of the wavelet and if its amplitude is proportional to the thickness of the layer and to a factor depending upon the reflection coefficient of one of the interfaces. Note that Widess (1973), Koefoed (1980), and de Voogd (1980, 1983), all considered only vertical plane waves incident upon a thin layer within a homogeneous medium; i.e. two equal-value coefficients with opposite polarities. Hence, their conclusions cannot be considered general.

Stratigraphic interpretation of thin layers was not emphasized until the late 1970s when advances in field acquisition techniques rendered seismic amplitude interpretation more reliable. Since then, there has been steady but not an extensive published volume of literature on the subject. Most of the investigations are non-analytical, with quantitative results obtained mostly from modelling. Ricker (1953) first studied the relationship between the resolution of the top and bottom of a thin layer and the wavelength of a source wavelet. Based on modelling results, Meissner and Meixner (1969) showed that single thin layers, as well as two thin layers, can deform the input wavelet due to complex interference between reflections from the various boundaries. Widess (1973), as shown

earlier, explicitly defined a thin layer and derived a mathematical expression relating the amplitude of the composite wavelet to the thickness of a single layer, as well as to the wavelength of the input wavelet. Meckel and Nath (1977) and Neidell and Poggiagliolmi (1977) discussed various aspects of stratigraphic interpretation, including the limits of both vertical and lateral resolution, as well as geological factors leading to waveform changes. However, most of their interpretations were based on modelling results. Koefoed and de Voogd (1980) showed that, within the linearity criterion discussed above, a thin layer may be replaced by an equivalent layer which gives the same reflection response but differs in thickness and in acoustic impedance. The results were applied to modelling the seismic response of coal seams for which the two-way traveltimes are less than the trace sampling interval. Similarly, Gochioco (1991) also studied the reflection responses of thin coal seams, although his emphasis was entirely on qualitative tuning and interference effects. Robertson and Nogami (1984) used complex attributes to delineate thin layers, and showed that, as the time thickness of the layer thins to a quarter period of the dominant seismic energy, there is an anomalous increase in instantaneous frequency, which remains high as the layer thins to zero thickness. This technique is demonstrated in Chapter 6 for a Glauconitic gas-filled sandbar in southern Alberta. Knapp (1990) discussed the relationship between the vertical resolution of thick beds, thin beds, and thin-bed cyclothems. However, the peak frequency of the input seismic signal used in his study was of the order of 500 Hz. This contrasts with the common peak frequency of about 30-50 Hz found in most exploration seismic data.

Almoghrabi and Lange (1986; 1988) combined the amplitude responses and AVO responses of a thin layer to normally incident plane waves. They used amplitude, frequency, and phase information of both P - P and mode-converted (P - S) waves to deduce lithological information about the thin layer. Their multi-parameter analysis leads to a flow-chart which can assist in identifying pore-fluid type. However, they considered only

the case of a thin layer bounded by two opposite-polarity reflection coefficients, and did not examine the case of a thin layer bounded by two equal-polarity reflection coefficients. Mazzotti (1991) also studied the AVO effects of layers in terms of amplitude, frequency, and phase indicators derived from complex attributes. He emphasized that differential interference with offset, i.e. offset-dependent tuning, must be considered in AVO interpretation of thin layers. In recent years, there has also been increasing emphasis on reservoir characterization where seismic amplitude information from thin reservoirs is correlated with reservoir parameters through modelling to deduce optimum development drilling locations. Neff's (1990; 1993) incremental pay thickness methods are good examples.

For the purpose of this dissertation, a thin bed is defined simply as a layer whose thickness is equal to or less than 1/4 of the predominant wavelength of the propagating seismic energy. Hence, the term "thickness of interest", which will be used throughout the dissertation, is defined as the thickness range between 0 to 1/4 of this wavelength.

1.4 Amplitude variation with offset (AVO)

Consider a plane P -wave with amplitude A_0 incident on the boundary between two isotropic and homogeneous media in welded contact. Boundary conditions, requiring the continuity of normal and tangential stresses and displacements at the boundary, lead to four equations with four unknowns. These unknowns correspond to the amplitudes of the reflected and refracted P - and S -waves. This is illustrated in Figure 1.1 where A_1 , A_2 , θ_1 and θ_2 are the amplitudes and incidence angles of the reflected and refracted P -waves and B_1 , B_2 , λ_1 and λ_2 are the amplitudes and incidence angles of the reflected and refracted S -waves, respectively.

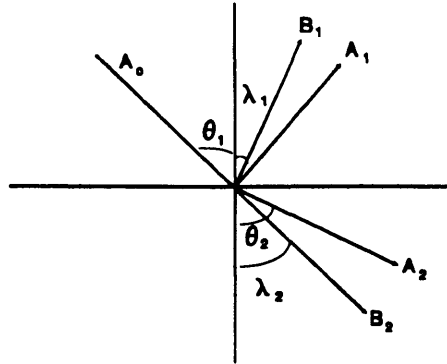


Figure 1.1 Waves generated at an interface by an incident P -wave.

If α_1 and β_1 are the P - and S -wave velocities of the upper (incident) medium, and α_2 and β_2 are those of the lower medium, then Snell's Law gives:

$$\frac{\sin\theta_1}{\alpha_1} = \frac{\sin\theta_2}{\alpha_2} = \frac{\sin\lambda_1}{\beta_1} = \frac{\sin\lambda_2}{\beta_2} = p$$

where p is commonly called the ray parameter. This means that once the incidence angle θ_1 is given, all the other angles can be found by the above expression.

Knotts (1899) and Zoeppritz (1919) developed independently the set of four equations, which can be found in many standard geophysics texts such as Telford *et al.* (1976). Muskat and Meres (1940) were among the first investigators to study the results of these equations, and they published tables of angle-dependent reflection and transmission coefficients for plane waves incident on elastic interfaces, using both P - and S -waves. Koefoed (1955) showed that the reflection coefficient's dependence on the incident angle was strongly affected by the value of the Poisson's ratio, which is defined as:

$$\sigma = \frac{\left(\frac{V_p}{V_s}\right)^2 - 2}{2\left[\left(\frac{V_p}{V_s}\right)^2 - 1\right]} \quad (1.3)$$

where V_p and V_s are the P - and S -waves velocities, respectively.

The Zoeppritz equations can be solved by setting up a 4x4 matrix and using a standard computer program for solving matrices. Bortfeld (1961) linearized these equations by assuming small changes in layer properties and both Aki & Richards (1980) and Shuey (1985) have derived approximate solutions to these equations based on similar assumptions.

Literature on the use of AVO in seismic exploration is extensive with many papers published over the last ten years. Most of these papers can be categorized into two groups. The first group focuses on the use of P -wave data only, using forward modelling or inversion of the amplitude variation to deduce a change in Poisson's ratio across the reflector. Since gas-saturated sands have lower values of Poisson's ratio than water-saturated sands, such a procedure can theoretically be used to predict the presence of gas. Ostrander (1984) discussed how gas sands can be detected on P -wave data when they are studied in CDP (common depth point) gather format instead of the conventional stack format. He pointed out that high-porosity gas sands tend to have abnormally low Poisson's ratios, and they should result in an increase in reflected P -wave energy with increasing angle of incidence if they are embedded into sediments with higher Poisson's ratios. However, in his example, the sand thickness is in excess of 30 m, and hence tuning effects are not considered. Wren (1984) also observed AVO changes in some P -wave reflection data for the Cardium Formation in Central Alberta, his emphasis being on the usefulness of partial stacks. In practice, many other factors can contribute to AVO effects (Ostrander, 1984; Neidell, 1986), and the method is far from straightforward.

The second group of AVO studies focuses on the use of both P -wave and S -wave data. Since pore-fluid type affects P -wave velocity significantly but S -wave velocity only slightly (Ensley, 1984), a change of pore-fluid such as from water to gas will lead to a P -wave amplitude anomaly without a corresponding S -wave amplitude anomaly. Conversely, a lateral change in lithology will produce amplitude anomalies for both P - and S -waves. Hence, by comparing the two data sets, one may be able to predict whether or not a P -wave AVO anomaly is the result of pore-fluid change or lithology change. Some authors (Tatham, 1982; McCormack *et al.*, 1984) also studied the relationship between changes in V_p/V_s and changes in physical properties of a formation. Almoghrabi and Lange (1986) stressed the importance of using a multi-parameter approach to evaluate pore fluid type from seismic amplitude distributions of both reflected P -waves and mode-converted S -waves. While the approach of using both P -wave and converted S -wave data is subjected to similar limitations as the use of P -wave data alone, it offers a potential advantage when applied to thin-bed analysis. This is because S -waves have a lower propagation velocity than P -waves and hence will suffer less differential tuning effects for the same thin bed, assuming that they have similar frequencies in the bed.

While the use of AVO anomaly can be informative, its interpretation is far from simple. Gas-saturated sands with low Poisson's ratios are one of many situations that could lead to AVO anomalies. Poley *et al.* (1985) demonstrated that when large velocity contrasts occur in or above the depths of interest, variations in recorded amplitude and phase with offset will be particularly pronounced. Eaton (1989) showed a similar result. Using a synthetic model of a 15-meter-thick gas sand buried to a depth of 1500 m, he showed that the Poisson's ratio estimated from inverting the AVO effects can exhibit significant errors if the free surface effect of a high velocity surface layer is not accounted for. Conversely, Jain (1987) showed that for Cretaceous gas prospects in central Alberta using recording spreads of typical length (2 km), the phase of reflected waves is stable and

amplitude changes on CDP gathers are too small to be mapped reliably in the presence of noise, due to surface waves and other sources. Rutherford and Williams (1989) separated gas sands into three classes: Class 1 have higher impedance than the encasing shale, with relatively large positive R_0 values, where R_0 is the normal incidence reflection coefficient; Class 2 have nearly the same impedance as the encasing shale and are characterized by values of R_0 near zero; Class 3 gas sands have lower impedance than the encasing shale with large negative values for R_0 . They showed that each class of sands has a distinct AVO characteristic. However, they considered sands that are relatively thick (50 meters or more) and hence ignored tuning effects. Their conclusions therefore may not be applicable to thin sands, such as the ones found in the Cretaceous formations of southern Alberta. Similarly, using seismic data from the Mestena Grande field in Texas, Burnett (1990) showed three categories of AVO characteristics which correspond to three production results. He attributed the differences between the modelling results and the real data partly to the presence of very thin beds.

Using the Monte Carlo method of analysis, Hampson (1991) showed that multi-layer AVO inversion is feasible, but the method still suffers from the problem of nonuniqueness. More recently, Kim *et al.* (1993) showed that anisotropy also has a significant effect on the AVO signature of P -waves for transversely isotropic media, and Xu *et al.* (1993) showed that AVO inversion may result in significant errors in velocity, density, and Poisson's ratio if inhomogeneous subsurface media are assumed to be homogeneous for the inversion.

1.5 Review of complex attributes

Consider a recorded seismic signal $x(t)$. The corresponding complex trace, $u(t)$ is defined as (Taner, 1979):

$$u(t) = x(t) + iy(t)$$

where $y(t)$ is the Hilbert transform of $x(t)$ (Bracewell, 1965); $y(t)$ is also called the quadrature of $x(t)$.

The instantaneous amplitude, $R(t)$, which is also called the amplitude envelope, is defined as:

$$R(t) = [x^2(t) + y^2(t)]^{\frac{1}{2}}.$$

and the instantaneous phase, $\phi(t)$, is defined as:

$$\phi(t) = \arctan \left[\frac{y(t)}{x(t)} \right].$$

Instantaneous frequency $w(t)$ is defined as:

$$w(t) = \frac{d\phi}{dt}.$$

Complex attributes have been familiar topics in electrical engineering ever since the 1940's, as discussed by Gabor (1946). However, possible applications to seismic signal analysis were not available in the geophysical literature until studies by Farnbach (1975), and Taner *et al.* (1977; 1979). These authors emphasized the advantages of the separation of the phase information from the amplitude information in the use of complex attributes. Robertson and Nogami (1984) studied the complex attributes of reflections from thin beds and reported an anomalous increase in the instantaneous frequency when the bed thinned to a value of $(1/8)\lambda_d$. Applying complex trace analysis, Rene *et al.* (1986) investigated the

polarization attributes of multi-component (P , SV , and SH) seismic surface waves. Using complex attributes, Scheuer and Oldenburg (1988) proposed a method to calculate local phase velocity by finding the trajectory of constant phase.

From the point of view of interpreting seismic data recorded over thin beds, complex attributes offer some unique benefits. Because complex attributes separate amplitude information from phase information, any low-amplitude subtle waveform changes can be detected more clearly by instantaneous phase and instantaneous frequency than is evident in the raw data. For this reason, as emphasized by both Taner *et al.* (1979) and Yilmaz (1987), instantaneous phase is a very useful tool for delineating discontinuities, faults, pinchouts, angularities and events with different dip attitudes. Also, the sudden increase in instantaneous frequency at the thickness equal to $(1/8)\lambda_d$ and below, as reported by Robertson and Nogami (1984), agrees with Widess' (1973) conclusion that in the same thickness range, the composite wavelet assumes the shape of the time derivative of the input wavelet. This increase in frequency is potentially a very powerful tool for delineating thin beds that have thicknesses below the value of $(1/8)\lambda_d$. This use of complex attributes is described in Chapter 6 in the study of a sandbar in southern Alberta.

1.6 Dissertation structure

This dissertation consists of seven chapters. Chapter 1 discusses the objectives of the dissertation, as well as a review of the concepts related to the seismic response of thin beds. Chapter 2 is a study of the amplitude behaviour of a reflected composite wavelet for normal-incidence reflections upon one and two thin layers. The emphasis is on developing analytical expressions with which one can predict the seismic amplitude behaviour of various geological models. Chapter 3 is similar to Chapter 2 in terms of content and

approach, except that the frequency behaviour is examined. In Chapter 4, complex attributes are used to examine subtle waveform changes for the normal-incidence models. The emphasis is a close examination of the usefulness of complex attributes in thin-bed interpretation, with model-based observations. Chapter 5 documents the study of amplitude, frequency, and complex attributes for the offset-dependent one-layer case. The emphasis is on quantitative changes as a function of lateral changes in Poisson's ratio. Chapter 6 is a study of field seismic data with the application of theories developed in Chapters 2 through 5. Finally, Chapter 7 is a summary of the results of the dissertation, and a discussion of the implication of the results. Future related research is also briefly discussed.

1.7 Hardware and software used

The numerical modelling data for normal-incidence study was obtained with the Outrider modelling package of Microseis Software Ltd., and the numerical modelling data for the offset-dependent study was generated with Dr. Lawton's modelling computer program. The complex attributes were generated using the Strata package, and the AVO analysis for the sandbar case study was performed with the AVO package, both of Hampson-Russell Software Services Ltd. All the above mentioned packages were run on a 486 PC. The synthetic seismogram plots and complex attribute plots were plotted with a Hewlett Packet dot-matrix plotter. All graphs were made using the Excel package, and all other diagrams and the text processing were done with Microsoft Word package, both of Microsoft Corporation.

Chapter 2 - Amplitude characteristics of seismic reflections from thin beds

2.1 Introduction

The most studied attribute of a wavelet in seismic interpretation for thin beds is its amplitude behaviour. As mentioned in Chapter 2, some authors define a thin bed according to the behaviour of the maximum amplitude of the reflected composite wavelet as a function of layer thickness. Before the common use of AVO, amplitude anomalies, such as bright spots and dim spots on conventional stack sections, were often used in stratigraphic interpretation to deduce the presence of hydrocarbons. Such attempts are often rendered unreliable by the presence of coal layers, which exhibit anomalously large reflection coefficients, and tuning effects of thin layers whose thicknesses vary laterally. Furthermore, most thin-layer interpretations are based on a single layer embedded in an infinitely homogeneous medium, i.e. two equal-magnitude but opposite-polarity reflection coefficients. The two analytical expressions relating amplitude to thickness [equations (1.1) and (1.2)] are also based on the same model. The question of whether or not they can be used if the reflection coefficients are of non-equal magnitude and/or the same polarity, or if more than two reflection coefficients are involved, is addressed in this chapter.

In the next section, the primary objective is to develop an equation which relates the amplitude of the reflected composite wavelet to the thickness of a thin bed for the general case. In section 2.3, this equation is tested against the results from numerical modelling to establish its validity, and is then used to predict the amplitude behaviour of a thin bed, given a particular geological model. Conversely, given a measured amplitude behaviour, this relationship can be used to predict certain geological parameters by

comparing the forward modelling results to the observed results on seismic data. The method is also used to develop an amplitude equation for two thin layers, i.e. a sequence of three reflection coefficients (section 2.4), and the results are compared to those for a single layer.

2.2 Theory

In this section, two expressions for the amplitude response of a thin bed for the general case of unequal reflection coefficients at the top and base of the bed are developed. The first is an extension of Widess' method, and is based on a sinusoidal approximation, whereas the second is derived directly from the expression for a Ricker wavelet, since this wavelet is used commonly in seismic modelling. Transmission losses and internal multiples are ignored since, as pointed out by Koefoed and de Voogd (1980), such effects are negligible provided the acoustic impedance ratio between the thin layer and the surrounding rock lies between the bounds of 0.5 and 2, which is the range usually encountered in clastic sequences. In our examples, the acoustic impedance ratio ranges from 0.75 to 1.52.

2.2.1 Sinusoidal approximation

Consider a thin bed embedded in an infinitely homogeneous medium. Let r_1 and r_2 be the reflection coefficients of the upper and lower interfaces, respectively. In general, there are four fundamentally different two-term reflectivity series, categorized as :

Type I: $\uparrow\downarrow$ opposite polarity and equal magnitude

Type II: $\uparrow\uparrow$ equal polarity and equal magnitude

Type III: $\uparrow\downarrow$ opposite polarity and unequal magnitude

Type IV: $\perp\perp$ equal polarity and unequal magnitude.

Following the approach of Widess (1973), the central portion of a zero-phase wavelet can be approximated by a cosine wave whose period is equal to the predominant period of the wavelet, where the predominant period is the trough to trough time. Choosing the centre of the thin bed as the zero-time reference, the amplitude of the composite reflected wavelet can be approximated as:

$$A_r = A_i r_1 \cos \left[\left(t + \frac{b}{V} \right) \frac{2\pi}{T_d} \right] + A_i r_2 \cos \left[\left(t - \frac{b}{V} \right) \frac{2\pi}{T_d} \right] \quad (2.1)$$

where A_i = maximum amplitude of the cosine wave, b = thickness of the thin bed, V = P -wave velocity within the thin bed, and T_d = predominant period of the source wavelet.

Expanding the cosine terms, we have:

$$A_r = A_i (r_1 + r_2) \cos \frac{2\pi t}{T_d} \cos \frac{2\pi b}{\lambda_d} + A_i (r_2 - r_1) \sin \frac{2\pi t}{T_d} \sin \frac{2\pi b}{\lambda_d} \quad (2.1a)$$

where λ_d = predominant wavelength of the source wavelet within the thin bed.

For sufficiently small b , $\sin \frac{2\pi b}{\lambda_d} \approx \frac{2\pi b}{\lambda_d}$ and

$\cos \frac{2\pi b}{\lambda_d} = 1 - 2 \left(\sin \frac{\pi b}{\lambda_d} \right)^2 \approx 1 - 2 \left(\frac{\pi b}{\lambda_d} \right)^2$. These are the thin-bed approximations. Using

these approximations, equation (2.1a) can be simplified to:

$$A_r \approx A_i (r_1 + r_2) \left[1 - 2 \left(\frac{\pi b}{\lambda_d} \right)^2 \right] \cos \frac{2\pi t}{T_d} + A_i (r_2 - r_1) \frac{2\pi b}{\lambda_d} \sin \frac{2\pi t}{T_d}$$

$$= M_1 \cos \frac{2\pi t}{T_d} + M_2 \sin \frac{2\pi t}{T_d} \quad (2.2)$$

where $M_1 = A_i(r_1 + r_2) \left[1 - 2 \left(\frac{\pi b}{\lambda_d} \right)^2 \right]$ and $M_2 = A_i(r_2 - r_1) \frac{2\pi b}{\lambda_d}$.

For maximum or minimum A_r , $\frac{dA_r}{dt} = 0$.

Therefore,
$$\frac{dA_r}{dt} = -\frac{2\pi}{T_d} M_1 \sin \frac{2\pi t}{T_d} + \frac{2\pi}{T_d} M_2 \cos \frac{2\pi t}{T_d} = 0.$$

Hence,
$$\tan \frac{2\pi t}{T_d} = \frac{M_2}{M_1},$$

and thus extreme values of A_r occur at times given by

$$t = \frac{T_d}{2\pi} \tan^{-1} \left(\frac{M_2}{M_1} \right).$$

Since we are using continuous cosine waves to derive the above expression, there is actually more than one value of t that would give maximum or minimum values of A_r . A value of $t + \frac{n\pi}{\omega}$, where n is an integer and ω is the angular frequency of the cosine wave, will lead to either maximum or minimum values of A_r . However, we are interested only in the extreme values of A_r for minimum values of t , therefore, we consider the case where $n = 0$ only.

Substituting this expression for t into equation (2.2), we obtain:

$$\begin{aligned}
A_{s_{\max}} &= M_1 \cos \frac{2\pi}{T_d} \left[\frac{T_d}{2\pi} \tan^{-1} \left(\frac{M_2}{M_1} \right) \right] + M_2 \sin \frac{2\pi}{T_d} \left[\frac{T_d}{2\pi} \tan^{-1} \left(\frac{M_2}{M_1} \right) \right] \\
&= M_1 \frac{M_1}{\sqrt{M_1^2 + M_2^2}} + M_2 \frac{M_2}{\sqrt{M_1^2 + M_2^2}} = \sqrt{M_1^2 + M_2^2}.
\end{aligned}$$

Therefore,

$$A_{s_{\max}} = A_i \left\{ (r_1 + r_2)^2 \left[1 - 2 \left(\frac{\pi b}{\lambda_d} \right)^2 \right]^2 + (r_2 - r_1)^2 \left(\frac{2\pi b}{\lambda_d} \right)^2 \right\}^{\frac{1}{2}}. \quad (2.3)$$

In equation (2.3), $A_{s_{\max}}$ has a positive value for the reflected composite wavelet peak and a negative value for the trough. Since equation (2.3) is derived from the interference of two continuous sine waves with the same period, the two roots should be identical in magnitude due to symmetry. Therefore, we need only consider the positive value of $A_{s_{\max}}$ and refer to $A_{s_{\max}}$ as the absolute maximum amplitude.

The subscript in $A_{s_{\max}}$ indicates that we are referring to the maximum amplitude of the reflected wavelet using sinusoidal approximation. We will later use $A_{r_{\max}}$ to represent the maximum amplitude of the reflected wavelet using Ricker approximation. The positive square root of equation (2.3) gives the absolute maximum amplitude of the reflection from a thin bed for the general case, provided that $b < \left(\frac{\lambda_d}{8} \right)$. For $r_1 = -r_2$, the first term in equation (2.3) is zero and the second term becomes $4\pi r_1 b A_i / \lambda_d$, which is identical to the expression derived by Widess (1973). For $r_1 = r_2 = r_i$, the second term is zero and the first term becomes $2A_i r_i \left(1 - 2\pi^2 b^2 / \lambda_d^2 \right)$, which approaches a value of $2A_i r_i$, as b approaches zero, as expected. For $|r_1| \neq |r_2|$, $A_{s_{\max}}$ receives contribution from both terms. Equation (2.3) also indicates that, except for the case of $r_2 = -r_1$, the absolute maximum amplitude of a composite wavelet reflected from the top and the

bottom of a thin bed is not linearly proportional to the bed thickness, but rather, the relationship is a second-order polynomial.

The fact that equation (2.3) is derived from using a continuous cosine wave leads to an interesting property. For a thin bed represented by two reflection coefficients of equal polarity, numerical results from equation (2.3) are close to modelling results one would obtain regardless of whether the source wavelet is zero-phase or 90°-phase (these results are presented in sections 2.3.2 and 2.3.4). However, if the coefficients are of opposite polarities, equation (2.3) gives values that are valid only for a 90°-phase source wavelet (sections 2.3.1 and 2.3.3). The reason for this can be explained graphically by considering the response of a Type II reflectivity sequence.

Figure 2.1a shows two schematic representations of two identical cosine waves separated by a distance less than 1/8 of their period. Note that a convolution of a cosine wave with the two reflection coefficients can be obtained by simply summing two cosine waves with the proper polarities and separated by the same time distance between the coefficients. Figure 2.1b shows the results of the summation of the two cosine curves; the boxed portions of the curves in both Figures 2.1a and 2.1b indicating the corresponding areas before and after summing. If we compare these two boxes to the corresponding boxes in Figures 2.1c and 2.1d for a zero-phase source wavelet, whose predominant period is equal to the period of the cosine wave, it is clear that they are very similar. Hence, equation (2.3) is a good approximation for the equal-polarity case with a zero-phase source wavelet. This is also true if the source wavelet is 90°-phase, since the peak region of a Ricker 90°-phase wavelet has the same shape as that of a zero-phase wavelet.

Figure 2.2 shows similar diagrams for Type I reflectivity. It is clear from Figure 2.2a that the portions of the cosine curves inside the box are quite different from those of the zero-phase wavelets in the box in Figure 2.2c. The much lower amplitude of the side lobe of the zero-phase wavelet results in this difference. However, in Figure 2.2e where a

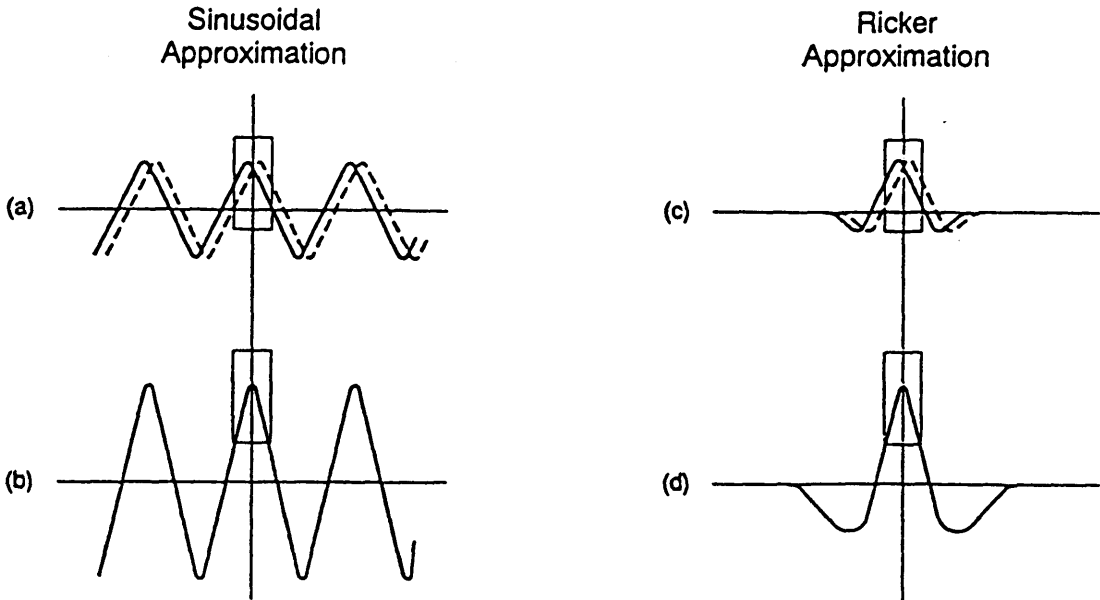


Figure 2.1 Sinusoidal and Ricker approximations for Type II ($\perp\perp$) reflectivity. (b) and (d) are schematic representations of summations of the two curves in (a) and (c), respectively.

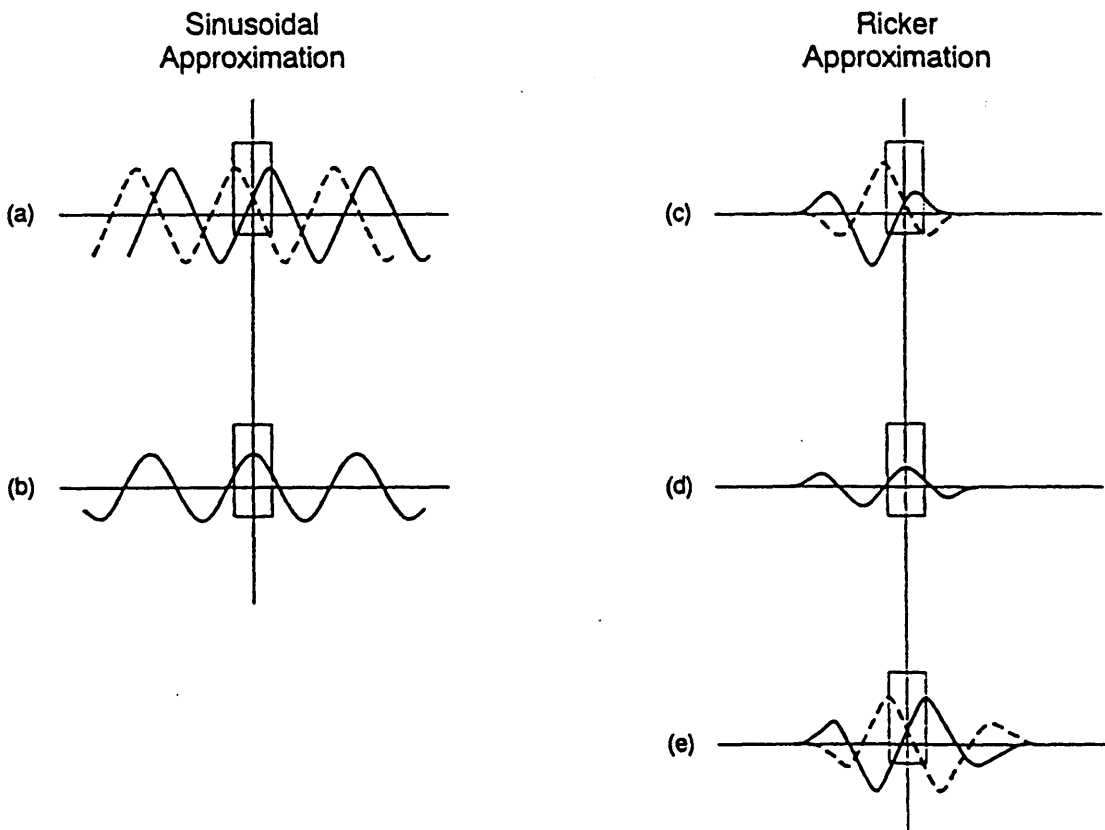


Figure 2.2 Sinusoidal and Ricker approximations for Type I ($\perp\perp$) reflectivity. (b) and (d) are summations for the two curves in (a) and (c), respectively. (e) shows the 90° -phase equivalent of (c).

90°-phase wavelet is used, the portions of the wavelets in the box resemble those of the cosine waves in the box in Figure 2.2a. Hence, for Type I reflectivity, equation (2.3) gives results that are comparable to that of a 90°-phase source wavelet, not that of a zero-phase source wavelet.

Figures 2.1 and 2.2 also explain two other features of equation (2.3). As shown in section 2.3, within the thickness of interest, the rate of change of the amplitude as a function of thickness is larger for Type I reflectivity than for Type II reflectivity. The reason is that, for the former case, the maximum amplitude of the reflected composite wavelet results from the summation of the cosine curves around the mid-point between a peak and a trough where the gradients of the curves are maximum. On the contrary, for latter case, the corresponding maximum amplitude is the result of the summation around the peaks of the cosine waves where the gradients are close to zero, resulting in a slower change in amplitude as the thickness varies.

The above amplitude property can also be studied mathematically. From equation (2.3), for Type I reflectivity, $A_{s\max} = \frac{4\pi r_1 A_i}{\lambda_d}$. Therefore, $\left(\frac{\partial A_{s\max}}{\partial b}\right)_I = \frac{4\pi r_1 A_i}{\lambda_d}$ which is a constant. Similarly, for Type II reflectivity,

$$A_{s\max} = 2A_i r_1 \left(1 - \frac{2\pi^2 b^2}{\lambda_d^2}\right)$$

$$\left(\frac{\partial A_{s\max}}{\partial b}\right)_{II} = -\left(\frac{8\pi^2 r_1 A_i}{\lambda_d^2}\right)$$

If $b = \left(\frac{1}{8}\right)\lambda_d$, $\left(\frac{\partial A_{s\max}}{\partial b}\right)_{II} = -\frac{\pi^2 r_1 A_i}{\lambda_d}$.

Thus, $\left| \left(\frac{\partial A_{s \max}}{\partial b} \right)_I \right| > \left| \left(\frac{\partial A_{s \max}}{\partial b} \right)_{II} \right|$ if b is $\left(\frac{1}{8} \right) \lambda_d$ or less.

The second feature is that, according to Widess (1973), the A_i in equation (2.3) is assumed to be the average of the input wavelet absolute peak and trough amplitudes. Figures 2.1c and 2.1d explain the reason for this assumption. For Type I reflectivity, the maximum amplitude of the composite wavelet is the result of the summation of the source wavelets around the mid-point between a peak and a trough. The amplitude in this area is much less than the maximum amplitude at the peak. For this reason, if a zero-phase wavelet is used in modelling as a source wavelet for the opposite-polarity case, the maximum amplitude of the reflected composite wavelet will always be lower than those calculated from equation (2.3) by a factor dependent on the functional form of the wavelet. However, we can use equation (2.8) which is derived specifically for a Ricker wavelet as a source wavelet for the Widess case.

Finally, a significant attribute of equation (2.3) is that, given any two-coefficient reflectivity series, it predicts the behaviour of the amplitude as a function of thickness for a thinly bedded sequence, assuming that the source wavelet has a predominant period and its central portion can be approximated by a sinusoid.

2.2.2 Ricker zero-phase wavelet

In the time domain, a Ricker zero-phase wavelet with the peak at $t = 0$ is given by Ricker (1940):

$$x(t) = A_i \left(1 - 2\pi^2 f_0^2 t^2 \right) e^{-\pi^2 f_0^2 t^2} \quad (2.4)$$

where A_i = wavelet peak amplitude and f_0 = maximum frequency of the amplitude spectrum of the wavelet (peak frequency). Given a Type I reflectivity, with reflection coefficients of opposite polarities and equal amplitudes, r , located at $-\Delta t$ and Δt , the convolution of the Ricker wavelet with this reflectivity can be written as:

$$R(t) = A_i r \left[1 - 2\pi^2 f_0^2 (t - \Delta t)^2 \right] e^{-\pi^2 f_0^2 (t - \Delta t)^2} - A_i r \left[1 - 2\pi^2 f_0^2 (t + \Delta t)^2 \right] e^{-\pi^2 f_0^2 (t + \Delta t)^2}$$

For $\Delta t \ll \tau$, where τ is the period of the wavelet, we can ignore second-order terms in Δt :

$$R(t) \approx A_i r e^{-\pi^2 f_0^2 t^2} \left\{ \left[1 - 2\pi^2 f_0^2 (t^2 - 2t\Delta t) \right] e^{\pi^2 f_0^2 2t\Delta t} - \left[1 - 2\pi^2 f_0^2 (t^2 + 2t\Delta t) \right] e^{-\pi^2 f_0^2 2t\Delta t} \right\}$$

Finally, approximating $e^{\pi^2 f_0^2 2t\Delta t} \approx 1 + 2\pi^2 f_0^2 t\Delta t$ and $e^{-\pi^2 f_0^2 2t\Delta t} \approx 1 - 2\pi^2 f_0^2 t\Delta t$ for small values of Δt ,

$$\begin{aligned} R(t) &\approx A_i r e^{-\pi^2 f_0^2 t^2} \left\{ \left[1 - 2\pi^2 f_0^2 (t^2 - 2t\Delta t) \right] \left[1 + 2\pi^2 f_0^2 t\Delta t \right] - \left[1 - 2\pi^2 f_0^2 (t^2 + 2t\Delta t) \right] \left[1 - 2\pi^2 f_0^2 t\Delta t \right] \right\} \\ &= A_i r 4\pi^2 f_0^2 \Delta t e^{-\pi^2 f_0^2 t^2} \left\{ 3t - 2\pi^2 f_0^2 t^3 \right\}. \end{aligned} \quad (2.5)$$

For maximum or minimum $R(t)$:

$$\frac{dR(t)}{dt} = A_i r 4\pi^2 f_0^2 \Delta t \left[-2t\pi^2 f_0^2 e^{-\pi^2 f_0^2 t^2} (3t - 2\pi^2 f_0^2 t^3) + e^{-\pi^2 f_0^2 t^2} (3 - 6\pi^2 f_0^2 t^2) \right] = 0$$

$$4\pi^4 f_0^4 t^4 - 12\pi^2 f_0^2 t^2 + 3 = 0$$

which yields

$$\therefore t = \pm \left(\frac{3 \pm \sqrt{6}}{2} \right)^{\frac{1}{2}} \frac{1}{\pi f_0} \quad (2.6)$$

Equation (2.6) shows that there are four roots for t , implying the existence of a total of four peaks and/or troughs for the reflected composite wavelet. Since we are interested in the absolute maximum amplitude, we will consider only the root that corresponds to a higher-amplitude peak or trough at minimum positive t .

$$\therefore t = \left(\frac{3 - \sqrt{6}}{2} \right)^{\frac{1}{2}} \frac{1}{\pi f_0} = \frac{0.5246}{\pi f_0} = \frac{K}{\pi f_0}$$

Hence, from equation (2.5), we obtain:

$$\begin{aligned} A_{r, \max} &= A_i r 4 \pi^2 f_0^2 \Delta t e^{\left(-\pi^2 f_0^2 \frac{K^2}{\pi^2 f_0^2} \right)} \left\{ \frac{3K}{\pi f_0} - \frac{2\pi^2 f_0^2 K^3}{(\pi f_0)^3} \right\} \\ &= A_i r 4 \pi f_0 e^{-K^2} \Delta t (3K - 2K^3) \\ &= 4\pi A_i r \Delta t f_0 M \end{aligned} \quad (2.7)$$

where $M = e^{-K^2} (3K - 2K^3) = 0.9759$ (since $K = 0.5264$).

Note that $\Delta f_0 = \frac{b}{V} f_0 = \frac{b}{\lambda_0}$ where f_0 and λ_0 are the peak frequency and peak

wavelength, respectively. As shown by Kallweit and Wood (1982), they are related to the predominant frequency f_d and the predominant wavelength λ_d by the following relations:

$$f_d = 1.28 f_0 \quad \text{and} \quad \lambda_d = \frac{\lambda_0}{1.28}$$

Hence, equation (2.7) can be expressed as:

$$\begin{aligned} A_{r_{\max}} &= \frac{4 \pi A_i r b M}{1.28 \lambda_d} = \frac{0.9759}{1.28} \left(\frac{4 \pi A_i r b}{\lambda_d} \right) \\ &= 0.76 \left(\frac{4 \pi A_i r b}{\lambda_d} \right) \end{aligned} \quad (2.8)$$

Equation (2.8) gives the maximum absolute amplitude of the reflected composite wavelet for Type I reflectivity for a Ricker zero-phase source wavelet. Equations (2.8) and (1.1) differ only by a constant equal to 0.76. However, in equation (1.1), A_i is the average amplitude of the peak and trough of the source wavelet, but in equation (2.8), A_i is simply the maximum amplitude of the peak.

For Type II reflectivity, the reflection amplitude $R(t)$ is given by:

$$R(t) = A_i r \left[1 - 2 \pi^2 f_0^2 (t - \Delta t)^2 \right] e^{-\pi^2 f_0^2 (t - \Delta t)^2} + A_i r \left[1 - 2 \pi^2 f_0^2 (t + \Delta t)^2 \right] e^{-\pi^2 f_0^2 (t + \Delta t)^2}$$

From symmetry, the maximum peak of the composite wavelet occurs at $t = 0$.

Hence, we have:

$$\begin{aligned} A_{r_{\max}} &= A_i r \left(1 - 2 \pi^2 f_0^2 (\Delta t)^2 \right) e^{-\pi^2 f_0^2 (\Delta t)^2} + A_i r \left(1 - 2 \pi^2 f_0^2 (\Delta t)^2 \right) e^{-\pi^2 f_0^2 (\Delta t)^2} \\ &\approx 2 A_i r \left(1 - 2 \pi^2 f_0^2 (\Delta t)^2 \right) \left(1 - \pi^2 f_0^2 (\Delta t)^2 \right) \end{aligned} \quad (2.9)$$

ignoring terms of $o(\Delta t^4)$ and higher for small Δt .

From equation (2.9), it is evident that, unlike Type I reflectivity analysis, terms of second order in Δt cannot be ignored for the Type II case, if the behaviour of $A_{r_{\max}}$ as a function of the bed thickness is to be studied. This is due to the fact that the rate of change of amplitude as a function of bed thickness is smaller for Type II reflectivity than that for Type I reflectivity. However, ignoring terms of $o(\Delta t^4)$, we can write:

$$\begin{aligned} A_{r_{\max}} &= 2 A_i r \left[1 - 3\pi^2 f_0^2 \Delta t^2 \right] \\ &= 2 A_i r \left[1 - 1.831 \left(\frac{\pi b}{\lambda_d} \right)^2 \right] \end{aligned} \quad (2.10)$$

$$A_{r_{\max}} = 2 A_i r \left[1 - 2 \left(\frac{\pi b}{\lambda_d} \right)^2 \right] + 0.34 A_i r \left(\frac{\pi b}{\lambda_d} \right)^2 \quad (2.11)$$

Comparing the sinusoidal approximation with the Ricker wavelet solution, we find that the first term in equation (2.11) is equivalent to equation (2.3) with $r = r_1 = r_2$. Thus, using sinusoidal approximation for a Ricker wavelet for the case of Type II reflectivity will introduce an error of $-0.34 A_i r \left(\frac{\pi b}{\lambda_d} \right)^2$ in the peak amplitude. This error is a function of the bed thickness and Figure 2.3 shows the error function between the two methods as a function of thickness calculated according to:

$$\text{error (\%)} = \frac{0.34 A_i r \left(\frac{\pi b}{\lambda_d} \right)^2}{2 A_i r \left[1 - 1.831 \left(\frac{\pi b}{\lambda_d} \right)^2 \right]} \times 100\%$$

From Figure 2.3, it is evident that the sinusoidal approximation for a Ricker wavelet is suitable in a Type II reflectivity earth model provided that the bed thickness is less than $(1/8)\lambda_d$, defining a 10% difference as the limit of acceptable deviation.

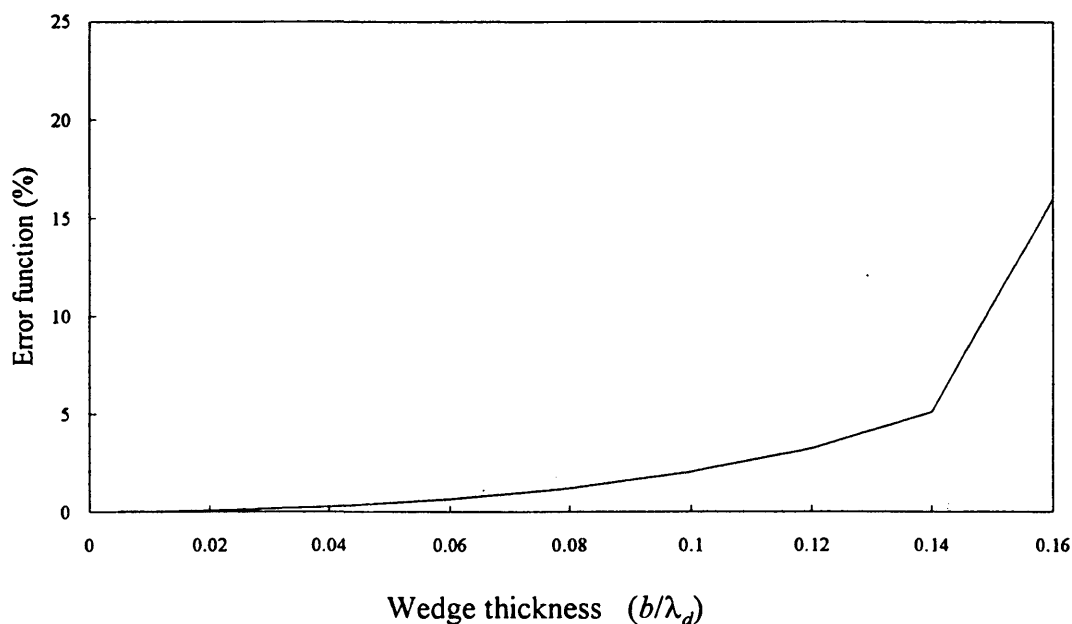


Figure 2.3 Comparison between sinusoidal and Ricker approximations for Type II reflectivity.

For Types III and IV reflectivity series, we can decompose the two reflectivities into sums of Types I and II reflectivities:

$$\begin{array}{c} r_2 \\ | \\ \hline r_1 \end{array} = \begin{array}{c} r_3 \\ | \\ \hline -r_3 \end{array} + \begin{array}{c} r_4 \\ | \\ \hline r_4 \end{array} \quad (2.12)$$

$$\begin{array}{c} r_1 \\ | \\ \hline r_2 \end{array} = \begin{array}{c} r_3 \\ | \\ \hline -r_3 \end{array} + \begin{array}{c} r_4 \\ | \\ \hline r_4 \end{array} \quad (2.13)$$

where $r_3 = \frac{r_2 - r_1}{2}$ and $r_4 = \frac{r_2 + r_1}{2}$.

However, for a thin-bed model, the wavelet formed by the convolution of the source wavelet with a Type I reflectivity is a 90°-phase wavelet (wavelet A), whereas the corresponding wavelet for Type II reflectivity is zero-phase (wavelet B). Therefore, the maximum amplitude of the composite event is not equal to the sum of the individual maxima of the two wavelets, but, since wavelets A and B have similar frequencies, their sum can be expressed as $A+iB$, so that the amplitude of the sum can be expressed as $\sqrt{R_a^2 + R_b^2}$, where R_a and R_b are the amplitudes of wavelets A and B , respectively. Thus, for Type III and IV reflectivities, the maximum amplitude of the reflected wavelet is given by:

$$A_{r_{\max}} = A_i \left\{ (2r_4)^2 \left[1 - 1.831 \left(\frac{\pi b}{\lambda_d} \right)^2 \right]^2 + 0.76^2 (2r_3)^2 \left(\frac{2\pi b}{\lambda_d} \right)^2 \right\}^{\frac{1}{2}}$$

Using $r_3 = \frac{r_2 - r_1}{2}$ and $r_4 = \frac{r_2 + r_1}{2}$, we obtain

$$A_{r_{\max}} = A_i \left\{ (r_1 + r_2)^2 \left[1 - 1.831 \left(\frac{\pi b}{\lambda_d} \right)^2 \right]^2 + 0.76^2 (r_2 - r_1)^2 \left(\frac{2\pi b}{\lambda_d} \right)^2 \right\}^{\frac{1}{2}} \quad (2.14)$$

Comparing the sinusoidal approximation as represented by equation (2.3) and the Ricker approximation as represented by equation (2.14) shows that these equations are similar if we introduce into equation (2.3) a coefficient M whose value depends on the source wavelet, i.e.

$$A_{s\max} = A_i \left\{ (r_1 + r_2)^2 \left[1 - 2 \left(\frac{\pi b}{\lambda_d} \right)^2 \right]^2 + M^2 (r_2 - r_1)^2 \left(\frac{2\pi b}{\lambda_d} \right)^2 \right\}^{\frac{1}{2}} \quad (2.15)$$

We have shown that for Type I reflectivity, M is 0.76 if the source wavelet is a Ricker wavelet.

2.3 Normal incidence, single-layer model

To study the amplitude response of a thin bed to vertically-incident plane waves, a simple wedge model (Figure 2.4) was used.

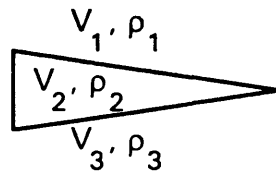


Figure 2.4 A wedge model.

Densities and velocities used for the models that represent the four types of reflectivities are listed in Table 2.1. The velocities were chosen to be typical of early Cretaceous formations in southern Alberta, and the densities were calculated from the velocities using the equation of Gardner (1974). For all four models, the reflection coefficients for the upper interface and lower interface are referred to as r_1 and r_2 , respectively. The geometry of the wedge model was set up so that the number of each trace in the synthetic seismograms is equal to the thickness of the wedge in metres at the trace location. In generating these seismograms, the Ricker wavelet is multiplied by the two reflection coefficients of each reflectivity series, and the two resulting wavelets separated by the same time interval as that separating the two corresponding reflection coefficients are summed to obtain the composite wavelet. Because of the thickness of

interest, the number of traces plotted for each synthetic seismogram will extend to only two to three metres more than the $(1/4)\lambda_d$ value. All synthetic seismograms shown in Figure 2.5 were generated by convolving a 31-Hz (peak frequency) Ricker wavelet with a two-term reflectivity series, since 31 Hz is a typical peak frequency on seismic data from the Western Canadian Sedimentary Basin. A zero-phase wavelet is chosen because a zero-phase wavelet gives the maximum vertical resolution compared to other phases, as shown by Berkout (1984), based on the second moments of wavelets. Other peak frequencies will also be used to test the frequency dependence of the equations developed in section 2.2. A 90°-phase wavelet will also be used whenever appropriate. Transmission losses and internal multiples were ignored, and all seismograms were generated with a sampling interval of 0.1 ms. The maximum amplitude of the input Ricker wavelet was arbitrarily set at 1000. For each seismogram generated, the maximum amplitude of each trace was picked, and these amplitudes were compared to those values predicted from equations (2.14) and (2.15).

Table 2.1 Lithologies, layer velocities, layer densities, and reflection coefficients for four models

Types of Reflectivity Series	Above Wedge V_1 (m/s) ρ_1 (kg/m ³)	Wedge V_2 (m/s) ρ_2 (kg/m ³)	Below Wedge V_3 (m/s) ρ_3 (kg/m ³)	r_1	r_2
I	non-porous sand 4270 2505	porous sand 3050 2303	non-porous sand 4270 2505	-0.2072	0.2072
II	porous sand 3050 2303	silt 3560 2395	non-porous sand 4270 2505	0.1047	0.1047
III	silt 3800 2434	porous sand 3050 2303	non-porous sand 4270 2505	-0.1371	0.2072
IV	porous sand 3050 2303	shale 3350 2359	non-porous sand 4270 2505	0.0596	0.1494

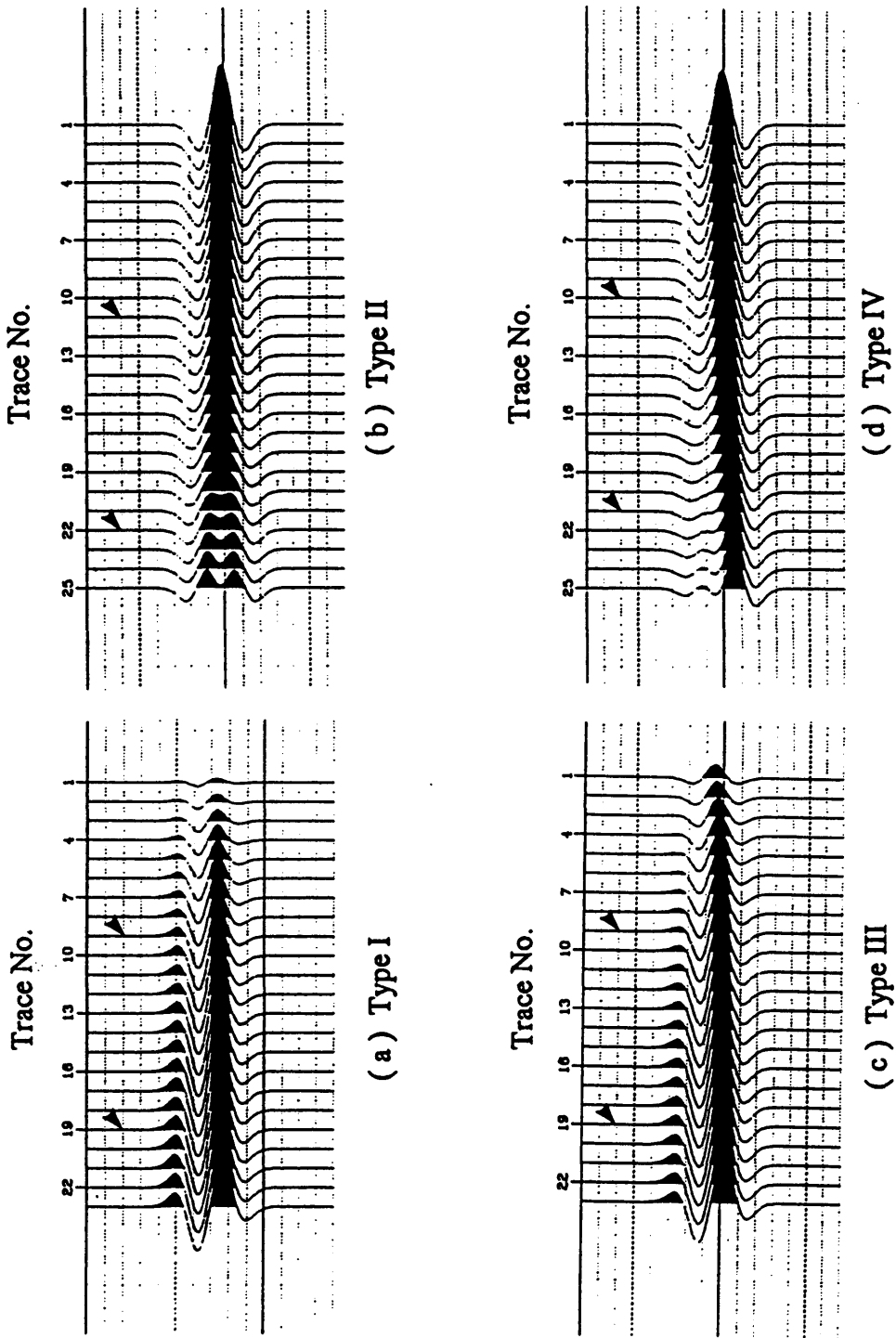


Figure 2.5 Synthetic seismograms for (a) Type I, (b) Type II, (c) Type III, and (d) Type IV reflectivities. The source wavelet is a 31-Hz Ricker wavelet, and the arrows indicate the $(1/8)\lambda_d$ and $(1/4)\lambda_d$ locations. Timing lines are at 10-ms intervals.

2.3.1 Type I reflectivity

This case represents a thin bed embedded in an homogeneous and isotropic medium. Although such a bed is rarely encountered in real geological situations, it is the most studied case in thin-bed interpretation because of its simplicity. Since $r_1 = -r_2 = -0.2072$, equations (2.14) and (2.15) reduce to:

$$A_{r\max} = 0.76 \left(\frac{4\pi A_i r b}{\lambda_d} \right) \text{ where } r = |r_1| = |r_2| \text{ and } A_{s\max} = M \left(\frac{4\pi A_i r b}{\lambda_d} \right) \text{ respectively.}$$

Recall that $A_{r\max}$ and $A_{s\max}$ correspond to Ricker and sinusoidal approximations, respectively. For a Ricker source wavelet, $M = 1$ if it is 90°-phase, and $= 0.76$ if it is zero-phase, M being a constant independent of frequency. To check these properties of M , Type I reflectivity was modelled six times with six different Ricker wavelets, three zero-phase wavelets with frequencies at 18 Hz, 31 Hz and 50, and three 90°-phase wavelets with the same frequencies. The numerical results are listed in Table 2.2 in Appendix A, and they are plotted in Figure 2.6.

In Figure 2.6, the Ricker and sinusoidal approximations are plotted only to a thickness slightly beyond the $(1/8)\lambda_d$ value. This is because these approximations are not valid beyond this thickness, if one assumes a 10% difference as the limit of acceptable agreement between these approximations and the modelled data. As Table 2.2 indicates, the differences between the modelled data and the sinusoidal and Ricker approximations are less than 10% for thicknesses less than the $(1/8)\lambda_d$ value. For thicknesses below $(1/16)\lambda_d$, the minor fluctuations in the differences are caused by the non-systematic round-off errors resulting from using a discrete sampling interval in the modelling process. As the thickness increases to beyond the $(1/16)\lambda_d$ value, the difference begins to increase steadily because the thin-bed assumption is slowly being violated. The modelled values are listed and plotted to a thickness slightly beyond the $(1/4)\lambda_d$ value, since our thickness

of interest is up to $(1/4)\lambda_d$ value. As shown in Figure 2.6, tuning occurs at about $(1/4)\lambda_d$ thickness.

In Figure 2.6, the amplitude values for the Ricker approximation are obtained by multiplying the corresponding amplitudes for sinusoidal approximation by the factor M . The results agree with the modelling results with a Ricker source wavelet for up to about $(1/8)\lambda_d$ thickness for all three frequencies. This implies that the Ricker approximation is correct and that M is indeed independent of frequency. However, modelled results in Figure 2.6 using a zero-phase source wavelet deviate from the Ricker approximation for all three frequencies more rapidly than the modelled results with a 90° -phase source wavelet from the sinusoidal approximation. The reason is that the summation of a Ricker wavelet with its reverse separated by Δt involves the side lobes of the wavelets (Figure 2.2c), requiring second-order terms to describe the results. However, second- and higher-order terms in Δt were ignored when the expression A_{\max} was derived for the case of $r_2 = -r_1$.

Based on the results shown in Figures 2.6, both the sinusoidal and Ricker approximations are good approximations for beds that are less than a thickness of $(1/8)\lambda_d$, and are independent of frequencies. They also indicate that, below this thickness, the function of the maximum amplitude versus thickness is a linear function whose gradient G is given by:

$$G = \frac{4M\pi A_i r}{\lambda_d} \quad (2.16)$$

Hence, we can determine the reflectivity by:

$$r = \frac{G\lambda_d}{4M\pi A_i} \quad (2.17)$$

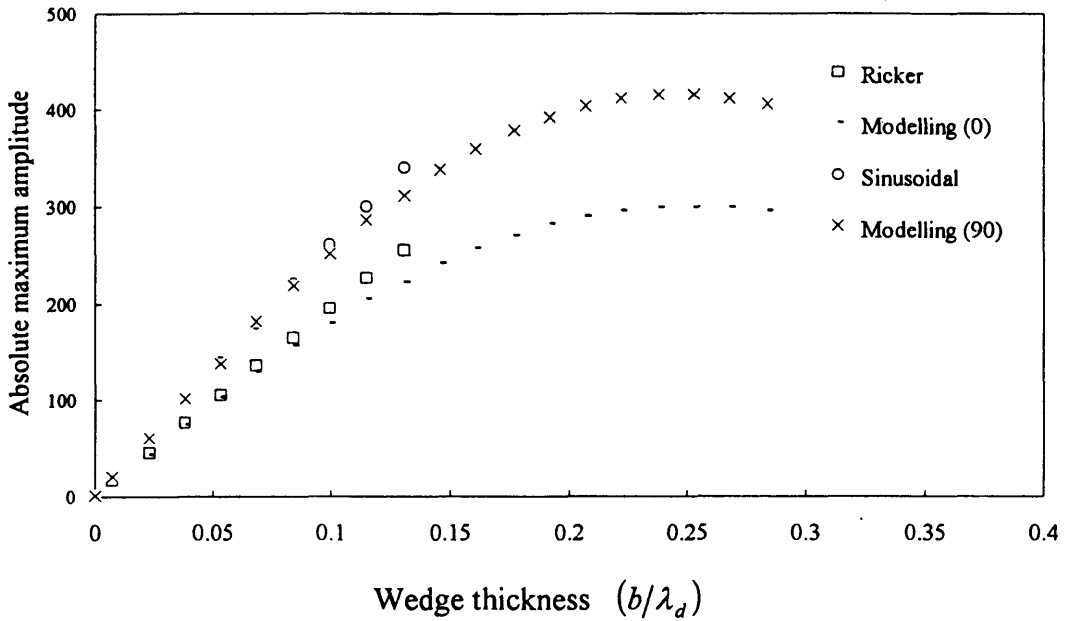


Figure 2.6a The amplitude response for Type I reflectivity (Γ^\perp) with a Ricker 18-Hz source wavelet whose maximum amplitude is 1000. Modelling (0°) and modelling (90°) are modelling results with zero-phase and 90° -phase wavelets, respectively.

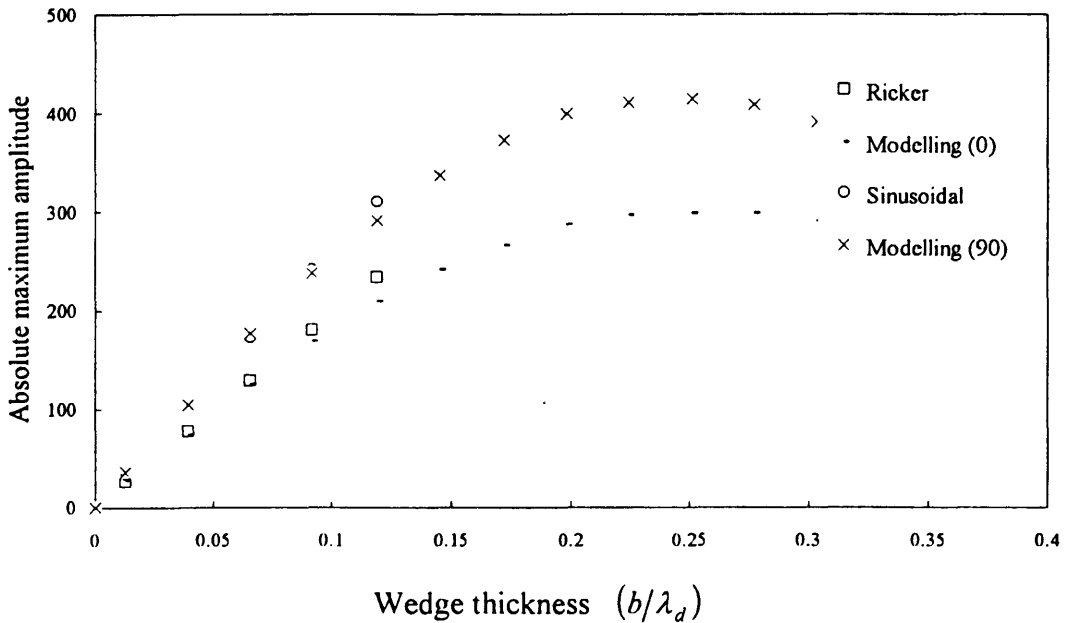


Figure 2.6b The amplitude response for Type I reflectivity (Γ^\perp) with a Ricker 31-Hz source wavelet whose maximum amplitude is 1000.

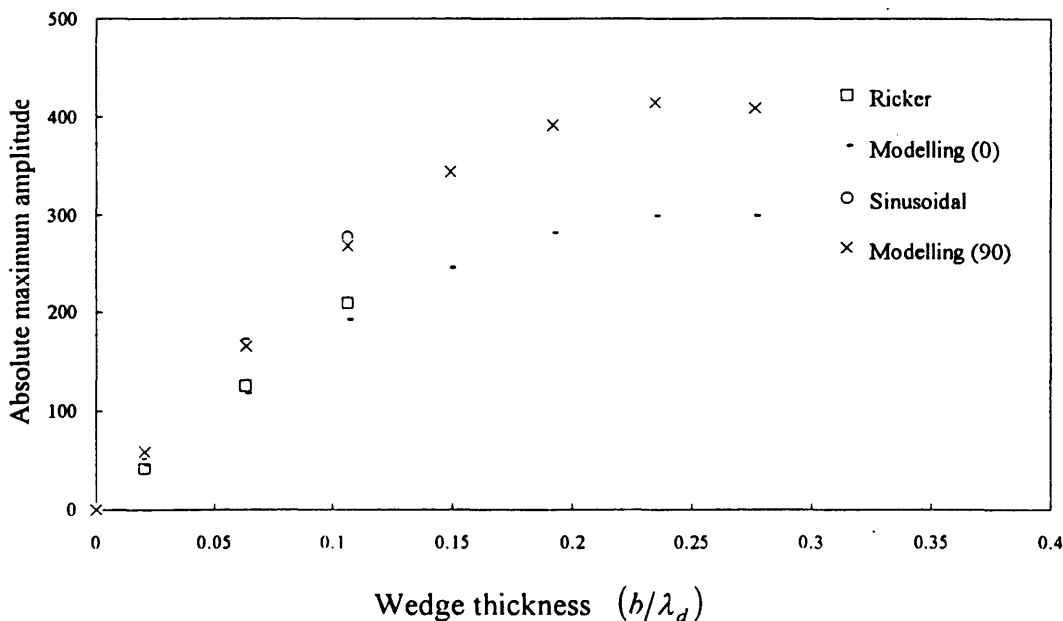


Figure 2.6c The amplitude response for Type I reflectivity (Γ^\perp) with a Ricker 50-Hz source wavelet whose maximum amplitude is 1000.

If the source wavelet is a Ricker wavelet, then M is 0.76. In real seismic data, the exact wavelet is rarely known; we can estimate M by modelling with the extracted wavelet from the data as the source wavelet.

2.3.2 Type II reflectivity

This case represents the thin bed overlain by a lower-velocity half-space and underlain by a higher-velocity half-space and with the two reflection coefficients having the same magnitude. Since $r_1 = r_2$, equations (2.14) and (2.15) reduce to $A_{r_{\max}} = 2A_r \left[1 - 1.831 \left(\frac{\pi b}{\lambda_d} \right)^2 \right]$ and $A_{s_{\max}} = 2A_r \left[1 - 2 \left(\frac{\pi b}{\lambda_d} \right)^2 \right]$ where $r = r_1 = r_2$. These two expressions differ only in one of the constants within the bracket, and the resulting difference between $A_{r_{\max}}$ and $A_{s_{\max}}$ as a function of b is rather small, as shown in Figure

2.3. To study these approximations, Type II reflectivity was modelled with six Ricker wavelets as was done for the Type I reflectivity model.

The amplitude results, shown in Figure 2.7, indicate that both the sinusoidal and Ricker approximations, i.e. equations (2.14) and (2.15) respectively, agree with the modelling results for all three input frequencies, although the modelled results agree slightly better with the Ricker approximation than with the sinusoidal approximation. This is to be expected since the input wavelets for the models are all zero-phase Ricker wavelets. However, the differences are small. At $(1/8)\lambda_d$ thickness, both approximations deviate less than 10% from the modelling results. There is no modelling result for $b = 0$; we simply use $A_r = 2A_i r$, which is the limiting value from both equations (2.14) and (2.15) as b goes to zero.

The numerical results for this reflectivity are tabulated in Tables 2.3 in Appendix A. In these tables and the corresponding figures, the numerical results from using a zero-phase Ricker wavelet are almost equivalent to the numerical results obtained from using its 90°-phase counterpart, assuming both wavelets have the same maximum amplitudes. Hence, the unlabelled modelled results are valid for both a zero-phase Ricker wavelet and its 90°-phase counterpart. The reason for this equivalence is explained in section 2.2.1 with Figures 2.1 and 2.2.

At about $(1/4)\lambda_d$ thickness, amplitude tuning is also observed. In this case, it is a minimum, and the wavelet exhibits a flat spot at this thickness (trace 20, Figure 2.5b). As the thickness increases further, the wavelet splits into two components. Beyond this point, if we measure the amplitude along the same time line along which the maximum is measured before the flat spot occurs, no tuning actually occurs, i.e. a trough starts to occur along that time line. The amplitude increase for thicknesses larger than $(1/4)\lambda_d$ is actually measured for one of two smaller wavelets.

We can conclude that, for models represented by Type II reflectivity, both the Ricker and the sinusoidal approximations are suitable for modelling the amplitude response of a thin bed as a function of its thickness. If the source wavelet is indeed a Ricker wavelet, then the Ricker approximation gives optimum results. However, in real data, one seldom knows the exact source wavelet, and the sinusoidal approximation may be used to obtain reasonable results.

2.3.3 Type III reflectivity

This case represents a thin bed overlain and underlain by higher-velocity half-spaces whose velocities are different. It is similar to Type I reflectivity except that its two reflection coefficients have different magnitudes. While Type I reflectivity is the most studied thin-layer model, Type III probably represents more common geological situations.

For this reflectivity sequence, Figure 2.8 shows that the Ricker approximation and the modelled results differ for the thickness range from $0.03\lambda_d$ to $0.08\lambda_d$, although the difference is still less than 10%. This is probably due to ignoring terms of $(\Delta t)^2$ and higher-order terms in the derivation of the opposite-polarity term in equation (2.14). For the thickness range between $0.09\lambda_d$ and $0.13\lambda_d$, the two results are almost identical. As the thickness increases further, they start to deviate rapidly. The sinusoidal approximation does not agree with the modelled results for the same reason as mentioned in the discussion for Type I reflectivity. In the limit of zero thickness, the amplitude is equal to $A_i(r_1 + r_2)$ which is also true for the Type IV reflectivity series. The numerical results are listed in Table 2.4 in Appendix A.

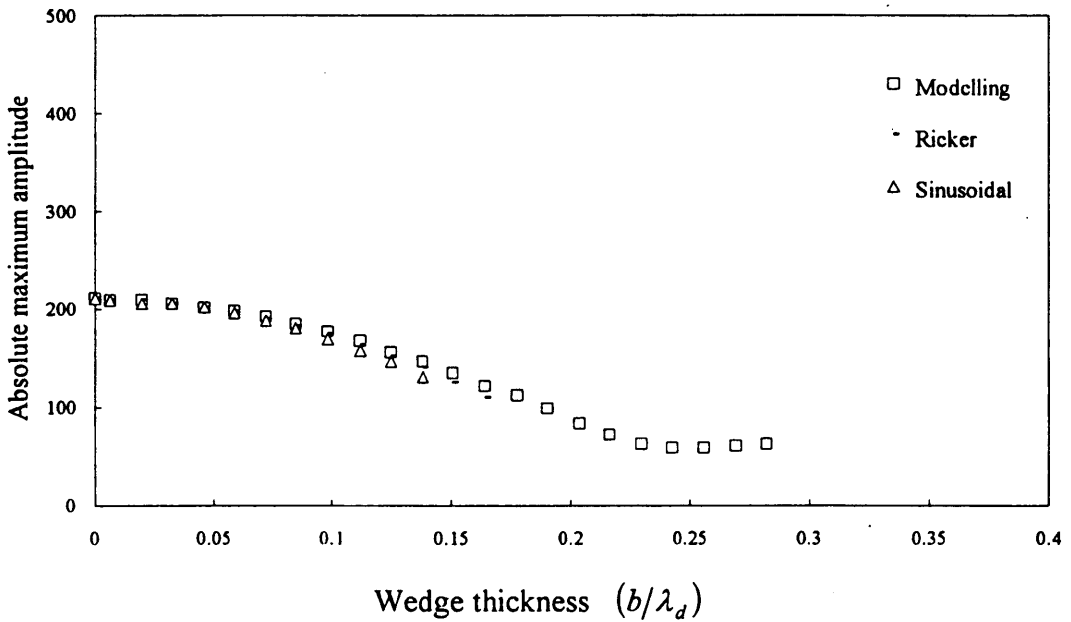


Figure 2.7a The amplitude response for Type II reflectivity ($\perp\perp$) with a Ricker 18-Hz source wavelet whose maximum amplitude is 1000.

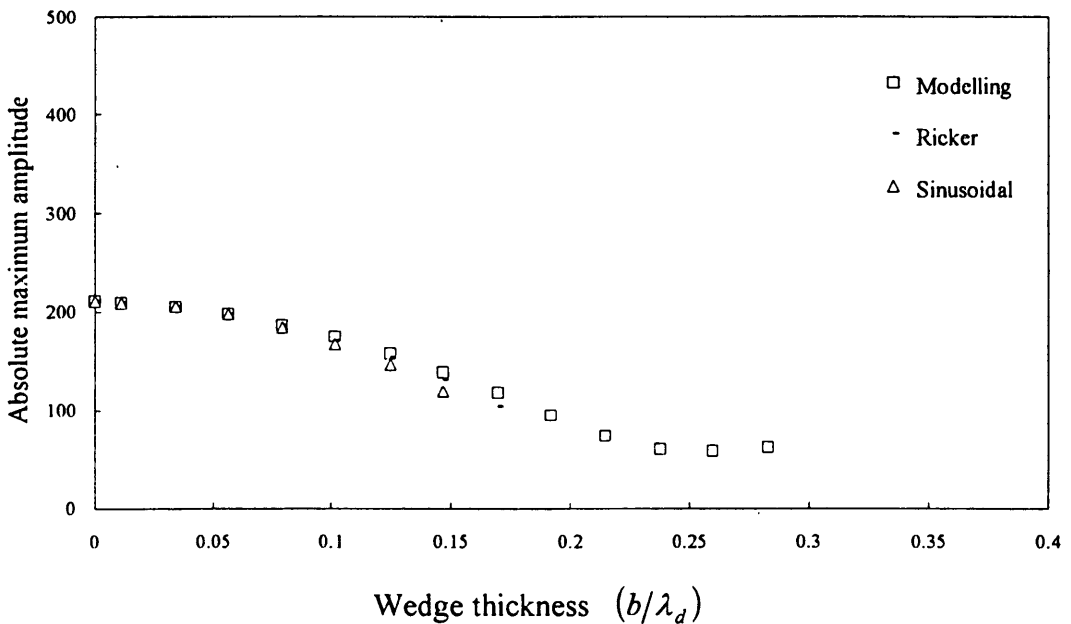


Figure 2.7b The amplitude response for Type II reflectivity ($\perp\perp$) with a Ricker 31-Hz source wavelet whose maximum amplitude is 1000.

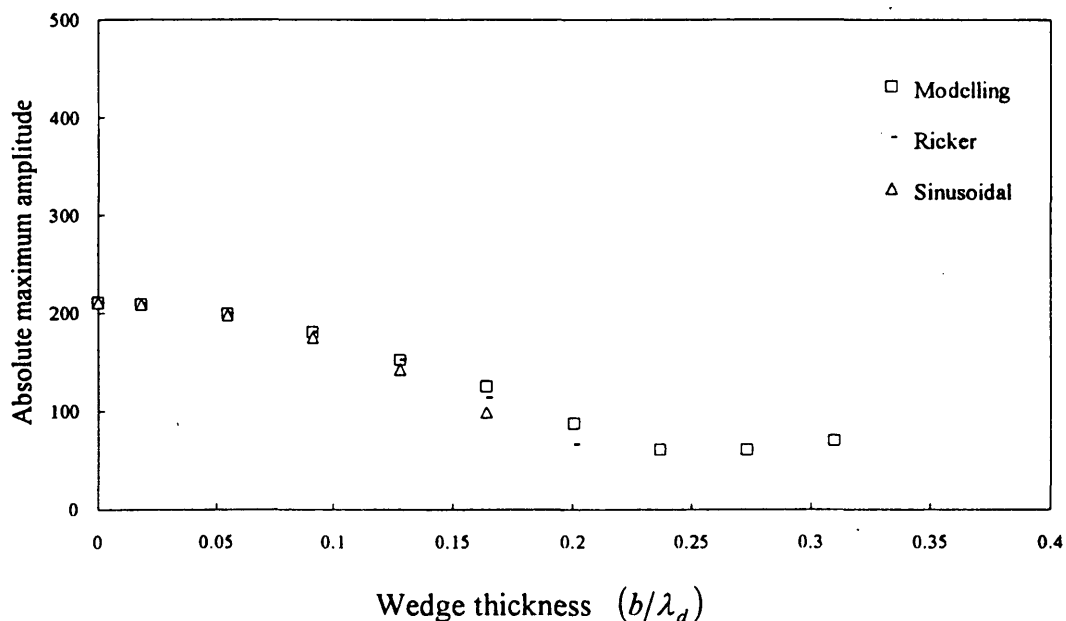


Figure 2.7c The amplitude response for Type II reflectivity ($\perp\perp$) with a Ricker 50-Hz source wavelet whose maximum amplitude is 1000.

Amplitude tuning also occurs at $(1/4)\lambda_d$ thickness. This is not surprising, since Type III reflectivity can be expressed as a linear superposition of Types I and II reflectivities. Although the Ricker approximation deviates from the modelled results more than the sinusoidal approximation does for small thicknesses, it agrees with the modelled results for larger thicknesses than does the sinusoidal approximation. This implies that the thin-bed assumption is a more stringent assumption for the sinusoidal approximation than it is for the Ricker approximation.

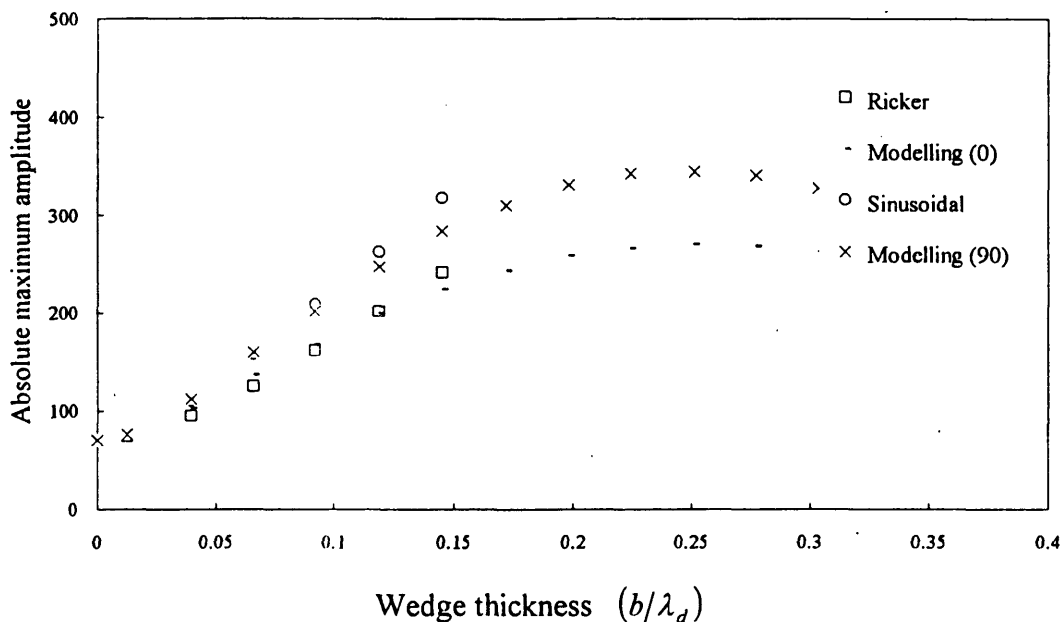


Figure 2.8 The amplitude response for Type III reflectivity (τ^{\perp}) with a Ricker 31-Hz source wavelet whose maximum amplitude is 1000.

2.3.4 Type IV reflectivity

This case represents a thin bed overlain by a lower-velocity half-space and underlain by a higher-velocity half-space. It is similar to Type II reflectivity except that its two reflection coefficients have different magnitudes. Figure 2.9 shows that the two approximations give very similar results, and both agree very well with the modelled results for thickness up to and slightly greater than the $(1/8)\lambda_d$ value. Note also that Type II and Type IV reflectivities, and hence any two-term reflectivity with reflection coefficients of the same polarity, can be better modelled with the two approximations than Type I and Type III reflectivities. The reason is that, for equal-polarity coefficients, the contribution from the opposite polarity term in equations (2.14) and (2.15) is very small, and hence the problem of neglecting $(\Delta t)^2$ is minimal, as mentioned earlier. The numerical results for this reflectivity can be found in Table 2.5 in Appendix A.

Amplitude tuning occurs also at $(1/4)\lambda_d$ thickness, which is a direct consequence of the fact that the equal-polarity term in equations (2.14) and (2.15) tunes at $(1/4)\lambda_d$, and the contribution from the opposite-polarity term is minimal, although it also tunes at a maximum at $(1/4)\lambda_d$ thickness.

2.4 Normal incidence, two-layer model

In real geological situations, a single thin layer embedded within a thick layer is not a common occurrence, particularly in the Western Canadian Sedimentary Basin. More often, a composite reflection is recorded from a series of thin layers. When interpreting such reflections, one has to be aware of the potential pitfalls of applying any theories developed for a single thin layer to a multi-layer model. For this dissertation, we will consider the case of two vertically adjacent thin layers, and leave the study of a greater number of layers for future research. The main objective is to investigate how the amplitude response of two thin layers differ from that of a single layer. In the following three sections, an equation based on the sinusoidal approximation describing the amplitude response of a two-layer case is developed, and its properties are discussed. Numerical modelling results are also compared to theoretical results.

2.4.1 Sinusoidal approximation

Two thin layers embedded between two homogeneous and isotropic half spaces can be represented graphically by three reflection coefficients. Let the reflection coefficients at the interfaces be r_1 , r_0 , and r_2 . Using the same approach as that used for a single thin layer, and taking time zero to be the event at r_0 , we can write:

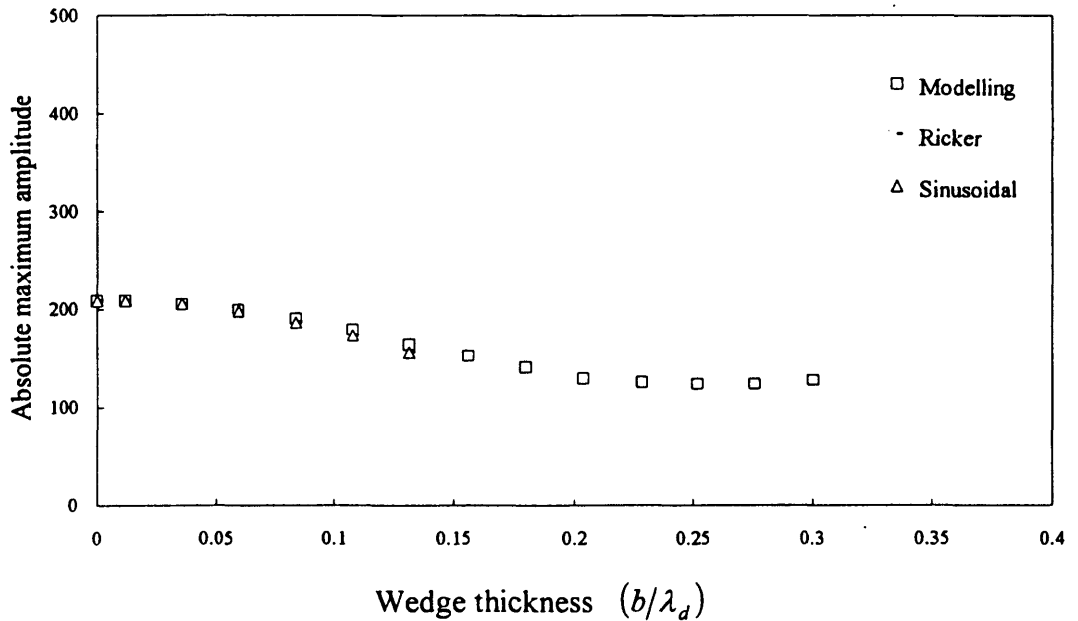


Figure 2.9 The amplitude response for Type IV reflectivity ($\perp\perp$) with a Ricker 31-Hz source wavelet whose maximum amplitude is 1000.

$$A_r = A_i r_1 \cos\left(t + \frac{2b_1}{V_1}\right) \frac{2\pi}{T_d} + A_i r_0 \cos\left(\frac{2\pi t}{T_d}\right) + A_i r_2 \cos\left(t - \frac{2b_2}{V_2}\right) \frac{2\pi}{T_d} \quad (2.16)$$

where A_r = maximum peak amplitude of the approximating cosine wave, b_1 = thickness of the top thin layer, b_2 = thickness of the bottom thin layer, V_1 = P -wave velocity of the top thin layer, V_2 = P -wave velocity of the bottom thin layer, T_d = predominant period of the source wavelet that the cosine wave is approximating.

Therefore, we have:

$$\begin{aligned} \frac{A_r}{A_i} = & r_1 \left[\cos\left(\frac{2\pi t}{T_d}\right) \cos\left(\frac{4\pi b_1}{V_1 T_d}\right) - \sin\left(\frac{2\pi t}{T_d}\right) \sin\left(\frac{4\pi b_1}{V_1 T_d}\right) \right] \\ & + r_2 \left[\cos\left(\frac{2\pi t}{T_d}\right) \cos\left(\frac{4\pi b_2}{V_2 T_d}\right) + \sin\left(\frac{2\pi t}{T_d}\right) \sin\left(\frac{4\pi b_2}{V_2 T_d}\right) \right] + r_0 \cos\left(\frac{2\pi t}{T_d}\right) \end{aligned}$$

$$= \left[r_1 \cos\left(\frac{4b_1\pi}{\lambda_{d_1}}\right) + r_2 \cos\left(\frac{4b_2\pi}{\lambda_{d_2}}\right) + r_0 \right] \cos\left(\frac{2\pi t}{T_d}\right) + \left[r_2 \sin\left(\frac{4b_2\pi}{\lambda_{d_2}}\right) - r_1 \sin\left(\frac{4b_1\pi}{\lambda_{d_1}}\right) \right] \sin\frac{2\pi t}{T_d}$$

Applying the thin-bed approximation so that, for small b , $\sin\left(\frac{4b_2\pi}{\lambda_{d_2}}\right) \approx \frac{4b_2\pi}{\lambda_{d_2}}$,

$$\sin\left(\frac{4b_1\pi}{\lambda_{d_1}}\right) \approx \frac{4b_1\pi}{\lambda_{d_1}}, \quad \cos\left(\frac{4b_1\pi}{\lambda_{d_1}}\right) \approx 1 - 2\left(\frac{2b_1\pi}{\lambda_{d_1}}\right)^2 \quad \text{and} \quad \cos\left(\frac{4b_2\pi}{\lambda_{d_2}}\right) \approx 1 - 2\left(\frac{2b_2\pi}{\lambda_{d_2}}\right)^2 :$$

$$\therefore \frac{A_r}{A_i} \approx \left\{ r_1 \left[1 - 2\left(\frac{2b_1\pi}{\lambda_{d_1}}\right)^2 \right] + r_2 \left[1 - 2\left(\frac{2b_2\pi}{\lambda_{d_2}}\right)^2 \right] + r_0 \right\} \cos\frac{2\pi t}{T_d} + \left[\frac{4b_2r_2\pi}{\lambda_{d_2}} - \frac{4b_1r_1\pi}{\lambda_{d_1}} \right] \sin\frac{2\pi t}{T_d}$$

$$\therefore A_r = M_3 \cos\frac{2\pi t}{T_d} + M_4 \sin\frac{2\pi t}{T_d} \quad (2.17)$$

$$\text{where } M_3 = A_i \left\{ r_1 \left[1 - 2\left(\frac{2b_1\pi}{\lambda_{d_1}}\right)^2 \right] + r_2 \left[1 - 2\left(\frac{2b_2\pi}{\lambda_{d_2}}\right)^2 \right] + r_0 \right\}$$

$$\text{and } M_4 = A_i \left[\frac{4b_2r_2\pi}{\lambda_{d_2}} - \frac{4b_1r_1\pi}{\lambda_{d_1}} \right]$$

Equation (2.17) is similar to equation (2.2). Hence, the maximum amplitude value is given by:

$$A_r = \sqrt{M_3^2 + M_4^2}$$

$$= A_i \left\langle \left\{ r_1 \left[1 - 2\left(\frac{2b_1\pi}{\lambda_{d_1}}\right)^2 \right] + r_2 \left[1 - 2\left(\frac{2b_2\pi}{\lambda_{d_2}}\right)^2 \right] + r_0 \right\}^2 + \left\{ \frac{4b_2r_2\pi}{\lambda_{d_2}} - \frac{4b_1r_1\pi}{\lambda_{d_1}} \right\}^2 \right\rangle^{\frac{1}{2}} \quad (2.18)$$

Equation (2.18) is similar to equation (2.15) with $M = 1$. However, applying the same method used in deriving equation (2.14) from the Ricker wavelet to the two-layer case leads to an unsolvable expression. Based on equations (2.14), (2.15), (2.18), by induction it is reasonable to modify equation (2.18) to:

$$A_r = A_i \left\langle \left\{ r_1 \left[1 - 1.831 \left(\frac{2b_1\pi}{\lambda_{d_1}} \right)^2 \right] + r_2 \left[1 - 1.831 \left(\frac{2b_2\pi}{\lambda_{d_2}} \right)^2 \right] + r_0 \right\}^2 + 0.76^2 \left\{ \frac{4b_2r_2\pi}{\lambda_{d_2}} - \frac{4b_1r_1\pi}{\lambda_{d_1}} \right\}^2 \right\rangle^{\frac{1}{2}} \quad (2.19)$$

for a Ricker wavelet. I define equation (2.19) the pseudo-Ricker approximation. If the two thin layers have the same P -wave velocities and densities, they become one layer with the thickness equal to the sum of b_1 and b_2 . Under this circumstance, r_0 becomes zero and equations (2.18) and (2.19) reduce to equations (2.14) and (2.15).

For the study of two layers, there are three fundamentally different types of reflectivity sequences. The first is the case where two successive reflection coefficients have the same polarity and the remaining coefficient has the opposite polarity. It can be represented diagrammatically by the symbol $\overline{\text{---}}\overline{\text{---}}\text{---}$; this reflectivity will be called the Type V reflectivity. The second is the case where the three reflection coefficients have alternating polarities, and can be represented by the symbol $\overline{\text{---}}\text{---}\overline{\text{---}}$ (Type VI reflectivity). The third is the case where all the three reflection coefficients are of the same polarity and can be represented by the symbol $\overline{\text{---}}\overline{\text{---}}\overline{\text{---}}$ (Type VII reflectivity). To obtain synthetic seismograms for these models, a wedge underlain by a thin layer was used (Figure 2.10). For each model, ten synthetic seismograms corresponding to five different thickness (2 m, 4 m, 6 m, 8 m and 10 m) for the underlying thin layer were generated, modelled with a 31 Hz Ricker wavelet and its corresponding 90°-phase counterpart as source wavelets. The maximum amplitudes of the source wavelets were set at 1000. As previously, the geometry of the

wedge was set so that the trace number is equal to the thickness of the wedge at the trace location. As with the single-layer models, transmission loss and multiples were ignored, normal incidence was assumed, and all models were generated with a time sampling interval of 0.1 ms. The velocities, densities and the resulting reflection coefficients for these three reflectivities are shown in Table 2.6. Figure 2.11 shows some examples of the synthetic seismograms generated for the two-layer study.

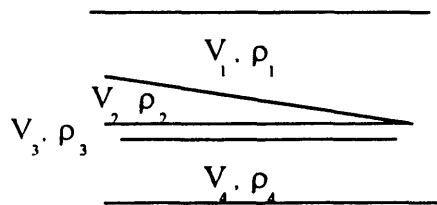


Figure 2.10 The wedge model for two-layer study.

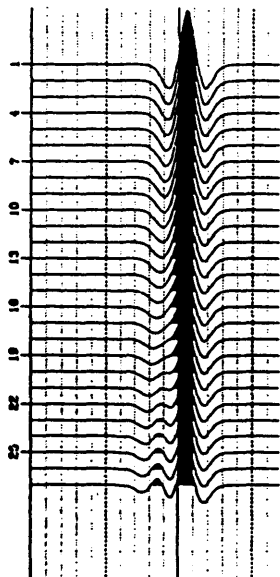
2.4.2 Type V reflectivity

For this reflectivity series, the lithologies and velocities chosen represent a coarsening-upward sequence. For example, the Bluesky Formation of the Lower Cretaceous period in Central Alberta is often a coarsening-upward sequence where the productive porous sand is underlain by silty sediments and capped by either impermeable shale or non-porous fine-grained sand. The numerical results are listed in Table 2.7 in Appendix A and plotted in Figure 2.12. For the modelling results with a 90° -phase source wavelet, and for all 5 thicknesses of the underlying layer, the reflected wavelet has the appearance of a zero-phase wavelet with the maximum absolute amplitude occurring at a trough. Hence, the troughs are picked for amplitude comparison. For the modelling results with a zero-phase source wavelet, the reflected wavelet approximates a 90° -phase wavelet for all the five synthetic seismograms. When the underlying layer thickness is less

Table 2.6 Lithologies, layer velocities, layer densities and reflection coefficients for the Type V, VI and VII reflectivity

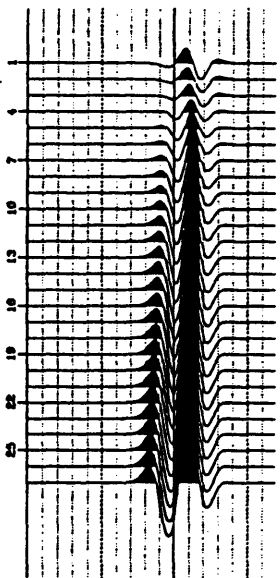
Reflectivity Series	Lithology V_1 (m/s) ρ_1 (kg/m)	Lithology V_2 (m/s) ρ_2 (kg/m)	Lithology V_3 (m/s) ρ_3 (kg/m)	Lithology V_4 (m/s) ρ_4 (kg/m)	r_1	r_0	r_2
V	non-porous sand 4270 2505	porous sand 3050 2303	silt 3800 2434	non-porous sand 4270 2505	-0.2072	0.1371	0.0722
	shale 3350 2359	porous sand 3050 2303	silt 3800 2434	shale 3350 2359			
VI	porous sand 3050 2303	shale 3350 2359	silt 3800 2434	non-porous sand 4270 2505	0.0596	0.0781	0.0722
	shale 3350 2359	porous sand 3050 2303	silt 3800 2434	shale 3350 2359			

(c) Type VII



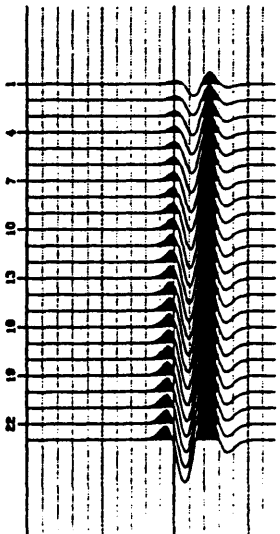
4 m

(b) Type VI

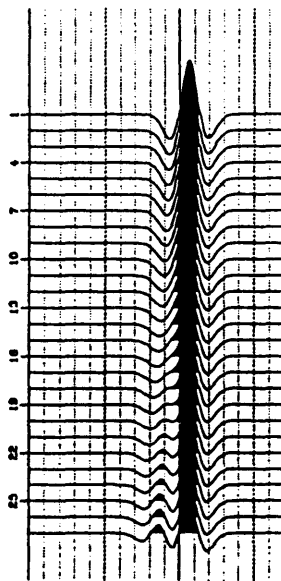


4 m

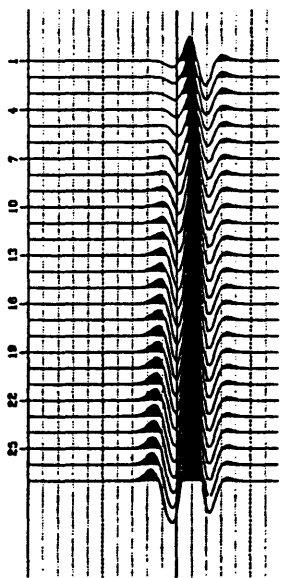
(a) Type V



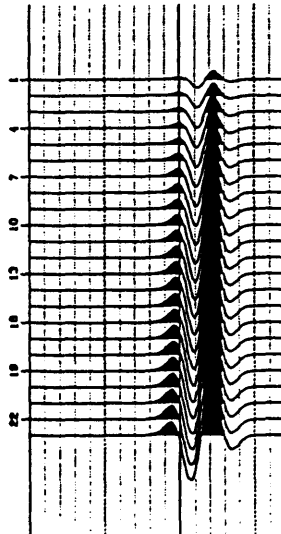
4 m



8 m



8 m



8 m

Figure 2.11 Synthetic seismograms for (a) Type V reflectivity, (b) Type VI reflectivity, and (c) Type VII reflectivity with underlying layer thicknesses 4 m and 8 m. The source wavelet is a Ricker 31-Hz wavelet. Timing lines are at 10-ms intervals.

than 6 metres, the peaks and troughs have almost identical amplitudes, with differences less than 1%. However, when the thickness of the underlying layer is more than 6 metres, the preceding troughs have slightly larger amplitudes than the peaks, in which case troughs are also picked for amplitude comparisons.

From the results in Figure 2.12, it is evident that the amplitude response of a two-layer model representing a Type V reflectivity sequence is different from that of a single layer. Firstly, for a single layer, it is shown in the last section that the thin-bed limit is approximately $(1/8)\lambda_d$, defined by the thickness at which the maximum amplitude of the reflected wavelet deviates by less than 10% from the sinusoidal approximation. For Type V reflectivity, however, this limit for the wedge is about $(1/16)\lambda_{d_1}$ when the underlying layer's thickness is $0.06\lambda_{d_2}$ (6 m) or less, where λ_{d_1} and λ_{d_2} are the predominant wavelengths in the wedge and the underlying thin layer, respectively. When the thickness of the underlying layer is $0.11\lambda_{d_2}$ (10 m), the modelled results differ drastically from that of the sinusoidal approximation. At this thickness for the underlying layer, the total thickness for the two layers is $0.13\lambda_d$ for a wedge thickness of $0.02\lambda_{d_1}$ (1.5 metres). This total thickness already exceeds the thin bed limit as defined in the last section.

The pseudo-Ricker approximation also agrees with the modelling results with a zero-phase source wavelet, though for a slightly lesser range of wedge thickness compared to the agreement between the sinusoidal approximation and the modelling results with a 90°-phase source wavelet. However, the agreement does imply that the pseudo-Ricker approximation is still a reasonable estimate for a Ricker wavelet for a wedge thickness of up to $0.04\lambda_{d_1}$ and an underlying thin layer of $0.06\lambda_{d_2}$ metres or less.

There are two other observations. The first one is the tuning thickness. For a single thin layer, this is at $0.25\lambda_d$ thickness. But if it is underlain by another thin layer, the maximum amplitude of the composite reflection occurs at a thickness of slightly less than the $0.25\lambda_d$ value for the top thin layer. For example, at 6 m for the underlying thin layer,

the wedge thickness at which maximum amplitude occurs is about $0.22\lambda_{d1}$ (Table 2.8c). If the wavelength λ_d is, for example, 100 m, the difference between $0.25\lambda_{d1}$ and $0.22\lambda_{d1}$ is 2.52 m. While this may seem small, it makes a great deal of differences in the economic evaluation of a potential reservoir if the areal extent is large. The second observation is that the synthetic seismograms in Figure 2.11a show that the phase of the composite wavelet does not appear to change as the thickness of the wedge increases, regardless of the thickness of the underlying thin layer.

2.4.3 Type VI reflectivity

For this reflectivity, the lithologies chosen reflect an interbedded sand and shale sequence typical of Lower Cretaceous formations in southern Alberta. For example, porous sands of the Viking Formation is often overlain by the Basal Fish Scale shale and underlain by the Joli Fou shale. A comparison between numerical modelling results and theoretical values are listed in Table 2.8 (Appendix A) and plotted in Figure 2.13. For modelling results with a 90° -phase source wavelet, the maximum amplitudes are peaks for small wedge thicknesses and then stabilize as troughs as the wedge thickness increases. The opposite occurs for a zero-phase source wavelet.

From Figure 2.13, the most notable difference between this reflectivity series and the Type V reflectivity series is that, regardless of the thickness of the underlying thin layer, as the wedge thickness increases from zero, the absolute maximum amplitude of the composite wavelet decreases initially, and then increases with increasing thickness. This is an important observation, since when interpreting trace amplitudes to deduce formation thicknesses, it is often assumed that the amplitudes will either increase or decrease continuously between zero thickness and the tuning thickness. This reflectivity shows that

such assumption could be misleading when one is dealing with an interbedded sand and shale sequence where the polarities of the reflection coefficients are alternating.

When the underlying layer thickness is $0.09\lambda_{d_2}$ (8 m) or more, the sinusoidal approximation leads to erroneous results, as the error between the theoretical results and the modelled results exceed 14%. However, when it is $0.06\lambda_{d_2}$ (6 m) or less, the results from the approximation agree well with the modelling results for wedge thicknesses up to $0.07\lambda_{d_1}$ (5 m) with most of the % differences well below 10%. For the pseudo-Ricker approximation, the theoretical results agree with the modelling results up to a wedge thickness of $0.04\lambda_{d_1}$ (3 m) with the underlying layer thickness being $0.04\lambda_{d_2}$ (4 m) or less. When the underlying thin layer's thickness is $0.06\lambda_{d_2}$ (6 m) or more, the approximation is not valid for any wedge thickness.

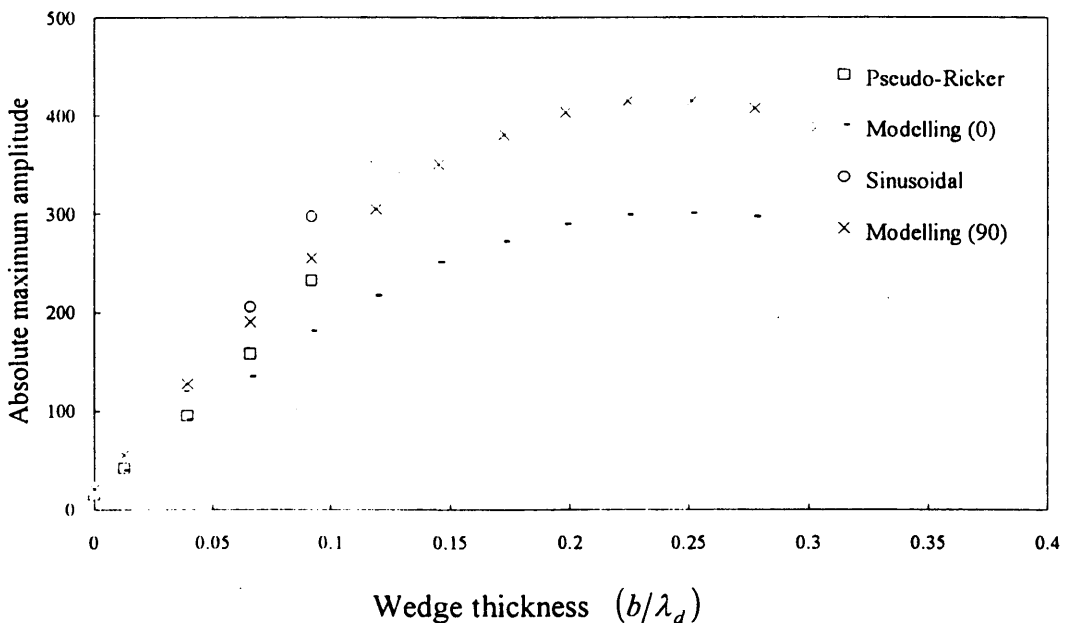


Figure 2.12a Comparison of modelling data with the sinusoidal and pseudo-Ricker approximations for Type V ($\begin{array}{c} | \\ \text{---} \\ | \end{array}$) reflectivity with an underlying thin layer 2-m thick.

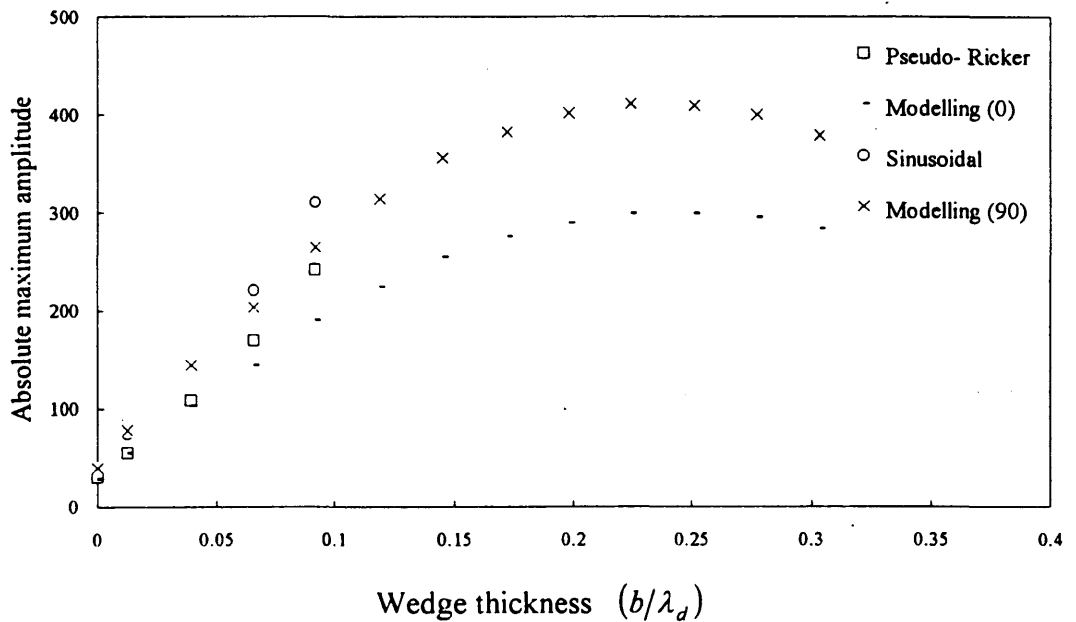


Figure 2.12b Comparison of modelling data with the sinusoidal and pseudo-Ricker approximations for Type V () reflectivity with an underlying thin layer 4-m thick.

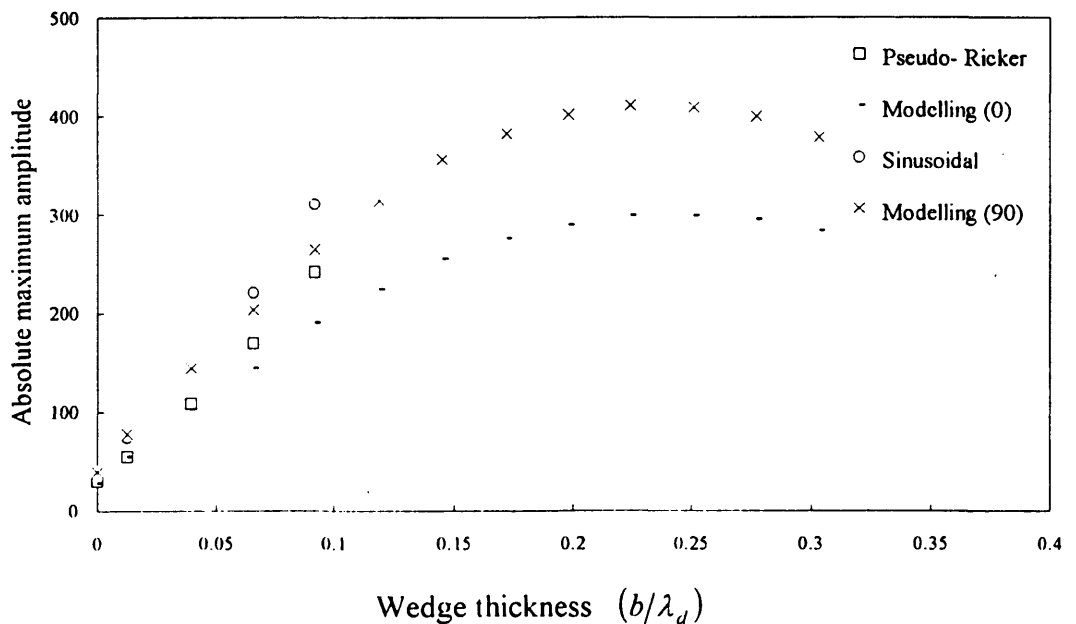


Figure 2.12c Comparison of modelling data with the sinusoidal and pseudo-Ricker approximations for Type V () reflectivity with an underlying thin layer 6-m thick.

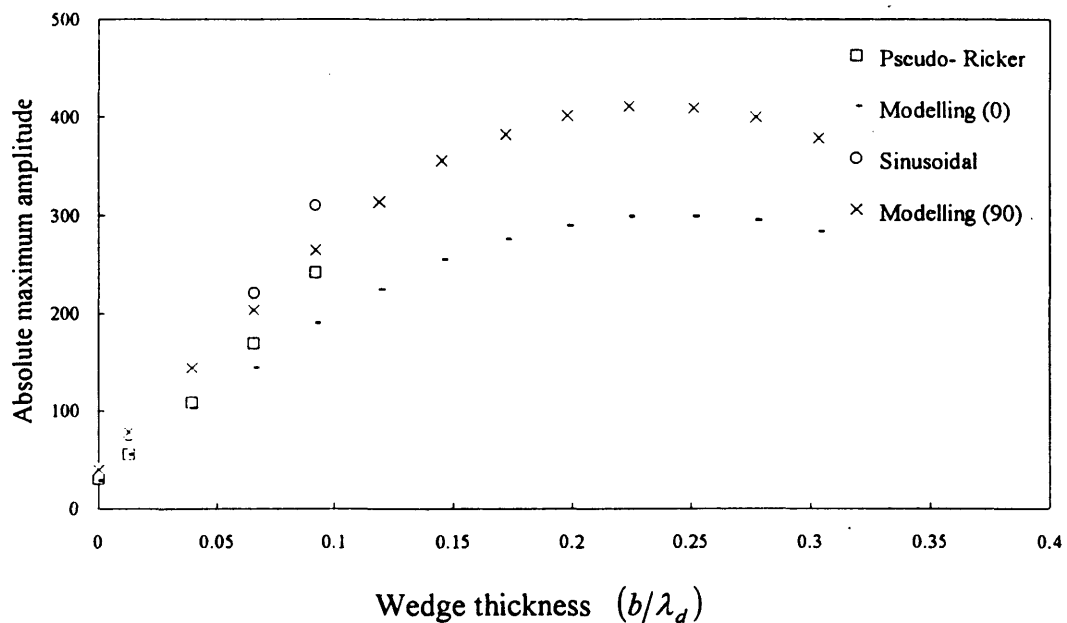


Figure 2.12d Comparison of modelling data with the sinusoidal and pseudo-Ricker approximations for Type V ($\begin{array}{c} | \\ \text{---} \\ | \end{array}$) reflectivity with an underlying thin layer 8-m thick.

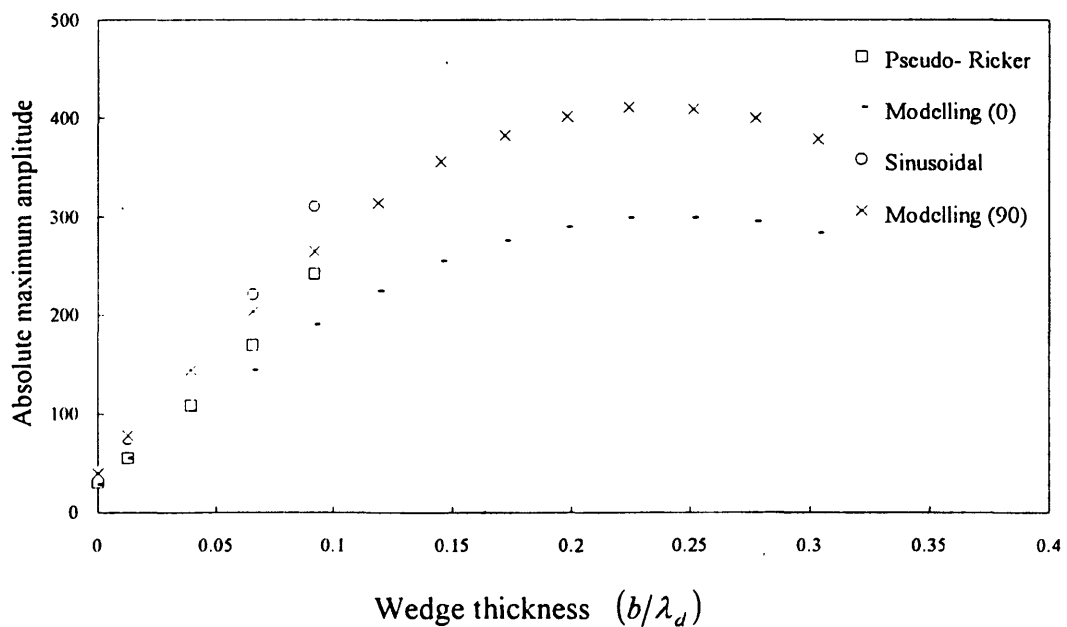


Figure 2.12e Comparison of modelling data with the sinusoidal and pseudo-Ricker approximations for Type V ($\begin{array}{c} | \\ \text{---} \\ | \end{array}$) reflectivity with an underlying thin layer 10-m thick.

With the presence of an underlying layer, Figure 2.13 indicates that, for all five values of underlying layer thicknesses, the maximum amplitude of the reflected composite wavelet occurs at approximately $0.29\lambda_{d_1}$ thickness for the wedge. This compares with a tuning thickness of $0.25\lambda_{d_1}$ for a single thin layer and $0.22\lambda_{d_1}$ for the Type V reflectivity. The difference between $0.25\lambda_{d_1}$ and $0.29\lambda_{d_1}$ is 4 m, assuming a wavelength of 100 m. This is a significant difference in the economic evaluation of a hydrocarbon reservoir, as many of the reservoirs in the Western Canadian Sedimentary Basin are only of the order of 3 to 5 m thick.

2.4.4 Type VII reflectivity

This reflectivity represents a typical fining-upward sequence, such as a sandbar deposited in a channel. For example, the Lower Cretaceous Glauconitic formation in southern Alberta contains channel facies. Among the three two-layer reflectivities studied, the Type VII reflectivity is the one that can be best modelled by the two approximations. Comparisons between theoretical and modelling results are shown in Figure 2.14. The numerical results are listed in Table 2.9 in Appendix A. For this reflectivity, the maximum amplitude is a decreasing function of the wedge thickness, and the tuning amplitude is a minimum.

For modelling results with a 90° -phase source wavelet, the maximum amplitude is a trough for small wedge thicknesses, and is a peak for larger wedge thicknesses. However, the range of the wedge thickness where this is true increases with the thickness of the underlying layer. From Figure 2.14, the modelling results and the sinusoidal approximation agree well for all the five underlying layer thicknesses, although the agreement deteriorates as the thickness of the underlying layer increases.

For the pseudo-Ricker approximation, Figure 2.14 shows that the agreement between the theoretical results and the modelling results are better than the agreement between the sinusoidal approximation and the corresponding modelled results. For example, even when the underlying layer thickness is $0.11\lambda_{d_2}$ (10 m), the % difference between the two sets of results is less than 10 up to a wedge thickness of $0.084\lambda_{d_1}$ (7 m) for a total thickness of $0.19\lambda_{d_2}$, which is considerably larger than the value $(1/8)\lambda_{d_2}$. The good agreement between the two sets of results implies indirectly that the pseudo-Ricker approximation is no less valid than the sinusoidal approximation, although it is not derived directly from the Ricker wavelet expression.

The behaviour of the tuning thickness of this reflectivity is different from that of the other two reflectivities. Firstly, the tuning amplitude is a minimum. Secondly, the tuning thickness shifts from a wedge thickness of approximately $0.25\lambda_{d_1}$ for an underlying layer thickness of $0.02\lambda_{d_2}$ (2 m) to a lower wedge thickness of approximately $0.20\lambda_{d_1}$ for an underlying thickness of $0.11\lambda_{d_2}$ (10 m). This contrasts with the tuning thicknesses of the Type V and Type VI reflectivities being constant for all the five underlying thicknesses.

2.5 Discussion

From the analysis of the single-layer models, several conclusions can be drawn that are useful for interpreting amplitudes of seismic reflections from thin geological formations. Type I reflectivity series is a singular case in that it is the only model for which the amplitude response as a function of thickness is linear within the thickness region where the thin-bed assumption is valid. All other cases are second-order polynomials. This implies that in exploration seismic data, interpretation of amplitudes for thin bed reflections to infer the thickness of the bed based on a linear relationship will lead

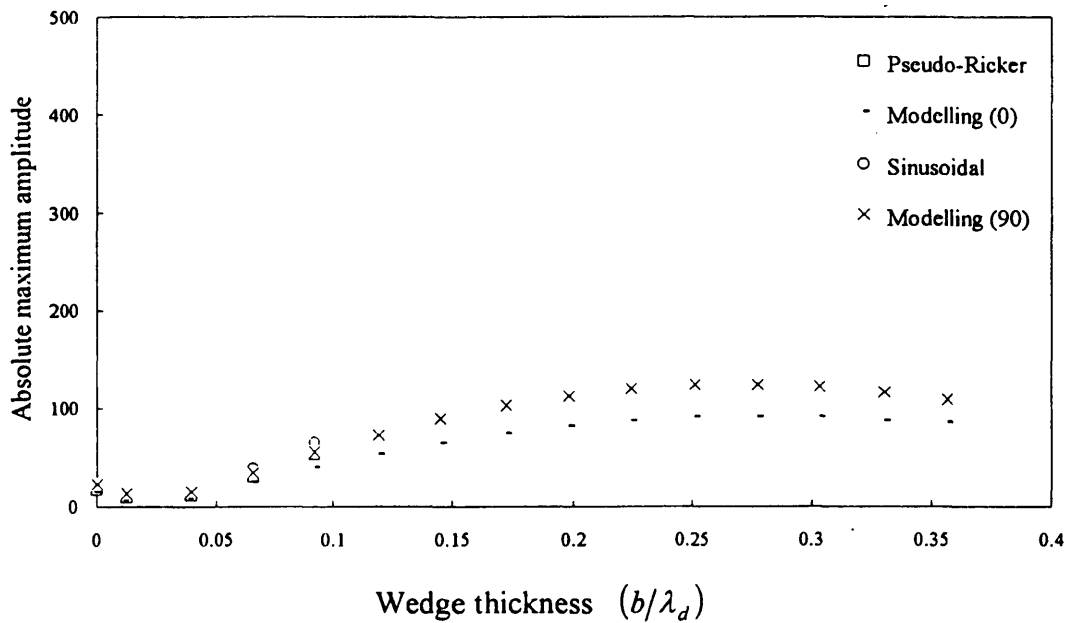


Figure 2.13a Comparison of modelling data with the sinusoidal and pseudo-Ricker approximations for Type VI ($\top\top$) reflectivity with an underlying thin layer 2-m thick.

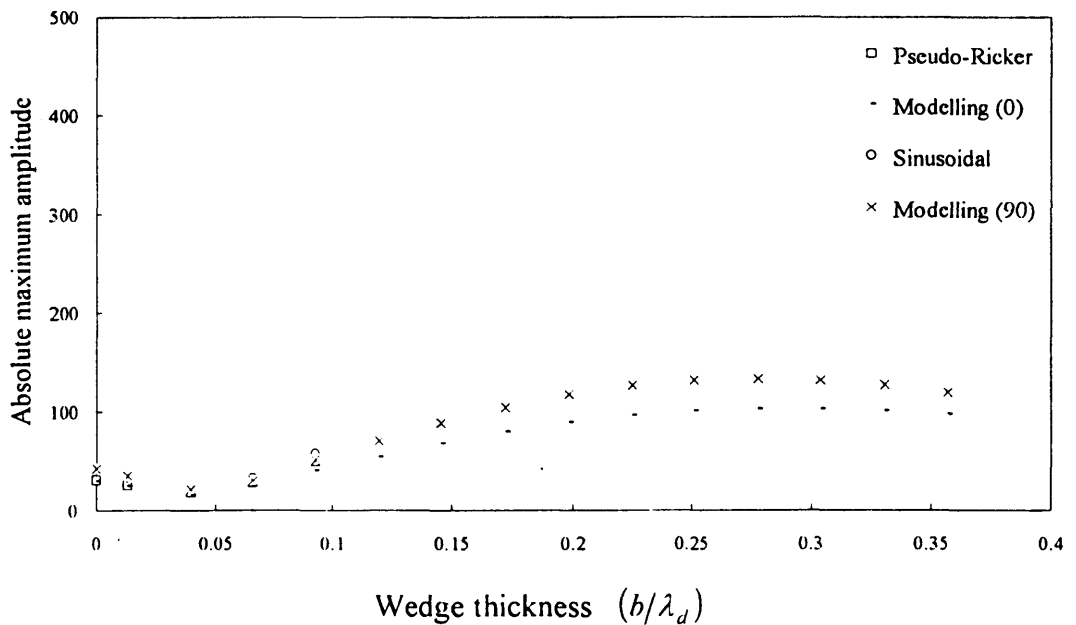


Figure 2.13b Comparison of modelling data with the sinusoidal and pseudo-Ricker approximations for Type VI ($\top\top$) reflectivity with an underlying thin layer 4-m thick.

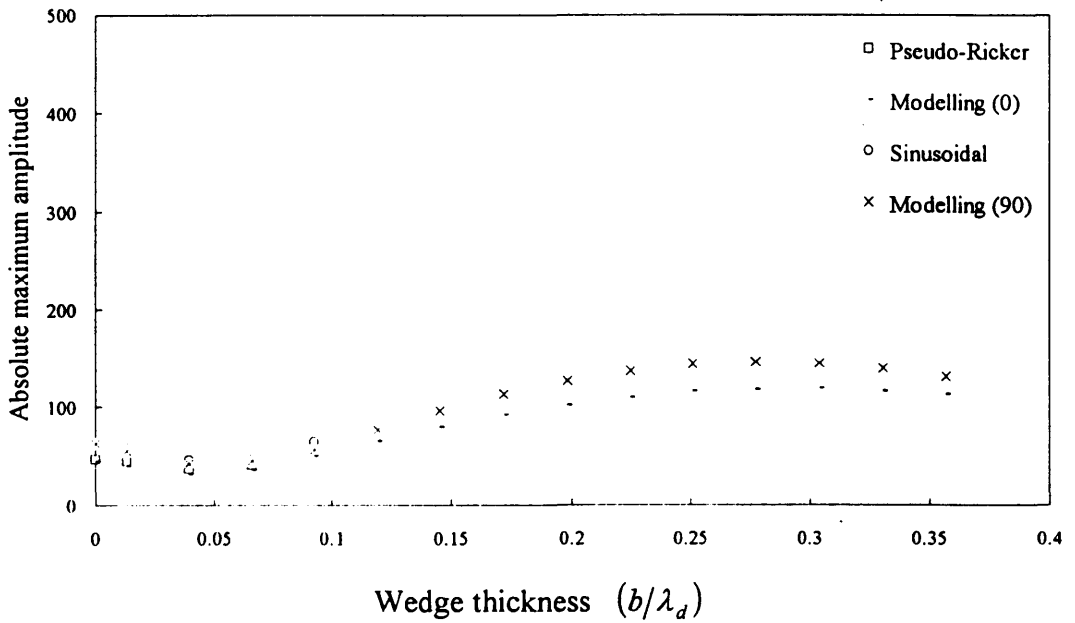


Figure 2.13c Comparison of modelling data with the sinusoidal and pseudo-Ricker approximations for Type VI (T T) reflectivity with an underlying thin layer 6-m thick.

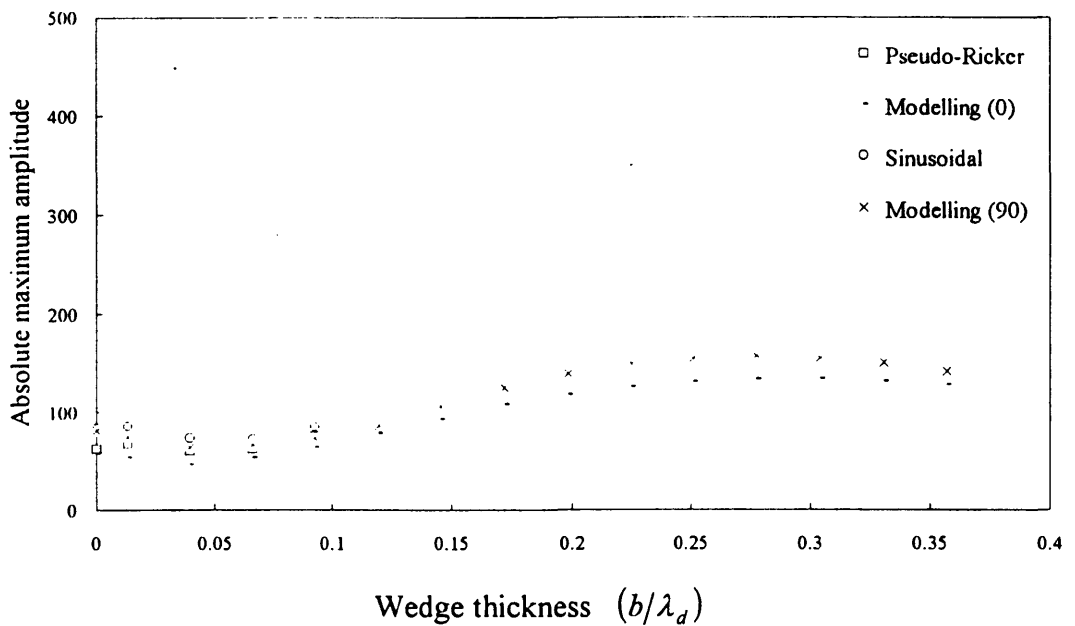


Figure 2.13d Comparison of modelling data with the sinusoidal and pseudo-Ricker approximations for Type VI (T T) reflectivity with an underlying thin layer 8-m thick.

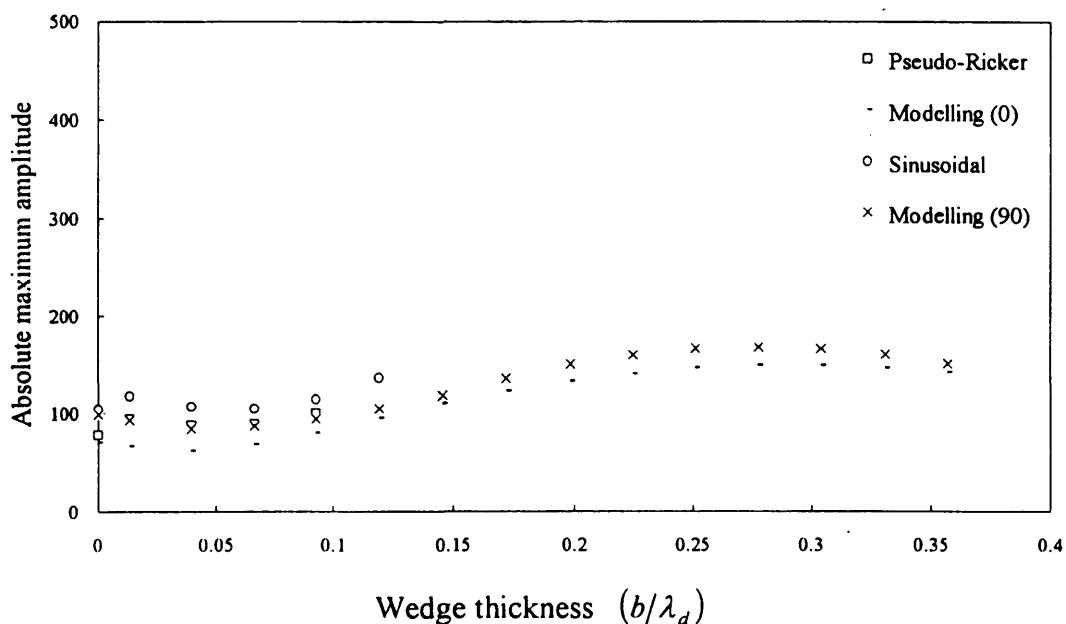


Figure 2.13e Comparison of modelling data with the sinusoidal and pseudo-Ricker approximations for Type VI ($\overline{\text{TTT}}$) reflectivity with an underlying thin layer 10-m thick.

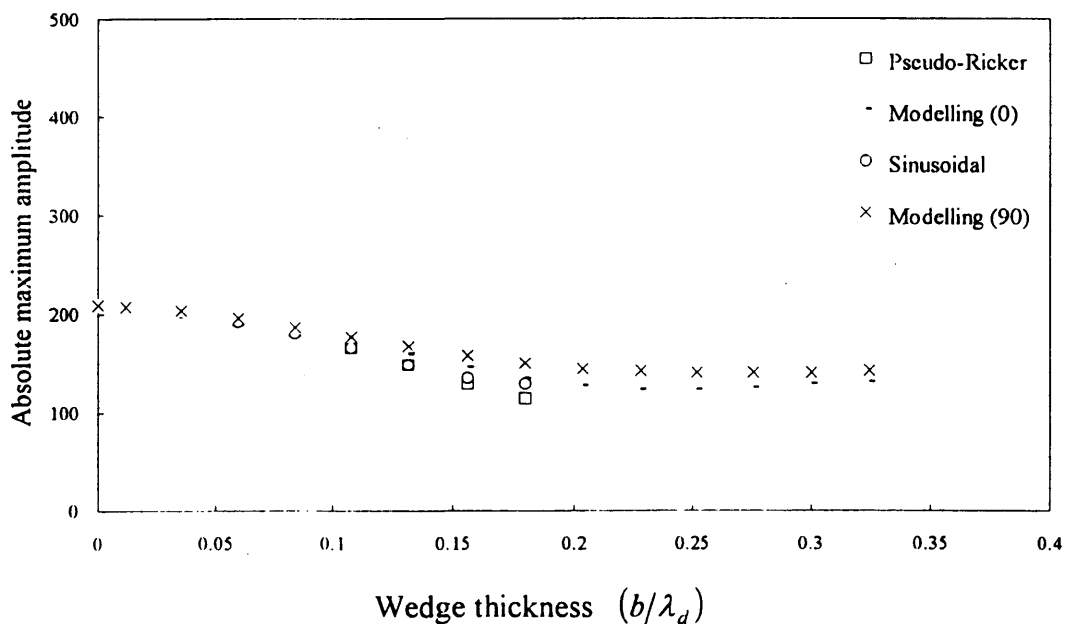


Figure 2.14a Comparison of modelling data with the sinusoidal and pseudo-Ricker approximations for Type VII ($\overline{\text{TTT}}$) reflectivity with an underlying thin layer 2-m thick.

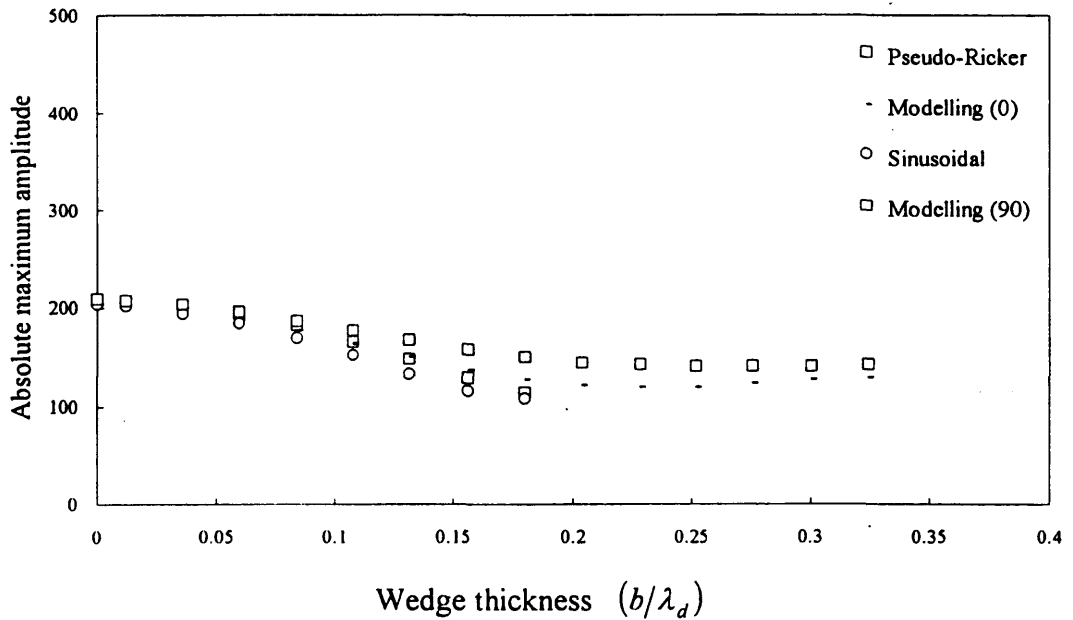


Figure 2.14b Comparison of modelling data with the sinusoidal and pseudo-Ricker approximations for Type VII ($\perp\perp\perp$) reflectivity with an underlying thin layer 4-m thick.

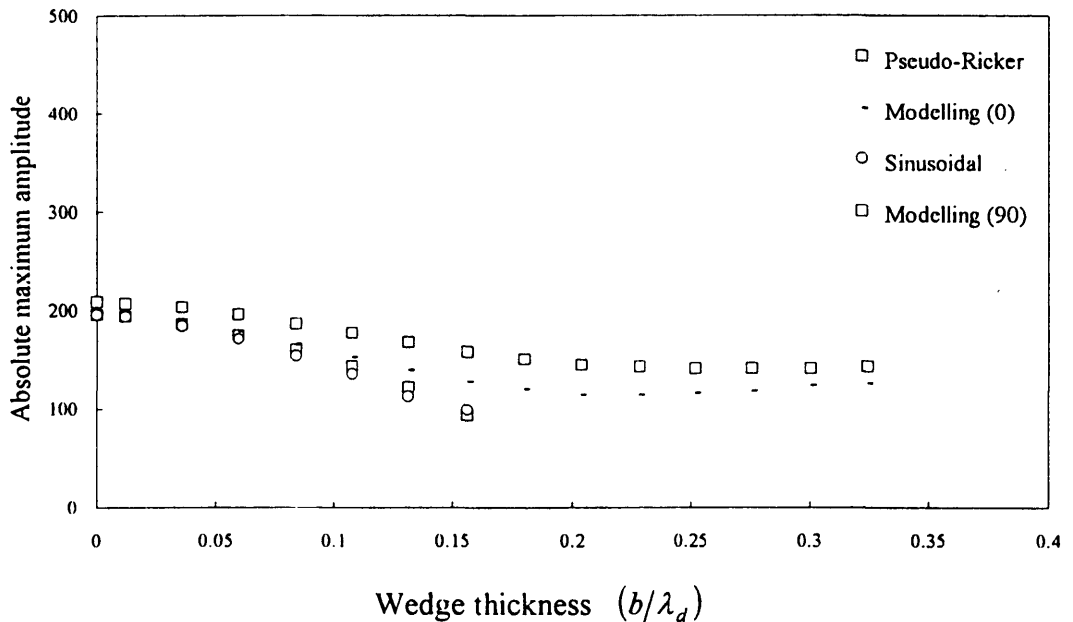


Figure 2.14c Comparison of modelling data with the sinusoidal and pseudo-Ricker approximations for Type VII ($\perp\perp\perp$) reflectivity with an underlying thin layer 6-m thick.

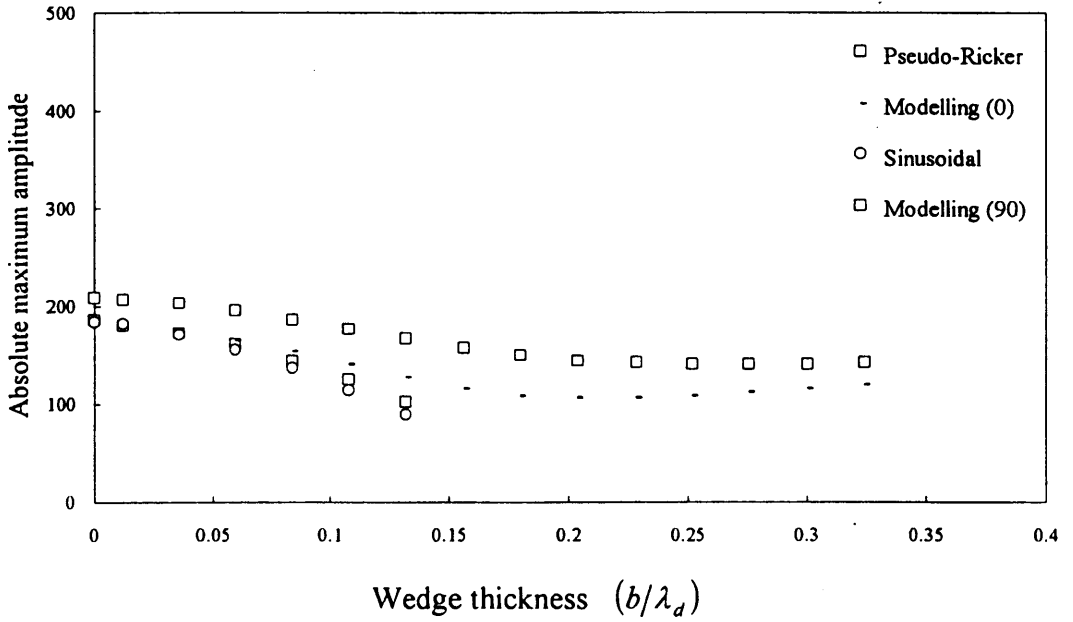


Figure 2.14d Comparison of modelling data with the sinusoidal and pseudo-Ricker approximations for Type VII ($\perp\perp\perp$) reflectivity with an underlying thin layer 8-m thick.

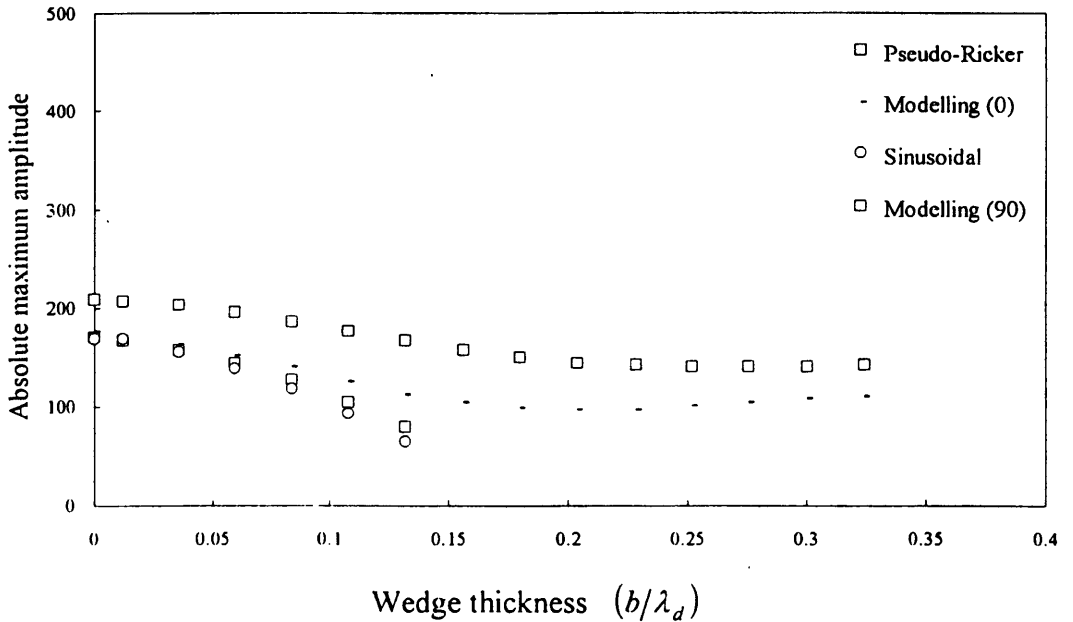


Figure 2.14e Comparison of modelling data with the sinusoidal and pseudo-Ricker approximations for Type VII ($\perp\perp\perp$) reflectivity with an underlying thin layer 10-m thick.

to erroneous results unless $r_2 = -r_1$.

Under the thin-bed assumption, the sinusoidal approximation is generally a reasonable approximation for a Ricker wavelet. This is significant, since, in real data we rarely know the exact wavelet. If the sinusoidal approximation is a good approximation for the Ricker wavelet, it is likely to be a good approximation for any wavelet whose phase is close to zero phase. In practice, the existence of a constant M in the sinusoidal approximation implies that, even if there is a stratigraphic sequence which can be represented by Type I reflectivity, one cannot calibrate the thickness according to the amplitudes observed on real seismic data unless the wavelet is known, or unless the data ties with at least with one well for the targeted formation. If there is no well tie, one may try to extract a wavelet from the data; if it approximates a zero-phase wavelet, then M is approximately 0.76. If it does not, one might be able to estimate M by modelling with the extracted wavelet as a source wavelet.

Equations (2.14) and (2.15) can be used in forward modelling to deduce the velocities of a thinly-layered sequence. For example, the velocity of the thin layer can be varied in these equations until the corresponding curves match with the observed results on real data that have been scaled appropriately. They may also be used to calibrate real data in a reservoir development program where the zero thickness limit of the reservoir rock is needed to be mapped from seismic data.

The analysis of the two-layer models also provides useful information for amplitude interpretation. Equations (2.18) and (2.19) clearly indicate that the theories developed for one single layer, i.e. equations (2.14) and (2.15), cannot be applied to a two-layer case. In particular, the results of Type VI reflectivity illustrate that, if the polarities of the reflection coefficients of a multi-layer reflectivity are alternating, the amplitude of the composite reflection may not uniformly increase or decrease as the thickness of a particular layer increases. Furthermore, the analysis shows that if a thin

layer is underlain by another thin layer whose thickness is constant, then as the thickness of the top thin layer changes, tuning occurs at a thickness which is slightly different from the $(1/4)\lambda_d$ value with respect to the top layer. Thus, if a two-layer reflection is mistaken to be a single-layer reflection, the estimated thickness of the formation will also be mistaken. This may lead to miscalculation of the economic value of a potential hydrocarbon reservoir.

In this chapter, seven reflectivity sequences with specific velocities, densities and Poisson's ratios are modelled. Conclusions drawn from the results of these models may not apply to models whose parameters are very different to the ones studied. However, for models with parameters close to the ones used in the study, the conclusions drawn for these seven reflectivity sequences are probably also valid. Furthermore, the limited conclusions already indicate the complexity in thin-bed seismic interpretation, which requires more research to solve many other issues not covered in this dissertation.

Chapter 3 - Frequency characteristics of seismic reflections from thin beds

3.1 Introduction

One of the important properties of a wavelet in thin-bed seismic interpretation is the frequency of the reflected composite wavelet. Widess (1973) concluded that for a bed whose thickness is below $(1/8)\lambda_{cb}$, the peak to trough time of the composite wavelet reflected from the top and bottom of the bed stays constant. This conclusion is based on visual inspection and is actually not analytically correct. Kallweit and Wood (1982) showed graphically that the peak-to-trough time keeps decreasing as the bed thins, and stabilizes only in the limit of zero separation. As shown later in this chapter, the analytical results for the peak frequency behaviour agree with their conclusion.

For any wavelet, it is evident from the definition of frequency that the peak frequency is inversely related to the peak-to-trough time. The peak frequency is defined as the frequency with the maximum amplitude in the frequency domain. This contrasts with the dominant frequency, which is defined as the frequency that corresponds to the wavelet peak-to-trough time. As a quantitative example, consider a Ricker wavelet centred at $t = 0$ with peak frequency f_0 (Ricker, 1940):

$$R(t) = (1 - 2\pi^2 f_0^2 t^2) e^{-\pi^2 f_0^2 t^2} \quad (3.1)$$

$$\frac{dR}{dt} = -4\pi^2 f_0^2 t e^{-\pi^2 f_0^2 t^2} - 2t\pi^2 f_0^2 e^{-\pi^2 f_0^2 t^2} (1 - 2\pi^2 f_0^2 t^2)$$

For the wavelet peak or trough (amplitude maximum or minimum):

$$\frac{dR}{dt} = 0$$

$$\therefore -4\pi^2 t f_0 e^{-\pi^2 f_0^2 t^2} - 2t\pi^2 f_0^2 e^{-\pi^2 f_0^2 t^2} (1 - 2\pi^2 f_0^2 t^2) = 0$$

Simplifying, we have

$$4\pi^4 f_0^4 t^3 - 6\pi^2 f_0^2 t = 0$$

$$4\pi^2 f_0^2 t^3 - 6t = 0$$

$t = 0$ is obviously a root, since the wavelet is centred at $t = 0$, which is the wavelet peak time. Therefore:

$$4\pi^2 f_0^2 t^2 = 6$$

$$\Rightarrow t = \pm \sqrt{\frac{3}{2}} \frac{1}{\pi f_0} = \pm \frac{0.39}{f_0}$$

The two other roots correspond to the two troughs of the wavelet, and since $t = 0$ coincides with the wavelet peak, $t = 0.39/f_0$ is in fact the peak to trough time for a Ricker wavelet. Therefore, the peak-to-trough time for a Ricker wavelet centred at $t = 0$ is inversely proportional to the peak frequency. Hence, analyzing the peak-to-trough time behaviour and analyzing the peak frequency behaviour are two different but equivalent ways of studying the same property of a wavelet. Lange and Almoghrabi (1988) studied the peak frequency behaviour of seismic reflections from thin beds as a function of both bed thickness as well as the incidence angle of the seismic raypath. Whereas using the

peak-to-trough time is a process of measurement, using the peak frequency offers the potential advantage of mathematical analysis, as shown in the next section. For this reason and the fact that there has been very little published literature on the use of the peak frequency as an aid in interpretation, it was chosen to be studied instead of the peak to trough time.

3.2 Theory

In this section, an exact frequency equation and a thin-bed frequency equation are derived for the one-layer case. Two corresponding frequency equations are also derived for the two-layer case. As for the amplitude study, transmission loss and internal multiples are ignored, and dispersion is not included.

3.2.1 Single-layer model

A simple model of a thin layer embedded between two thick layers can be represented by two reflection coefficients with magnitudes r_1 and r_2 and traveltimes t_1 and t_2 respectively from the top of the upper thick layer (Figure 3.1).

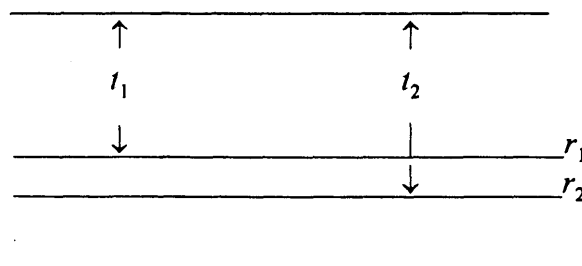


Figure 3.1 A simple thin-layer model.

The spectrum of the reflectivity series is:

$$X(f) = r_1 e^{i2\pi f t_1} + r_2 e^{i2\pi f t_2} \quad (3.2)$$

$$= [r_1 \cos(2\pi f t_1) + r_2 \cos(2\pi f t_2)] + i[r_1 \sin(2\pi f t_1) + r_2 \sin(2\pi f t_2)].$$

The corresponding amplitude spectrum is then:

$$\begin{aligned} A(f) &= \sqrt{[r_1 \cos(2\pi f t_1) + r_2 \cos(2\pi f t_2)]^2 + [r_1 \sin(2\pi f t_1) + r_2 \sin(2\pi f t_2)]^2} \\ &= \sqrt{r_1^2 + r_2^2 + 2r_1 r_2 [\cos(2\pi f t_1) \cos(2\pi f t_2) + \sin(2\pi f t_1) \sin(2\pi f t_2)]} \\ &= \sqrt{r_1^2 + r_2^2 + 2r_1 r_2 \cos(2\pi f \Delta t)} \end{aligned}$$

where $\Delta t = t_2 - t_1$ is the two-way traveltime within the thin layer.

The amplitude spectrum of a Ricker wavelet with peak frequency f_0 is (Ricker, 1953):

$$A_R(f) = \left(\frac{f}{f_0}\right)^2 e^{-\left(\frac{f}{f_0}\right)^2} \quad (3.3)$$

Hence, the amplitude spectrum of a composite wavelet formed by the convolution of a Ricker wavelet with a two-term reflectivity series is:

$$\begin{aligned} R(f) &= A(f) A_R(f) \\ &= \left(\frac{f}{f_0}\right)^2 e^{-\left(\frac{f}{f_0}\right)^2} \sqrt{r_1^2 + r_2^2 + 2r_1 r_2 \cos(2\pi f \Delta t)}. \end{aligned}$$

In order to determine the peak frequency, differentiate $R(f)$ with respect to f and set $dR(f)/df$ to zero:

$$\frac{dR(f)}{df} = \left(\frac{f}{f_0}\right)^2 e^{-\left(\frac{f}{f_0}\right)^2} \frac{-2r_1r_2 [2\pi\Delta t \sin(2\pi f\Delta t)]}{2\sqrt{r_1^2 + r_2^2 + 2r_1r_2 \cos(2\pi f\Delta t)}} + \sqrt{r_1^2 + r_2^2 + 2r_1r_2 \cos(2\pi f\Delta t)} \left[2\left(\frac{f}{f_0}\right) \frac{1}{f_0} e^{-\left(\frac{f}{f_0}\right)^2} + \left(\frac{f}{f_0}\right)^2 \left(-2\frac{f}{f_0}\right) \frac{1}{f_0} e^{-\left(\frac{f}{f_0}\right)^2} \right] = 0.$$

Simplifying and using f_p to denote peak frequency, results in:

$$f_p [r_1r_2 \pi\Delta t \sin(2\pi f_p \Delta t)] = [r_1^2 + r_2^2 + 2r_1r_2 \cos(2\pi f_p \Delta t)] \left[1 - \left(\frac{f_p}{f_0}\right)^2 \right] \quad (3.4)$$

where f_p is the peak frequency sought. Equation (3.4) gives the peak frequency of a composite wavelet formed by the convolution of a Ricker wavelet with a two-term reflectivity sequence. Hence, it will be called the exact peak frequency equation. Because of the complexity in the way that f_p appears in equation (3.4), it cannot be solved for analytically, but it can be solved for iteratively. The derivation of equation (3.4) makes no reference to whether the angle of incidence is normal or offset-dependent. All it requires is the two-way traveltime between the two reflection coefficients. Hence, it can be used for both normal incidence and non-normal incidence, i.e., in general, r_1 and r_2 in equation (3.4) may be offset-dependent.

The thin-bed approximation can also be applied to the exact peak frequency equation. By assuming that Δt is small so that $\sin(2\pi f_p \Delta t) \approx 2\pi f_p \Delta t$ and $\cos(2\pi f_p \Delta t) \approx 1$,

$$f_p r_1 r_2 \pi \Delta t (2 \pi f_p \Delta t) = (r_1^2 + r_2^2 + 2 r_1 r_2) \left[1 - \left(\frac{f_p}{f_0} \right)^2 \right]$$

$$f_p^2 (2 r_1 r_2 \pi^2 \Delta t^2) = k^2 \left[1 - \left(\frac{f_p}{f_0} \right)^2 \right]$$

where $k^2 = r_1^2 + r_2^2 + 2 r_1 r_2 = (r_1 + r_2)^2$. Rearranging terms, we have

$$f_p^2 \left[2 r_1 r_2 \pi^2 \Delta t^2 + \frac{k^2}{f_0^2} \right] = k^2$$

$$f_p^2 = \frac{k^2 f_0^2}{2 r_1 r_2 \pi^2 \Delta t^2 f_0^2 + k^2}$$

or

$$f_p = f_0 \left[1 + \frac{2 \pi^2 r_1 r_2 f_0^2 \Delta t^2}{k^2} \right]^{-\frac{1}{2}}$$

$$\therefore f_p \approx f_0 \left[1 - \frac{\pi^2 \Delta t^2 f_0^2 r_1 r_2}{k^2} \right] \quad (3.5)$$

assuming $\pi^2 \Delta t^2 f_0^2 r_1 r_2 \ll k^2$.

Equation (3.5) is defined here as the thin-bed peak frequency equation, since Δt is assumed to be very small. Since k^2 is always positive, equation (3.5) indicates that, if a Ricker wavelet is convolved with a two-term reflectivity sequence whose terms are separated by a small time interval, then the peak frequency of the composite wavelet will decrease as Δt increases if r_1 and r_2 are of the same polarity, and vice versa if r_1 and r_2 are of opposite polarities. As will be shown in the next section, equation (3.5) is a good

approximation for Types II and IV reflectivity sequences, but less good for Types I and III cases. This is because if r_1 and r_2 are of opposite polarities but close in magnitude, k can be very small, resulting in an abnormally large value for f_p in equation (3.5). For the case where $r_2 = -r_1$ (Type I reflectivity), equation (3.5) is invalid because of the singularity due to $k = 0$. However, this case can be studied in a different manner. Putting $r_2 = -r_1$ in the exact peak frequency equation (equation 3.4), we obtain:

$$\begin{aligned}
 f[-r_1^2 \pi \Delta t \sin(2\pi f_p \Delta t)] &= [2r_1^2 - 2r_1^2 \cos(2\pi f_p \Delta t)] \left[1 - \left(\frac{f_p}{f_0} \right)^2 \right] \\
 -f \pi \Delta t \sin(2\pi f_p \Delta t) &= 2[1 - \cos(2\pi f_p \Delta t)] \left[1 - \left(\frac{f_p}{f_0} \right)^2 \right] \\
 &= 2[2 \sin^2(\pi f_p \Delta t)] \left[1 - \left(\frac{f_p}{f_0} \right)^2 \right] \\
 &= 4 \sin^2(\pi f_p \Delta t) \left[1 - \left(\frac{f_p}{f_0} \right)^2 \right]
 \end{aligned}$$

Making the thin-bed approximation $\sin(2\pi f_p \Delta t) \approx 2\pi f_p \Delta t$ for small Δt , we have:

$$f_p^2 2 \pi^2 \Delta t^2 = 4 \pi^2 f_p^2 \Delta t^2 \left[\left(\frac{f_p}{f_0} \right)^2 - 1 \right]$$

$$\left(\frac{f_p}{f_0} \right)^2 - 1 = \frac{1}{2}$$

$$\therefore f_p = \sqrt{\frac{3}{2}} f_0 \quad (3.6)$$

This is identical to the results obtained by Lange and Almoghrabi (1988) although the approach used in this dissertation is different. Lange and Almoghrabi (1988) followed the conclusion of Widess (1973) and assumed that a reflected composite wavelet assumes the shape of the derivative of the source wavelet when the bed thins to $(1/8)\lambda_d$, and the shape remains constant as the bed continues to thin to zero. They then took the first derivative with respect to time of the amplitude spectrum of a Ricker wavelet, and solved for the new peak frequency. In the approach presented in this dissertation, there is no assumption about the shape of the reflected composite wavelet, regardless of the thickness of the bed; the only assumption is that the bed has to be sufficiently thin for the thin-bed assumption to be valid. Furthermore, as will be shown in section 3.3.1, the calculated peak frequency does not occur when the bed thickness is equal to $(1/8)\lambda_d$ as suggested by Widess (1973) and Lange and Almoghrabi (1988), but it is actually the limiting value for the peak frequency as the bed thickness approaches zero. Indirectly, this limiting behaviour also agrees with the conclusion of Kallweit and Wood (1982) about the limiting behaviour of the peak to trough time (see section 1.3).

Combining the results of Widess (1973), Lange and Almoghrabi (1988), and the results deduced from equation (3.4), it is concluded that as the thickness of a thin-bed represented by a Type I reflectivity sequence decreases, the peak frequency of the reflected composite wavelet will increase. As the thickness of the bed reduces to the limiting value of zero, the shape of the reflected composite wavelet will approach the shape of the derivative of the source wavelet, and the limiting peak frequency value is given by $\sqrt{\frac{3}{2}} f_0$ where f_0 is the peak frequency of the source wavelet.

3.2.2 Two-layer model

The mathematical procedure used for establishing the peak frequency versus thickness relationship for a single layer was employed to derive similar equations for two thin layers embedded in thick layers. Figure 3.2 shows this model and is characterized by the reflection coefficients r_1 , r_2 , and r_3 and traveltime t_1 , t_2 , and t_3 :

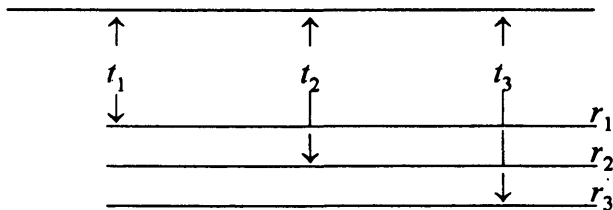


Figure 3.2 Two thin layers embedded in two thick layers.

The spectrum of the reflectivity series is:

$$\begin{aligned}
 X(f) &= r_1 e^{i2\pi f t_1} + r_2 e^{i2\pi f t_2} + r_3 e^{i2\pi f t_3} \\
 &= [r_1 \cos(2\pi f t_1) + r_2 \cos(2\pi f t_2) + r_3 \cos(2\pi f t_3)] \\
 &\quad + i[r_1 \sin(2\pi f t_1) + r_2 \sin(2\pi f t_2) + r_3 \sin(2\pi f t_3)]. \quad (3.7)
 \end{aligned}$$

Therefore, the corresponding amplitude spectrum is:

$$A(f) = \sqrt{\left[\begin{aligned} &[r_1 \cos(2\pi f t_1) + r_2 \cos(2\pi f t_2) + r_3 \cos(2\pi f t_3)]^2 \\ &+ [r_1 \sin(2\pi f t_1) + r_2 \sin(2\pi f t_2) + r_3 \sin(2\pi f t_3)]^2 \end{aligned} \right]}$$

Simplifying, we obtain:

$$A(f) = \left[\begin{array}{l} r_1^2 + r_2^2 + r_3^2 + 2r_1r_2 \cos(2\pi f \Delta t_{12}) + 2r_2r_3 \cos(2\pi f \Delta t_{23}) \\ + 2r_3r_1 \cos(2\pi f \Delta t_{31}) \end{array} \right]^{\frac{1}{2}}$$

where $\Delta t_{12} = t_2 - t_1$, $\Delta t_{23} = t_3 - t_2$, and $\Delta t_{31} = t_3 - t_1$

Hence, using the expression for the amplitude spectrum of a Ricker wavelet as given in equation (3.3), the amplitude spectrum of a composite wavelet formed by the convolution of a Ricker wavelet with a three-term reflectivity is:

$$R(f) = A(f) A_R(f) = \left(\frac{f}{f_0} \right)^2 e^{-\left(\frac{f}{f_0} \right)^2} \left[\begin{array}{l} r_1^2 + r_2^2 + r_3^2 + 2r_1r_2 \cos(2\pi f \Delta t_{12}) \\ + 2r_2r_3 \cos(2\pi f \Delta t_{23}) + 2r_3r_1 \cos(2\pi f \Delta t_{31}) \end{array} \right]^{\frac{1}{2}}$$

As for the single layer case, for the maximum value of $R(f)$, i.e. the peak frequency, we can differentiate $R(f)$ with respect to f and set the derivative to zero. Doing so, and simplifying, we obtain:

$$\begin{aligned} & f_p \left[r_1 r_2 \pi \Delta t_{12} \sin(2\pi f_p \Delta t_{12}) + r_2 r_3 \pi \Delta t_{23} \sin(2\pi f_p \Delta t_{23}) + r_3 r_1 \pi \Delta t_{31} \sin(2\pi f_p \Delta t_{31}) \right] \\ & = \left[\begin{array}{l} r_1^2 + r_2^2 + r_3^2 + 2r_1r_2 \cos(2\pi f_p \Delta t_{12}) + 2r_2r_3 \cos(2\pi f_p \Delta t_{23}) \\ + 2r_3r_1 \cos(2\pi f_p \Delta t_{31}) \end{array} \right] \left[1 - \left(\frac{f_p}{f_0} \right)^2 \right] \end{aligned} \quad (3.8)$$

Equation (3.8) gives the peak frequency of a composite wavelet formed by the convolution of a Ricker wavelet with a three-term reflectivity sequence, and involves no approximation. If we put $r_3 = 0$, equation (3.8) reduces to equation (3.4).

If the thin-bed approximation is applied, equation (3.8) becomes:

$$\begin{aligned}
2\pi^2 f_p^2 [r_1 r_2 \Delta t_{12}^2 + r_2 r_3 \Delta t_{23}^2 + r_3 r_1 \Delta t_{31}^2] &= [r_1^2 + r_2^2 + r_3^2 + 2r_1 r_2 + 2r_2 r_3 + 2r_3 r_1] \left[1 - \left(\frac{f_p}{f_0} \right)^2 \right] \\
&= h^2 - h^2 \left(\frac{f_p}{f_0} \right)^2 \\
\therefore f_p^2 \left[s^2 + \frac{h^2}{f_0^2} \right] &= h^2
\end{aligned}$$

where $h^2 = (r_1 + r_2 + r_3)^2$ and $s^2 = 2\pi^2 (r_1 r_2 \Delta t_{12}^2 + r_2 r_3 \Delta t_{23}^2 + r_3 r_1 \Delta t_{31}^2)$

$$\begin{aligned}
\therefore f_p &= f_0 \left[1 + \frac{f_0^2 s^2}{h^2} \right]^{-\frac{1}{2}} \\
&\approx f_0 \left[1 - \frac{f_0^2 s^2}{2h^2} \right] \tag{3.10}
\end{aligned}$$

assuming $\frac{f_0^4 s^4}{h^4} \ll 1$, which is valid for small Δt_{ij} . Equation (3.10) gives the peak frequency of a composite wavelet reflected from two thin beds embedded in two thick layers. It is the two-layer equivalent of equation (3.5), and reduces to it for $r_3 = 0$. As with equation (3.5), equation (3.10) suffers from a singularity if h is very small. In a sequence of thin beds of clastic rocks, the polarities of the reflection coefficients are often alternating, and the probability of h being small is quite high. This limits the usefulness of equation (3.10). Nevertheless, if h is not small, it gives a good approximation, as shown for a Type VII reflectivity model later in the chapter. However, one can always use equation (3.8), the exact peak frequency equation for two layers, and which can be solved by iteration. We shall study all these properties in more detail in section 3.4.

3.3 Normal incidence, single-layer model

In this section, results from equations (3.4) and (3.5) are compared with results from numerical modelling for normally incident plane waves. For this study, the wedge model and the corresponding synthetic traces for the four types of reflectivities are the same as those discussed in section 2.3. The peak frequency of each synthetic trace was found by the maximum value of its amplitude spectrum. However, in both equations (3.4) and (3.5), if $\Delta t = 0$, that is, for zero bed thickness, $f_0 = f_p$. As with the amplitude study in Chapter 2, understanding the behaviour of peak frequency as a function of the bed thickness was the main objective of this work.

3.3.1 Type I reflectivity

Figure 3.3 is a plot of the results of equation (3.4) for this model for three different input Ricker wavelets with peak frequencies of 18 Hz, 31 Hz, and 50 Hz. The exact peak frequency equation is solved by iteration using a computer program. A range of frequencies of ± 6 Hz centred around the source wavelet's peak frequency is substituted into equation (3.4) at a frequency step of 0.01 Hz until equation (3.4) is solved for f_p . Also shown are the corresponding results from numerical models. All numerical results are listed in Table 3.1 in Appendix B.

Figure 3.3 shows that values predicted by equation (3.4) agree exactly with values from numerical modelling for the three different frequencies used. This implies that the peak frequency equation is independent of frequency. The results show that, for Type I reflectivity, the peak frequency of the composite reflected wavelet increases monotonically as the bed thickness decreases. However, the gradient is non-linear and is frequency-dependent. For example, when the wedge thickness changes from 1 m to 13 m, the percentage decrease expressed in terms of f_0 is 1.8% for $f_0 = 18$ Hz and 13.9% for $f_0 = 50$

Hz. Note that at $b = 13$ m, the wedge is only slightly larger than $(1/4)\lambda_d$ for $f_0 = 50$ Hz (see Table 3.1). In processing seismic data collected over thin geological formations, geophysicists often attempt to increase the high-frequency content of the data to increase its vertical resolution. The above results indicate that, even if the thickness is below resolution, higher frequencies are still preferable, because they are more sensitive to changes in bed thickness than are lower frequencies.

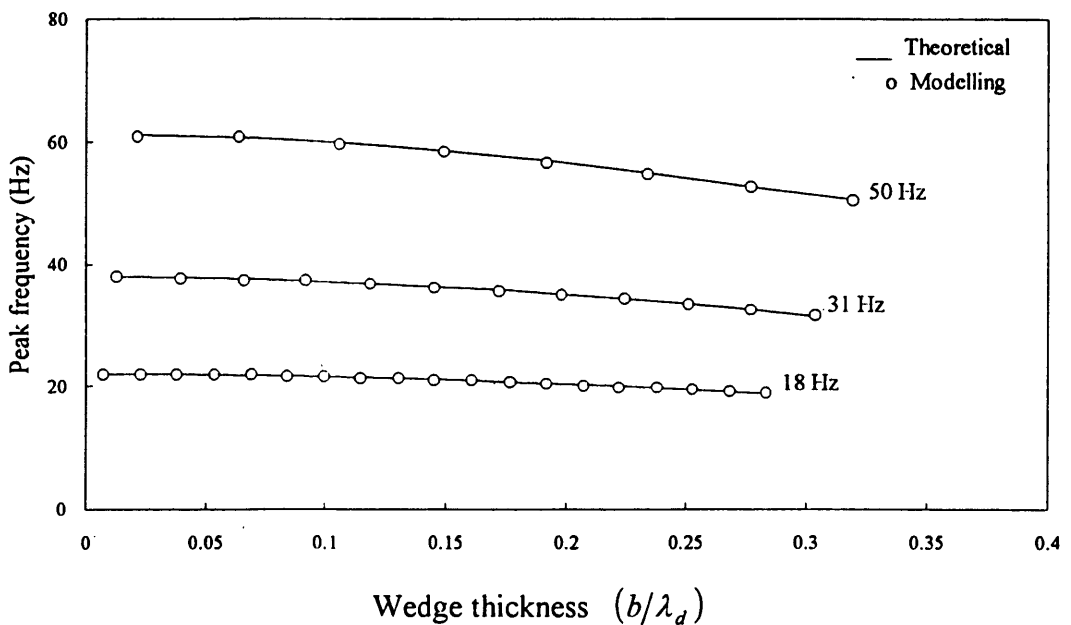


Figure 3.3 Peak frequency values vs. thickness for Type I reflectivity (τ^\perp).

3.3.2 Type II reflectivity

For this reflectivity sequence, the results from both the exact peak frequency equation and the thin-bed approximation agree well with the modelling results (Figure 3.4). Both results are frequency-independent. Since the exact peak frequency equation does not contain any approximations, it is expected to agree with the modelling results for all thicknesses. The results from the thin-bed peak frequency equation, however, will

agree with the modelling results only for thicknesses for which the thin-bed approximation remains valid. In Figure 3.4, the two results start to deviate at thickness of about $0.23\lambda_d$ for all three frequencies tested. However, the deviation is relatively small; for example, for the source frequency of 50 Hz and at the thickness of $0.24\lambda_d$, the result from the thin-bed peak frequency equation (33.5 Hz) is only 7.7% less than that of the modelling result (36.3 Hz). As with Type I reflectivity, the deviation is more observable for the higher frequency than for the lower frequency. The numerical results are listed in Table 3.2 in Appendix B.

For both Type I and Type II reflectivity studies, three input peak frequencies were used, the purpose being to verify that the equations are frequency-independent. For Types III and IV reflectivities, only the results obtained for a 31 Hz Ricker source wavelet will be presented. The presented results are valid for the specific models used, and may not be valid for similar reflectivity sequences whose reflection coefficients have significantly different magnitudes. However, equation (3.4) can always be used to study more different types of models.

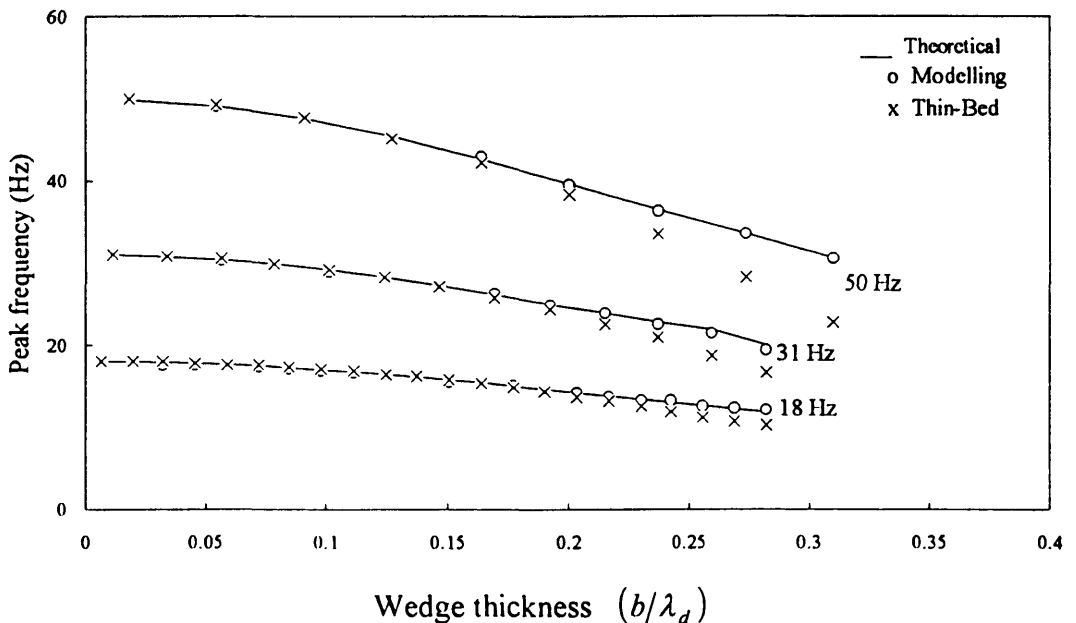


Figure 3.4 Peak frequency values vs. thickness for Type II reflectivity (\perp).

3.3.3 Type III reflectivity

It was shown in section 2.2 that this reflectivity can be expressed as the sum of Types I and II reflectivities. Since the peak frequencies for both types of reflectivities increase slowly as the bed thickness decreases, similar behaviour may be expected of Type III reflectivity. However, the data plotted in Figure 3.5 show that, as the thickness of the wedge increases, the calculated exact peak frequency of the reflected composite wavelet first increases, reaches a maximum at about $0.093\lambda_d$, and then slowly decreases. This behaviour is observed only for Type III reflectivity among the four types of reflectivities studied.

The results from the thin-bed peak frequency equation agree with the modelling results for thickness only up to about $0.03\lambda_d$. Above this thickness, the peak frequency values increase sharply and diverge rapidly from the modelling results. As explained in section 3.1, the reason is the small numerical value of the factor (r_1+r_2) in the denominator of equation (3.5). For the Type III reflectivity model used in this dissertation, $(r_1+r_2) = 0.0702$. For example, this is almost three times smaller than the value of 0.2098 for Type II reflectivity model. The numerical results are listed in Table 3.3 in Appendix B.

3.3.4 Type IV reflectivity

For this reflectivity sequence, the behaviour of the peak frequency of the reflected composite wavelet is similar to that for Types I and II reflectivities. Figure 3.6 shows the results for a 31 Hz Ricker wavelet as the source wavelet. Both the exact peak frequency equation and the thin-bed peak frequency equation lead to results which are consistent with the modelling results. They all indicate that the peak frequency slowly decreases as the thickness of the wedge increases. The numerical results are tabulated in Table 3.4 in Appendix B.

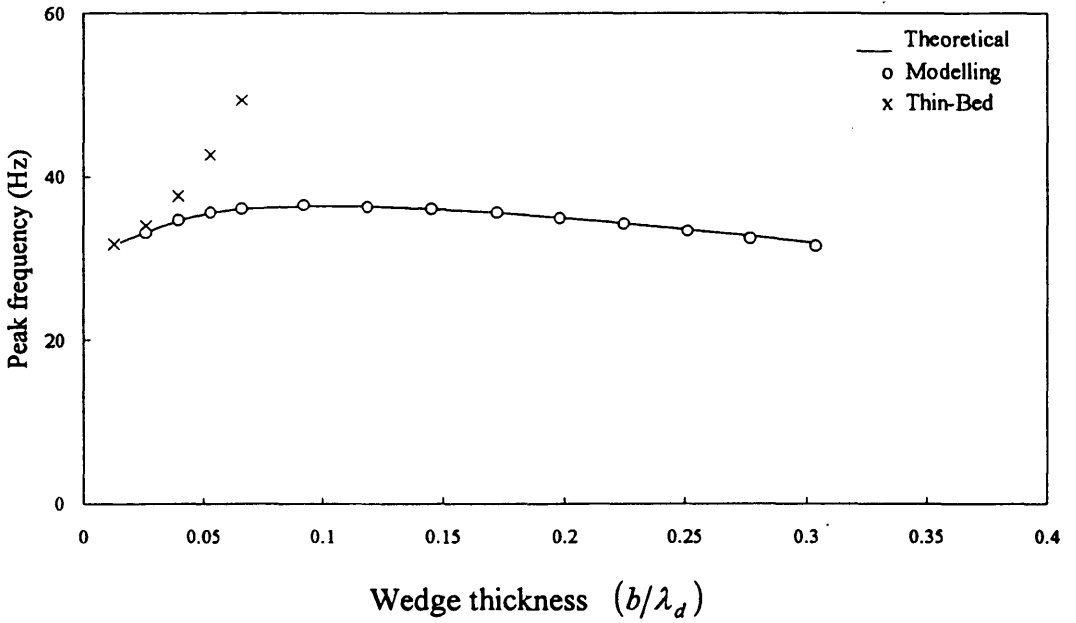


Figure 3.5 Peak frequency values vs. thickness for Type III reflectivity (\perp).

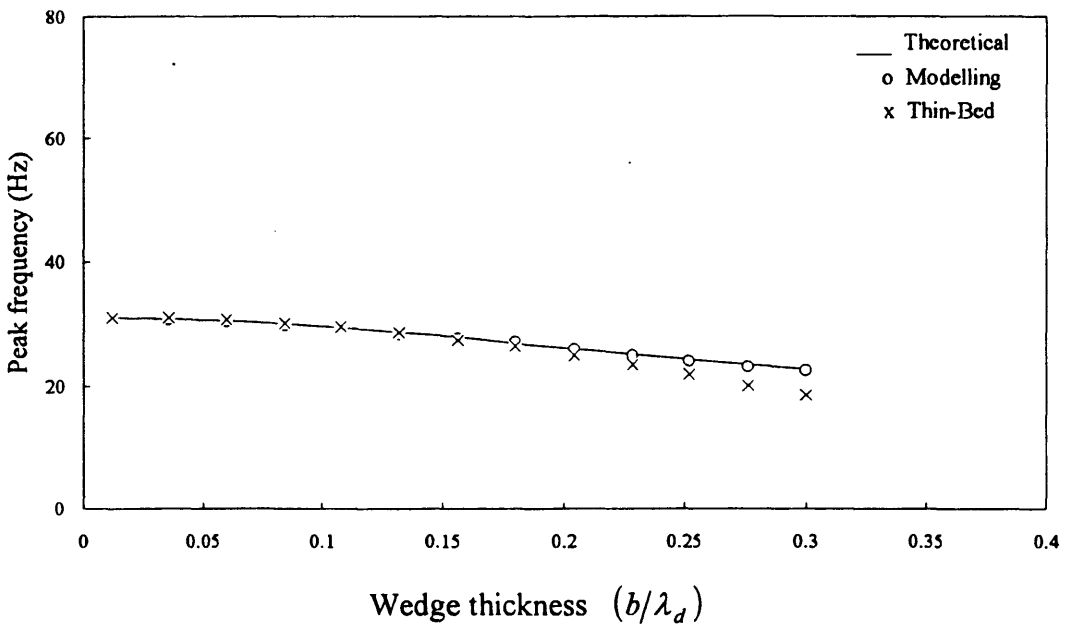


Figure 3.6 Peak frequency values vs. thickness for Type IV reflectivity ($\perp\perp$).

3.4 Normal incidence, two-layer model

In this section, the results calculated from equations (3.8) and (3.10) are compared with those from numerical modelling for Types V, VI, and VII reflectivities. The modelling traces are the same corresponding traces as used for the amplitude study in section 2.4. These equations are also used to generate curves of peak frequency versus thickness for each type of reflectivity sequence. The purpose is to study the behaviour of the peak frequency response of a thin layer as a function of its thickness in the presence of a second, underlying thin layer. Only a 31-Hz Ricker wavelet was used, since the approach has been shown to be frequency-independent.

3.4.1 Modelling comparison of Types V, VI, and VII reflectivity series

The results from equations (3.8) and (3.10) and the modelling results are plotted in Figures 3.7, 3.8, and 3.9 for Types V, VI, and VII reflectivity sequences, respectively. However, the results from equation (3.10) are plotted only in Figure 3.9 for Type VII reflectivity, since this equation is valid only for the situation where r_1 , r_2 and r_3 are all of the same polarity. For Types V and VI reflectivities, one of the reflection coefficients has a polarity opposite to that of the other two. Under this circumstance, the denominator in equation (3.10) can become very small and lead to erroneously large frequency values even for small bed thicknesses. For example, for Types V and VI reflectivities and a wedge thickness of 1 m underlain by a layer 2 m thick, the peak frequencies given by equation (3.10) are 3027 Hz and 1714 Hz respectively for a 31-Hz source wavelet. This problem is similar to the situation of Type III reflectivity where the thin-bed frequency equation leads to much larger frequency values for wedge thicknesses larger than 3 m when r_1 and r_2 are of opposite polarities. However, when r_1 , r_2 and r_3 are all of the same

polarity, the equation leads to results that agree well with the modelling results, as shown in Figure 3.9.

Figures 3.7 to 3.9 indicate that equation (3.8) agrees very well with the modelling results for a two-layer model. This is expected since it was derived using the same approach as that used for the exact peak frequency equation for the one-layer case and involves no approximations. Figure 3.9 also shows the results of equation (3.10) for Type VII reflectivity. The results from equation (3.10) agree well with the modelling results and with the results from equation (3.8) for wedge thickness below $(1/8)\lambda_d$. Even at a wedge thickness of $0.2\lambda_d$, the difference between the frequency values obtained using the approximation and the numerical modelling results is less than 8%. Hence, it is concluded that equation (3.10) gives good results if the layers are represented by reflection coefficients which all have the same polarity.

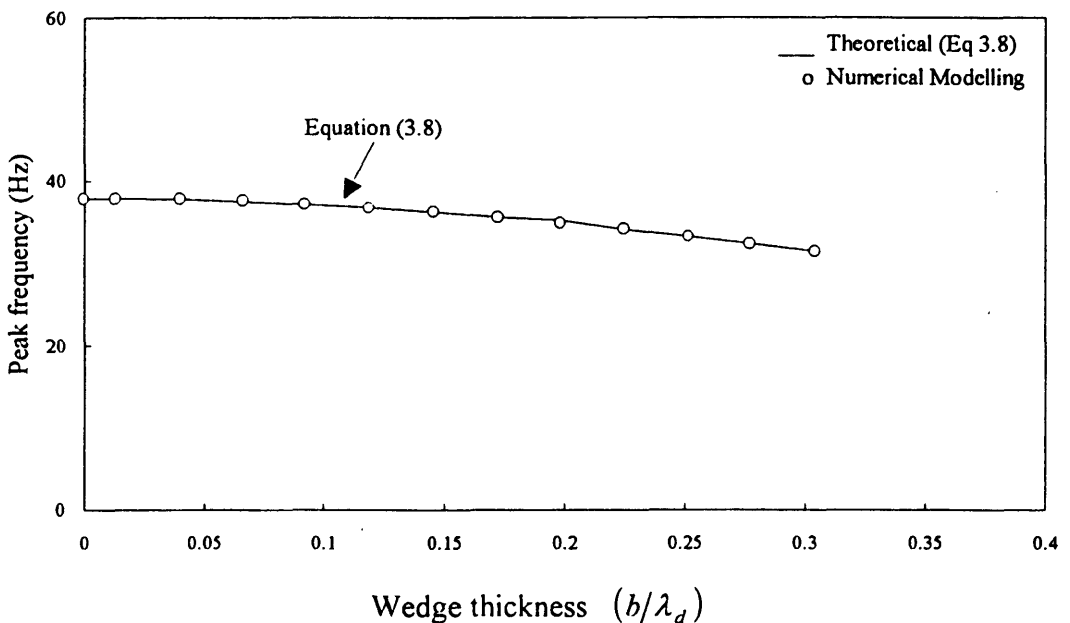


Figure 3.7 Peak frequency comparison between equation (3.8) and modelling for Type V reflectivity ($\begin{array}{c} | \\ \text{---} \\ | \end{array}$). The source wavelet is a 31-Hz Ricker wavelet, and the underlying layer is 2-m thick.

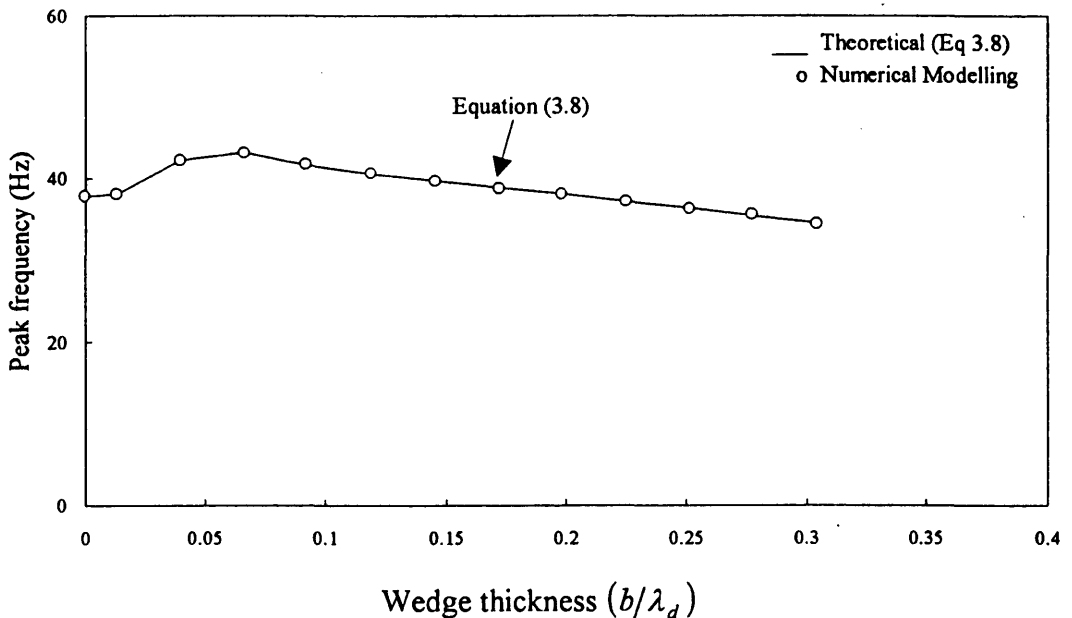


Figure 3.8 Peak frequency comparison between equation (3.8) and modelling for Type VI reflectivity ($\begin{array}{c} | \\ \text{---} \\ \text{---} \end{array}$). The source wavelet is a 31-Hz Ricker wavelet, and the underlying layer is 4-m thick.

3.4.2 Frequency dependence of Types V, VI, and VII reflectivity series

In this section, equation (3.8) is used to examine the peak frequency behaviour as a function of bed thickness for the three types of two-layer reflectivities. The same two-layer model is used for all computations, i.e. a wedge is underlain by a thin layer. The purpose is to investigate how the presence of an underlying thin layer affects the frequency behaviour of the wedge response. Three thicknesses - $0.021\lambda_{d_2}$ (2m), $0.063\lambda_{d_2}$ (6m), and $0.105\lambda_{d_2}$ (10m) - are chosen for the underlying thin layer, and for each of these thicknesses, the wedge varies from zero thickness to slightly larger than the $0.25\lambda_{d_1}$ value, where λ_{d_1} and λ_{d_2} are the predominant wavelengths in the wedge and the underlying thin layer, respectively. A 31-Hz Ricker wavelet is used as the source wavelet for all cases.

Figures 3.10, 3.11, and 3.12 show the peak frequencies for Types V, VI, and VII reflectivities, respectively, as calculated by equation (3.8).

Types V and VII reflectivities reduce to Type I and Type II reflectivities in the absence of the underlying layer. The presence of the underlying layer does not alter the behaviour of their peak frequency as a function of the wedge thickness. Regardless of the thickness of the underlying layer, for both reflectivities, the peak frequency is a slowly decreasing function of the wedge thickness. Furthermore, the frequency values with the underlying layer thickness being $0.063\lambda_{d_2}$ or less do not differ significantly from the corresponding values when the underlying layer is absent. When the underlying layer thickness is $0.21\lambda_{d_2}$, the peak frequencies are only about 2 to 3 Hz lower than the corresponding values with the underlying layer absent, which is around 10 % different for both reflectivities.

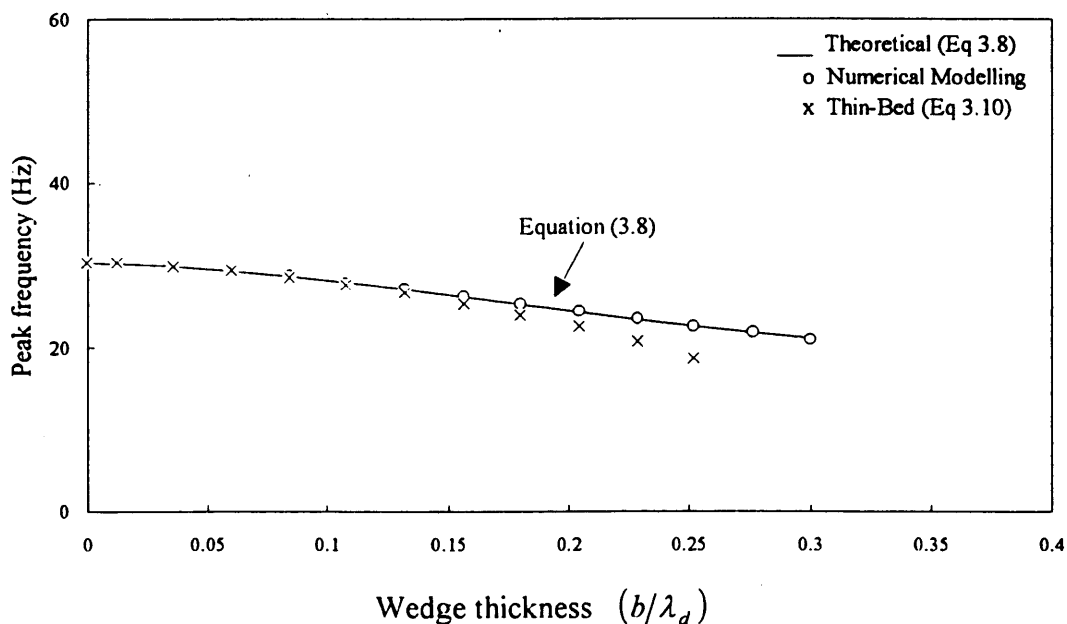


Figure 3.9 Peak frequency comparison between equation (3.8) and modelling for Type VII reflectivity ($\perp\perp\perp$). The source wavelet is a 31-Hz Ricker wavelet, and the underlying layer is 6-m thick.

For Type VI reflectivity, the results are quite different. In the absence of the underlying layer, this reflectivity reduces to a Type I reflectivity. However, the peak frequency of Type I reflectivity slowly decreases with the wedge thickness, whereas the peak frequency of Type VI reflectivity increases with the wedge thickness for small wedge thickness and then decreases slowly for greater thickness. For example, when the underlying layer thickness is $0.021\lambda_{d_2}$, there is a maximum value at about $0.066\lambda_{d_1}$; when it is $0.063\lambda_{d_2}$ or larger, the maximum occurs around $0.093\lambda_{d_1}$. This is similar to the frequency behaviour of Type III reflectivity. Furthermore, the differences between the frequency values in the presence of the underlying layer and those in its absence are significantly larger than that of Type V and Type VII reflectivities. For example, for a wedge thickness of $0.093\lambda_{d_1}$, the frequency values with the underlying layer thickness being $0.063\lambda_{d_2}$ is about 15% larger than the value without the underlying layer. This compares with 3% for Type V reflectivity and 4% for Type VII reflectivity. Another difference is that, for Type V and Type VII reflectivities, for the same wedge thickness, the peak frequency decreases with increasing thickness of the underlying layer. For Type VI reflectivity, however, the behaviour is fairly complex. First, for wedge thicknesses larger than $0.15\lambda_{d_1}$ (11 m), the peak frequency increases with the underlying layer thickness. For wedge thicknesses less than $0.15\lambda_{d_1}$, the peak frequency values are greatest when the underlying layer thickness is $0.063\lambda_{d_2}$. It is evident that there is some frequency tuning effect for this reflectivity that is absent for the other two reflectivity models.

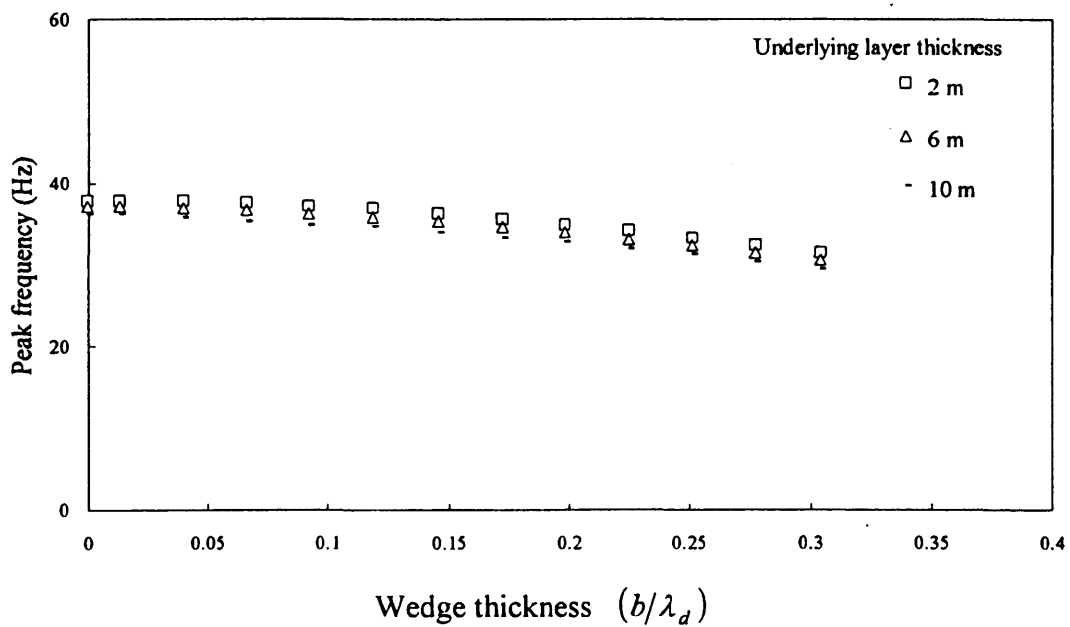


Figure 3.10 Peak frequency values from equation (3.8) for Type V reflectivity ($\begin{array}{c} | \\ \hline \end{array}$).

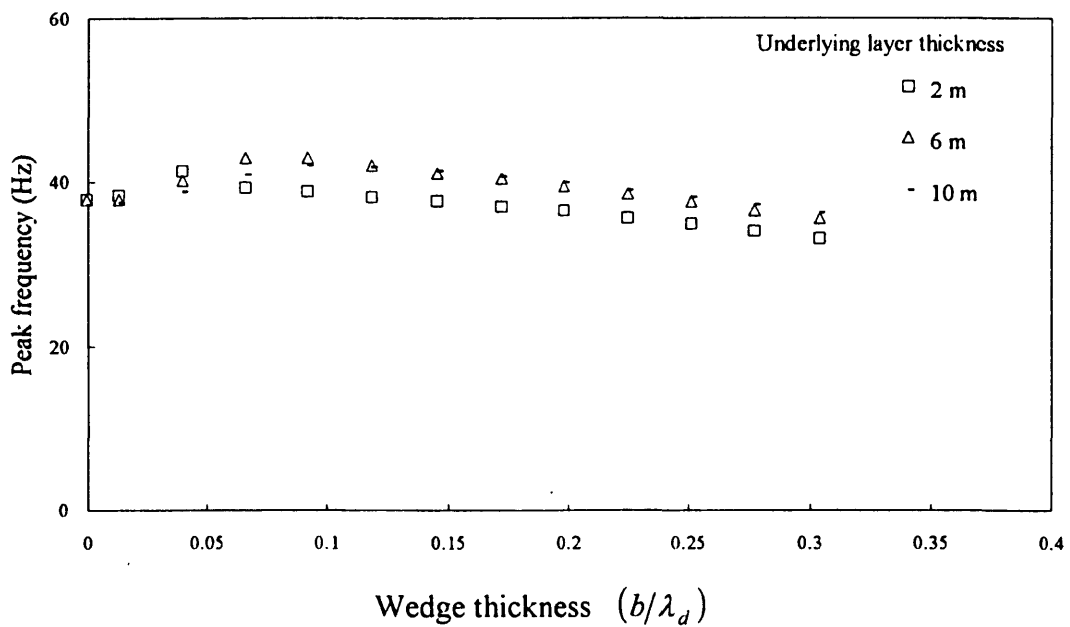


Figure 3.11 Peak frequency values from equation (3.8) for Type VI reflectivity ($\begin{array}{c} | \\ \hline | \\ \hline \end{array}$).

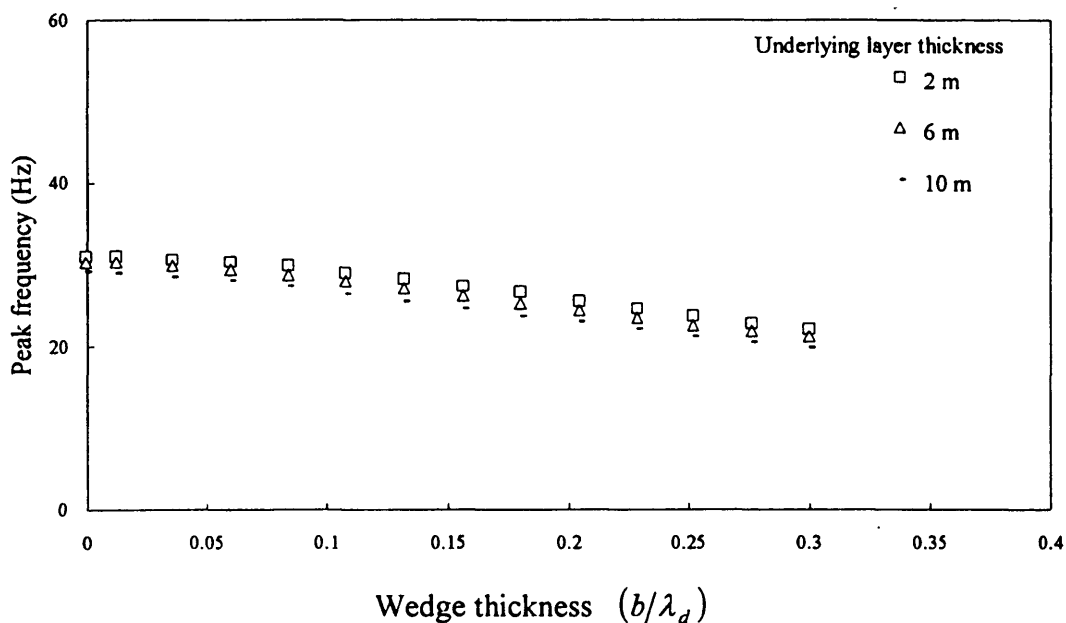


Figure 3.12 Peak frequency values from equation (3.8) for Type VII reflectivity ($\perp\perp\perp$).

3.5 Discussion

Both the exact peak frequency equations (3.4 and 3.8) and the thin-bed peak frequency equations (3.5 and 3.10) have been developed for the single-layer and two-layer models. Although equations (3.4) and (3.8) give exact values for the peak frequency of seismic reflections from a two-term and three-term reflectivity series respectively, they are complicated expressions and are not suitable for predicting the behaviour of the peak frequency as a function of thickness in a qualitative manner. Under the thin-bed assumption, however, they reduce to much simpler expressions, i.e. equations (3.5) and (3.10), respectively, and can be used to predict the behaviour of the peak frequency as a function of thickness in a qualitative manner. Thus, for layers which satisfy the thin-bed assumption, the qualitative behaviour of the peak frequency of seismic reflections from these layers can be understood readily with these simplified equations.

In stratigraphic interpretation of seismic data, emphasis traditionally has always been placed on the amplitude of the reflected wavelet, whereas its frequency behaviour has not been widely used. This is probably due to the fact that variations in amplitude can be related to variations in physical properties such as the velocity and density through the definition of the reflection coefficient in a straightforward manner. By contrast, relationships between the peak frequency of a reflected wavelet and any properties of a geological formation have not yet been firmly established.

From the analysis of the single-layer models in section 3.3, several conclusions can be drawn. It was shown in Chapter 2 that Type I reflectivity is a singular case in its amplitude behaviour in that it is the only reflectivity for which the amplitude response as a function of thickness is linear under the thin-bed assumption. The analysis in section 3.3 shows that Type I reflectivity is also a singular case in its peak frequency behaviour in that, as the bed thickness approaches zero, it is the only two-term reflectivity for which the peak frequency of its reflected composite wavelet approaches the value of the peak frequency of the derivative of the source wavelet, which is equal to $\sqrt{3/2}f_0$, where f_0 is the peak frequency of the source wavelet. However, at zero thickness, there is no reflection and the peak frequency curves in Figure 3.3 should have the same values as the peak frequencies of the source wavelets. Thus, there is a discontinuity at zero thickness for the peak frequency curves of Type I reflectivity.

For Types II, III, and IV reflectivity series, Figures 3.4, 3.5, and 3.6 show that, as the layer thickness approaches zero, the peak frequencies approach the values of the peak frequencies of the source wavelets, as predicted by equation (3.5). Furthermore, these figures also indicate that Type III reflectivity is the only reflectivity that exhibits frequency tuning effect at approximately the $0.1\lambda_d$ thickness. Thus, in a geological setting which can be modeled by a single thin bed, if the seismic data shows a frequency tuning effect, the setting can probably be represented by a Type III reflectivity sequence.

Equations (3.4) and (3.5) can be used for forward modeling, and the results can then be compared to observed results from seismic data. If the two sets of results differ significantly, parameters can then be selectively modified in equations (3.4) and (3.5) until a match is obtained. This will assist the geophysicists in the interpretation process in identifying the possible geological changes that contribute to any observed changes or anomalies in seismic data.

For the two-layer models, only Type VI reflectivity exhibits frequency tuning. As shown in Chapter 2, this is also the only three-term reflectivity sequence for which the amplitude as a function of thickness does not monotonically decrease as the thickness approaches zero thickness: tuning occurs at the wedge thickness of $0.05\lambda_d$. Thus, the results of the amplitude and peak frequency studies for two-layer models imply that, in interpreting seismic data reflected from geological formations that can be represented by reflection coefficients with alternating polarities, special care must be taken if the seismic data is used to deduce the thickness of the formations. Equations (3.8) and (3.10) can be used for forward modeling in a similar manner as discussed earlier for equations (3.4) and (3.5).

Chapter 4 - Complex attributes of thin beds

4.1 Introduction

The use of complex attributes in hydrocarbon exploration has not been widely discussed in published literature since Taner *et al.* (1977, 1979) proposed and discussed their potential usefulness. As White (1991) pointed out, while they are very useful in describing waveform changes, complex attributes do not lend themselves to direct interpretation. However, the localized nature of their calculations and the separation of amplitude information from phase information strongly suggest that they could be effective tools to detect subtle waveform changes and hence subtle geological changes. For example, Robertson and Nogami (1984) and Robertson and Fisher (1988) have demonstrated the use of complex attributes for a thin wedge represented by Type I reflectivity sequence. An important result discussed in these papers is the increase in instantaneous frequency as the wedge thins to below $(1/8)\lambda_d$.

The first objective of this chapter is to review and discuss the properties of attributes. The emphasis is on their unique characteristics as well as pitfalls for use in seismic interpretation. The second objective is to study their properties in terms of the seismic response of thin beds. As with the amplitude and frequency studies in the two previous chapters, the complex attributes of the seismic responses of a single layer and two layers embedded in two half spaces to normally-incident plane waves are examined. The complex attributes of the offset-dependent seismic reflections of a single layer embedded in two half spaces are studied in Chapter 5.

4.2 Properties of complex attributes

The attributes are reviewed in the order of the instantaneous amplitude, which solely deals with the time-variant amplitude of the signal, then the instantaneous phase, which describes the localized phase of the signal, and finally the instantaneous frequency, which is simply the derivative of the instantaneous phase. In terms of using the complex attributes to delineate subtle waveform changes, only the instantaneous phase and the instantaneous frequency are useful. The instantaneous amplitude is the amplitude envelope of the signal and hence masks all subtle waveform changes. However, it can be used for the quantitative study of seismic reflection amplitudes.

4.2.1 Instantaneous amplitude

From an interpretation point of view, instantaneous amplitude, whose definition is given in section 1.5, highlights bright spots, lateral amplitude variations caused by thin-bed tuning, as well as major lithological changes. However, it is not very useful for stratigraphic interpretation where subtle waveform changes signify corresponding subtle geological changes. When amplitude information is needed, it offers the advantage of being phase-independent so that it gives information which is indicative of lithological changes without being contaminated by the phase of the input wavelet. For example, a zero-phase source wavelet reflected from a single interface has an amplitude envelope which is identical to that resulted when the source wavelet is the 90°-phase counterpart of the zero-phase wavelet. However, if we measure the amplitudes of the reflected wavelets directly, the maximum amplitude of the zero-phase source wavelet is always larger than that for its 90°-phase counterpart, assuming that they have the same total energy.

The instantaneous amplitude is also significant in that the time at the peak of the envelope is the time where the instantaneous frequency is equal to the wavelet's average

Fourier spectral frequency weighted by its amplitude spectrum. This was shown by Robertson and Nogami (1984) for zero-phase wavelets. However, Saha (1987) showed that this is true for any wavelet, not just for zero-phase wavelets. This equivalence is the geophysical extension of the assertion by Ackroyd (1970) that the instantaneous frequency of an analytic signal at a given time is a measure of the centre frequency corresponding to the normalized first moment of the power of the signal at that time. Hence, to learn about the spectral characteristics of the wavelet, one can first obtain the amplitude envelope, pick the envelope peak time, and then obtain the instantaneous frequency at the corresponding time. In fact, Mazzotti (1991) defined this instantaneous frequency as the barycentral frequency and used it as one of his three APF.VO (amplitude, phase, frequency versus offset) indicators. The use of complex attributes for offset-dependent models is presented in section 5.4.

There is an important aspect of the Hilbert transform, which could affect the results of all three complex attributes. The following discussion is a summary of both Bracewell's (1965) and Wallace's (1991) discussions. Consider a function $f(x)$ which contains some d.c. bias. The Hilbert transform of $f(x)$ is defined as (Bracewell, 1965):

$$F_H(x) = \frac{1}{\pi} \int_{-\infty}^{\infty} \frac{f(x') dx'}{x' - x} \quad (4.1)$$

$$= \frac{-1}{\pi x} * f(x)$$

where $*$ denotes convolution. Thus, in the frequency domain, the spectrum of $F_H(x)$ is equal to the multiplication of the spectrum of $-1/(\pi x)$ with the spectrum of $f(x)$. However, the Fourier spectrum of $-1/(\pi x)$ is equal to $i \operatorname{sgn}(s)$, where $\operatorname{sgn}(s)$ represents the signum function defined as:

$$\text{sgn}(s) = \begin{cases} -1 & s < 0 \\ 0 & s = 0 \\ 1 & s > 0 \end{cases} \quad (4.2)$$

Therefore, after the multiplication, the spectrum of $f(x)$ undergoes a 90° -phase rotation, resulting in the exchanging of the real and imaginary components. However, the imaginary component of the Fourier transform is an odd function and hence cannot possess a d.c. bias. Thus, when the real component is swapped into the imaginary component, the d.c. bias is zeroed out. If we perform two successive Hilbert transforms on $f(x)$, the resultant will be equal to $-f(x)$ (the minus sign results from i^2 or $(-i)^2$, less the d.c. bias).

This property of the Hilbert transform can significantly affect the calculation of the attributes. Consider a signal $x(t)$, which has a d.c. bias. Let $x_0(t)$ simply be $x(t)$ less the d.c. bias. Then, we can write:

$$x_0(t) = x(t) - \bar{x}$$

where \bar{x} is the arithmetic mean of $x(t)$. Suppose we perform the Hilbert transform on both $x_0(t)$ and $x(t)$. Since the corresponding quadrature components, $y_0(t)$ and $y(t)$, can contain no d.c. bias, they are identical. The amplitude envelopes, $A_0(t)$ and $A(t)$, are then $A_0(t) = \sqrt{x_0^2(t) + y_0^2(t)}$ and $A(t) = \sqrt{x^2(t) + y^2(t)}$. Hence, $A_0(t) \neq A(t)$, since $x_0(t) \neq x(t)$. Similarly, if θ_0 and θ are the corresponding instantaneous phases, then:

$$\theta_0 = \tan^{-1} \left[\frac{y_0(t)}{x_0(t)} \right] \neq \theta = \tan^{-1} \left[\frac{y(t)}{x(t)} \right]$$

and the corresponding instantaneous frequency will also be different. This means that, if a seismic trace does contain d.c. bias, the attribute calculations will be erroneous if the corresponding quadrature trace is obtained by transforming the real trace into the frequency domain, rotating the phase spectrum by 90° , and inverse transforming the trace back into the time domain.

Most seismic traces in conventional final format have low-cut filters applied to them, and there is no problem with the attribute calculations, since low-cut filters successfully remove d.c. bias. However, for thin-bed interpretation, the seismic data and any relevant modelling data may be studied within a narrow time window. The potential pitfall is that, for a short time window of a trace which leads to a large frequency sampling interval in the frequency domain, any low frequency components may appear as d.c. bias, and hence will be removed during the attribute calculations. On real seismic traces, the minimum frequency, typically around 10 Hz, allows for time windows down to 100 ms before temporal-aliasing (large Δf in the frequency domain) becomes a problem. Alternatively, the attributes can be calculated for the entire trace and the results within the time zone of interest can then be studied.

One final interesting property of the Hilbert transform is that, since the application of two Hilbert transforms in succession reverses the phases of all components due to the $i\text{sgn}(s)$ function, it follows that the result will be the negative of the original function. That is, for a function $f(x)$,

$$\text{if } F_H = \left(\frac{-1}{\pi x} \right) * f(x)$$

$$\text{then } f'(x) = \left(\frac{-1}{\pi x} \right) * F_H = -f(x).$$

In equation (4.1), if the kernel had been chosen as $[j\pi(x'-x)]^{-1}$ instead of $[\pi(x'-x)]^{-1}$, the transformation would have been strictly reciprocal, for then the effect would have been to multiply the spectrum by $(\text{sgn } s)$, and two such multiplications produce no net change. The custom is to sacrifice the symmetry in favor of the property that the Hilbert transform of a real function should also be a real function (Bracewell, 1965).

4.2.2 Instantaneous phase

The instantaneous phase is calculated by the relationship:

$$\theta_i(t) = \tan^{-1} \left[\frac{y(t)}{x(t)} \right] \quad (4.3)$$

where $x(t)$ is the seismic trace and $y(t)$ is the corresponding quadrature trace. It is a localized measurement and is independent of the amplitude. Applying the phasor representation of simple harmonic motion to signals with time-variant amplitudes and periods, one can visualize the instantaneous phase as the angle shown in Figure 4.1 where both $A(t)$ and $\theta_i(t)$ are both time-variant. Using a similar representation, White (1991) showed a similar diagram, shown in Figure 4.2, for a portion of a seismic trace. In his diagram, the real function $x(t)$ is plotted as the vertical axis and the quadrature function $y(t)$ as the horizontal axis. The vector is rotating anti-clockwise and the angle of the vector to the vertical axis gives the instantaneous phase and the rate of rotation the instantaneous frequency. At the inflection point, the rotational velocity of the vector slows down and reverses direction momentarily (i.e. negative instantaneous frequency) before continuing its anti-clockwise motion. This illustrates an important property of the instantaneous phase; whenever a seismic trace exhibits an inflection point without having crossed the time axis, i.e. the zero-amplitude axis, the instantaneous phase will always

exhibit a rather abrupt character change due to the phasor vector rotating clockwise around the inflection point as opposed to the general anti-clockwise rotation. This phase character change is defined as inflection phase anomaly.

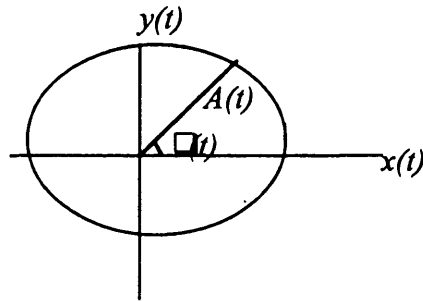


Figure 4.1 Phasor representation of instantaneous amplitude and instantaneous phase. The rate of rotation is the instantaneous frequency.

The inflection phase anomaly has an important implication for thin-bed interpretation. Since interference is an implicit component of thin-bed reflections, inflections are common occurrences in these reflections. For example, doublets are often observed in such reflections (Figures 2.5.b and 2.5.d). While such reflections can often be observed directly on seismic traces, they may not be evident if the amplitudes are relatively small. Hence, the instantaneous phase is a good tool to delineate subtle interference patterns, and in general, it is an effective tool to show subtle lateral waveform changes. Both Taner *et al.* (1979) and Yilmaz (1987) emphasized that the instantaneous phase displays are effective in showing discontinuities, faults, pinchouts, onlaps, angular conformities, and events with different dip attitudes which interfere with one another. All these events are accompanied by lateral changes in the wavelet shape due to interference. However, to interpret any instantaneous phase anomalies and extract meaningful geological information, one still has to rely on modelling and then compare the modelling results with real data.

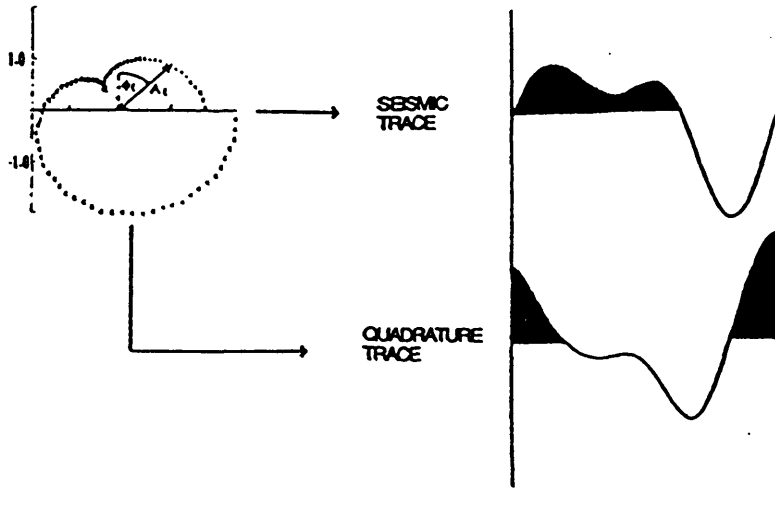


Figure 4.2 Phasor representation of a portion of a seismic trace (from White, 1991).

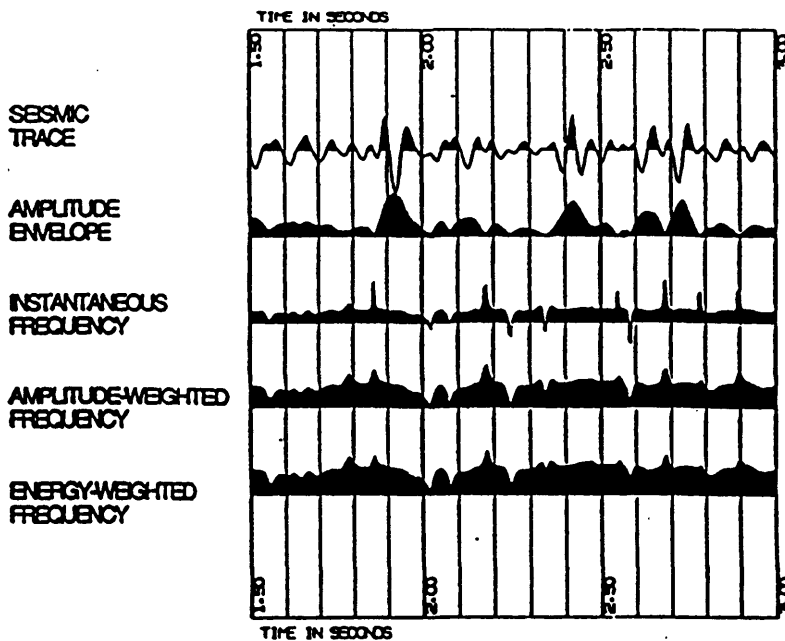


Figure 4.3 Comparison of weighted and unweighted instantaneous frequencies (White, 1991).

Finally, the instantaneous phase plots often have a sawtooth appearance when their numerical values are plotted without the use of colours. This is because they are always plotted between $-\pi$ and $+\pi$ (modulo $\pm\pi$). Farnbach (1975) plotted the instantaneous phase as a continuously increasing function, but he was studying only a pulse, and his method of plotting would not be suitable for a continuous seismic trace that has numerous pulses.

4.2.3 Instantaneous frequency

The instantaneous frequency is defined as the first derivative of the instantaneous phase, i.e.

$$f_i = \frac{d\theta_i}{dt} \quad (4.4)$$

It bears a relationship to the Fourier frequency spectrum; Robertson and Nogami (1984) showed that the instantaneous frequency at the time that coincides with the corresponding amplitude envelope peak is equal to the first moment of the wavelet's amplitude spectrum for a zero-phase wavelet. Bodine (1986) showed that this is also true for constant-phase Ormsby wavelets. Saha (1987) further generalized this and proved that this is true for all wavelets. In recent years, there have been some studies investigating the possibility of using this particular instantaneous frequency for interpretation. For example, Bodine (1986) and Robertson and Fisher (1988) called this instantaneous frequency the response frequency, and studied its properties as a function of bed thickness. Mazzotti (1991) called it the barycentral frequency and studied it as a function of source-receiver offset. His study shows that the barycentral frequency does not change significantly with offset. However, the studies are preliminary and further research is needed before conclusions can be drawn as to its usefulness in interpretation of seismic data. In all subsequent

discussions, the term 'barycentral frequency' will be used to denote the instantaneous frequency that occurs at the time of the envelope maximum.

The most unique property of instantaneous frequency is that it can be abnormally high compared to its Fourier frequency components of the wavelet, and it can also be negative, as discussed in the previous section. As shall be shown later, some of these abnormal values occur around inflection phase anomalies and low-amplitude troughs. Thus, instantaneous frequency and instantaneous phase can be very useful tools to delineate subtle waveform character changes due to thin-bed wavelet interference.

Instantaneous frequency is similar to instantaneous phase in that they both illustrate lateral continuity of waveform character and are independent of amplitude. Hence, they are also useful tools for delineating geological features such as pinchouts, angular unconformities, onlaps, faults, and channels etc. Robertson and Nogami (1984) reported an increase in instantaneous frequency when a thin bed reduces in thickness to a value equal to $(1/8)\lambda_d$. This property could be used to detect the presence of thin beds, as discussed in Chapter 6 in the study of a gas-saturated sandbar. However, since it is the derivative of the instantaneous phase, an instantaneous frequency section tends to appear slightly noisier than the corresponding phase section due to the high-frequency enhancement property of differentiation. Furthermore, as discussed by White (1991), abnormally large frequency values tend to occur at times when amplitudes are relatively small, and hence are less reliable. To improve the reliability of the frequency values and to minimize the spikiness of its appearance, an amplitude-weighted instantaneous frequency section can be used instead, as illustrated in Figure 4.3 (White, 1991). It shows a portion of the seismic trace, its amplitude envelope, instantaneous frequency, as well as the corresponding amplitude-weighted instantaneous frequency. The result of the amplitude-weighted frequency is self-evident in the figure. From the interpretation point of view, the magnitudes of the frequency and phase values are not particularly significant; it is their

lateral continuity and change of character that are of interest to seismic interpreters. In this regard, the colour displays are extremely useful visual aids. The quantitative use of instantaneous frequency and phase to derive geological information remains a subject of present and future research.

4.3 Normal incidence, single-layer model

In this section, the instantaneous amplitude, frequency, and phase characteristics of the seismic response of a thin layer to normally-incident plane waves are examined. The same synthetic seismograms for the four reflectivities (shown in Figure 2.5) used for amplitude and frequency studies of Chapters 2 and 3 are used for attributes analysis, although only the attributes with a 31 Hz Ricker wavelet as a source wavelet are studied. The attributes for the corresponding 90° -phase wavelet as a source wavelet need not be studied, since the corresponding instantaneous amplitude and frequency plots for the two cases are identical, and the two corresponding phase plots differ only by a constant. The colour schemes used for the attribute displays have been found to be very effective and are adequate for the following study.

4.3.1 Instantaneous amplitude

Figure 4.4 shows instantaneous amplitude displays for Types I, II, III, and IV reflectivities respectively. The instantaneous amplitudes for Type I ($\overline{\text{T}}^{\perp}$) and Type III ($\overline{\text{T}}^{\perp}$) reflectivities have a similar appearance with only one evident difference. The tuning thickness for both models is approximately at trace 19. In Figure 4.4, each colour change represents an amplitude change of 28 units. The result is that, for Type III reflectivity, the tuning amplitude maximum can be observed at a location very close to trace 19. However, for Type I reflectivity, the colour that represents the maximum amplitude

stretches from trace 13 to trace 23, although its tuning amplitude is higher than that of the Type III reflectivity. Thus, a very localized amplitude maximum may be indicative of the presence of two reflection coefficients which have opposite polarities and unequal amplitudes. Furthermore, the amplitude envelope of Type I reflectivity (Figure 4.4a) is symmetrical about the peaks of the envelopes, whereas that of Type III reflectivity is slightly asymmetrical. The difference is reasonable, given that the two reflection coefficients of Type III reflectivity have unequal amplitudes. However, as Figure 4.4d shows, this is not the case for Type IV reflectivity.

For Types II ($\perp\perp$) and IV ($\perp\perp$) reflectivities, the instantaneous amplitudes are almost identical between trace 1 and trace 10, which is approximately the $(1/8)\lambda_d$ thickness for both models. Beyond trace 10, the amplitude envelope of Type II reflectivity retains its symmetry about the peak of the envelope, whereas that of Type IV reflectivity starts to exhibit asymmetry due to the unequal amplitudes of its two reflection coefficients. The amplitude envelope of Type II reflectivity also shows clearly the effect of wavelet splitting at trace 19. Tuning, which corresponds to amplitude minima for these two types of reflectivities, is not as clearly defined as it is for Types I and III reflectivities. The reason is that, for Type II reflectivity, the tuning minimum occurs at about trace 22. But the wavelet splitting starts at trace 19, beyond which a central trough starts to develop. The amplitude of this trough along the line of symmetry continues to decrease as thickness increases, and thus, the colour scheme does not show the tuning minimum clearly. A similar reason holds for Type IV reflectivity.

4.3.2 Instantaneous phase

The instantaneous phase is independent of amplitude and is very effective for outlining subtle waveform changes that are not visually clear on conventional seismic data

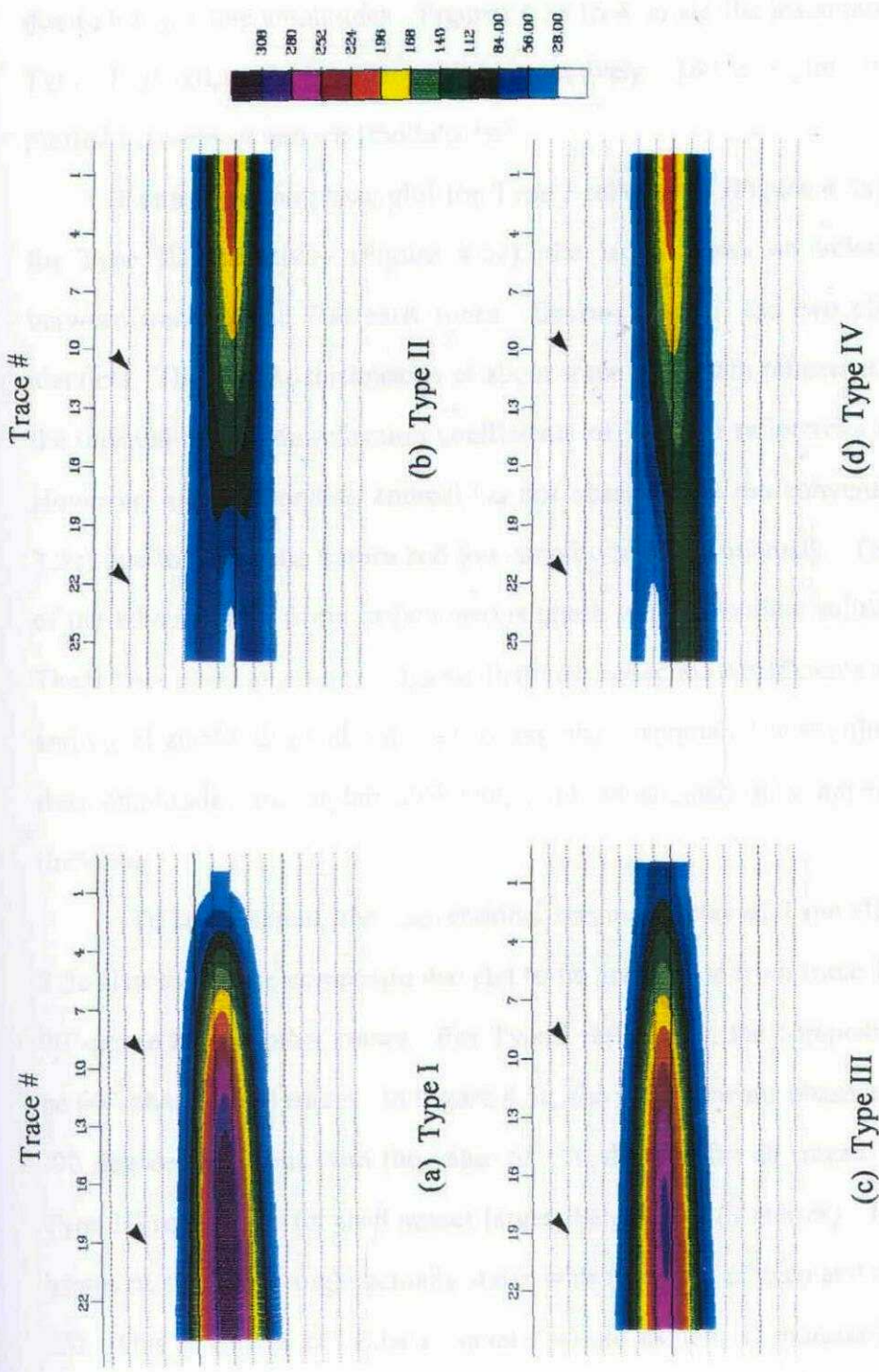


Figure 4.4 Instantaneous amplitudes for (a) Type I ($\perp\perp$), (b) Type II ($\perp\perp$), (c) Type III ($\perp\perp$), and (d) Type IV ($\perp\perp$) reflectivities. The source wavelet is a 31 Hz Ricker wavelet, and the arrows indicate the $(1/8)\lambda_d$ and $(1/4)\lambda_d$ locations. Timing lines are at 10 ms intervals.

due to low relative amplitudes. Figures 4.5a to 4.5d are the instantaneous phase plots for Types I, II, III, and IV reflectivities respectively. In these plots, the phase angles are plotted between $-\pi$ and $+\pi$ (modulo $\pm\pi$).

Comparing the phase plot for Type I reflectivity (Figure 4.5a) with the phase plot for Type III reflectivity (Figure 4.5c), the latter shows an inflection phase anomaly between traces 1 and 7 at early times. Beyond trace 7, the two phase plots are almost identical. The $(1/8)\lambda_d$ thickness is at about trace 9 for both reflectivities. It is evident that the unequal-amplitude reflection coefficients of Type III reflectivity lead to this anomaly. However, a corresponding anomaly is not observed on the conventional display (Figure 2.5c) due to the subtle nature and low amplitude of the anomaly. This is a good example of the advantage of using instantaneous phase plots to outline subtle waveform changes. These two phase plots also suggest that two reflection coefficients of opposite polarities and equal amplitudes will not lead to any phase anomaly for any thickness. However, if their amplitudes are slightly different, a phase anomaly may appear below the $(1/8)\lambda_d$ thickness.

To some extent, the conventional seismic display of Type III reflectivity in Figure 2.5c also shows the composite wavelet to be zero-phase from trace 1 to about trace 6 and 90° -phase for the other traces. For Type I reflectivity, the composite wavelet appears to be 90° -phase for all traces. In Figure 4.5a, the instantaneous phase starts with the value of -90 degrees and ends with the value of $+90$ degrees for all traces. This is also true for Type III reflectivity for thicknesses larger than $0.08\lambda_d$ (6 metres). For the first six traces, however, the phase angle actually starts with the value of zero and ends with the value of -90 . This is what a zero-phase wavelet would exhibit, as indicated by the instantaneous phase plots of Types II and IV reflectivities shown in Figures 4.5b and 4.5d respectively.

For Types II and IV reflectivities, the instantaneous phase plots (Figures 4.5b and 4.5d) are almost identical from trace 1 to approximately trace 15. Beyond this trace, there

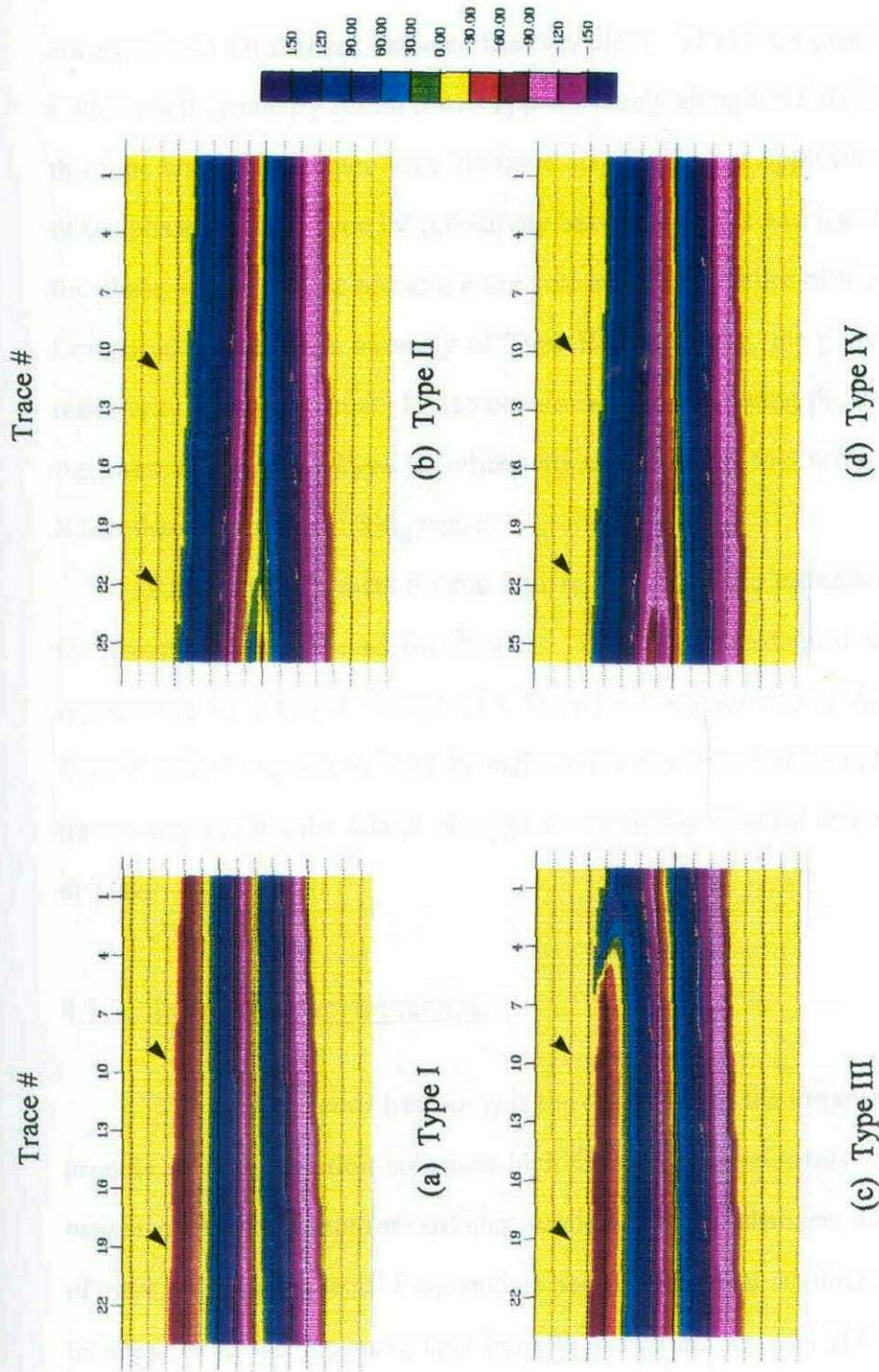


Figure 4.5 Instantaneous phases for (a) Type I (Γ^{\perp}), (b) Type II ($\perp\perp$), (c) Type III (\perp^{\perp}), and (d) Type IV ($\perp\perp$) reflectivities. The source wavelet is a 31 Hz Ricker wavelet, and the arrows indicate the $(1/8)\lambda_d$ and $(1/4)\lambda_d$ locations. Timing lines are at 10 ms intervals.

are significant differences between the two plots. The phase plot for Type II reflectivity exhibits odd symmetry for all traces approximately along the time line L. Before and after this time line, phase angles have the same magnitudes but opposite signs. This is also true of the phase plot for Type IV reflectivity between trace 1 and trace 15. Beyond trace 15, the phase angles start to reveal the unequal-amplitude nature of the reflection coefficients. Compared to the phase anomaly of Type III reflectivity, the phase anomaly of Type IV reflectivity is more gradual. It also occurs close to the tuning thickness (trace 21) whereas the phase anomaly for Type III reflectivity occurs at the first 6 traces where the thickness is less than half of the $(1/8)\lambda_d$ value.

Based on the results for the four reflectivities, the instantaneous phase is effective for detecting subtle waveform changes. Hence, for geological situations which can be represented by a lateral change of a Type I reflectivity into a Type III reflectivity, or a Type II reflectivity into a Type IV reflectivity, the instantaneous phase plot of the seismic traces may outline the lateral changes more clearly than the corresponding conventional display.

4.3.3 Instantaneous frequency

The instantaneous frequency is the derivative of the instantaneous phase. Since the process of differentiation enhances high frequency components, instantaneous frequency may also be a good tool for outlining subtle waveform changes. From a quantitative point of view, the instantaneous frequency is perhaps the most significant attribute in that it can be negative as well as being very large (e.g. 500 Hz for a 31 Hz Ricker source wavelet). Figures 4.6a to 4.6d are the instantaneous frequency plots for Types I, II, III, and IV reflectivities.

For Type I and III reflectivities, the instantaneous frequency plots (Figures 4.6a and 4.6c) show some common characteristics. They both exhibit an increase in frequency as the thickness thins to about the $(1/8)\lambda_d$ value, as reported by Robertson and Nogami (1984). They also span a similar range of frequencies for corresponding traces. However, the instantaneous frequency for Type I reflectivity is symmetrical for all thicknesses, but for Type III reflectivity, it shows an anomaly which corresponds to the inflection phase anomaly in Figure 4.6c between traces 1 and 6. At approximately trace 19, it also shows a pattern slightly different from the corresponding location in the instantaneous frequency for Type I reflectivity, whereas the corresponding instantaneous phase plots do not show a corresponding difference. Thus, the instantaneous frequency is even a more sensitive tool for outlining subtle waveform changes than the instantaneous phase.

For Types II and IV reflectivities, the instantaneous frequency plots (Figures 4.6b and 4.6d) are also similar from trace 1 to trace 9. They also exhibit the frequency tuning effect as reported by Robertson and Nogami (1984). Thus, frequency tuning is merely a function of the bed thickness regardless of whether the amplitude is a minimum (Types I and III reflectivities) or maximum (Types II and IV reflectivities). However, the frequency tuning effect for Types I and III reflectivities occurs at about the $(1/8)\lambda_d$ thickness, and remains until the bed thins to zero thickness. For Types II and IV reflectivities, the effect covers a smaller thickness range, namely from about trace 1 to trace 5, which is equivalent to a thickness range of zero thickness to about the $(1/16)\lambda_d$ thickness.

Furthermore, for Type II reflectivity, the instantaneous frequency pattern is symmetrical. The doublets, starting at about trace 16 (Figure 4.6b), appear as elongated balloons buried one inside another. This zone corresponds to the troughs between the doublets in Figure 2.5b. This is also the zone where the instantaneous frequency has very large negative values. A similar zone also occurs in Figure 4.6d for Types IV reflectivity,

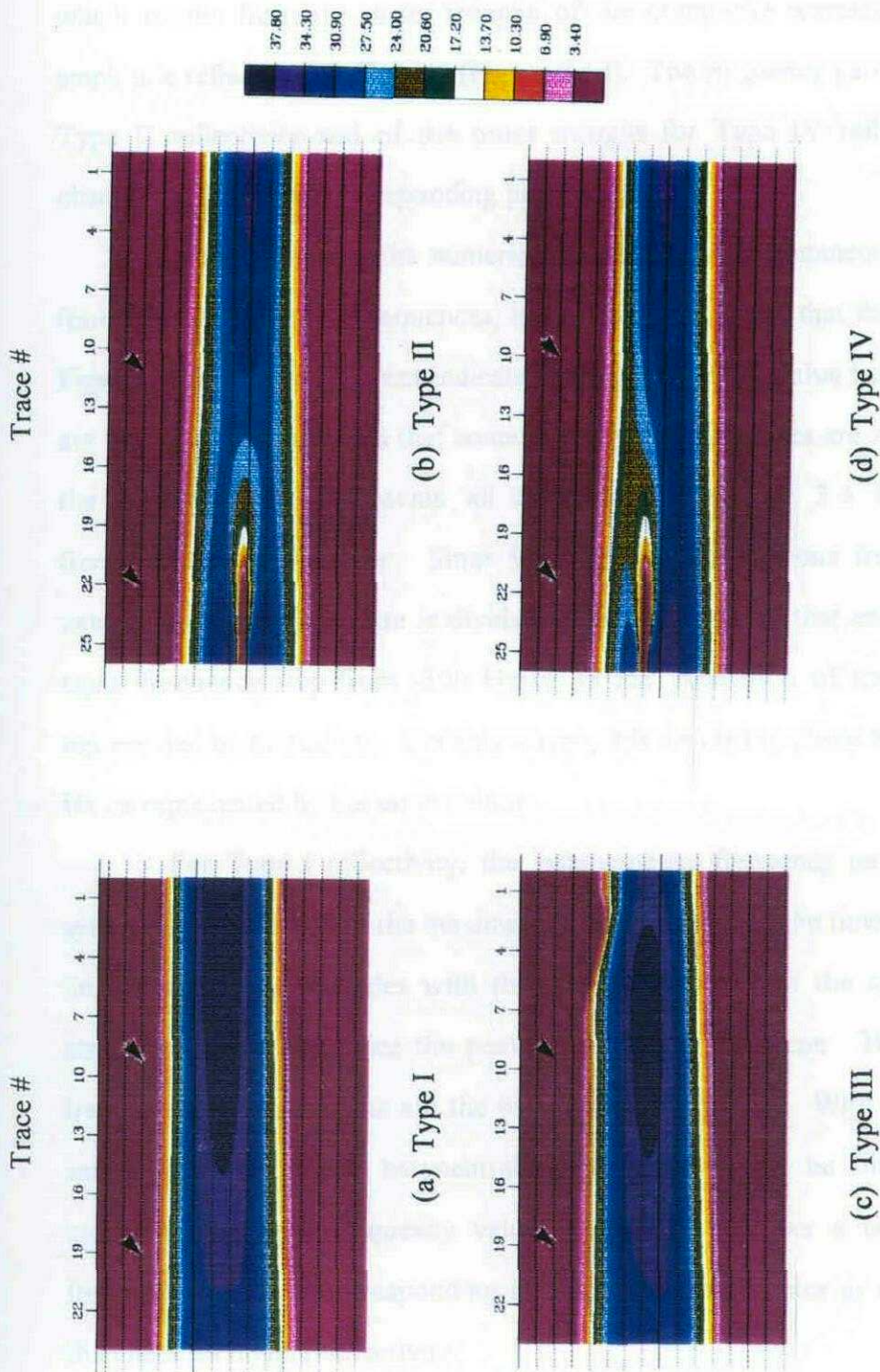


Figure 4.6 Instantaneous frequencies for (a) Type I (\top), (b) Type II (\perp), (c) Type III (\top), and (d) Type IV (\perp) reflectivities. The source wavelet is a 31 Hz Ricker wavelet, and the arrows indicate the $(1/8)\lambda_d$ and $(1/4)\lambda_d$ locations. Timing lines are at 10 ms intervals.

which results from the onset troughs of the composite wavelets due to the unequal-amplitude reflection coefficients (Figure 2.5d). The frequency patterns of the doublets for Type II reflectivity and of the onset troughs for Type IV reflectivity are both more observable than their corresponding phase patterns.

Before examining the numerical values of the instantaneous frequencies for these four types of reflectivity sequences, it must be pointed out that the colour palette used in Figures 4.7a to 4.7d does not indicate the existence of negative frequencies, although they are present. The reason is that some of negative frequencies are as large as -300 Hz, and the colour palette represents all frequencies less than 3.4 Hz, including negative frequencies, in red colour. Since 99% of the instantaneous frequencies have positive values, if the colour palette is divided up in a manner so that each colour represents an equal frequency step from -300 Hz to 38 Hz, then 99% of the frequencies would be represented by one colour. For this reason, it is decided to allow all frequencies below 3.4 Hz be represented by the same colour.

For Type I reflectivity, the instantaneous frequency pattern (Figure 4.6a) is a symmetrical pattern with the maximum values lying along the time line of symmetry. This line of symmetry coincides with the line of symmetry of the corresponding amplitude envelope, along which lies the peak values of the envelope. Hence, the instantaneous frequencies along this line are the barycentral frequencies. With the Ricker wavelet as a source wavelet, these barycentral frequencies would be slightly larger than the corresponding peak frequency values. Table 4.1 shows a comparison of the peak frequencies and the corresponding instantaneous frequencies as a function of the wedge thickness for Type I reflectivity.

Table 4.1 Peak frequencies and corresponding barycentral frequencies for Type I reflectivity as a function of the wedge thickness.

Thickness (m)	Peak frequency (Hz)	Barycentral frequency (Hz)
1	37.9	41.2
3	37.7	41.1
5	37.4	40.8
7	37.2	40.5
9	36.8	40.1
11	36.2	39.5
13	35.5	38.8
15	34.9	37.8
17	34.3	36.9
19	33.4	35.6
21	32.5	34.2
23	31.6	33.2

Table 4.1 shows that the barycentral frequency is about 3 Hz higher than the peak frequency for small thicknesses and is only about 2 Hz higher for larger thicknesses. The reason for smaller differences at larger thicknesses is because the peak frequency shifts to lower values for larger thicknesses. In the limit of shifting the peak frequency to zero, it should be equal to the barycentral frequency. Hence, the lower the peak frequency, the closer the values of the two frequencies should be. However, it must be emphasized that maximum instantaneous frequency values are fundamentally functions of interference patterns and may occur at times other than the corresponding amplitude envelope peak time. The barycentral frequencies are also maximum instantaneous frequencies only for Type I reflectivity.

For Type II reflectivity, the instantaneous frequency pattern (Figure 4.7b) is also symmetrical. However, the barycentral frequencies are maxima and correspond to the weighted averages of the Fourier amplitude spectra only for a thickness up to about $0.15 \lambda_d$ (trace 13). The barycentral frequency is 35.0 Hz for trace 1 and decreases slowly to 29.4 Hz for trace 13. The corresponding Fourier peak frequencies are 31.0 Hz and 27.1

Hz. Beyond this thickness, doublets start to occur with troughs forming along the line of symmetry. Because of these troughs, the barycentral frequencies along this line are no longer maxima and do not correspond to the weighted average frequencies in the corresponding amplitude spectra. When the thickness is $0.25\lambda_d$ (trace 22) or greater, the instantaneous frequencies along the troughs become negative, with magnitudes which may be very large. For example, at a thickness of 24 m and 25 m, the instantaneous frequencies at the trough are -51.6 Hz and -183 Hz respectively. These frequencies are negative because the troughs never cross the zero amplitude line (Figure 2.5b); i.e. these frequencies correspond to a inflection phase anomaly as explained in section 4.2.2. They are also large because the inflection phase anomaly occurs over only a very short time interval. Such behaviour suggests that the instantaneous frequency is an effective tool to delineate subtle changes in waveform interference patterns.

For Type III reflectivity, there is an anomaly in the instantaneous frequency plot (Figure 4.6c) at the onsets of the composite reflections between traces 1 and trace 6. The corresponding conventional seismic data (Figure 2.5c) does not show a corresponding anomaly. But an examination of the numerical values of the instantaneous frequency shows that there are negative frequencies associated with this anomaly. For example, for trace 4, the first three live samples have instantaneous frequencies of -0.9 Hz, -7.9 Hz, and -2.9 Hz, respectively. This implies that there are inflection phase anomalies in the leading portions of these wavelets that are unobservable in conventional display. Furthermore, the barycentral frequencies are also equal to the weighted average frequencies in the corresponding Fourier amplitude spectra and behave similarly to the peak frequencies as a function of thickness. For example, the barycentral frequency is 35.8 Hz for trace 1, increases slowly to a maximum 39.6 Hz for trace 7, and then decreases slowly to 33.7 Hz for trace 23. The corresponding peak frequencies are 31.7

Hz, 36.4 Hz (also a maximum), and 31.5 Hz. The differences between the two sets of frequencies also decrease as thickness increases.

For Type IV reflectivity, the instantaneous frequency (Figure 4.6d) also exhibits some large negative values between traces 23 to 25. For example, the instantaneous frequency is -216 Hz for trace 25 at the red colour in Figure 4.7d. This portion of the trace corresponds to the low-amplitude trough ahead of the large peak in Figure 2.5d. This is not an inflection phase anomaly, since the trace crosses the zero amplitude line. Furthermore, the numerical values of the barycentral frequencies indicate that they correspond to the weighted average frequencies of the Fourier amplitude spectra only in the thickness range of $0.01\lambda_d$ to about $0.16\lambda_d$ (trace 1 to trace 13). Beyond the thickness of $0.16\lambda_d$, the barycentral frequencies increase with increasing thickness. Together with the instantaneous frequency results for Type II reflectivity, this frequency behaviour implies that the barycentral frequency will correspond to the weighted average of the Fourier amplitude spectrum only if the portion of the trace that is enclosed by the envelope appears to be a single wavelet. If that portion is a doublet or includes part of another wavelet such as its tail or onset, then the barycentral frequency will deviate from the weighted average frequency of the corresponding Fourier amplitude spectrum.

4.4 Normal incidence, two-layers model

In this section, the complex attributes of Types V, VI, and VII reflectivities are examined. In section 2.4, the thickness of the underlying layer was varied, with values of 2 m, 4 m, 6 m, 8 m, and 10 m. To limit the number of complex attributes displays to a reasonable size, only the attributes for the 4 m and 8 m cases for each of the three reflectivities are examined. The input traces for these attributes are the same as the corresponding traces for amplitude study in section 2.4.

4.4.1 Instantaneous amplitude

Two instantaneous amplitude plots for Type V reflectivity are shown in Figures 4.7a and 4.7d. Compared with Figure 4.4a, which is the instantaneous amplitude plot for Type I reflectivity, all three amplitude plots appear identical for traces beyond trace 4. The only differences lie in the first three traces where the amplitudes are slightly different among the three plots. The results imply that instantaneous amplitude may not be very indicative of the presence of multiple thin layers, i.e. it is not an effective tool to indicate the difference between Type I and Type V reflectivities.

The instantaneous amplitude plots for Type VI reflectivity are shown in Figures 4.7b and 4.7e. As shown in section 2.4.3, these are the only models where the amplitude of the reflected composite wavelet exhibits a minimum when plotted as a function of thickness. The instantaneous amplitude plots also show the corresponding minimum. However, this minimum is only vaguely observable for the 4 m case, but is clearly evident between trace 1 and trace 8 for the 8 m case, i.e. between a wedge thickness of 1 m and 8 m. Beyond a wedge thickness of 8 m, the two plots are similar to each other and to the instantaneous amplitude plot for Type I reflectivity (Figure 4.5a). The results suggest that if there is a stratigraphic sequence represented by Type VI reflectivity, the instantaneous amplitudes of the reflected composite wavelets may indicate the alternating nature of the polarities of the reflection coefficients.

For Type VII reflectivity, the instantaneous amplitudes for the two cases (Figures 4.7c and 4.7f) are identical. This implies that the amplitude envelopes of the composite wavelets for this reflectivity are not sensitive to the thickness of the underlying layer. However, compared to Figure 4.4d, which is the instantaneous amplitude plot for Type IV reflectivity, the amplitude envelopes for Type VII reflectivity are significantly broader than those of Type IV reflectivity for wedge thicknesses below 13 m. The additional positive

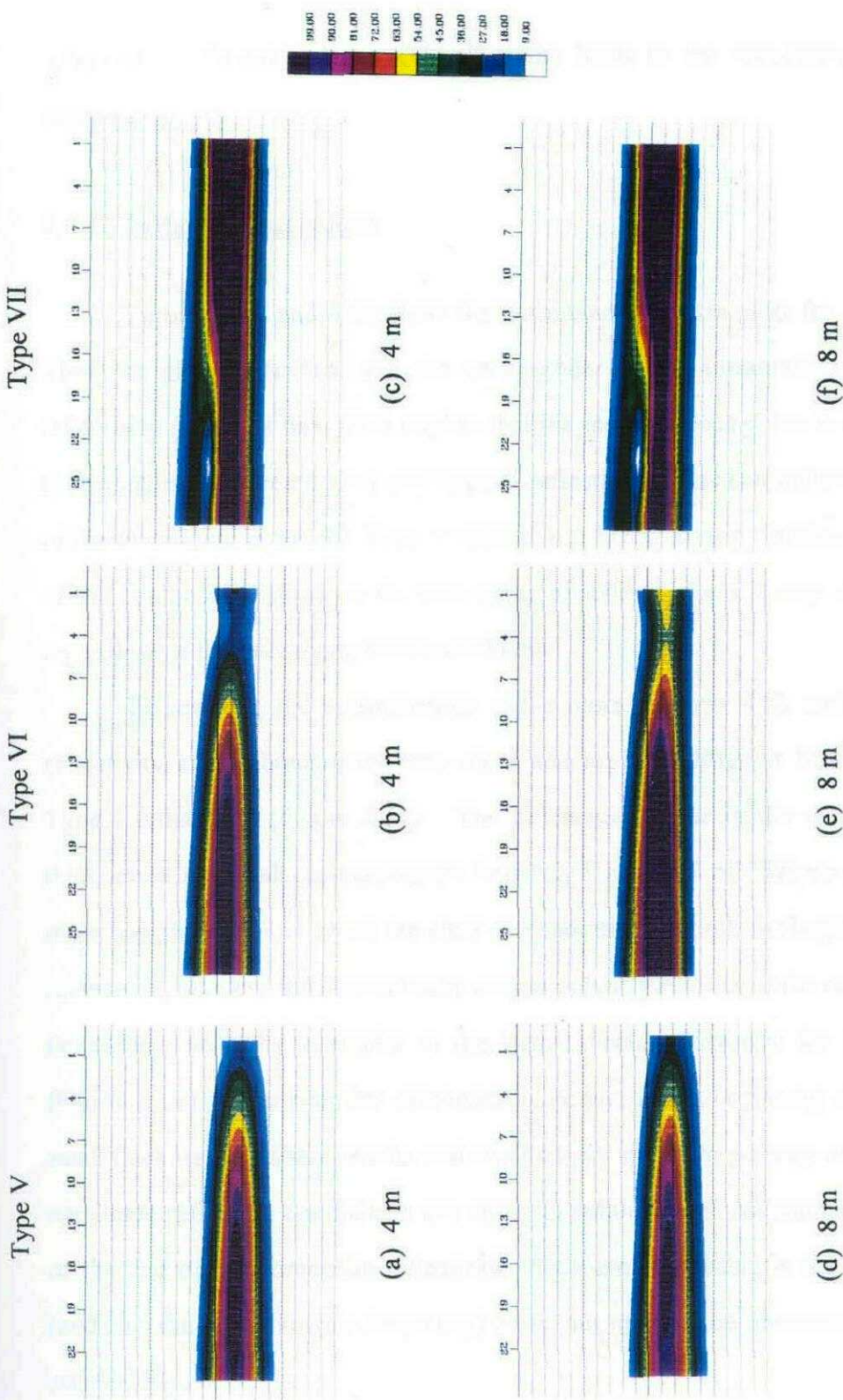


Figure 4.7 Instantaneous amplitudes for Types V, VI and VII with underlying layer thicknesses 4 m and 8 m. The source wavelet is a Ricker 31 Hz wavelet. Timing lines are at 10 ms intervals.

reflection coefficient in Type VII reflectivity leads to the broadening of the composite wavelets.

4.4.2 Instantaneous phase

Figures 4.8a and 4.8d show the instantaneous phase plots for Type V reflectivity. They are almost identical and are very similar to the instantaneous phase of Type I reflectivity (Figure 4.6a). This implies that the instantaneous phase is not an effective tool to distinguish between Type I and Type V reflectivities, nor is it indicative of the thickness of the underlying layers for Type V reflectivity. This, in turn, implies that the waveforms of the composite reflections for both types of reflectivities are very similar to each other regardless of the underlying layer's thickness.

In contrast, the instantaneous phase plots (Figures 4.8b and 4.8e) for Type VI reflectivity are different from each other and are also different from the phase plot for Type I reflectivity (Figure 4.5a). The differences occur in the zone where the wedge thicknesses are small, approximately between 1 m and 9 m. Where the thickness of the underlying layer is 4 m, there are clear discontinuities in both the beginning and end of the reflections, whereas the discontinuity occurs only in the onset of the reflections for the 8 m thickness case. This is similar to the instantaneous phase plot for Type III reflectivity (Figure 4.6c) where a similar discontinuity occurs in the beginning of the reflections for small thicknesses. These results indicate that, for opposite-polarity reflectivities, unequal-amplitude reflection coefficients can result in subtle waveform anomalies in the beginning or the end of the composite reflections which are observable in the instantaneous phase (and also the instantaneous frequency) plots, but may not be observable on a conventional seismic display.

For Type VII reflectivity, the instantaneous phase plots are shown in Figures 4.8c and 4.8f. If these two plots are compared to the instantaneous phase plot for Type IV reflectivity (Figure 4.5d), they are similar from trace 1 to approximately trace 18, i.e. from a wedge thickness of 1 m to 18 m. Beyond 18 m, there is a difference in the patterns among the three phase plots. Furthermore, the central patterns of the phase plots shift to the thinner part of the wedge as the underlying layer thickens. For example, the pattern starts at trace 23 for Type IV reflectivity, but starts at traces 21 and 19 for the 4 m and 8 m cases respectively for Type VII reflectivity. Thus, for Type VII reflectivity, the instantaneous phase is not indicative of the presence of an underlying thin layer if the thin layer under investigation is only a few metres thick, or equivalently, close to or less than $(1/8)\lambda_d$. But if the underlying thin layer is close to $(1/4)\lambda_d$ thick, then in conjunction with forward modelling, it may be possible to estimate its thickness from the instantaneous phase displays.

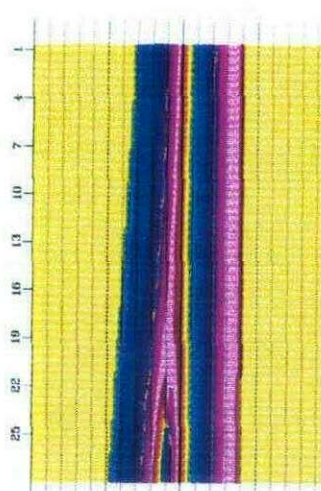
4.4.3. Instantaneous frequency

Instantaneous frequency plots for Type V reflectivity are shown in Figures 4.9a and 4.9d. The differences between the two plots are small for wedge thicknesses below 16 m (trace 16). They are also similar to the instantaneous frequency plot for Type I reflectivity (Figure 4.7a) for the same range of thicknesses. Above 16 m, however, there is a slight difference. The symmetrical pattern for Type I reflectivity is distorted by the presence of the underlying layer, and the distortion increases as the underlying layer thickens. In contrast, the instantaneous phase plots for these models (Figures 4.5a, 4.8a and 4.8d) are not sensitive to the presence of an underlying layer for the entire range of wedge thickness. Obviously, the high-frequency enhancement characteristics of differentiation contributes to the difference between the instantaneous phase and the

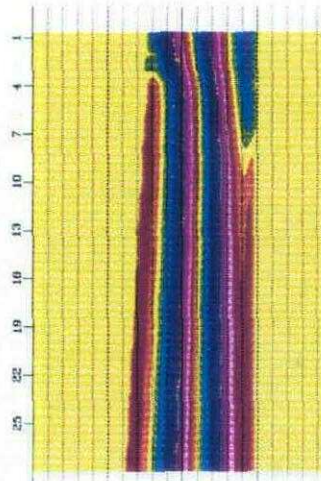
Type VII

Type VI

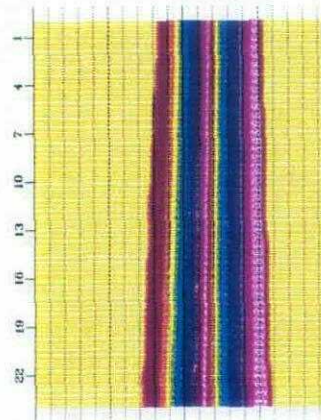
Type V



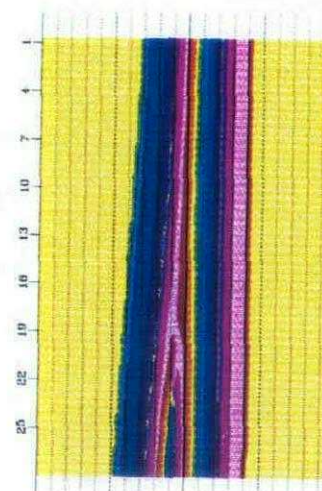
(c) 4 m



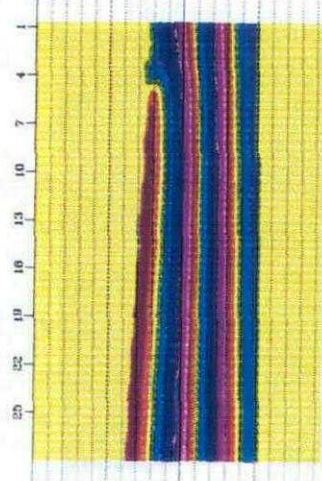
(b) 4 m



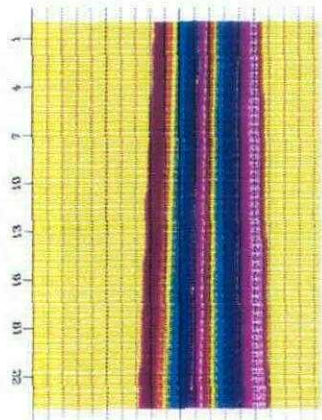
(a) 4 m



(f) 8 m



(e) 8 m



(d) 8 m

Figure 4.8 Instantaneous phases for Types V, VI and VII with underlying layer thicknesses 4 m and 8 m. The source wavelet is a Ricker 31 Hz wavelet. Timing lines are at 10 ms intervals.

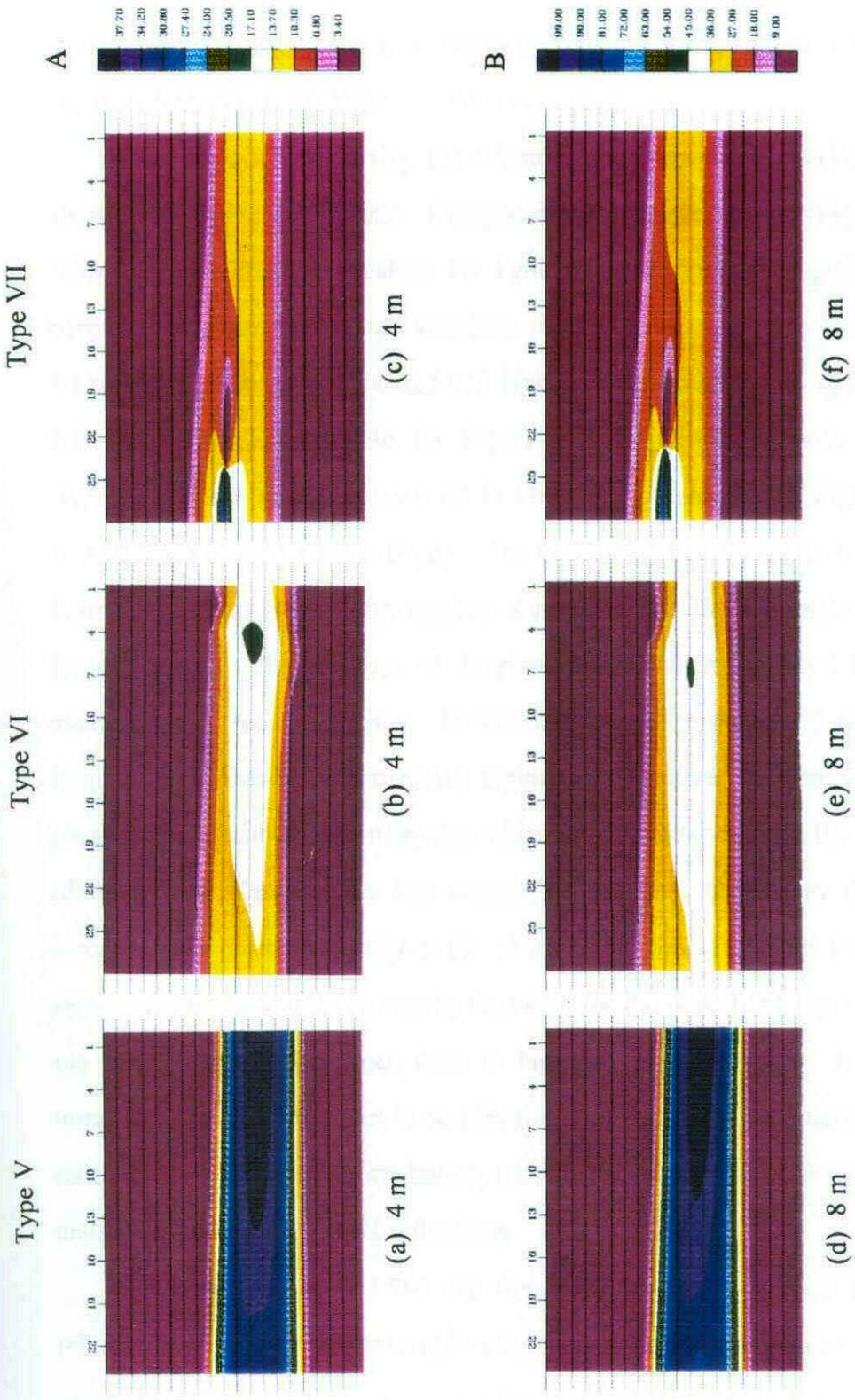


Figure 4.9 Instantaneous frequencies for Types V, VI and VII with underlying layer thicknesses 4 m and 8 m. The source wavelet is a Ricker 31 Hz wavelet. Timing lines are at 10 ms intervals. Colour legend A is for Type V reflectivity, colour legend B is for Types VI and VII reflectivity.

instantaneous frequency in this instance. Finally, there are no unexpectedly large or negative frequencies for Type V reflectivity.

For Type VI reflectivity, the instantaneous frequency plots (Figures 4.9b and 4.9e) show some distinctive features. Compared to the frequency plot (Figure 4.6a) for Type I reflectivity, the frequency values for Type VI reflectivity are significantly higher at the corresponding time and spatial locations. Furthermore, frequency tuning effects for Type VI reflectivity are more localized and higher in numerical values (green areas in Figures 4.9b and 4.9e). For example, for Type I reflectivity, the frequency values in the tuning region are in the neighbourhood of 38 Hz (deep purple area in Figure 4.6a), compared with 50 Hz for Type VI reflectivity. This behaviour also agrees with the behaviour of the Fourier spectrum, which also exhibits a maximum at the corresponding trace locations (section 3.4.2). The locations of the phase anomalies in Figures 4.8b and 4.8e are also evident in the frequency plots. An examination of the numerical values shows that the frequencies in these two anomalous regions are negative. Evidently, there are inflection phase anomalies in these two regions which are not observable on the conventional display of the seismic data due to low relative amplitudes. Similar to the behaviour of the instantaneous phase, the magnitudes of the anomalies at the tail ends of the composite reflections decrease with increasing thickness for the underlying layer. This is also true of the tuning region (the green dots in Figures 4.9b and 4.9e). It is evident that the instantaneous frequency plot is an effective tool to differentiate between Types I and VI reflectivities. With proper modelling, it may also be used to estimate the thickness of the underlying layer for Type VI reflectivity.

Figures 4.9c and 4.9f are the instantaneous frequency plots for Type VII reflectivity. They are similar to each other, and the shifting of patterns as discussed for the corresponding phase plots is also evident in these two plots. Compared to Figure 4.6d, which is the instantaneous frequency plot for Type IV reflectivity, the biggest difference

occurs near the $(1/4)\lambda_d$ thickness. In this location, Type IV reflectivity exhibits a low frequency trend which turns negative as the wedge thickness increases to 23 m (red area in Figure 4.6d). This negative frequency trend is also flanked by two higher frequency trends (blue and purple area). For Type VII reflectivity, for both 4 m and 8 m thickness cases, there is a negative frequency trend starting at approximately trace 18, which changes abruptly into a high frequency trend at approximately traces 25 and 24 respectively. The negative frequencies range from a fraction of a hertz to below -100 Hz, while the high frequency trend is of the order of 100 Hz. Thus, instantaneous frequency is useful to differentiate a Type IV reflectivity situation from a Type VII reflectivity case, provided that the thickness of the overlying layer is close to the $(1/4)\lambda_d$ value. However, it may not be very indicative of the thickness of the underlying layer, given the similarity between Figures 4.9c and 4.9f.

4.5 Discussion

In thin-bed interpretation of reflection seismic data, the term 'stratigraphic interpretation' is synonymous with waveform analysis. The objective is to derive from the reflected wavelet as much relevant information as possible about geological formations with thicknesses that are below seismic resolution. For this purpose, the instantaneous amplitude is the least useful, since it is the envelope of the wavelet and masks all subtle waveform changes. Nevertheless, it offers the advantage of being phase-independent, and is a useful tool for studying the total energy contained in a wavelet or in a wave packet. The instantaneous phase and the instantaneous frequency are more informative of waveform changes, as shown in the one-layer and two-layer models. However, the use of all three attributes for seismic interpretation is still in early development. Up to the present, they have been used largely in a pattern-recognition manner, and more research is

needed to understand various aspects of their applications. In particular, the potential use of these attributes in a quantitative manner and their direct association to geological parameters needs to be investigated.

For the one-layer models, instantaneous phase is rather sensitive to the amplitudes of the two reflection coefficients. For, example, the phase anomaly for Type III reflectivity (Figure 4.5c) compared to the phase plot for Type I reflectivity (Figure 4.5a) clearly shows the effect of the unequal-amplitude reflection coefficients for Type III reflectivity. Type IV reflectivity also reveals a phase anomaly (Figure 4.6d) which is absent in the phase plot for Type II reflectivity (Figure 4.6b). Evidently, any asymmetry in the seismic event can be detected by its instantaneous phase.

The instantaneous frequency plots for one-layer models also reveal corresponding differences between Types I and III reflectivities, and between Types II and IV reflectivities (Figure 4.7). This is to be expected, since instantaneous frequency is the first derivative of the instantaneous phase. However, the existence of abnormally large and/or negative instantaneous frequencies implies that it is potentially the best attribute for thin-bed interpretation, since these abnormal frequencies are fundamental products of wavelet interference.

For the two-layer models, Type VI reflectivity is the only reflectivity for which instantaneous amplitude may be useful to reveal the nature of the alternating polarities of its reflection coefficients. The amplitude minimum shown in Figure 2.13 can also be observed in Figure 4.7. However, this attribute does not appear to be sensitive to the existence of an underlying thin layer for both Types V and VII reflectivities.

Instantaneous phase and instantaneous frequency also appear to be particularly useful for Type VI reflectivity. As also demonstrated by the instantaneous phase and frequency plots for Type III reflectivity, opposite-polarity reflection coefficients having unequal amplitude often results in subtle interference patterns which may be difficult to

detect on conventional seismic display due to low relative amplitudes but may reveal themselves as inflection phase anomaly and abnormal frequencies in the two attribute plots.

Finally, the presented complex attributes results are valid for the models used in this dissertation. Since complex attributes are very sensitive to small waveform changes, very different characters may be observed if the magnitudes of the reflection coefficients of any two-term and/or three-term reflectivity sequences are significantly different from the ones used in the models studied.

Chapter 5 - Offset-dependent seismic properties

5.1 Offset-dependent properties of thin beds

In this chapter, offset-dependent tuning effects and anomalous AVO effects due to a lateral change of Poisson's ratio, σ , within a thin layer are examined. The importance of this work is that many gas reservoirs have a lower Poisson's ratio than the neighbouring strata, and thus exhibit anomalous offset-dependent amplitude behaviour. However, if the reservoirs are thin, offset-dependent tuning also has a strong impact on the offset-dependent amplitude behaviour of the reflections. Hence, from the interpretation point of view, it is important to understand the characteristics of both the effect of offset-dependent tuning and the anomalous AVO response due to a lateral change of Poisson's ratio.

Several authors have cited the importance of offset-dependent tuning of thin beds for AVO analysis. For example, Swan (1991) discussed the measurement of AVO in a finely-layered medium and demonstrated again the errors due to offset-dependent tuning. Using a synthetic wedge model, Allen and Peddy (1993) showed the apparent AVO effects due to offset-dependent tuning for a thin layer, and Juhlin and Young (1993) showed that, for a high-velocity layer embedded in a homogeneous rock, thin-bed tuning affects its AVO response more than does the response of a low-velocity layer, given comparable simple interface responses. However, although it has been recognized that offset-dependent tuning effects of thin beds could negate or overwhelm AVO effects due to a lateral change of σ , a quantitative study is absent in published literature.

To simplify the discussion, in the remainder of this chapter, the term *single-interface effect* is defined as the anomalous AVO effect due solely to a lateral change of σ , and the term *tuning effect* is defined as the offset-dependent tuning effect. In section 5.2,

using four two-term reflectivity series whose parameters are outlined in Table 5.1, a quantitative relationship between tuning and single-interface effects for a thin bed example is studied. Similar studies for peak frequency and complex attributes are presented in sections 5.3 and 5.4, respectively.

5.2 Amplitude versus offset for a thin layer

Consider a thin layer embedded in a thick homogeneous medium (Figure 5.1). Assume the Poisson's ratios in zones A and B are 0.3 and 0.1, respectively, and that the lateral change in Poisson's ratio is due to different P -wave velocities in the two zones. The corresponding S -wave velocities are assumed to be the same. The amplitudes of the traces for all CDP (common-depth-point) gathers whose reflection points are within zone A, such as the reflection point P (Figure 5.1), are equal for the same angles of incidence. But if the traces of one of these CDP gathers are compared to the traces of a CDP gather whose reflection point lies within zone B such as the reflection point Q (Figure 5.1), the amplitudes will be different for traces with the same angles of incidence. However, the differences in these two CDP gathers cannot be attributed solely to the lateral change in Poisson's ratio, since the different P -wave velocities in Zones A and B will result in different P -wave traveltimes, and hence different *tuning effects* in the two zones. Consequently, any calculations of the values of Poisson's ratio in each zone and on its magnitude of change between the two zones will be incorrect unless the two differential *tuning effects* are taken into account.

The objective in this section is to show, in the presence of a lateral change in Poisson's ratio within a thin layer, the amounts that *tuning* and *single-interface effects* contribute to the reflection amplitudes at normal incidence as well as a function of source-receiver offset. The approach is to use numerical modelling to illustrate the change in

amplitude as a function of offset for a reflection from a thin layer as σ for the layer changes from a value representative of a nonporous sand (0.3) to a value representative of a gas-saturated porous sand (0.1). These amplitude changes are then compared to the corresponding amplitude changes of the same layer but with the thickness increased such that there is no interference between the upper interface and the lower interface.

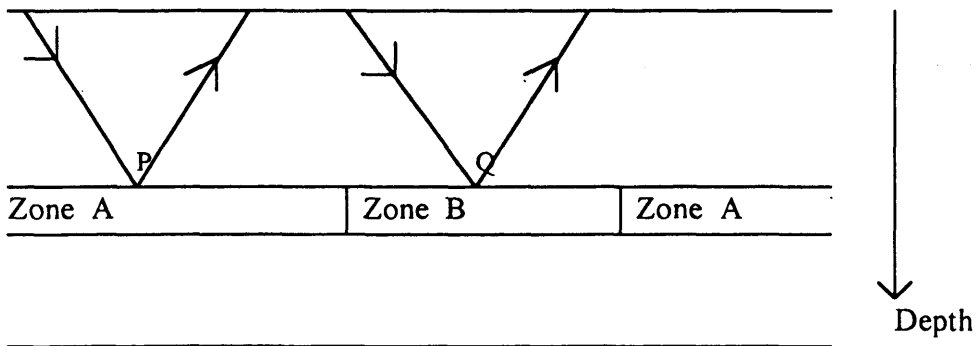


Figure 5.1 Thin-layer model with a lateral change in Poisson's ratio. Zones A and B have different P -wave velocities and densities. S -wave velocities in the two zones are equal.

Alternatively, the amplitude changes of the reflections from a thin bed embedded in a homogeneous medium as σ changes from 0.3 to 0.1 are compared to the corresponding amplitude changes of the reflections from its upper interface alone. The former amplitude changes include the contributions of the reflections from both the upper and lower interfaces (hence include *tuning*), and are dependent on three factors: the offset-dependent reflection coefficients of the upper interface, the offset-dependent reflection coefficients of the lower interface, and the offset-dependent travelt ime delay between the upper and the lower interfaces. For the latter approach, the amplitude changes are caused solely by the *single-interface effect* of the upper interface.

Both P -wave reflections and converted S -wave reflections are studied. Since the S -wave has a lower propagation velocity than the corresponding P -wave, it is less affected

by *tuning* than is *P*-wave for the same layer thickness, assuming the same source wavelet is considered for both waves. For this dissertation, results from only a single thin layer are presented. The geometry of the model for the four reflectivities is shown in Figure 5.2. The incidence angle, i , spans a range of 0° to about 50° . The top and the bottom layers are referred to as layer 1 and layer 3 respectively, and the thin layer is referred to as layer 2. Four models were studied, for thicknesses of layer 2 of 1 m, 5 m, 9 m, and 13 m. Table 5.1 shows the reflectivity types used for the study. The velocities were chosen to be typical of Lower Cretaceous formations in southern Alberta, and the densities were calculated from the velocities using the equation of Gardner *et al.* (1974). There are two sets of values for layer 2, corresponding to values of σ of 0.3 and 0.1. Note that the *S*-wave velocities do not change for the two values of σ , and only the *P*-wave velocities and the densities change.

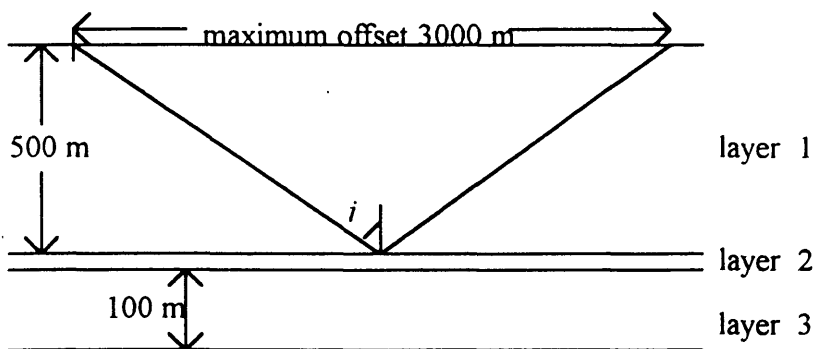


Figure 5.2 A single thin layer model for AVO study. Geophone group spacing is 50 m with the near-offset at 50 m.

All shot gathers were generated using raytracing, and all the reflection coefficients were obtained by solving the exact Zoeppritz' (1919) equations using the method of Aki and Richards (1980). A 31-Hz Ricker wavelet was used as a source wavelet, and the Poisson's ratio for layers 1 and 3 was kept constant at 0.3 for all models. Spherical

divergence was not compensated, but transmission losses were included to allow accurate calculations of the reflection coefficients. Free surface effects, as discussed by Eaton (1989), were also included. For P -wave reflections, the vertical component of the total wavefield was computed, and for converted S -wave reflections, the radial component was computed.

Table 5.1 Layer lithologies, velocities, densities, and reflection coefficients for four models for AVO study. Layer 1, layer 2, and layer 3 correspond to the layers in Figure 5.1.

Reflectivity Types	layer 1		layer 2				layer 3	
	V_1 (m/s)	S_1 (m/s)	V_2 (m/s)	S_2 (m/s)	V_3 (m/s)	S_3 (m/s)	V_4 (m/s)	S_4 (m/s)
	ρ_1 (kg/m ³)		ρ_2 (kg/m ³)		ρ_3 (kg/m ³)		ρ_4 (kg/m ³)	
	$\sigma = 0.3$		$\sigma = 0.1$		$\sigma = 0.3$		$\sigma = 0.3$	
I		nonporous sand 4270 2280 2505	porous sand 2444 1629 2180	porous sand 3050 1629 2303	porous sand 4270 2280 2505	porous sand 3050 1629 2303	nonporous sand 4270 2280 2505	nonporous sand 4270 2280 2505
IA		porous sand 3050 1629 2303	nonporous sand 3421 1629 2371	nonporous sand 4270 1629 2505	nonporous sand 4270 1629 2505	porous sand 3050 1629 2303	porous sand 3050 1629 2303	porous sand 3050 1629 2303
II		porous and 3050 1629 2303	silt 2854 1903 2270	silt 3560 1903 2434	nonporous sand 4270 2280 2505	nonporous sand 4270 2280 2505	nonporous sand 4270 2280 2505	nonporous sand 4270 2280 2505
IIA		nonporous sand 4270 2280 2505	silt 2854 1903 2270	silt 3560 1903 2434	porous sand 3050 1629 2303	porous sand 3050 1629 2303	porous sand 3050 1629 2303	porous sand 3050 1629 2303

For each reflectivity, the following shot gathers were obtained:

- P -wave and S -wave shot gathers reflected from the top interface of layer 2 with $\sigma = 0.3$ (single-interface reflections).
- P -wave and S -wave shot gathers reflected from the top interface of layer 2 with $\sigma = 0.1$ (single-interface reflections).
- P -wave and S -wave shot gathers reflected from the top and base of layer 2 with $\sigma = 0.3$ for each of the four layer 2 thicknesses (1 m, 5 m, 9 m, and 13 m).

- P -wave and S -wave shot gathers reflected from the top and base of layer 2 with $\sigma = 0.1$ for each of the four layer 2 thicknesses (1 m, 5 m, 9 m, and 13 m).

For each reflectivity, a total of twenty shot gathers were then obtained. As σ in layer 2 was lowered from 0.3 to 0.1, the S -wave velocity was kept constant and the P -wave velocity was lowered according to equation (1.3). The density was then lowered correspondingly, according to the equation of Gardner *et al.* (1974). In all shot gather displays, static shifts have been applied to the traces so that, effectively, all reflections on the upper interface of layer 2 occur at the same time. This is done mainly to avoid a discontinuous appearance in the corresponding complex attributes colour displays in section 5.4.

For those reflectivities where there is no critical angle at either the upper or lower interfaces, traces were recorded up to a maximum incidence angle of approximately 50° . Where a critical angle exists at either interface, traces were recorded only up to within 2 to 4 degrees of the critical angle. For each trace, the maximum absolute amplitude was recorded, and the change in the maximum absolute amplitude for each pair of traces, as σ changes from 0.3 and 0.1, was calculated according to:

$$\text{change} = \frac{A_{\max 1} - A_{\max 3}}{A_{\max 3}} \times 100\% \quad (5.1)$$

where $A_{\max 1}$ and $A_{\max 3}$ are the maximum absolute amplitudes with $\sigma = 0.1$ and 0.3, respectively. For the shot gathers involving only reflections from single interfaces, i.e. from the top of layer 2, such changes represent *single-interface effects*. For all the other shot gathers involving both the upper and lower interfaces of layer 2, the changes have the combined effects of changes in σ and *tuning*.

In all subsequent discussion, the term incidence angle always refers to the incidence angle at the upper interface of layer 2, unless otherwise specified. Backus (1992) showed that, for a thin layer, AVO modelling of P -waves will not be accurate unless the locally-converted shear wave is included. He stated that contributions from $PSPP$ and $PPSP$ reflections (locally converted shear waves) are often of first-order in importance on P -wave seismograms. Since the delay in times for $PSPP$ and $PPSP$ reflections is not significant compared to the $PPPP$ reflection (primary reflection) time if the layer is thin, both $PSPP$ and $PPSP$ contributions have been included in all P -wave shot gathers. Following the same argument, the contributions of PS , $PPSS$ (primary reflections), $PPPS$, $PSPS$, and $PSSS$ (locally converted reflections) reflections have all been included in all converted S -wave shot gathers. Figure 5.3 shows an example of how the locally converted shear waves affect the amplitude analysis for Type I reflectivity.

In Figure 5.3, the numerical modelling results for Type I reflectivity obtained from equation (5.1) are shown for the 5 m thickness for layer 2 (dotted curves). They are the same curves for the 5 m case in Figures 5.5a and 5.5b; hence they include the contributions of locally converted shear waves. The solid curves are the corresponding curves without the contributions of locally converted shear waves. For converted S -wave reflections, the contribution of locally converted waves is negligible. For P -wave reflections, however, the change in amplitude is much larger if locally converted shear waves are included for incident angles larger than 27° . Beyond the incident angle of 47° , the change in amplitude is twice as large if locally converted shear waves are included.

5.2.1 Type I reflectivity

The shot gathers when layer 2 is 5 m thick are shown in Figure 5.4, with maximum amplitudes being the peaks of the composite wavelets. There is an observable but small

increase in P -wave reflection amplitudes for the far-offset traces as σ changes from 0.3 to 0.1 (Figures 5.4a and 5.4c). For the S -wave reflections, there are no observable differences between the two seismograms for the two values of σ (Figures 5.4b and 5.4d). The amplitude results for the P -wave and the converted S -wave of Type I reflectivity are plotted in Figure 5.5, with maximum amplitudes being the peaks of the composite wavelets. There are three significant observations from Figure 5.5.

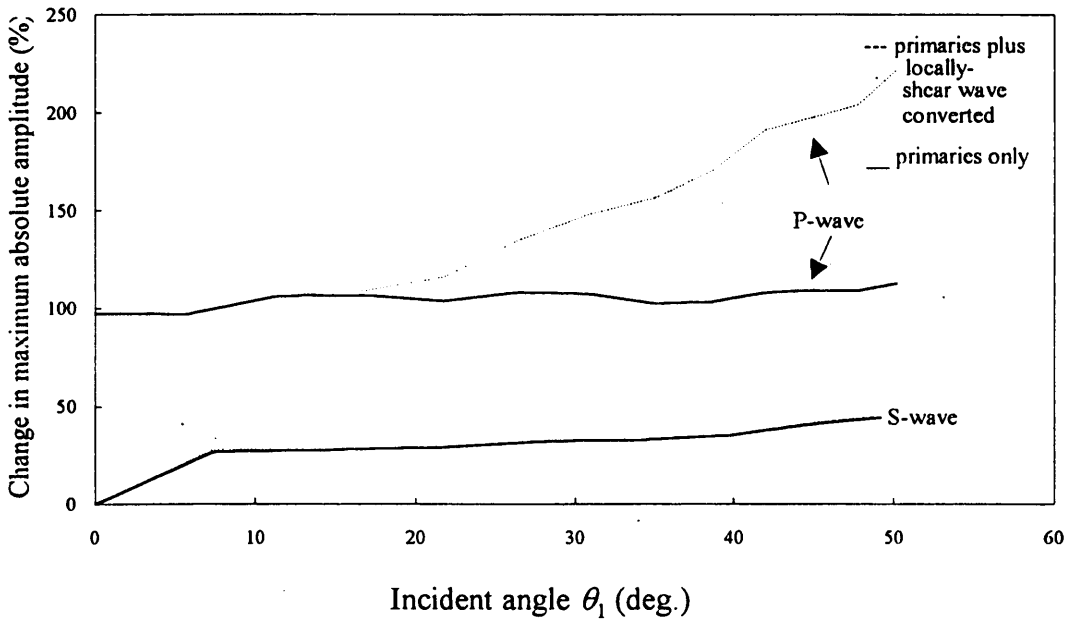


Figure 5.3 Comparison between the primary reflections only (PP and $PPPP$ for P -waves; PS and $PPSS$ for S -waves) and primary reflections plus locally converted waves ($PSPP$ and $PPSP$ for P -waves; $PPPS$, $PSPS$, and $PSSS$ for S -waves) for Type I reflectivity (τ^\perp) for both P -waves and S -waves.

Firstly, for both PP and PS reflections, as σ decreases from 0.3 to 0.1, the amplitude changes are positive for all offsets for both the single interface and layer 2; i.e. the maximum amplitudes increase as σ in layer 2 decreases from 0.3 to 0.1. This change

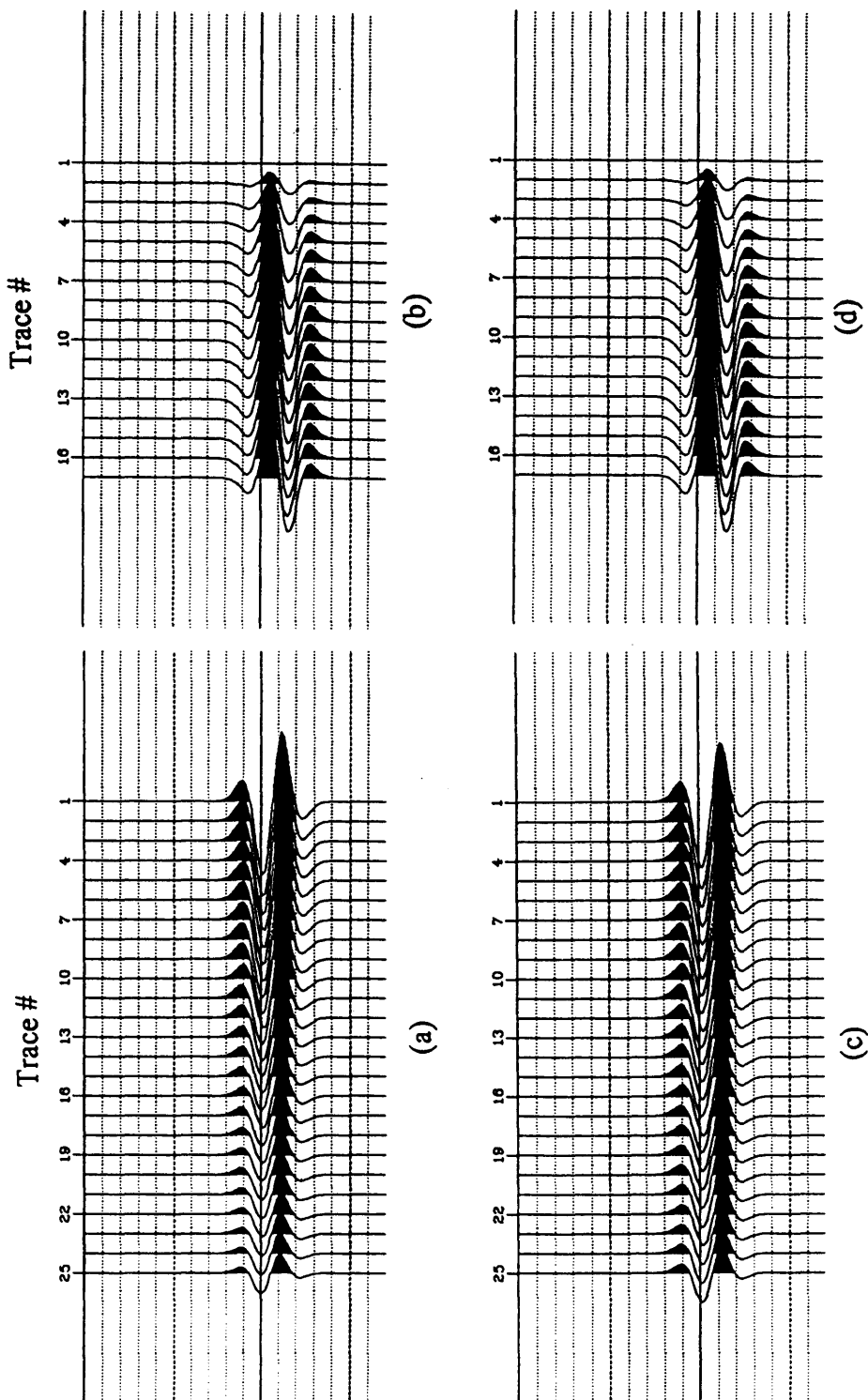


Figure 5.4 Shot gathers for Type I reflectivity at 5-m thickness: (a) P -wave, $\sigma = 0.3$; (b) S -wave, $\sigma = 0.3$; (c) P -wave, $\sigma = 0.1$; (d) S -wave, $\sigma = 0.1$. Timing lines are at 10-ms intervals.

in amplitude also increases as a function of offset for both the single interface and the thin layer, except for the thinnest case (1 m).

Secondly, since the P -wave velocity is lowered and the S -wave velocity is kept constant as σ changes from 0.3 to 0.1, the amplitudes from the shot gathers with $\sigma = 0.1$ will be less affected by *tuning* for both the P -wave and converted S -wave reflections compared to the corresponding amplitudes with $\sigma = 0.3$. However, this effect is greater for P -wave reflections, since the two-way traveltime involves the lower P -wave velocity in both the downgoing and upgoing directions, whereas the converted S -wave reflections only involve the lower P -wave velocity in the downgoing direction. This explains why the differences between the results for the single interface and the P -wave are consistently larger than those between the single interface and the converted S -wave for all the corresponding layer 2 thicknesses, as illustrated in Figure 5.5.

Thirdly, for P -wave reflections, *tuning effect* significantly contributes to the observed AVO effect. For example, at a thickness of 5 m for layer 2, the amplitude change is 50% higher for near offsets and about 100% higher for far offsets compared to the corresponding results for the single interface. However, when layer 2 is only 1 m thick, the change in amplitude decreases rapidly for incidence angles larger than 15° ; at about 27° for the incidence angle, the change in amplitude becomes less than the corresponding value for the single interface. The *tuning effect* becomes negligible only when layer 2 is greater than about 13 m thick.

Therefore, in exploring for a target which can be represented by Type I reflectivity, an anomalous lateral increase in P -wave reflection amplitudes as a function of offset can still be a potential indication of a lateral change of σ and a corresponding lower P -wave velocity. However, if the layer is thin, using directly the observed amplitude changes as a function of offset to deduce the value of σ , using a procedure such as the method suggested by Yu (1985), can be erroneous unless the *tuning effect* is compensated for.

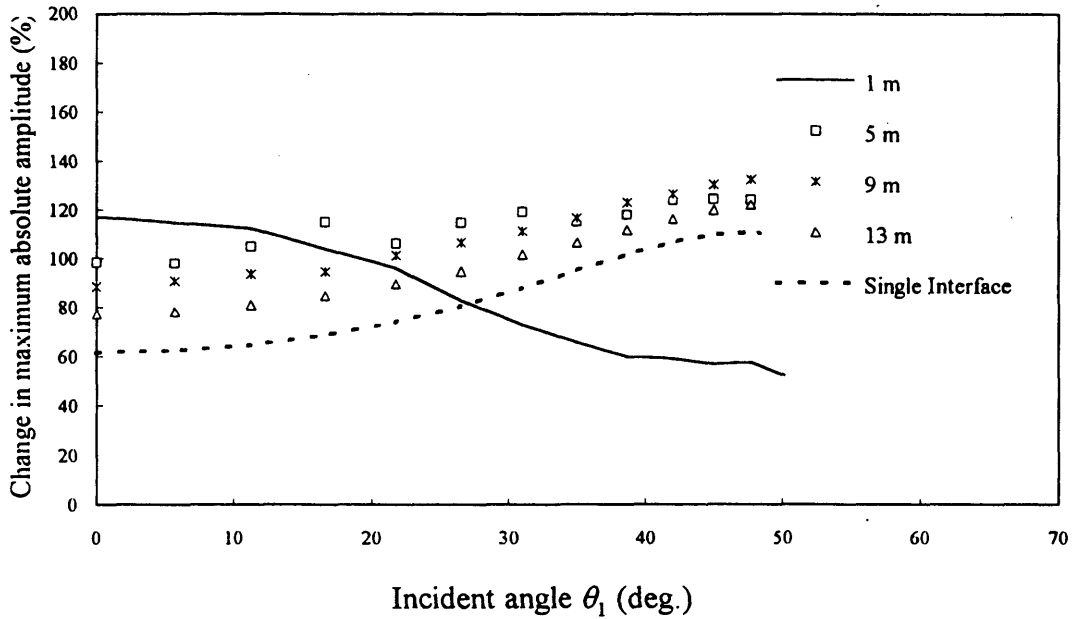


Figure 5.5a Change in maximum absolute amplitude of *P*-wave event for Type I reflectivity for a change from $\sigma = 0.3$ to $\sigma = 0.1$ in layer 2.

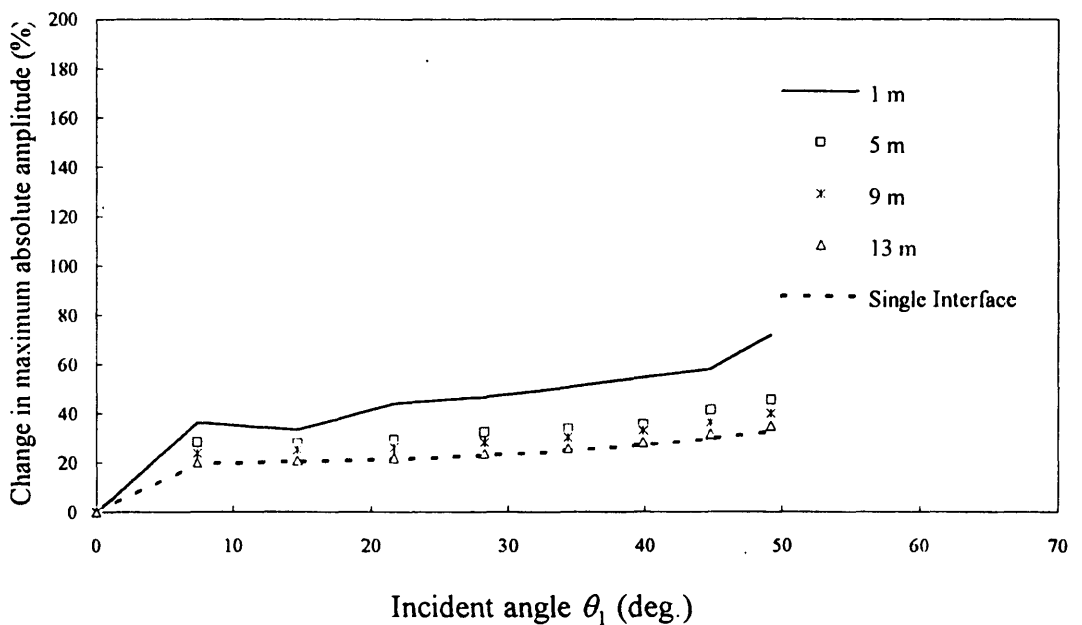


Figure 5.5b Change in maximum absolute amplitude of *S*-wave event for Type I reflectivity for a change from $\sigma = 0.3$ to $\sigma = 0.1$ in layer 2.

For converted S -wave reflections, the results are similar, but the magnitudes of the changes are considerably smaller than the corresponding changes for P -wave reflections (Figure 5.5b). The differences between the changes for the single interface and the corresponding changes for the thin bed for various layer 2 thicknesses are also much smaller. This is to be expected, since S -wave reflections suffer less from *tuning* than do the corresponding P -wave reflections. For example, at a thickness of 5 m for layer 2, the amplitude changes are only slightly higher than the corresponding changes for the single interface.

Comparing the results of the P -wave and converted S -wave reflections of Type I reflectivity, it is evident that the use of S -waves for AVO analysis of thin-bed reflections would be more indicative of lateral changes in lithology than P -waves. To use P -wave reflections to deduce the value of σ when thin beds are involved, the effect of *tuning* must be accounted for before valid conclusions can be drawn.

5.2.2 Type IA reflectivity

Type IA reflectivity is simply the reverse polarity of Type I reflectivity, that is, if Type I is represented as $\overline{\text{T}}^{\perp}$, then Type IA can be represented as $\perp\overline{\text{T}}$, with the magnitudes of all the reflection coefficients being equal for each type. For normal incidence, the reflected composite wavelets for Types I and IA reflectivities have identical amplitude characteristics (if transmission loss is ignored) but opposite polarities. However, for offset-dependent modelling, there are more differences, the most significant being that, for Type I reflectivity, there is no critical angle at the top of layer 2, and the critical angle at the lower interface will never be reached. However, for Type IA reflectivity the critical angle at the top of layer 2 is 46° (for $\sigma = 0.3$) and 63° (for $\sigma = 0.1$) for this particular velocity model.

The shot gathers for the 5 m case are shown in Figure 5.6, and the amplitude results are plotted in Figure 5.7. In Figure 5.6c, the P -wave seismogram with $\sigma = 0.1$ shows a polarity reversal at trace 12. This is caused by a polarity reversal in PP and $PPPP$ reflections at incidence angles of 26° and 21° , respectively. An examination of the reflection coefficients for the PP , $PPPP$, $PPSP$, and $PSPP$ reflections indicates that the phase reversals are a consequence of the fact that the sum of these reflections appears to be constrained to have a value close to zero so that a significant increase in the value of one of these reflection coefficients causes another reflection coefficient to change sign. In Figure 5.7, negative values represent a drop in maximum absolute amplitude as σ decreases from 0.3 to 0.1, and vice versa. For P -wave reflections from a single interface, the maximum absolute amplitudes decrease substantially as σ changes from 0.3 to 0.1, with a minimum change exhibited at about an incidence angle of 26° . For converted S -wave reflections, the maximum absolute amplitudes increase only slightly for incidence angles less than approximately 30° and increase rapidly for angles approaching the critical angle.

For P -wave reflections from the thin layer, Figure 5.7a shows that the amplitude behaviour is similar to that of the single interface for all thicknesses of layer 2 other than the 1 m case. For the thickness of 1 m, the amplitude change also follows closely that of the single interface except in the incidence angle range of approximately 20° to 30° , over which the changes in amplitude are considerably smaller compared with those from the single interface. Thus, for P -wave reflections from a Type IA reflectivity series, *tuning effect* is small unless the layer is extremely thin relative to the wavelength of the wavelet. In this example, 1 m with a 31 Hz source wavelet is equivalent to $0.01\lambda_s$.

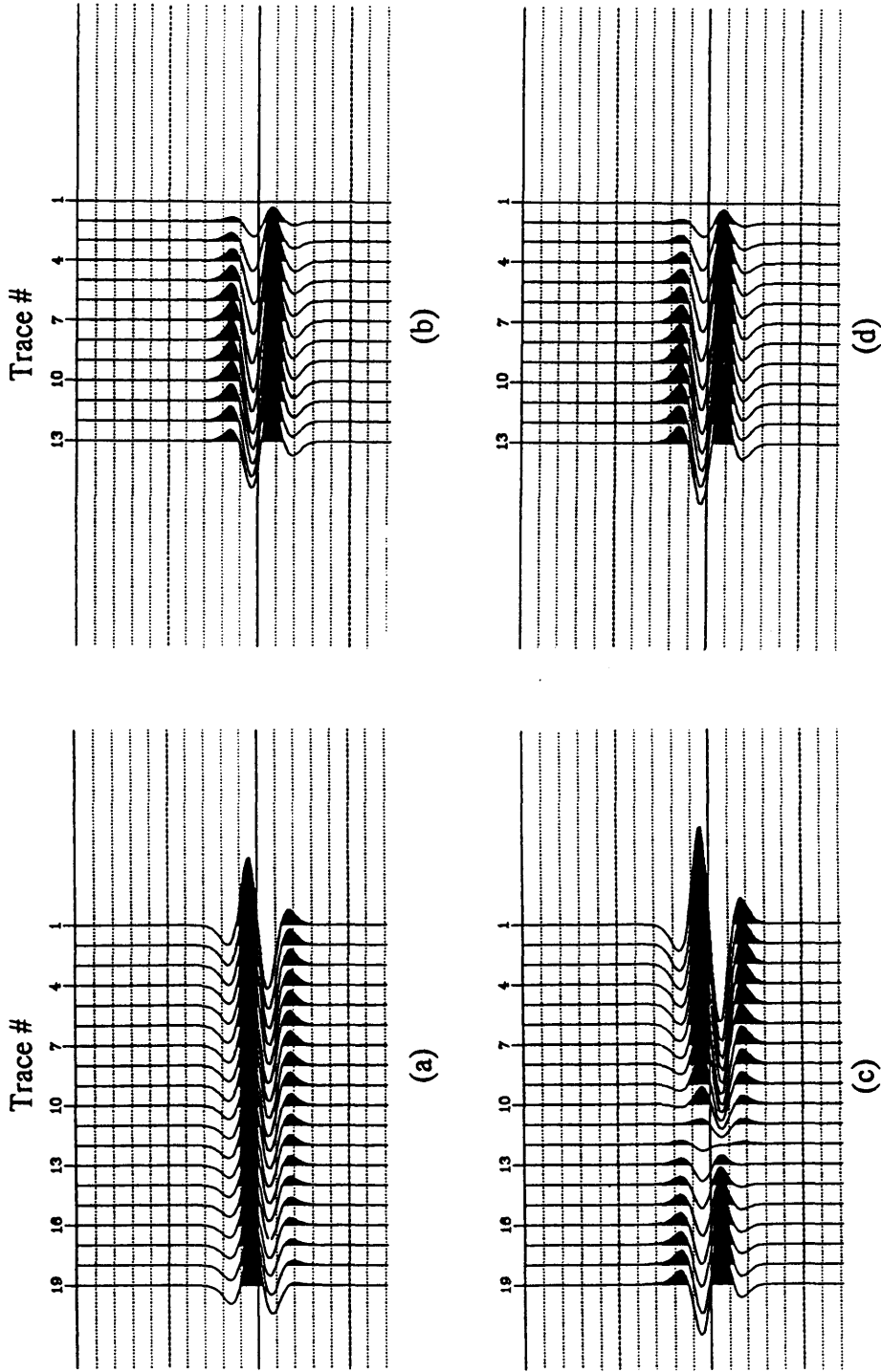


Figure 5.6 Shot gathers for Type IA reflectivity at 5-m thickness: (a) P-wave, $\sigma = 0.3$; (b) S-wave, $\sigma = 0.1$; (c) P-wave, $\sigma = 0.1$; (d) S-wave, $\sigma = 0.1$. Timing lines are at 10-m intervals.

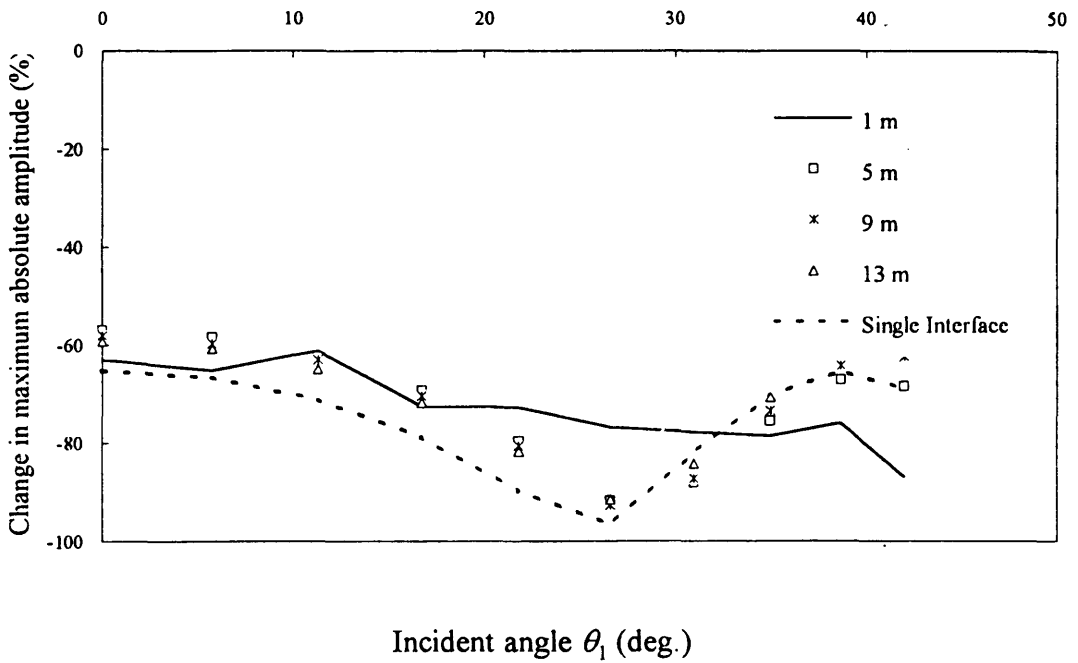


Figure 5.7a Change in maximum absolute amplitude of P -wave event for Type IA reflectivity for a change from $\sigma = 0.3$ to $\sigma = 0.1$ in layer 2.

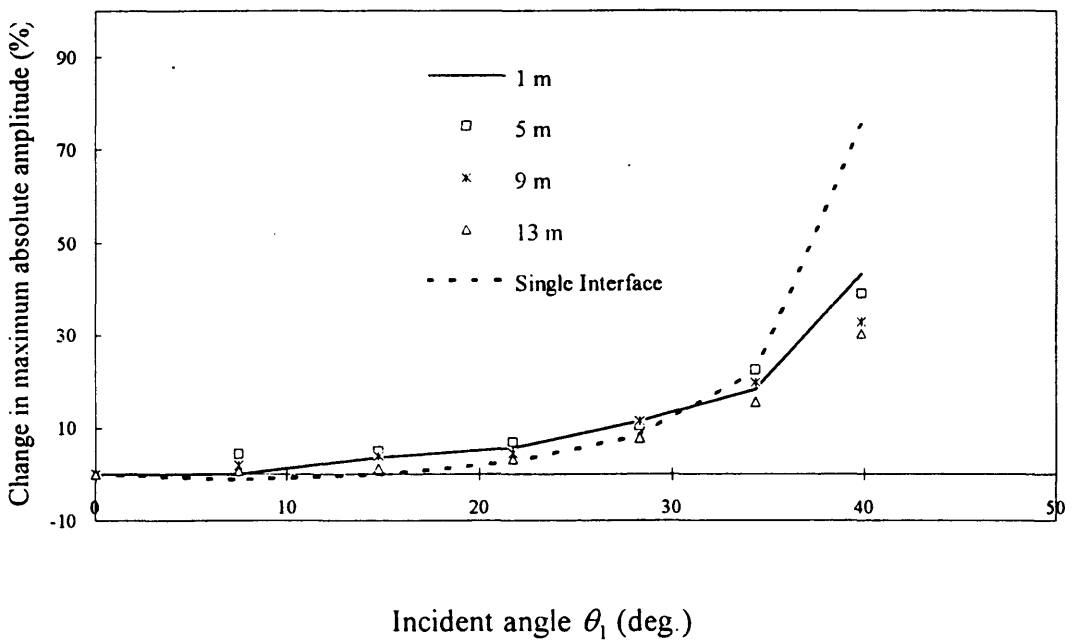


Figure 5.7b Change in maximum absolute amplitude of S -wave event for Type IA reflectivity for a change from $\sigma = 0.3$ to $\sigma = 0.1$ in layer 2.

For converted S -wave reflections (Figure 5.7b), the amplitude changes are positive for all layer 2 thicknesses, and all are below 10% for incidence angles less than approximately 26° . They are also very close to the corresponding values for the single interface from 0° to about 35° . Beyond 35° , *tuning effects* start to dominate the amplitude behaviour. This is important, since when interpreting AVO anomalies, far-offset traces are often needed to determine a robust amplitude gradient in order to deduce σ .

Thus, unlike Type I reflectivity, *single-interface effects* for both P -wave and converted S -wave reflections of Type IA reflectivity are not seriously affected by *tuning effects* for angles of incidence below 40° and for thickness of layer 2 greater than about $0.01\lambda_d$.

5.2.3 Type II reflectivity

Type II reflectivity may have critical incidence angles on both the upper and lower interfaces of layer 2. For the model used in this dissertation, the critical angles on the upper and lower interfaces for P -wave reflections are 59° and 56.5° respectively ($\sigma = 0.3$). If $\sigma = 0.1$, there is no critical angle on the upper interface for P -wave reflections, since the P -wave velocity for the thin layer would have decreased to 2854 m/s, but there is still a critical angle of 41.9° at the lower interface.

As σ changes from 0.3 to 0.1 for layer 2, the P -wave velocities of layer 2 for Types II and IIA reflectivities are lowered to the extent that one of the two zero-offset reflection coefficients changes polarity. For example, when σ is 0.3 for layer 2, the zero-offset reflection coefficients of Type II reflectivity are 0.1047 for both the upper and lower interfaces. But when σ is 0.1, the two reflection coefficients become -0.0448 for the upper interface and 0.2838 for the lower interface, which resembles a Type III reflectivity.

The shot gathers for this reflectivity with 5 m thickness for layer 2 are plotted in Figure 5.8. The differences between the P -wave and S -wave reflection amplitudes for $\sigma = 0.3$ and the corresponding amplitudes for $\sigma = 0.1$ are very small on a visual basis. However, the amplitude results in Figure 5.9 show that, for both P -wave and converted S -wave reflections, *single-interface effects* are strongly and adversely affected by *tuning effects*. In Figure 5.9a, the amplitude change curve for the single interface is negative from an incidence angle of zero to about 27° , and becomes positive for larger angles of incidence. The negative values are results of the low-magnitude reflection coefficients for the interface when σ is 0.1 compared to the much larger-magnitude reflection coefficients when σ is 0.3. The situation is reversed for angles of incidence larger than 27° . For the analysis involving both interfaces of layer 2, the amplitude changes are not as angle-dependent as that of the single interface. It is also evident that *tuning effects* become dominant in that the amplitude changes increase with increasing thickness of the thin layer. For example, the change in amplitude with offset for the 1 m case is approximately zero, which implies that *tuning effect* has negated the *single-interface effect* almost completely. For the 13 m case, the amplitude change is about 90%, indicating that a lateral change in lithology should be detectable easily.

An unexpected observation evident in Figure 5.9a. is that, as the thickness of layer 2 increases, one would expect the amplitude curves in Figure 5.9a to approach the single interface curve, as is the case for Type I reflectivity. However, this behaviour is not observed in Figure 5.9a, the reason being that, for the single-interface curve, the amplitude results represent the effect of the change of σ for the upper interface of layer 2. However, for Type II reflectivity, an examination of the offset-dependent reflection coefficients shows that the reflection coefficients of the lower interface of layer 2 are much larger in magnitude than those of the upper interface for all incidence angles when σ is 0.1.

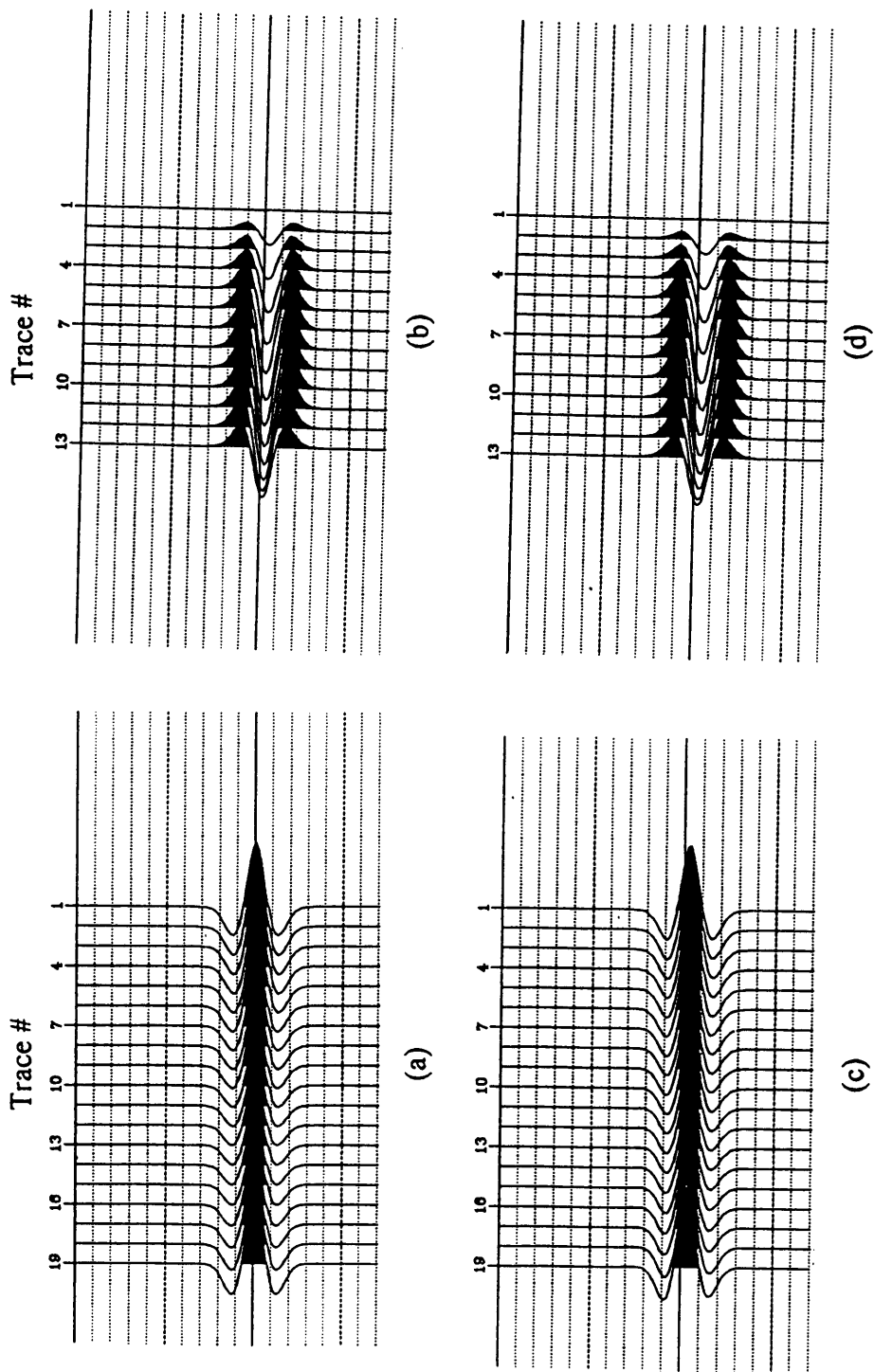


Figure 5.8 Shot gathers for Type II reflectivity at 5-m thickness: (a) *P*-wave, $\sigma = 0.3$; (b) *S*-wave, $\sigma = 0.3$; (c) *P*-wave, $\sigma = 0.1$; (d) *S*-wave, $\sigma = 0.1$. Timing lines are at 10-ms intervals.

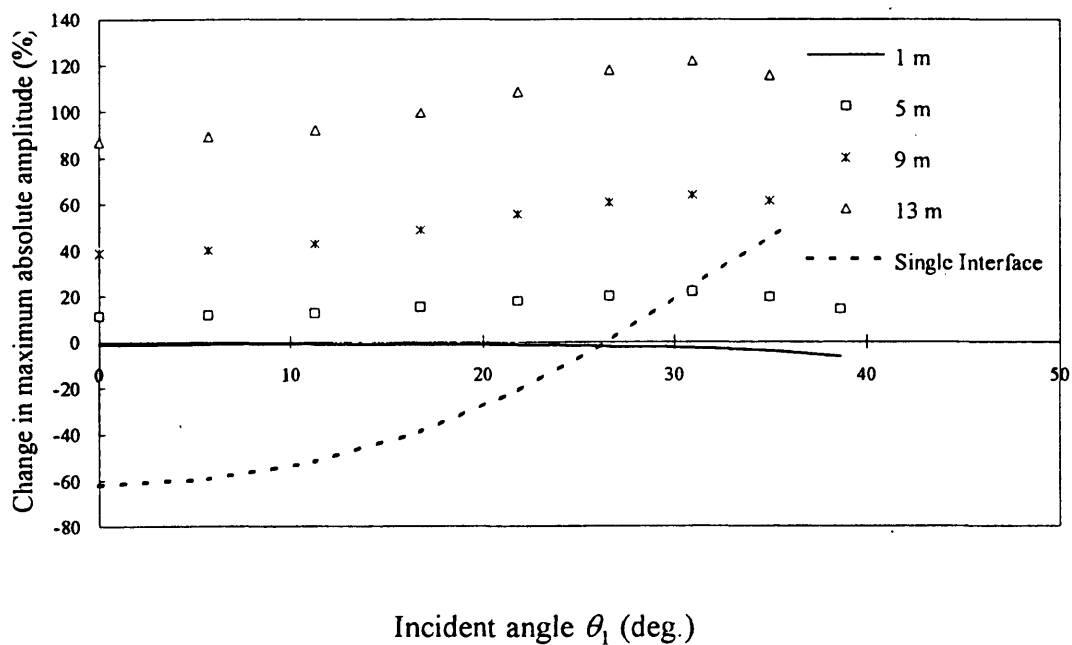


Figure 5.9a Change in maximum absolute amplitude of P -wave event for Type II reflectivity for a change from $\sigma = 0.3$ to $\sigma = 0.1$ in layer 2.

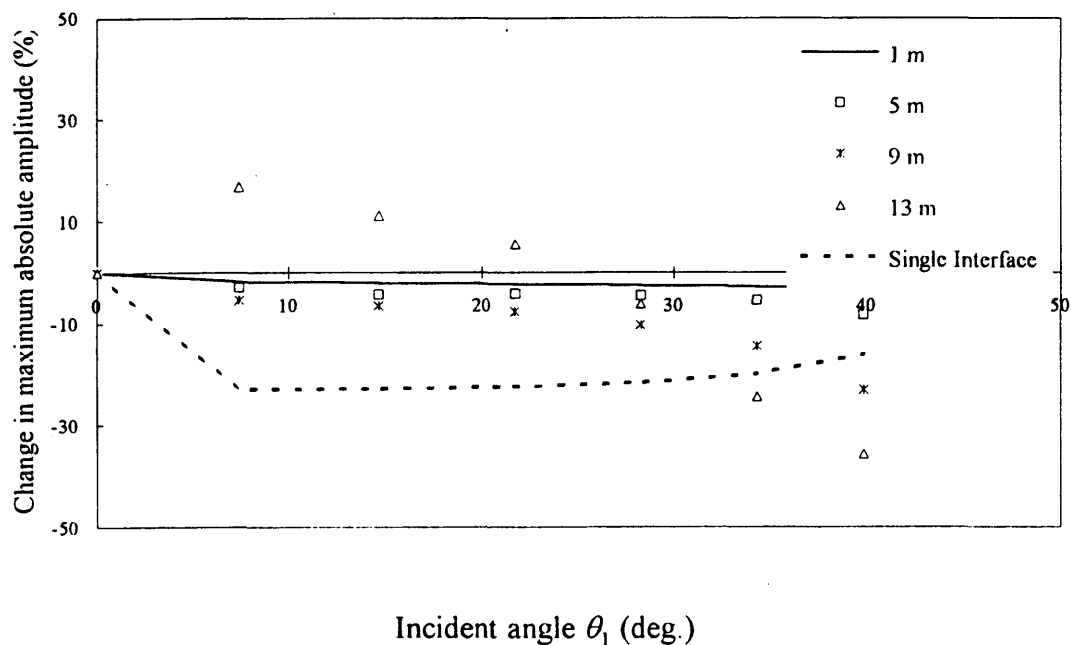


Figure 5.9b Change in maximum absolute amplitude of S -wave event for Type II reflectivity for a change from $\sigma = 0.3$ to $\sigma = 0.1$ in layer 2.

Consequently, the absolute maximum amplitudes of the composite reflections are determined from the lower interface more than from the upper interface, and the amplitude curves for layer 2 in Figure 5.9a are more representative of how *tuning* has altered the *single-interface effect* for the lower interface.

For converted *S*-wave reflections (Figure 5.9b), the single-interface curve shows an amplitude decrease of approximately 20% as σ changes from 0.3 to 0.1 for layer 2. However, when the thickness of layer 2 is 5 m or less, the *single-interface effect* is largely overwhelmed by the *tuning effect*. For the 9 m case, the *single-interface effect* is again diminished by *tuning*, but only for incidence angles below 33°. However, the amplitude behaviour of the curve for the 13 m case is different. For angles of incidence below 25°, the *tuning* effect is so strong that it reverses the trend of the *single-interface effect*. For larger incidence angles, the curve changes from being positive to negative, and decreases rapidly as a function of the incidence angle. This abnormal behaviour is probably also a result of the amplitude change curves for layer 2 being more representative of how *tuning* alters the *single-interface effect* for the lower interface.

From the above discussion and from Figure 5.9, it is evident that for any reflections from geological formations that can be represented by the Type II reflectivity, the reflection amplitudes cannot be simply used to deduce any meaningful lithological data before *tuning effects* are removed. Furthermore, the possibility of a reversal of the polarity of the reflection coefficients on the top interface must be considered as σ is lowered.

5.2.4 Type IIA reflectivity

Type IIA reflectivity is represented as $\overline{\Gamma\Gamma}$, with the magnitudes of the reflection coefficients being all equal. The shot gathers for the 5 m case are shown in Figure 5.10.

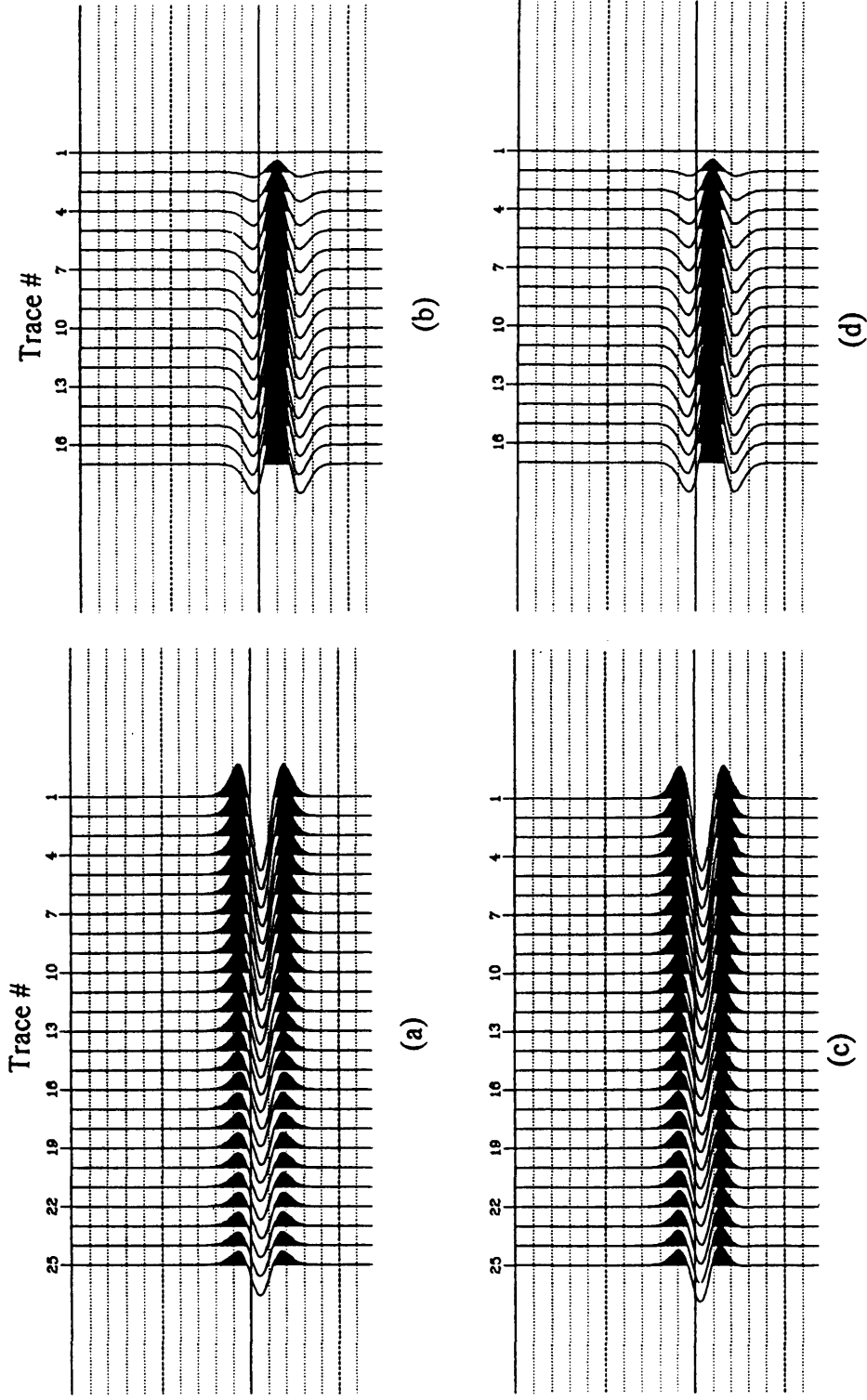


Figure 5.10 Shot gathers for Type IIA reflectivity at 5-m thickness: (a) P -wave, $\sigma = 0.3$; (b) S -wave, $\sigma = 0.3$; (c) P -wave, $\sigma = 0.1$; (d) S -wave, $\sigma = 0.1$. Timing lines are at 10-ms intervals.

For this reflectivity, no critical angles are involved, and the *single-interface effect* is also altered significantly by the *tuning effect*. For *P*-wave reflections, the single-interface effect as represented by the single-interface curve in Figure 5.11a indicates that, as σ decreases from 0.3 to 0.1, the maximum absolute amplitude increases by more than 130% for the zero-offset reflection and by more than 200% for reflections whose incidence angles range from 35° to 50° . However, Figure 5.11a also shows that *tuning* systematically cancels the *single-interface effect*. For the 1 m case, *tuning* practically nulls the *single-interface effect* completely. As the thickness of layer 2 increases, the curves approach that of the single interface, implying that the *tuning effect* decreases and the *single-interface effect* increases. This is because, unlike Type II reflectivity, for $\sigma = 0.1$, the much larger reflection coefficients are at the upper interface so that the amplitude results are always dominated by the reflection from the upper interface. However, even at a layer 2 thickness of 13 m, the *tuning effect* has still influenced the *single-interface effect*.

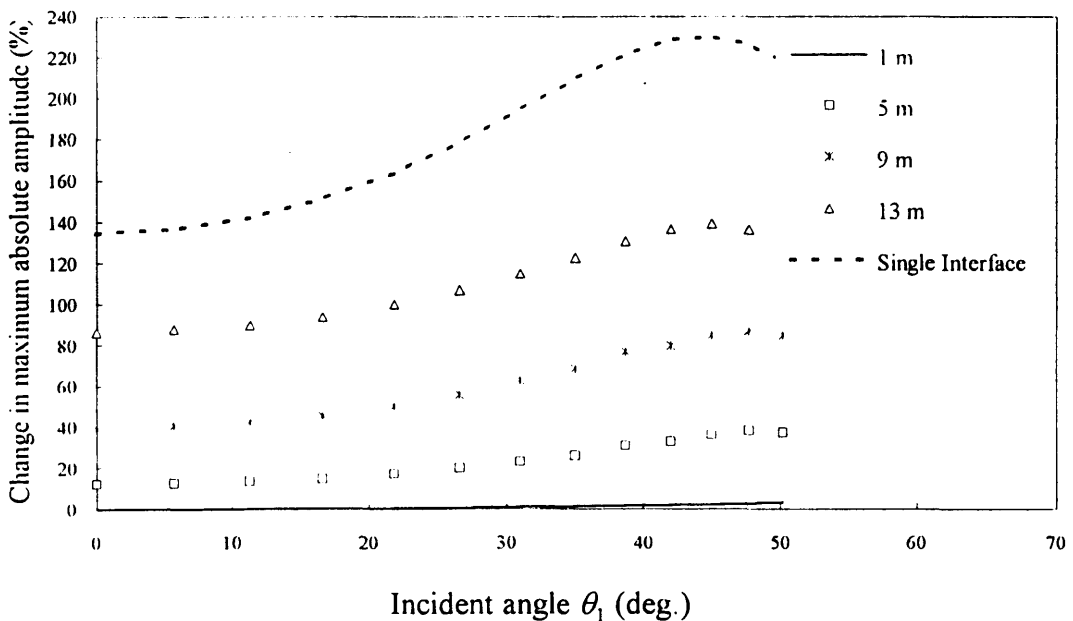


Figure 5.11a Change in maximum absolute amplitude of *P*-wave event for Type IIA reflectivity for a change from $\sigma = 0.3$ to $\sigma = 0.1$ in layer 2.

For converted S -wave reflections, the results are similar to those of P -wave reflections. Figure 5.11b shows that *tuning effect* is dominant for the 1 m, 5 m, and 9 m cases that there is practically no observable *single-interface effect*. However, for the 13 m case, the *tuning effect* becomes secondary, modifying the *single-interface effect* only slightly. Since the S -wave has a lower propagating velocity, in general, it will suffer less of a tuning effect than the corresponding P -wave reflections. Type IIA reflectivity is a good example.

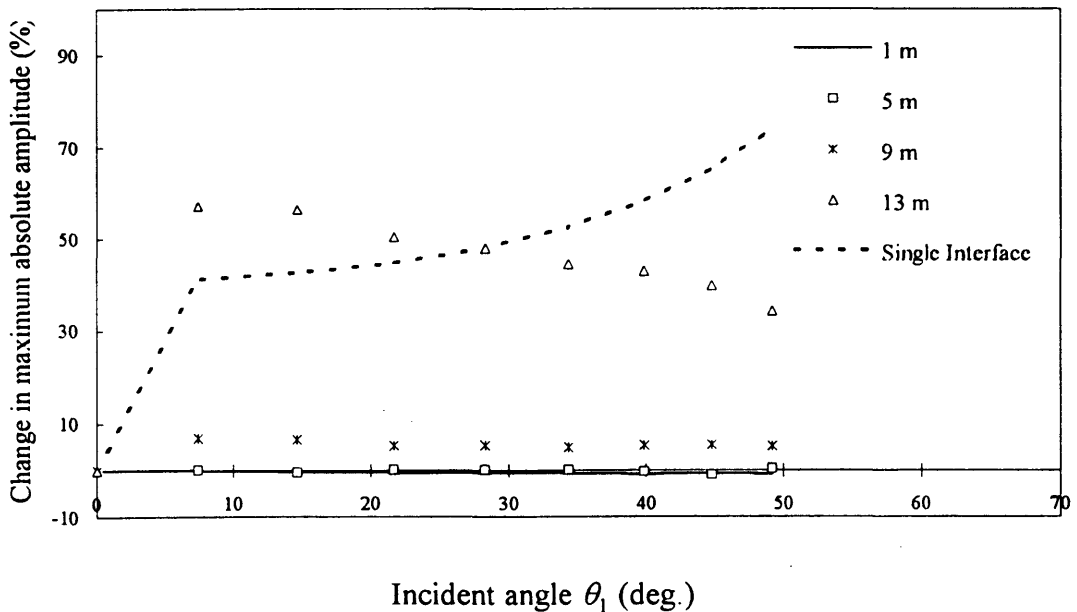


Figure 5.11b Change in maximum absolute amplitude of S -wave event for Type IIA reflectivity for a change from $\sigma = 0.3$ to $\sigma = 0.1$ in layer 2.

5.3 Offset-dependent peak frequency analysis

In this section, the offset-dependent peak frequency behaviour of a composite reflection from a thin bed is presented. The use of variations in peak frequency as an aid in seismic interpretation has not been extensively investigated, apart from recent studies by

Lange and Almoghrabi (1988) and Mazzotti (1991). The main objective is to investigate how the peak frequency responds to a change in the Poisson's ratio for both the reflected P -wave and the converted PS -wave.

For obtaining some understanding of the peak frequency behaviour as a function of the incidence angle for a thin bed, the same four reflectivity models and shot gathers used in section 5.3 were examined. Each of these models has layers 1 m, 5 m, 9 m, and 13 m thick and for each of these thicknesses, peak frequencies were studied for reflected P -waves and converted S -waves with $\sigma = 0.3$ for layer 2, as well as for the case where $\sigma = 0.1$. The source wavelet for all cases is a 31 Hz Ricker wavelet. Since the same shot gathers used in section 5.3 are used for the peak frequency analysis, the P -wave results include PP , $PPPP$, $PPSP$, and $PSPP$ reflections, whereas the S -wave results include PS , $PPSS$, $PSSS$, $PSPS$, and $PPPS$ reflections. Where no critical angle is involved, a maximum incidence angle of 50° is allowed; where a critical angle is involved either at the upper or lower interface, the study covered an incident angle range up to slightly less than the critical angle.

To simplify the discussion, f_{p1} and f_{p3} will be used to denote the peak frequencies of the composite reflections when $\sigma = 0.1$ and 0.3 in layer 2, respectively.

5.3.1 Type I reflectivity

Type I reflectivity series is represented symbolically by \top and involves no critical angles. For all four thicknesses, there are no phase changes in any of the reflections for incidence angles below 50° . The offset-dependent peak frequencies for this reflectivity are plotted in Figure 5.12. For the reflected P -wave (Figure 5.12), the following observations are made:

- Regardless of thickness, f_{p1} are slightly lower than f_{p3} , probably due to the fact that, when $\sigma = 0.1$, the P -wave velocity in layer 2 is lowered so that the time thickness of the layer is larger.
- The differences between f_{p1} and f_{p3} vary with thickness. For example, f_{p3} is about 2 Hz higher for large angle of incidence for both the 1 m and 13 m cases; for the 5 m case, f_{p3} is only fractionally higher for all angles of incidence
- f_{p1} and f_{p3} are both highest for the 5 m case for angles of incidence less than 40° ; for angles of incidence larger than 40° , f_{p1} and f_{p3} for the 9 m and 13 m cases are about the same or fractionally higher than for the 5 m case. These imply some frequency tuning, consistent with results for Type III reflectivity (Figure 3.5).
- Differences between f_{p1} and f_{p3} are small and may be difficult to detect on real seismic data.

For reflected S -wave (Figures 5.12c and 5.12d), the following observations are made:

- For all thicknesses, and for the same reason mentioned for the P -wave discussion, f_{p3} are slightly higher than f_{p1} for all angles of incidence.
- Tuning effect observed for P -waves for the 5 m case is absent in S -wave reflections.
- f_{p1} and f_{p3} both decrease as thickness increases, but do not change significantly as a function of the incident angle.
- differences in f_{p1} and f_{p3} are probably too small for meaningful interpretation on real data.

The results for Type I reflectivity suggest that peak frequencies of P -wave reflections in pre-stack gather format are more useful for studying lateral changes of the

Poisson's ratio, whereas those of *S*-wave are more indicative of lateral changes in thickness. In practice, however, the changes are less than 2 Hz and may therefore be difficult to detect on real seismic data.

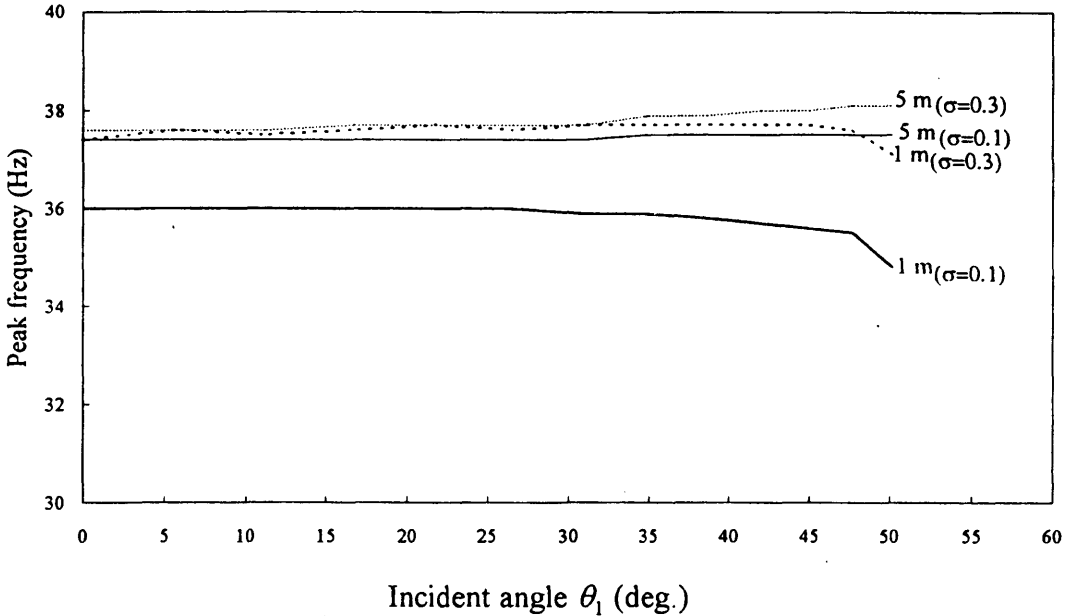


Figure 5.12a Peak frequencies versus angle of incidence for layer 2 thicknesses of 1-m and 5-m for reflected *P*-waves of Type I reflectivity.

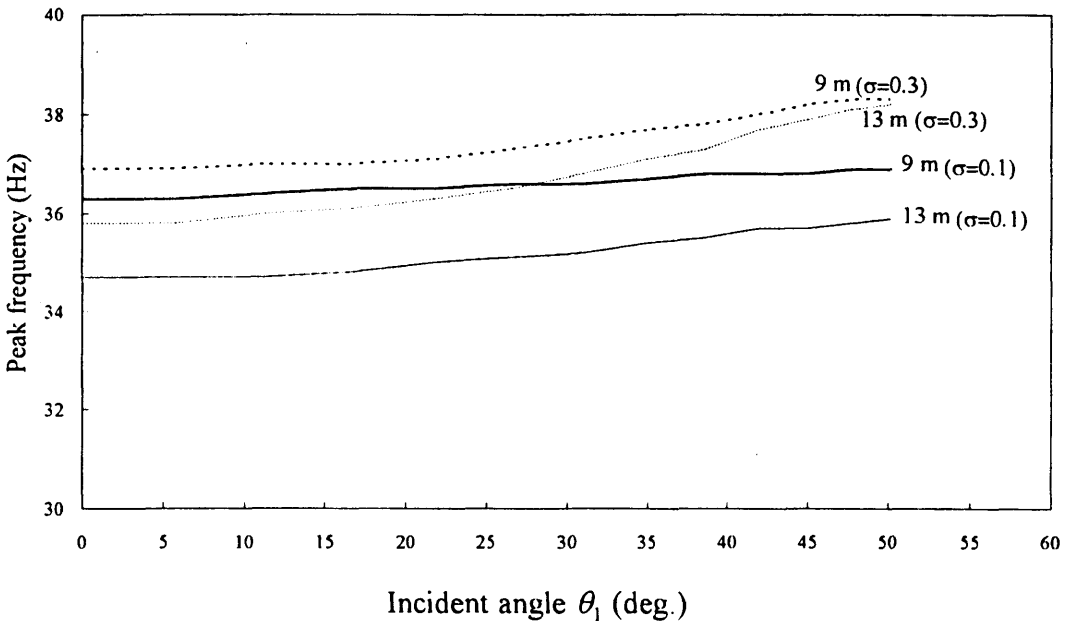


Figure 5.12b Peak frequencies versus angle of incidence for layer 2 thicknesses of 9-m and 13-m for reflected *P*-waves of Type I reflectivity.

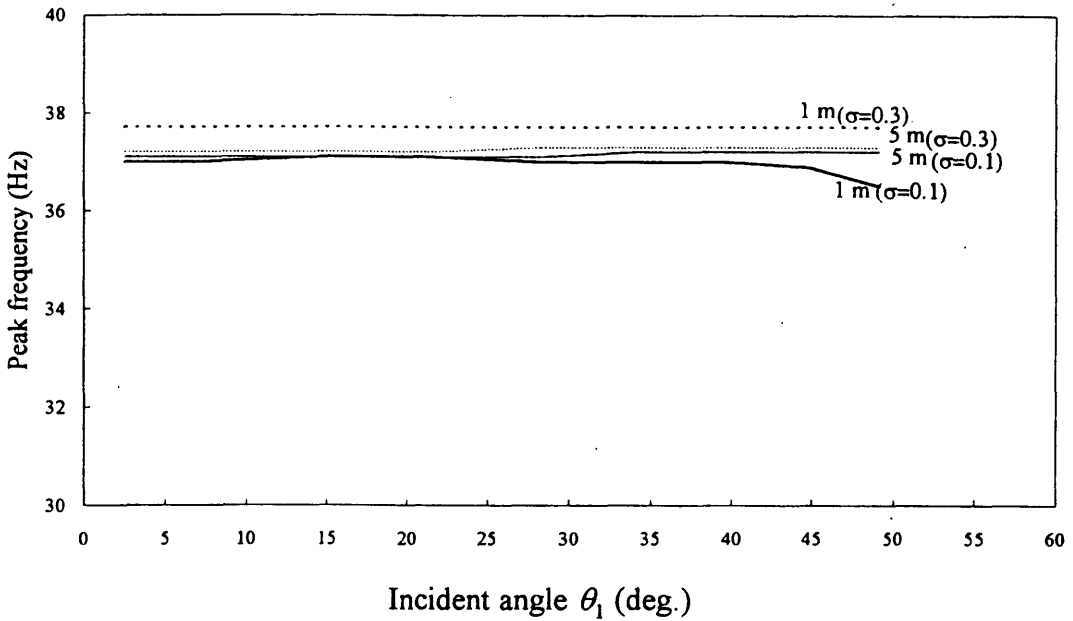


Figure 5.12c Peak frequencies versus angle of incidence for layer 2 thicknesses of 1-m and 5-m for reflected S -waves of Type I reflectivity.

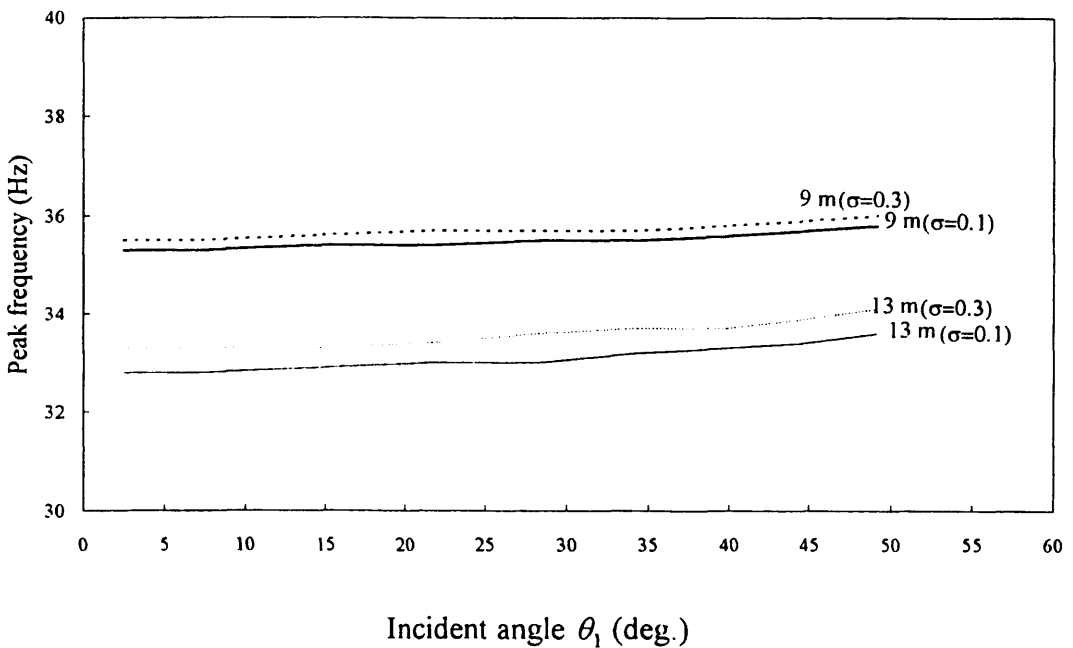


Figure 5.12d Peak frequencies versus angle of incidence for layer 2 thicknesses of 9 m and 13 m for reflected S -waves of Type I reflectivity.

5.3.2 Type IA reflectivity

For the Type IA reflectivity model used, there is a critical angle of 45.6° at the upper interface of layer 2 for PP reflections when σ is 0.3 for the layer. Hence, the peak frequencies were calculated only up to the incidence angle of approximately 42° for the P -wave seismogram and 40° for the S -wave seismogram. In section 5.2.2, it was shown that an anomalous decrease in amplitude occurs for P -wave reflections when σ is 0.1 for layer 2 due to polarity reversals in PP and $PPPP$ reflections at incidence angles of 26° and 21° . A similar frequency anomaly is also observed for the P -wave peak frequency. From Figures 5.13a and 5.13b, which show the results for P -wave reflections, the following observations are made:

- All f_{p3} values are clustered around 37 Hz for angles of incidence up to 30° and do not vary significantly as a function of the incidence angle nor as a function of the thickness.
- Beyond 30° , f_{p3} is strongly dependent on incidence angle for the 1 m case. This is also true of the 5 m case beyond the incidence angle of 35° , though to a lesser extent.
- f_{p1} is very anomalous in the incidence angle range of 21° to 40° : for the 1 m and 5 m cases, f_{p1} are substantially lower than the f_{p3} , whereas the reverse is true of the 9 m and the 13 m cases.
- PP reflections change polarity at about 26° , which is also approximately where a minimum and a maximum would occur if smooth curves are drawn for the 1 m and 13 m cases, respectively.

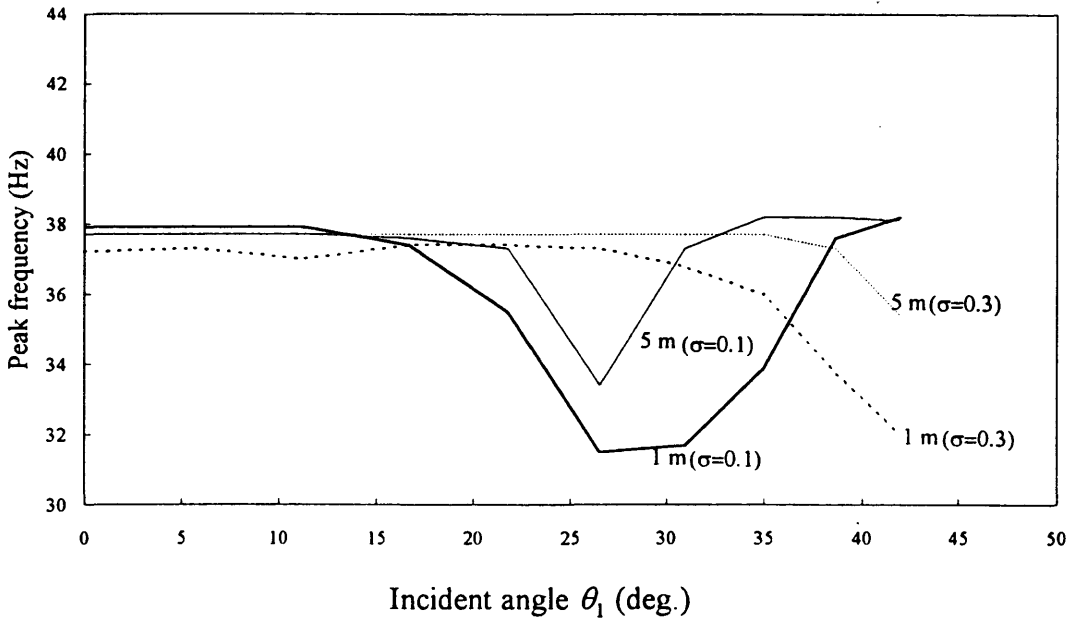


Figure 5.13a Peak frequencies versus angle of incidence for layer 2 thicknesses of 1-m and 5-m for reflected *P*-waves of Type IA reflectivity.

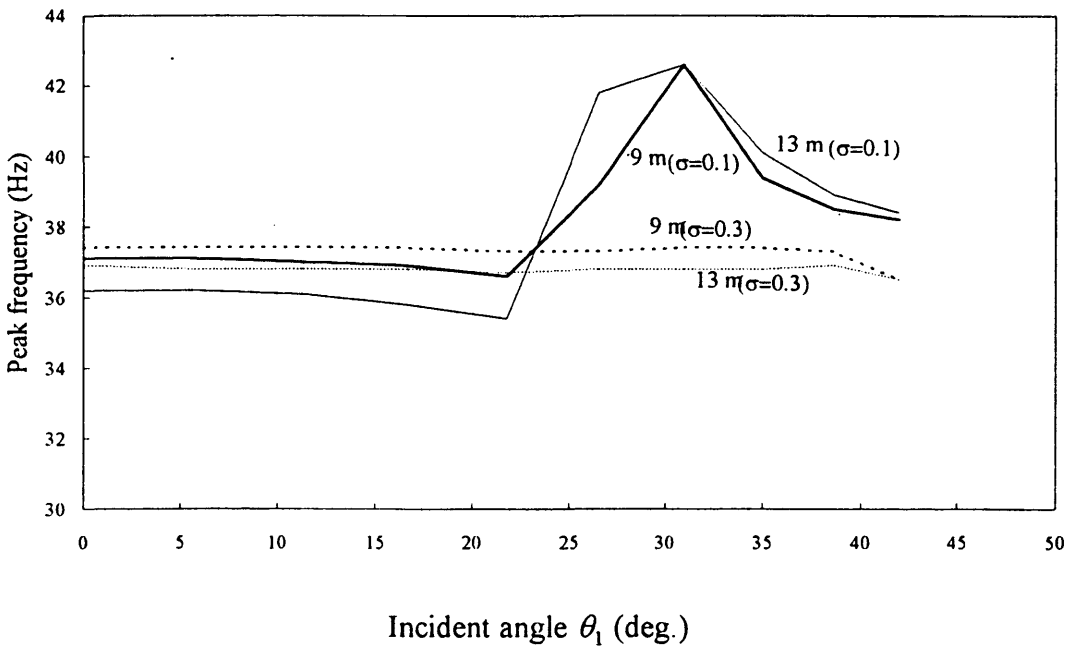


Figure 5.13b Peak frequencies versus angle of incidence for layer 2 thicknesses of 9-m and 13-m for reflected *P*-waves of Type IA reflectivity.

For the converted S -wave, there are no phase changes for the two primary reflections (PS and $PPSS$ reflections), and the peak frequency results are shown in Figures 5.7c and 5.7d. The following observations are made:

- f_{p1} and f_{p3} are close to each other for all thicknesses of layer 2.
- f_{p1} and f_{p3} both decrease as thickness increases for a constant angle of incidence.

The results for Type IA reflectivity indicate that peak frequencies of S -wave reflections are not useful for studying lateral changes in Poisson's ratio. Conversely, the P -wave results suggest that peak frequencies of P -wave reflections are useful in revealing lateral changes in Poisson's ratio. However, the majority of hydrocarbon traps within clastic sequences resembles Type I reflectivity more than they do Type IA reflectivity. This will limit the practical application of this interesting frequency anomaly.

The P -wave frequency anomalies shown in Figure 5.13 are probably frequency tuning effects similar to the tuning effects observed for Type III reflectivity (Figure 3.5), for which a frequency maximum occurs at about $0.9\lambda_d$. Thus, the traveltimes for the various wave components probably play an important role in the frequency tuning observed in Figures 5.13.

5.3.3 Type II reflectivity

For Type II reflectivity, the model tested has a critical angle of 41.9° at the lower interface when σ is 0.1 for the thin layer (section 5.2.3). For PP and $PPPP$ reflections, r_1 and r_2 are of opposite polarities if σ is 0.1 for the thin layer, but are of the same polarity if σ is 0.3. The P -wave peak frequencies are plotted in Figures 5.14a to 5.14b. From these figures, the following observations are made:

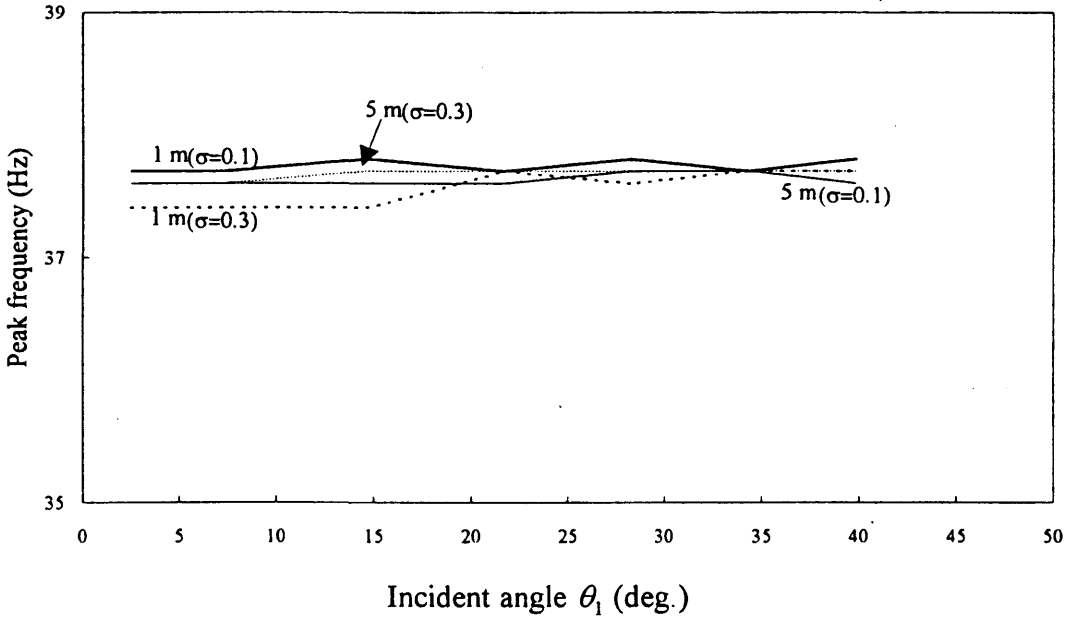


Figure 5.13c Peak frequencies versus angle of incidence for layer 2 thicknesses of 1-m and 5-m for reflected S -waves of Type IA reflectivity.

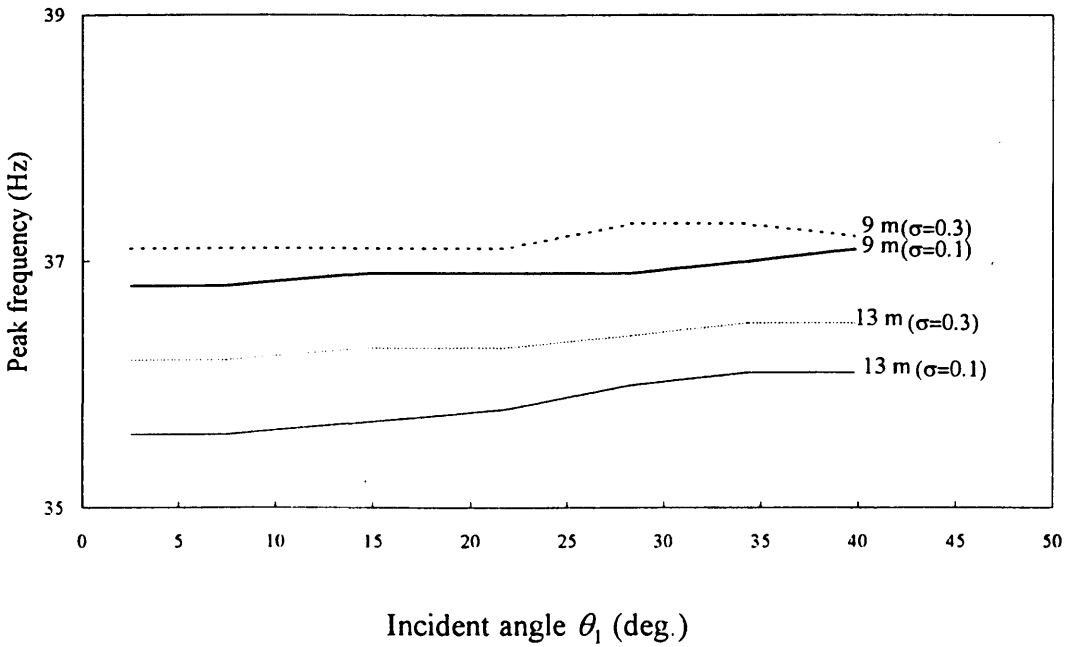


Figure 5.13d Peak frequencies versus angle of incidence for layer 2 thicknesses of 9-m and 13-m for reflected S -waves of Type IA reflectivity.

- f_{p1} is higher than f_{p3} for all layer 2 thicknesses and for all angles of incidence, with the differences increasing as layer 2 thickness increases.
- f_{p1} is more angle-dependent than is f_{p3} .
- For the 9 m and 13 m cases, a significant lateral change in the peak frequency may be a good indication of a lateral change in Poisson's ratio. For the velocities chosen for this model, the $(1/8)\lambda_d$ thickness is 11 m for $\sigma = 0.3$ and is 9 m for $\sigma = 0.3$.

For converted S -wave reflections (Figures 5.14c and 5.14d), both r_1 and r_2 are of the same polarity for all the reflections. The following observations are made:

- For the 1 m and 5 m thicknesses, f_{p1} and f_{p3} are not significantly different, nor are they angle-dependent.
- For the 9 m and 13 m thicknesses and for incidence angles larger than 30° , f_{p1} and f_{p3} are mildly angle-dependent, and they differ only by about 1 to 2 Hz.

The results for Type II reflectivity indicate that P -waves would be more useful than converted S -waves for investigating a lateral change in the Poisson's ratio. The P -wave peak frequencies are particularly useful if the formation is greater than $(1/8)\lambda_d$ in thickness. However, if the P -wave frequency change is accompanied by a corresponding S -wave frequency change, the changes are probably due to reasons other than a lateral change in Poisson's ratio.

5.3.4 Type IIA reflectivity

For Type IIA reflectivity, there are no critical angles involved for the model studied. For PP and $PPPP$ reflections, they are of opposite signs if σ is 0.1, but are of the same sign if σ is 0.3. This polarity property is similar to that of Type II reflectivity. The numerical results are plotted in Figure 5.15.

For the P -wave reflections (Figures 5.15a and 5.15b), the following observations are made:

- f_{p1} and f_{p3} are close in value for all angles of incidence for the case where layer is 1 m thick.
- f_{p1} is significantly higher than f_{p3} for all the other thicknesses of layer 2 and for all incidence angles.

For converted S -wave reflections (Figures 5.16c and 5.16d), the following observations are made:

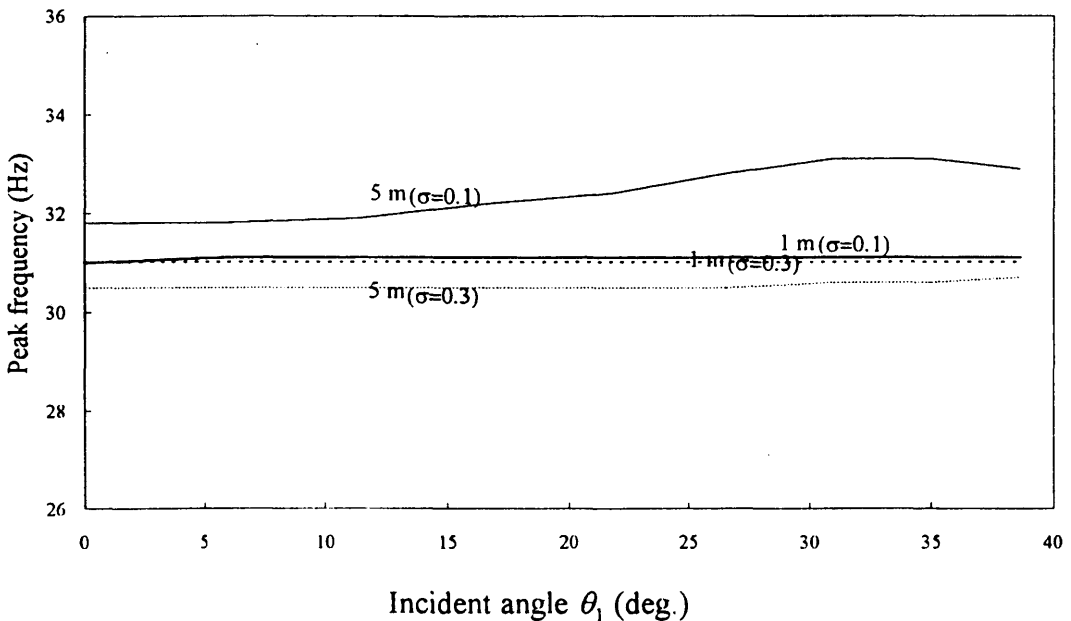


Figure 5.14a Peak frequencies versus angle of incidence for layer 2 thicknesses of 1-m and 5-m for reflected P -waves of Type II reflectivity.

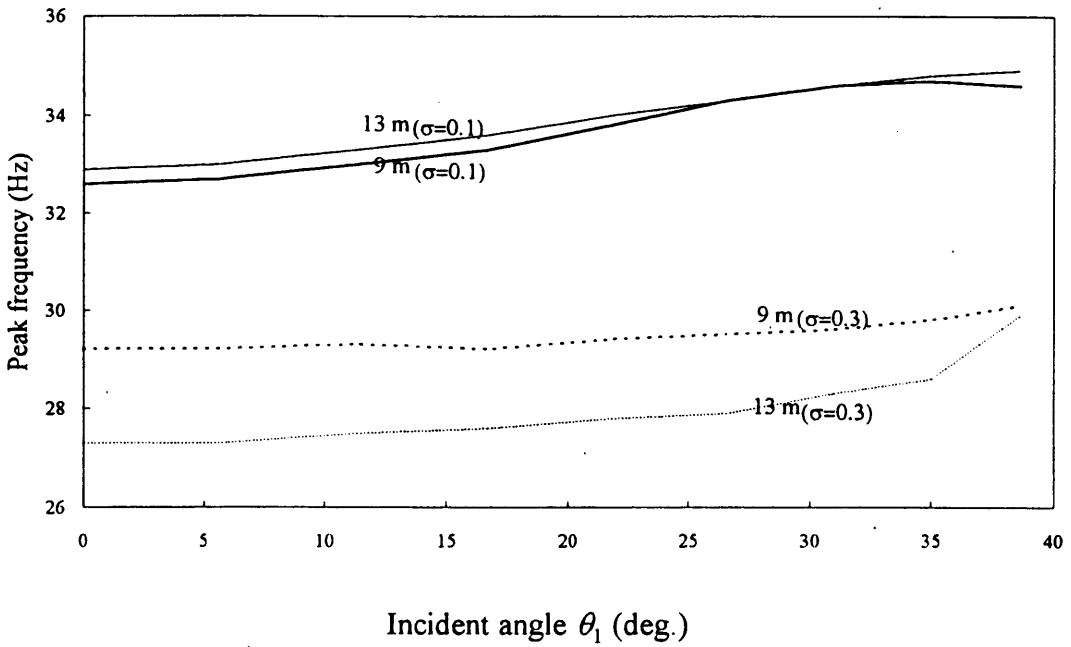


Figure 5.14b Peak frequencies versus angle of incidence for layer 2 thicknesses of 9-m and 13-m for reflected *P*-waves of Type II reflectivity.

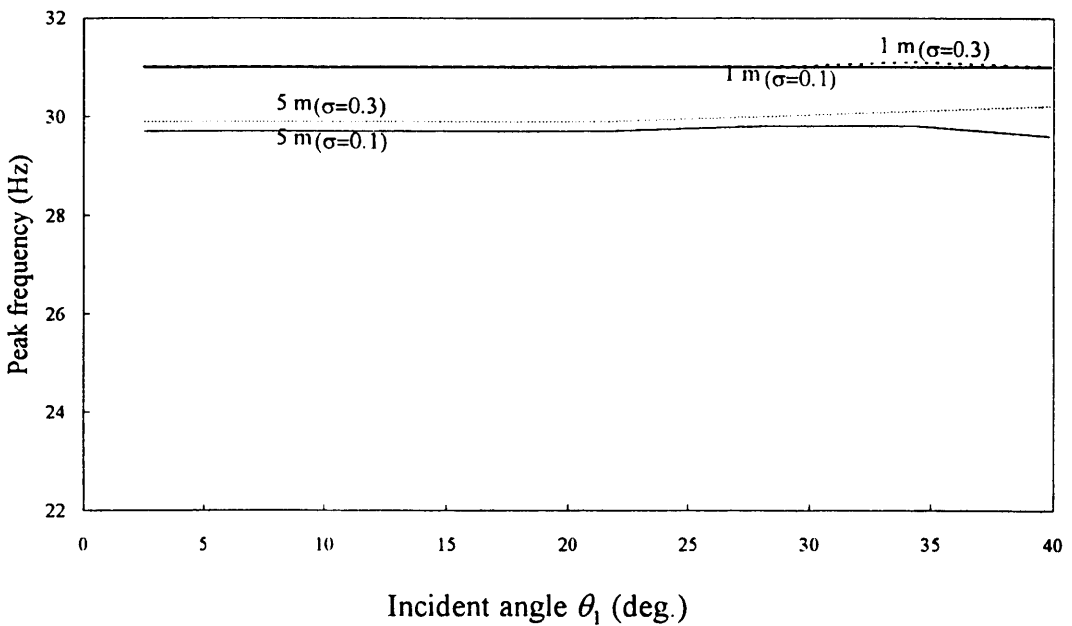


Figure 5.14c Peak frequencies versus angle of incidence for layer 2 thicknesses of 1-m and 5-m for reflected *S*-waves of Type II reflectivity.

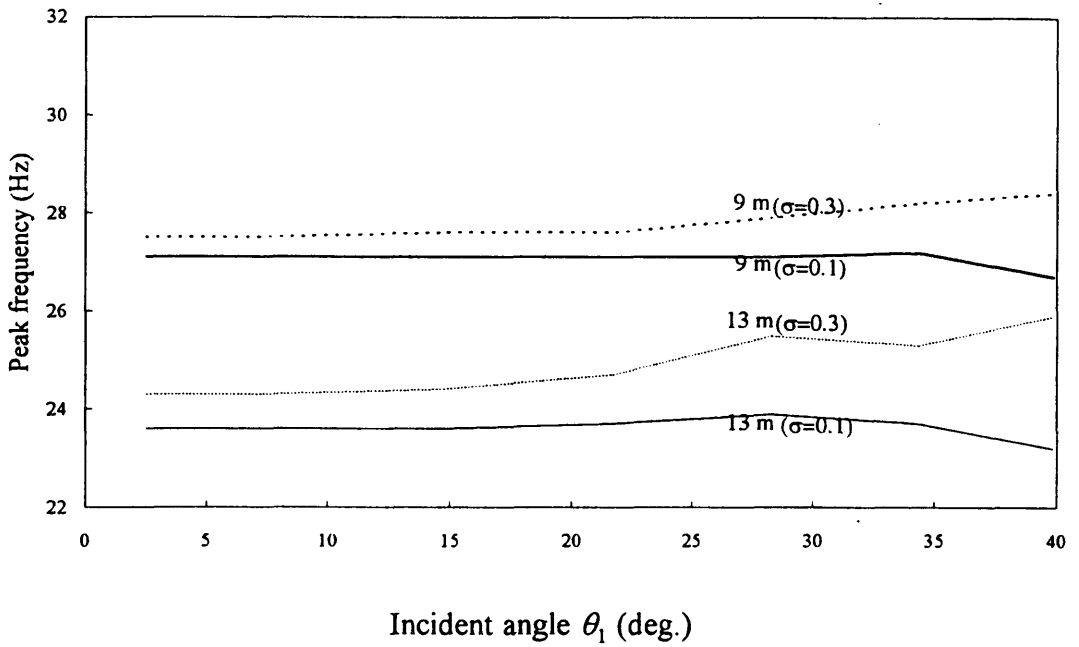


Figure 5.14d Peak frequencies versus angle of incidence for layer 2 thicknesses of 9-m and 13-m for reflected *S*-waves of Type II reflectivity.

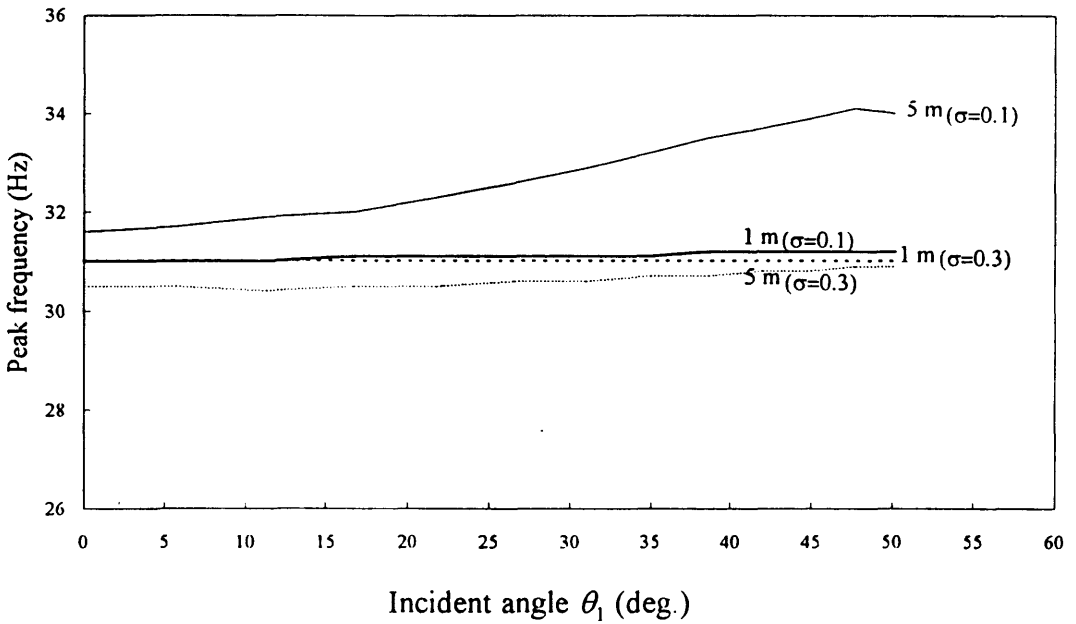


Figure 5.15a Peak frequencies versus angle of incidence for layer 2 thicknesses of 1-m and 5-m for reflected *P*-waves of Type IIA reflectivity.

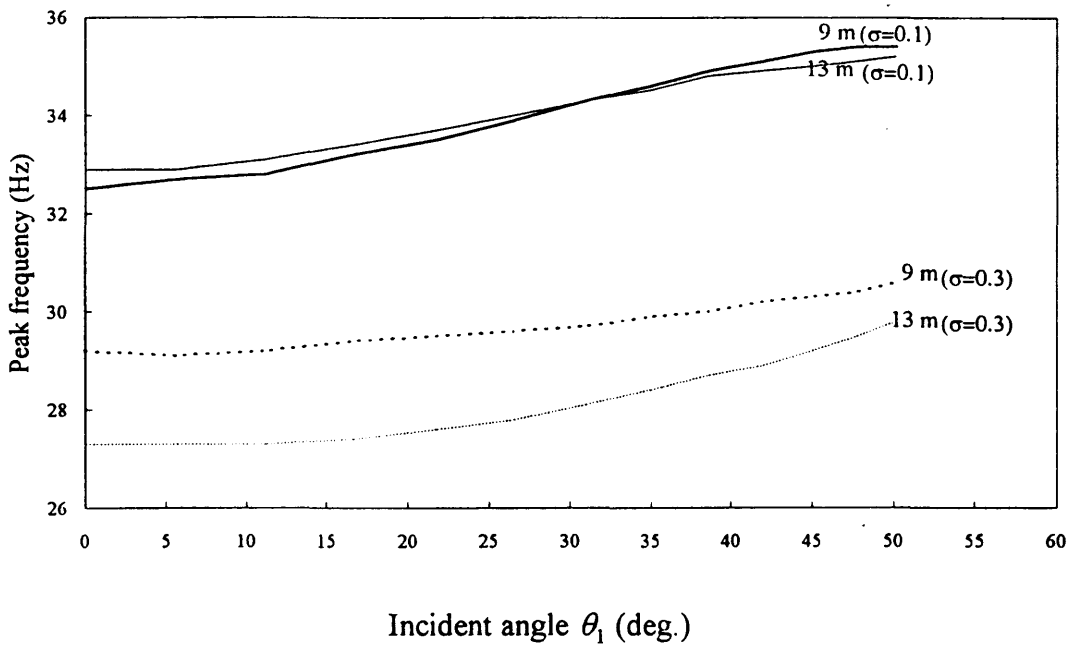


Figure 5.15b Peak frequencies versus angle of incidence for layer 2 thicknesses of 9-m and 13-m for reflected P -waves of Type IIA reflectivity.

- There is little difference between f_{p1} and f_{p3} for all four thicknesses.
- f_{p1} and f_{p3} do not change significantly as a function of the incidence angle, although they both slowly decrease with thickness.

The frequency results for Type IIA reflectivity indicate that the reflected P -wave frequencies as a function of the incidence angle are useful for studying lateral changes in the Poisson's ratio, but the corresponding converted S -wave frequencies are not. This situation is similar to that of the Type II reflectivity. Hence, if corresponding P -wave and S -wave offset-dependent frequency anomalies are observed, they are probably due to reasons other than lateral changes in Poisson' ratio.

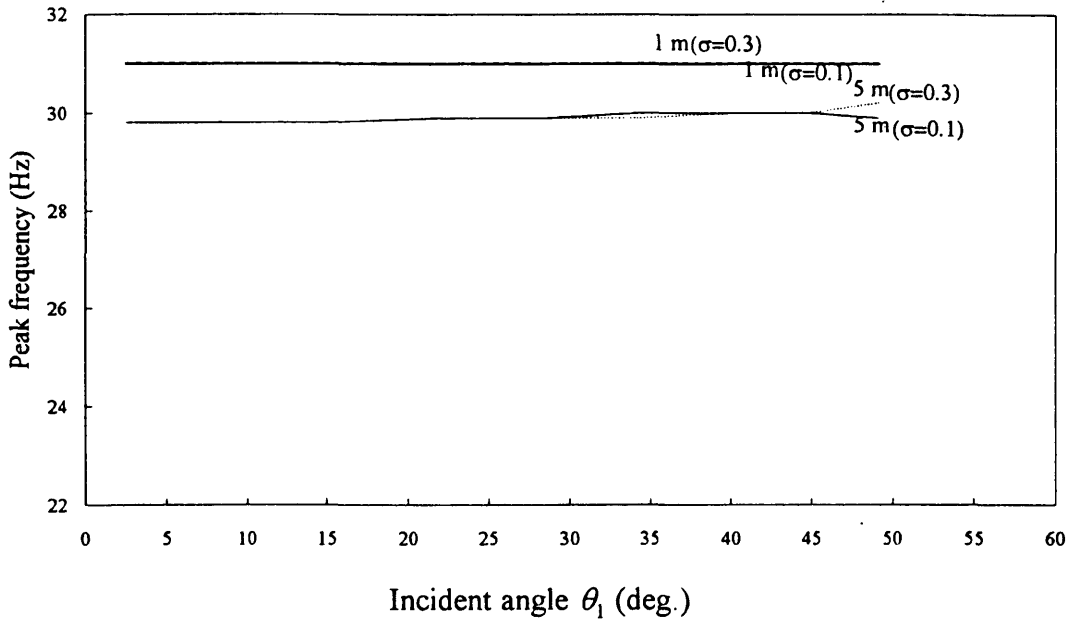


Figure 5.15c Peak frequencies versus angle of incidence for layer 2 thicknesses of 1-m and 5-m for reflected *S*-waves of Type IIA reflectivity.

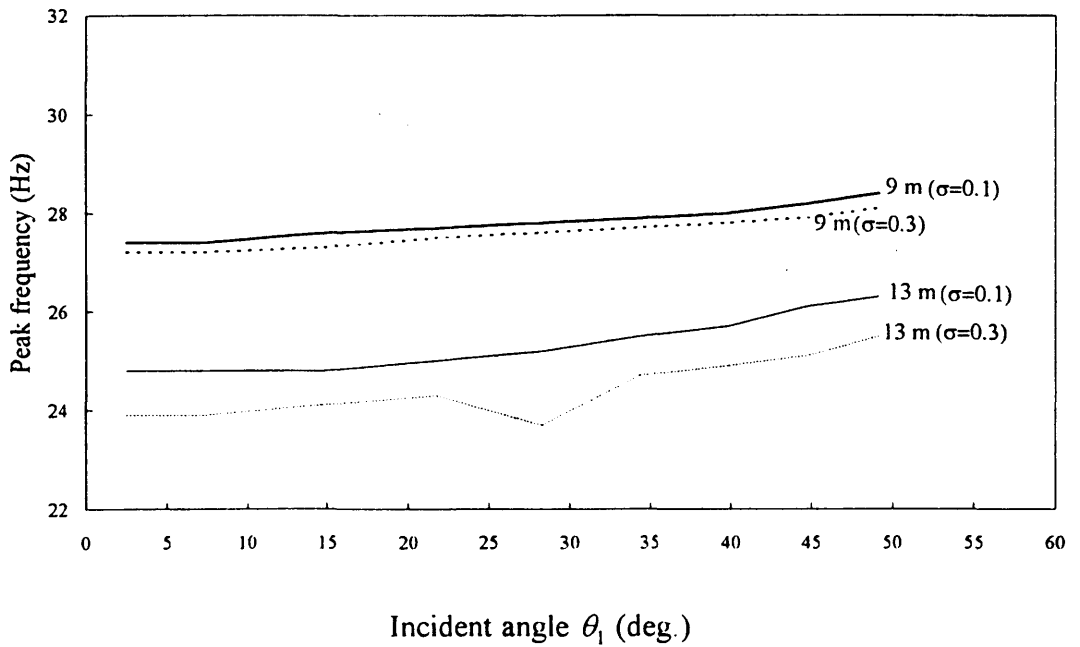


Figure 5.15d Peak frequencies versus angle of incidence for layer 2 thicknesses of 9-m and 13-m for reflected *S*-waves of Type IIA reflectivity.

5.4 Offset-dependent properties of complex attributes

The use of complex attributes to study offset-dependent properties of seismic data has not been widely discussed in the geophysical literature. Using the instantaneous amplitude, the instantaneous frequency, and the instantaneous phase values at the peak of the amplitude envelope, Mazzotti (1991) defined three corresponding indicators and studied their changes as a function of source-receiver offsets. He concluded that both the amplitude and phase indicators were useful for detecting effects that are related to interference among reflectors and to critical angle phenomena, in terms of phase changes and amplitude variations. The frequency indicator, however, was mainly controlled by the spectrum of the propagating wavelet. His study included five synthetic models and an actual data set. In Chapter 6, the differences in the complex attributes of seismic reflections from a channel sandbar as a function of source-receiver offset are discussed in a case study.

Although both Mazzotti (1991) and the case study in Chapter 6 discuss some potential uses of complex attributes as a function of offset in seismic interpretation, the subject is still in its introductory stage and needs more research to establish the manner in which the attributes can be used effectively for stratigraphic interpretation. For example, both Mazzotti (1991) and the case study in Chapter 6 only consider *P*-wave reflections. Future research should be extended to include *S*-wave reflections, since they have larger transit times and hence different interference patterns. This subject will be particularly important in the future when the use of shear waves for seismic interpretation is more widespread, and also when field acquisition techniques have advanced to the stage where wide angle reflections (reflections close to and beyond critical angles) can be reliably interpreted.

To study the offset-dependent properties of complex attributes for seismic reflections from a thin bed, the approach is similar to the one used for the offset-dependent frequency study in section 5.3. The attributes for the thin-bed reflections with $\sigma = 0.3$ are compared to those with $\sigma = 0.1$ in the thin bed. Since the main purpose is to investigate how a change of σ in the thin bed would affect the three attributes, only the 5 m case will be studied. The *P*- and *S*-wave shot gathers for the 5 m case used in sections 5.2 and 5.3 are also used for the attribute study.

All four reflectivities, namely Types I, IA, II, and IIA, were studied. The results for Type I reflectivity indicate that the three attributes are not sensitive to a change of σ in the thin bed, and the results for Type IIA reflectivity are quite similar to the results of Type II reflectivity. Hence, only the results for Types IA and II reflectivities are presented in this dissertation.

Figures 5.6 and 5.8 are the shot gathers of Types IA and II reflectivities for the 5 m case for both *P*-wave and *S*-wave reflections. Except in the case of the *P*-wave shot gathers for Type IA reflectivity, there appears little difference between seismograms with $\sigma = 0.1$ in layer 2 and for $\sigma = 0.3$ in layer 2. This implies that any lateral change in Poisson's ratio may not be visually detectable on conventional displays when tuning occurs for *S*-wave reflections of Type IA reflectivity and for both *P*-wave and *S*-wave reflections from a Type II reflectivity sequence. As shown in the next several sections, their complex attributes show more differences by nature of their calculations.

5.4.1 Instantaneous amplitude

Figure 5.16 show the instantaneous amplitudes for Type IA reflectivity. The *P*-wave instantaneous amplitudes for $\sigma = 0.1$ exhibit an anomaly at approximately traces 9 to 11. This anomaly is also evident in the conventional display (Figure 5.6) and appears as an

amplitude decrease in Figure 5.7a. The reason for this anomaly is that both *PPPP* and *PP* reflections undergo a phase change at the incidence angles of approximately 21° and 26° respectively. The other three displays ($\sigma = 0.3$ for *P*-wave and the two *S*-wave cases) do not undergo such phase changes, and hence have no similar anomalies. Thus, in interpreting geological models that can be represented by Type IA reflectivity, the instantaneous amplitudes of *P*-wave reflections may be useful for detecting lateral changes in σ . For the amplitude envelopes of *S*-wave reflections, there is little difference between the two cases of σ and are not useful for detecting lateral changes in σ .

Figure 5.17 shows the amplitude envelopes for Type II reflectivity. There are no outstanding differences between the envelopes for the two values of σ for both *P*-wave and *S*-wave reflections. For *P*-wave reflections, there is an increase in amplitude as σ changes from 0.3 to 0.1 at an incidence angle of about 31° (trace 13). For *S*-wave reflections, however, there is a slight decrease in amplitude at approximately the incidence angle of 28° (trace 9) as σ changes from 0.3 to 0.1. However, the changes in amplitudes in either case are not large and may be difficult to detect on real data.

The above results indicate that the instantaneous amplitude is not particularly useful for detecting lateral changes in σ , except for the *P*-wave reflections of Type IA reflectivity. However, it may depend on the colour scheme used in plotting the amplitudes. If enough colours are used for a set of data with a large dynamic range, some of the amplitude changes as σ changes from 0.3 to 0.1 may be more visible.

5.4.2 Instantaneous phase

The instantaneous phase plots for Type IA reflectivity are shown in Figure 5.18. The phase plot for *P*-wave reflections with $\sigma = 0.1$ (Figure 5.18a) shows the corresponding anomaly that is observed on the amplitude envelope. Although there is no

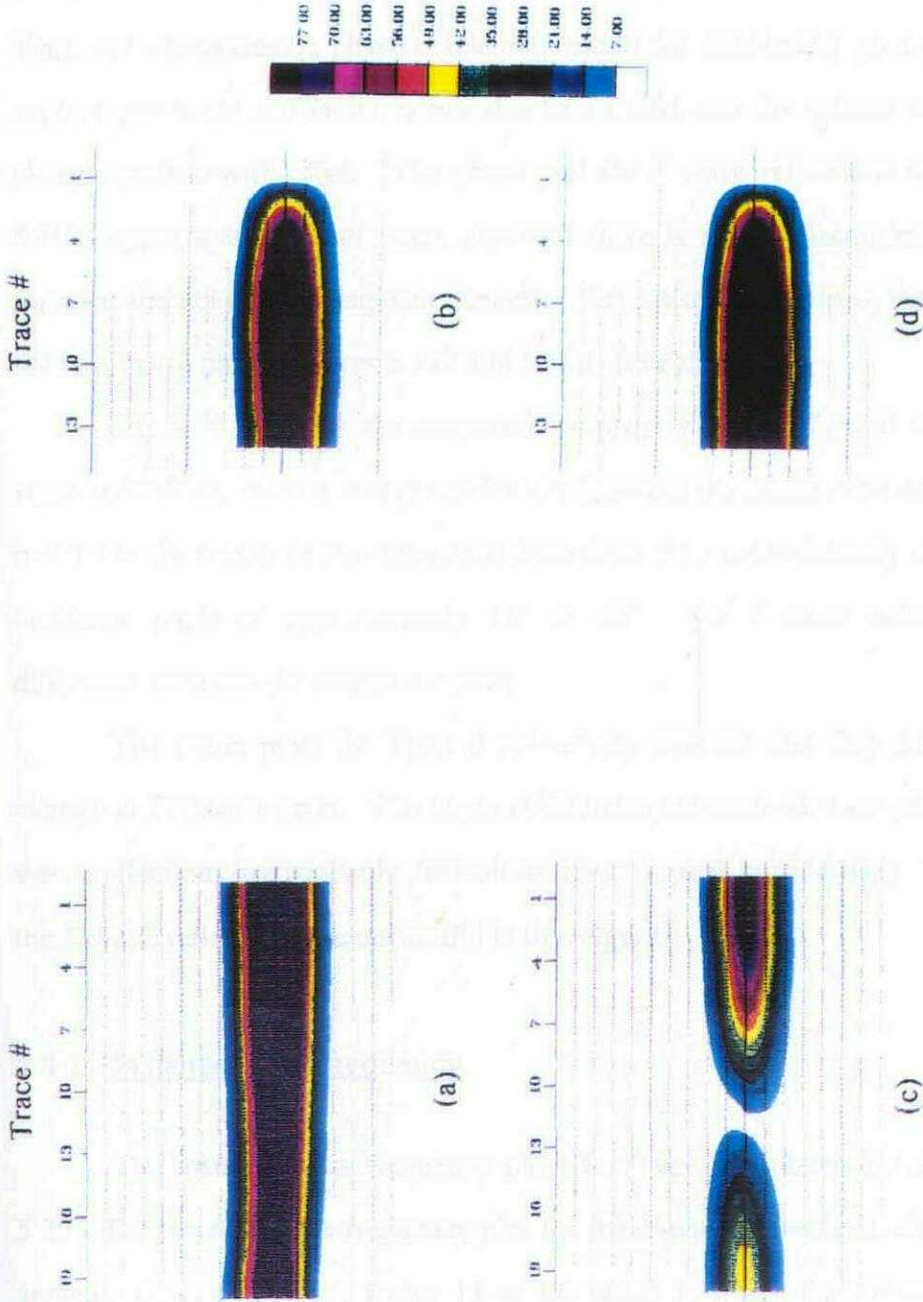


Figure 5.16 Instantaneous amplitudes for Type IA reflectivity at 5-m thickness: (a) P -wave, $\sigma = 0.3$; (b) S -wave, $\sigma = 0.3$; (c) P -wave, $\sigma = 0.1$; (d) S -wave, $\sigma = 0.1$. Timing lines are at 10-ms intervals.

discontinuity geologically, this phase plot shows several discontinuities. As mentioned in the last section, this is the region where both the *PP* and *PPPP* reflections change phase. Thus, the instantaneous phase is not only useful for delineating geological discontinuities such as pinchouts and faults, it can also be a useful tool for seismic anomalies showing a phase variation with offset. The phase plot for *P*-wave reflections with $\sigma = 0.3$ (Figure 5.18b) appears more continuous, although there is also a discontinuity in the far-offset traces at the tail of the composite wavelet. For *S*-wave reflections, the difference between the two phase plots (Figures 5.13c and 5.13d) is negligible.

Figure 5.19 shows the instantaneous phase plots for Type II reflectivities. For *P*-wave reflections, there is a slight difference between the phase plots between $\sigma = 0.3$ and $\sigma = 0.1$ at the onsets of the reflections from trace 7 to approximately trace 21, i.e. from an incidence angle of approximately 16° to 45° . For *S*-wave reflections, there is no difference between the two phase plots.

The phase plots for Type II reflectivity indicate that they are not sensitive to a change in Poisson's ratio. The slight differences between the two phase plots for the *P*-wave reflections are probably difficult to detect in real seismic data. The phase plots for the *S*-wave reflections are not useful in this regard.

5.4.3 Instantaneous frequency

The instantaneous frequency plots for Type IA reflectivity are shown in Figure 5.20. The instantaneous frequency plot for the *P*-wave reflections with $\sigma = 0.1$ shows an anomaly at approximately traces 11 to 13, which is where the *PP* and *PPPP* reflections change polarities. There are negative frequencies near this anomaly, which corresponds to the frequency anomalies shown in Figures 5.13a and 5.13b, and are absent in the frequency plot for $\sigma = 0.3$. However, in this latter plot, there is a phase inflection anomaly

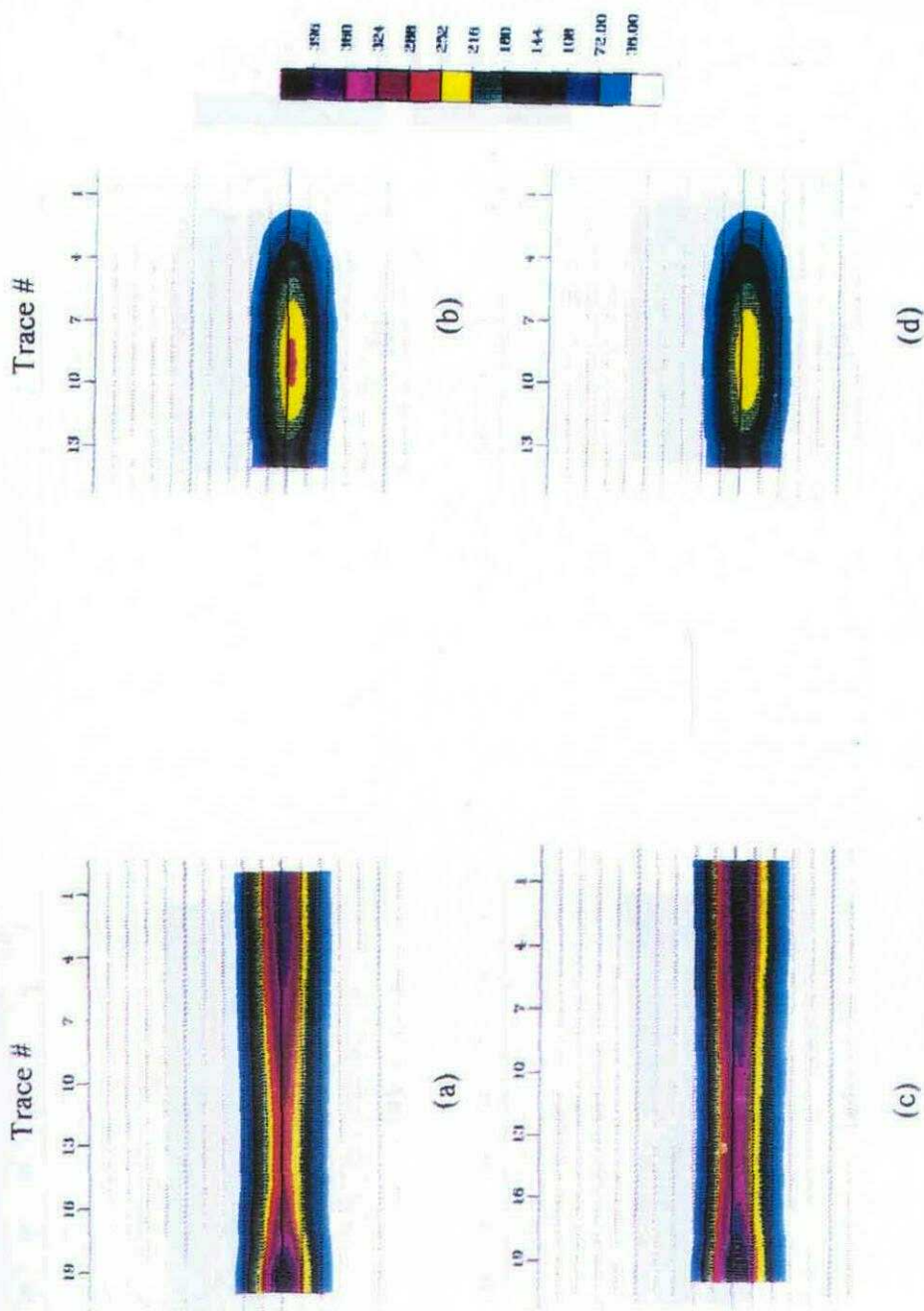


Figure 5.17 Instantaneous amplitudes for Type II reflectivity at 5-m thickness: (a) P-wave, $\sigma = 0.3$; (b) S-wave, $\sigma = 0.3$; (c) P-wave, $\sigma = 0.1$; (d) S-wave, $\sigma = 0.1$. Timing lines are at 10-ms intervals.

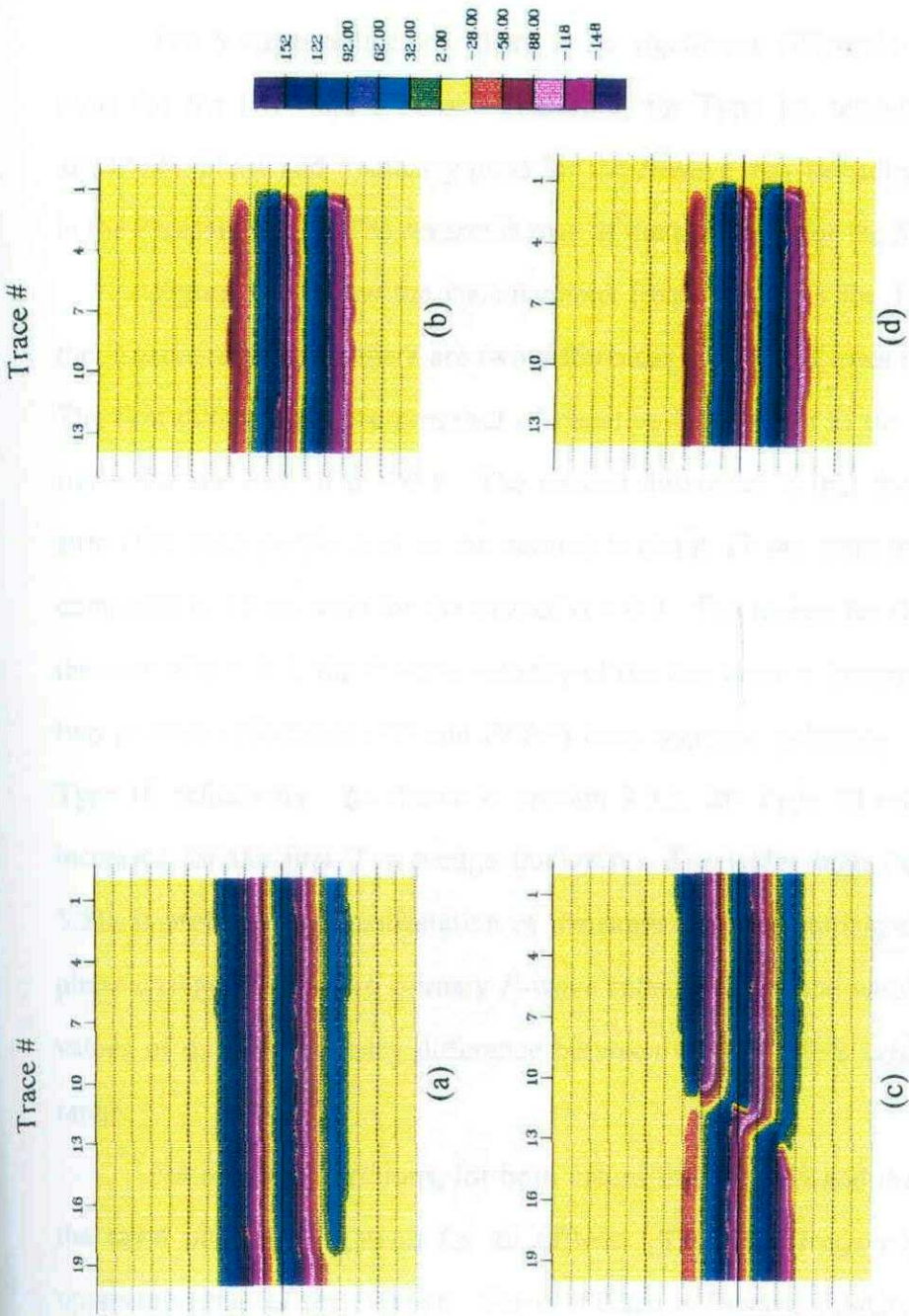


Figure 5.18 Instantaneous phases for Type IA reflectivity at 5 m thickness: (a) P -wave, $\sigma = 0.3$; (b) S -wave, $\sigma = 0.3$; (c) P -wave, $\sigma = 0.1$; (d) S -wave, $\sigma = 0.1$. Timing lines are at 10 ms intervals.

at the tails of the far-offset traces. The instantaneous frequency values here are also negative.

For S -wave reflections, there is no significant difference between the frequency plots for the two values of σ . Therefore, for Type IA reflectivity, the instantaneous amplitude, phase and frequency plots for the P -wave may be indicative of a lateral change in the Poisson's ratio. The reverse is true of the attributes for the S -wave reflections.

Figure 5.21 show the instantaneous frequency plots for Type II reflectivity. For the P -wave reflections, there are two differences evident between the two frequency plots. The first difference is the presence of negative frequencies at the onsets of the far-offset traces for the case of $\sigma = 0.1$. The second difference is that the central high-frequency strip (the deep purple area at the centre) is about 17 ms wide for the case of $\sigma = 0.1$ compared to 10 ms wide for the case of $\sigma = 0.3$. The reason for this difference is that, for the case of $\sigma = 0.1$, the P -wave velocity of the thin layer is lowered to a value so that the two primary reflections (PP and $PPPP$) have opposite polarities. This is equivalent to a Type III reflectivity. As shown in section 3.3.3, for Type III reflectivity, the frequency increases for the first 7 m wedge thickness. The wider high frequency strip in Figure 5.21b is probably the manifestation of the same frequency tuning effect. Since there is no phase change for the two primary P -wave reflections for the whole offset range for both values of σ , this frequency difference between the two plots exists for the whole offset range.

For S -wave reflections, for both values of σ , the PS and the $PPSS$ reflections have the same polarity (negative) for all offsets. Thus, the frequency effects observed are opposite to that of the P -wave. For $\sigma = 0.1$, the P -wave velocity is lowered so that the time thickness is corresponding larger than it is when σ is 0.3. Since PS and $PPSS$ reflections have the same polarity, the frequency will be lower as the time thickness of the

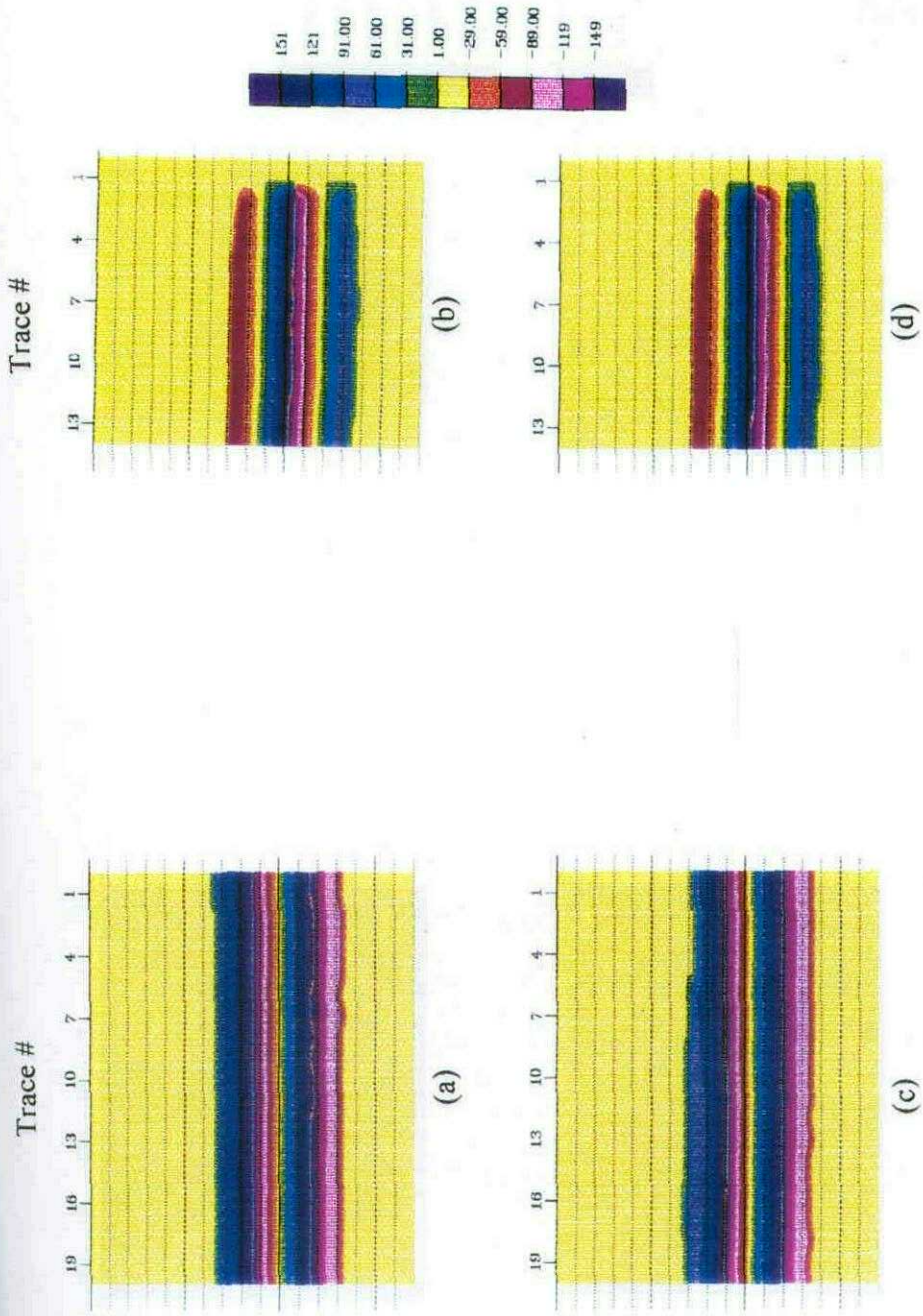


Figure 5.19 Instantaneous phases for Type II reflectivity at 5 m thickness: (a) P-wave, $\sigma = 0.3$; (b) S-wave, $\sigma = 0.3$; (c) P-wave, $\sigma = 0.1$; (d) S-wave, $\sigma = 0.1$. Timing lines are at 10 ms intervals.

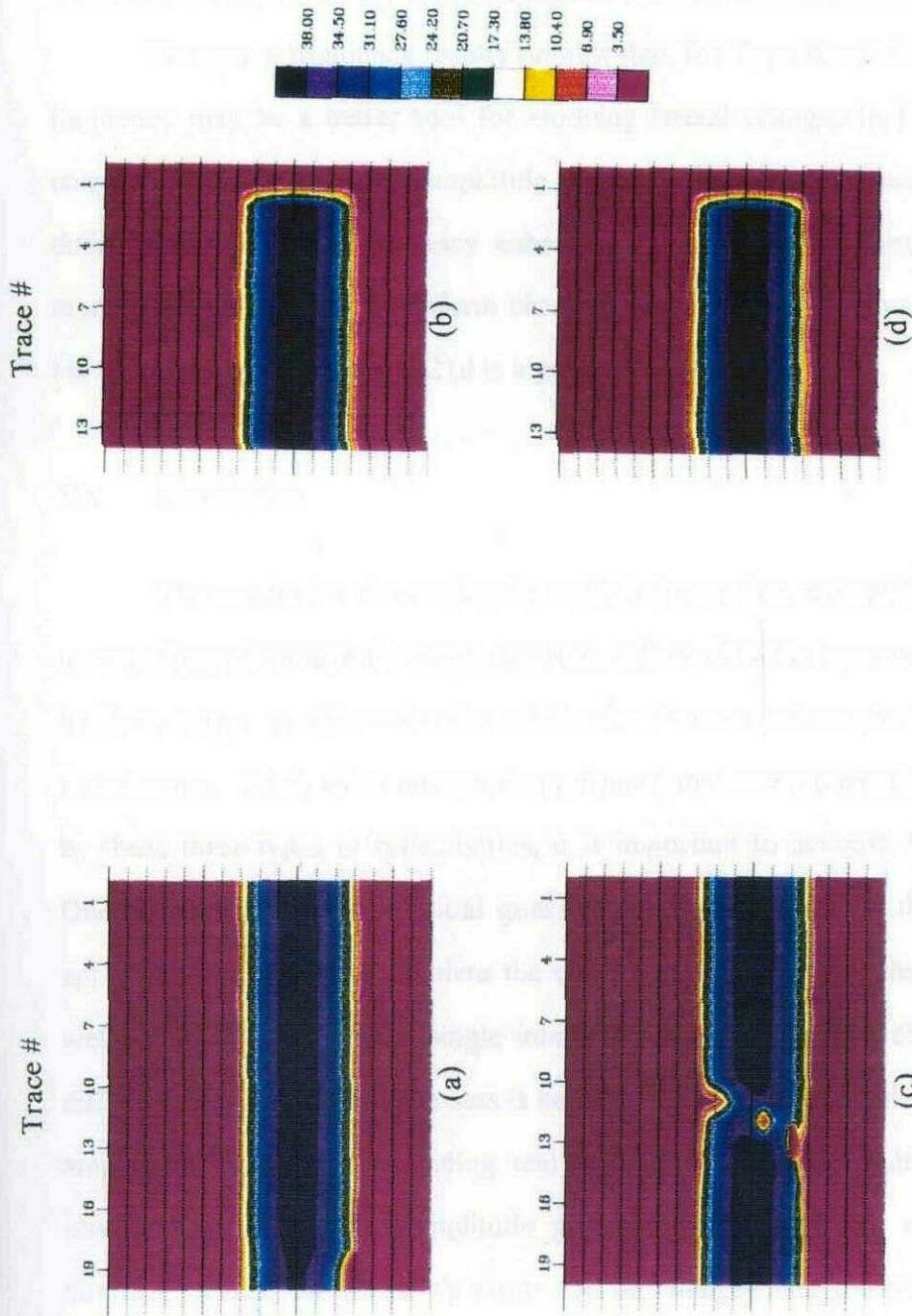


Figure 5.20 Instantaneous frequencies for Type IA reflectivity at 5 m thickness: (a) P-wave, $\sigma = 0.3$; (b) S-wave, $\sigma = 0.3$; (c) P-wave, $\sigma = 0.1$; (d) S-wave, $\sigma = 0.1$. Timing lines are at 10 ms intervals.

thin layer increases, as illustrated in section 3.3.4. This is what is observed in Figures 5.21c and 5.21d, where the high frequencies are more consistent when $\sigma = 0.3$.

The above frequency results suggest that, for Type II reflectivity, the instantaneous frequency may be a better tool for studying lateral changes in Poisson's ratio than the corresponding phase and amplitude plots. Since instantaneous frequency is the differentiation (a high-frequency enhancement operation) of instantaneous phase, it is more sensitive to subtle waveform changes than the instantaneous phase. The difference between Figures 5.21c and 5.21d is a good example.

5.5 Discussion

The results for the amplitude study indicate that, except for Type IA reflectivity, tuning effects dominate the single-interface effect when the layer is thin. The influence can be fairly large, as shown by the results for *P*-wave reflections of Type I, II, and IIA reflectivities. Thus, when interpreting seismic data from sequences that can be represented by these three types of reflectivities, it is important to account for the effect of tuning. One approach is to make initial guess at the Poisson's ratios, then forward model and apply equation (5.1) to calculate the change in amplitude for the thin bed reflections as well as for those from the single interface, i.e. the top interface of the thin bed. The difference between these data sets is attributable to tuning. If this difference is x , then the amplitudes of the corresponding real seismic data can be multiplied by $(1-x)$. If the resulting amplitudes and amplitude gradient differ from that of the modelled single-interface results, the Poisson's ratios can be changed and the modelling process can be repeated again. This procedure can be iterated until the chosen Poisson's ratios lead to agreement between the modelled single-interface amplitudes and the adjusted amplitudes

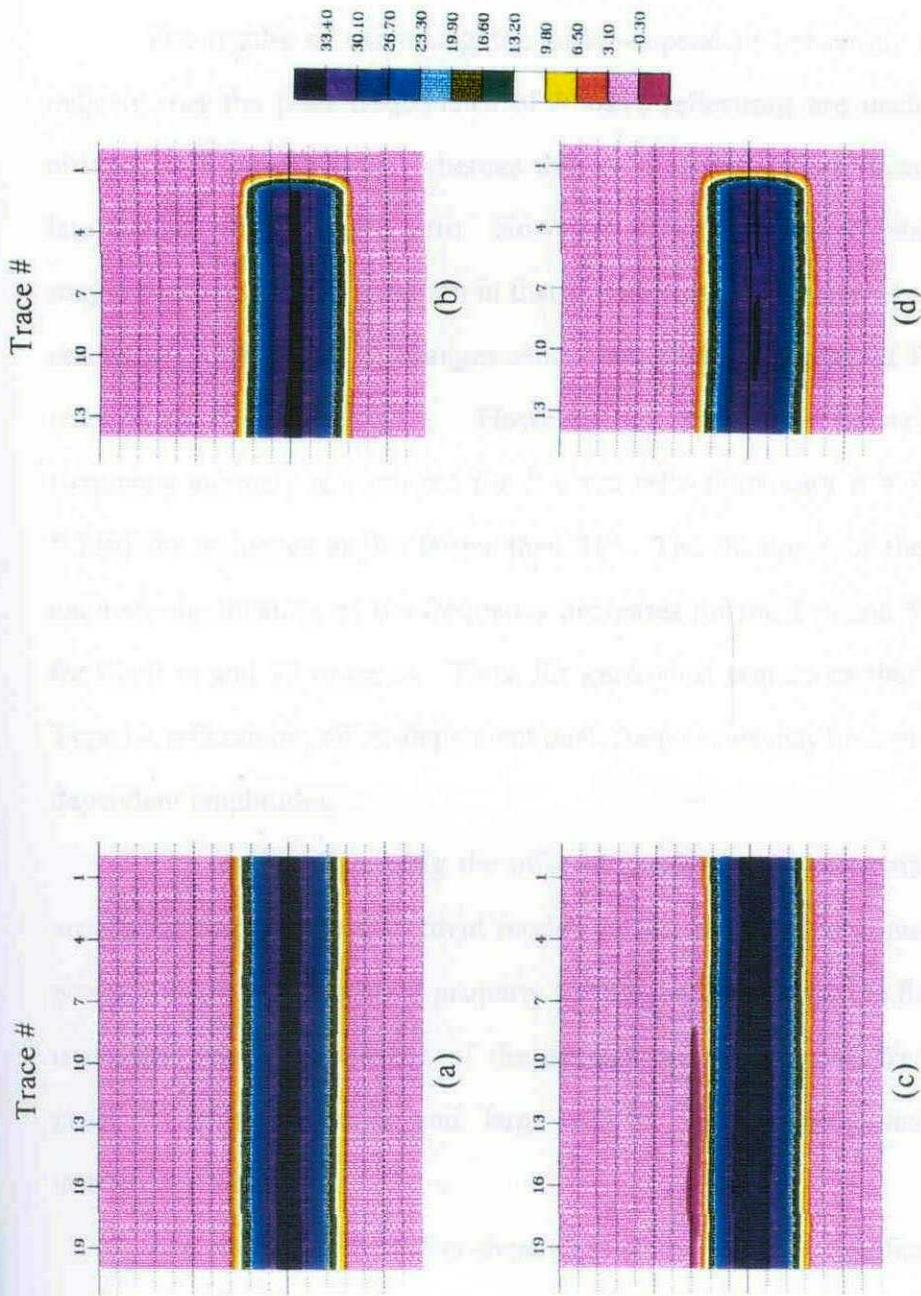


Figure 5.2.1 Instantaneous frequencies for Type II reflectivity at 5 m thickness: (a) *P*-wave, $\sigma = 0.3$; (b) *S*-wave, $\sigma = 0.3$; (c) *P*-wave, $\sigma = 0.1$; (d) *S*-wave, $\sigma = 0.1$. Timing lines are at 10 ms intervals.

of the data. The final values of the chosen Poisson's ratios can then be interpreted as representative values for the Poisson's ratios of the geological formations modelled.

The results of examining the offset-dependent behaviour of the peak frequency indicate that the peak frequencies of *P*-wave reflections are useful for revealing lateral changes in Poisson's ratio, whereas that of *S* wave are significantly less affected by a lateral change in Poisson's ratio. However, using both sets of peak frequencies together may lead to better interpretation in that if both sets of frequencies are equally affected, the reason is probably due to changes other than a lateral change of Poisson's ratio. This is true of all four reflectivities. However, for Type IA reflectivity, a most interesting frequency anomaly is observed for *P*-wave reflections with $\sigma = 0.1$ (Figures 5.13a and 5.13b) for incidence angles larger than 21° . The thickness of the thin layer affects this anomaly significantly, as the frequency decreases for the 1 m and 5 m cases, but increases for the 9 m and 13 m cases. Thus, for geological sequences that can be represented by Type IA reflectivity, offset-dependent peak frequencies may be more revealing than offset-dependent amplitudes.

The results of studying the offset-dependent complex attributes of several models are similar to the normal-incident models in that they are very much empirical tools. At present, their most important property for thin-bed interpretation for both types of models is perhaps the characteristics of the instantaneous phase and frequency, which exhibits phase inflection anomaly and large and/or negative frequencies for low-amplitude interference patterns.

The results for the offset-dependent study has some significant implications for the use of conventional common-depth-point (CDP) seismic sections in interpretation. The results of the study show that the amplitudes, frequencies, and phases of seismic reflections as a function of offset can undergo significant changes if there is a lateral change of Poisson's ratio from the location of one CDP to another. If the traces are

stacked as in a CDP stacked section, these changes will be smeared and may not be detectable.

The results in sections 5.2, to 5.4 also indicate that most of the significant changes occur for incidence angles larger than 25° . In exploring for gas reservoirs in clastics rocks in western Canada, much seismic data have been acquired with a maximum offset of less than 1500 m, resulting in a maximum incidence angle of 30° at the target depth of about 1000 m. Thus, if the data are 30 fold, only two or three traces may have incidence angles larger than 25° , and when the traces within a CDP are stacked together, any offset-dependent anomalies may disappear. This is probably one of the reasons why AVO analyses have not been particularly successful in exploring for clastic reservoirs in Cretaceous Formations in western Canada. In future exploration of these reservoirs, it would be beneficial to record longer offsets to ensure a maximum incidence angle of 35° or more.

In this offset-dependent study, four reflectivity series with specific velocities, densities, and Poisson's ratios are used. The conclusions drawn from these four models may not apply to similar reflectivities with reflection coefficients which are very different from the ones used in the models. However, the results from these four models do indicate the complexity of interpreting AVO anomalies for thin beds, and additional research is required to obtain a more general understanding of AVO behaviour in thinly bedded sequences.

Chapter 6 - Case studies

6.1 Introduction

In this chapter, two case studies using field seismic data are presented in which seismic properties of thin beds are investigated. The first case study is an interpretation of seismic data over a sandbar within a fluvial channel in southern Alberta, the emphasis being on the potential use of AVO and complex attributes. The second case study is an investigation of a sheet sand within a graben in central Alberta, concentrating on the behaviour of amplitude, peak frequency, and complex attributes as function of the thickness of the sand layer.

6.2 Sandbar example

In early 1986, Summit Resources Ltd. and Alberta Energy Company, both of Calgary, Alberta, acquired a seismic template in southern Alberta using a 3-km-long seismic line. The purpose was to investigate the seismic signature of the gas-bearing sandbar. Unfortunately, the well does not have a sonic log, so that no forward modelling could be performed directly using data from this well.

A 21-fold seismic line was acquired over the well in January, 1986. The seismic data revealed an identifiable anomaly across the well location, consisting of drape over the sandbar, phase reversal attributed to gas-saturated sands, and an apparent Mississippian low structure below the gas-bearing sands. The objective of the study is to investigate the seismic response of the channel-sand anomaly in terms of amplitude-versus-offset (AVO) effects and complex attributes as a function of source-receiver offset. Because of

confidentiality, all seismic shotpoint location numbers have been omitted, and the wells are referred to only symbolically.

6.2.1 Geological background

In general, the stratigraphy and regional setting in the area under study are very similar to those in the Little Bow area of southern Alberta, as discussed by Hopkins *et al.* (1982). Figure 6.1 shows an informal stratigraphic column for the study area. The Upper Mannville Glauconitic Member is represented by two lithofacies, (a) a regional sequence, and (b) channel features which are shale and sand-filled. The regional sequence consists of a shoaling-upward cycle from the Ostracod limestones and Bantry shales; the shoaling sequence carries through to delta plain carbonaceous shales and coals. Delta-front sands and localized shore face sands within the regional sequence can form thin reservoirs if trapping by channel truncation and/or sufficient structural reversal occurs. The entire sequence from the Ostracod limestone to delta-plain sediments is rarely more than 40 m in thickness. Following the deposition of the regional sequence, a series of major channels down-cut through it and generally, but not always, also through the underlying Ostracod and Bantry Members. Within the channels, large, discrete bars of varying thicknesses were deposited which can completely fill the channel with clean, medium-to-coarse-grained quartzose sand. The sand bars can be up to 40 m thick with an areal extent of up to 2.5 km².

The subject well penetrated a 40-m channel section which had completely eroded the Ostracod/Bantry section. The channel fill consists of a basal sand, 21 m thick, over which lies 18 m of silty/sandy shale and a 1-m layer of carbonaceous shale which caps the entire channel-fill sequence. Logs indicate that the sand bar has an average porosity of 23

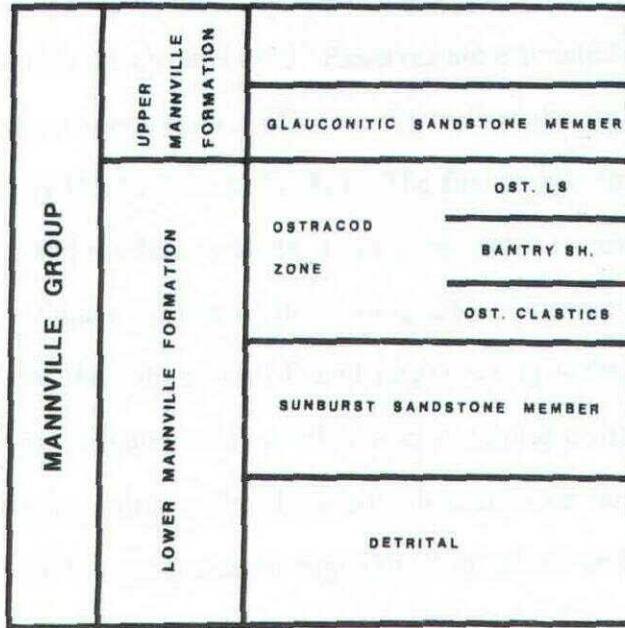


Figure 6.1 Informal stratigraphic column for the study area modified after Glaister (1959) and Energy Resources Conservation Board (1978).

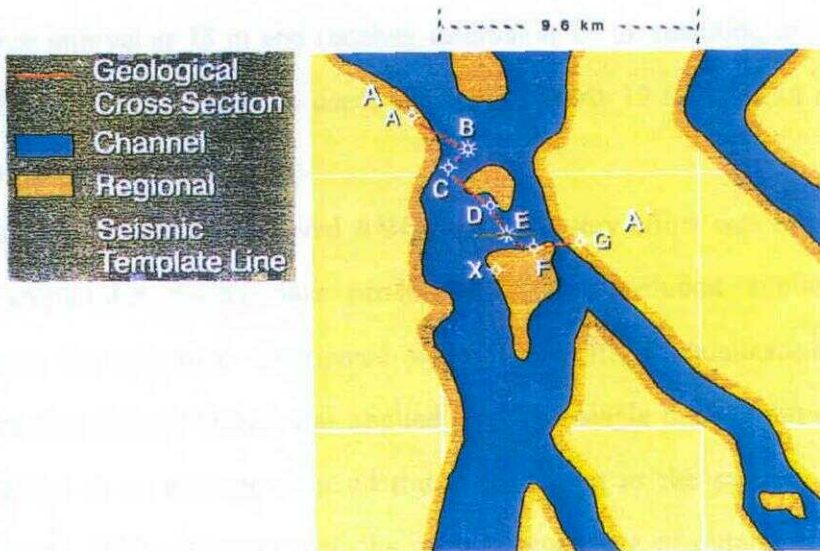


Figure 6.2 Interpreted Glauconitic channels in the study area.

percent. Production testing and log analysis indicate that 8 m of gas pay are present above a 13-m water leg within the channel sand. Reserves are estimated at five billion cubic feet.

The subsurface interpretation of channel trends in the study area is based on two steps, as discussed by Hopkins *et al.* (1982). The first step is to map the absence of the Ostracod limestone and the Bantry shale, and the second is to map channel-filled deposits from various logs. Figure 6.2 shows the geologically interpreted channel position in the area, the locations of the subject well E and neighbouring wells, and the location of the template seismic line. Figure 6.3 is a schematic structural cross-section through well E and some of the neighbouring wells. It clearly illustrates the sand-channel event through the subject well, with the porous sands highlighted in yellow and the gas-producing zone in red.

6.2.2 Geophysical background

The seismic line was acquired with *P*-wave vibrators as the energy source, and recorded with 128 traces per record. A spread of 1600-25-0-25-1600 m was employed, with source interval at 75 m and receiver interval at 25 m, resulting in 21-fold data. Four Mertz vibrators over 32 m were used, sweeping linearly 12 times at 14 seconds each time, with frequency 13 to 75 Hz.

Because the study involved AVO analysis, every effort was made to preserve true relative amplitudes during data processing. This included application of gain to compensate for spherical divergence without any trace equalization. Also, surface-consistent shot deconvolution was applied (i.e., one single deconvolution operator, which was obtained as an average over all traces belonging to the same shot, was applied to those traces.) This contrasts with the normal procedure of obtaining one deconvolution operator for each trace and applying it to that trace alone. The surface-consistent

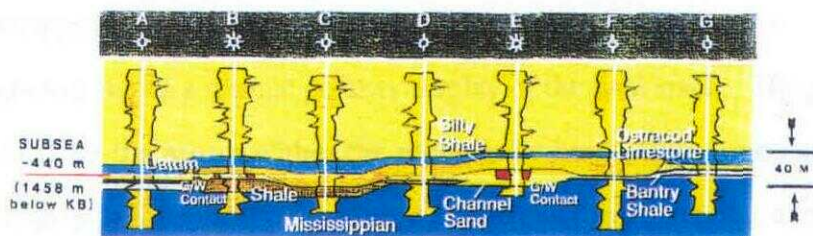


Figure 6.3 Schematic structural cross-section A-A' (Figure 6.2). The logs (gamma on the left and sonic on the right) are generalized and are plotted for aesthetic purpose only.

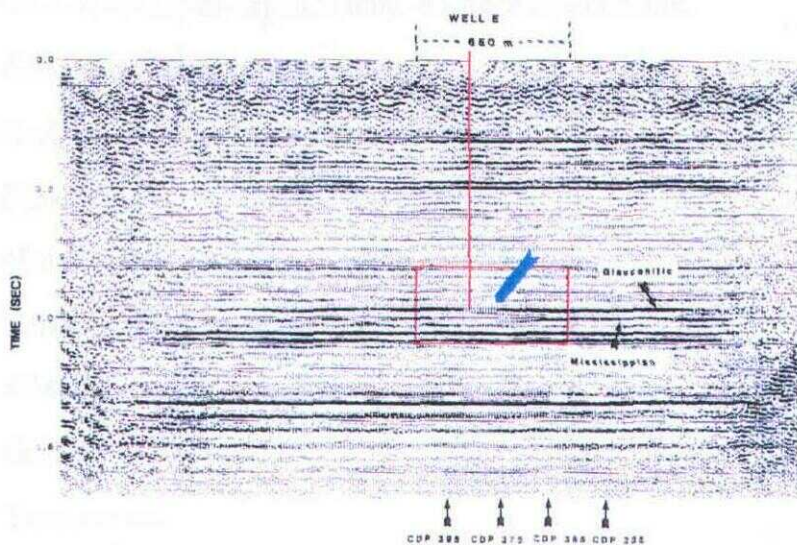


Figure 6.4 Final full-offset stack of the seismic line. The gas sandbar anomaly is indicated inside the rectangle. The Glaucconitic reflection is a trough along the top of the sandbar and is a peak in off-sand bar areas.

deconvolution was an attempt to preserve the amplitude characteristics for each wavelet corresponding to each shot. After stacking, long-window rms (root-mean-square) scaling was applied to each trace to ensure that the rms amplitudes did not significantly differ from trace to trace. Table 6.1 summarizes the processing flow.

Figure 6.4 shows a normal polarity display of the final stack. The gas-bearing sand bar is indicated by the arrow within the rectangular box. Here, one can observe drape over the gas sands, phase reversal probably due to their low velocity, and a Mississippian low. Moreover, the amplitudes of the peaks along the drape above the sand bar decrease over the sand bar, while the reversal also shows clear amplitude variations. In the next two sections, this anomaly will be analyzed in terms of AVO effects and complex attributes.

Table 6.1 Processing steps for seismic template line.

-
1. Demultiplex,
 2. Gain-spherical divergence only, no trace equalization,
 3. Geophone phase compensation,
 4. Surface-consistent shot deconvolution,
 5. Elevation and weathering corrections,
 6. NMO correction - first pass,
 7. Surface-consistent statics,
 8. NMO correction - second pass,
 9. Gather,
 10. Trim statics,
 11. Stack - 21 fold,
 12. Filter - band-pass, 10/15-75/85 Hz,

13. Scaling - multiple window, 50-350 ms, 350-1600 ms.

6.2.3 Amplitude variation with offset analysis

To investigate the AVO effects of the gas-bearing sand bar, two partial stacks were generated, namely a near-offset stack (offset range from 0 to 1050 m), and a far-offset stack (offset range from 1050 to 1600 m). For the zone of interest, after first-break muting, the full-offset stack and the near-offset stack are 16-fold and 8-fold, respectively.

Figures 6.5a, b, and c show the seismic anomaly (boxed) for full-offset, near-offset, and far-offset stacks, respectively. These stacks correspond to the data within the rectangular box in Figure 6.4. The anomaly appears to be significantly different on the near-offset stack from that on the far-offset stack, and, as expected, the full-offset stack is the average of the other two. The anomaly in the near-offset stack (Figure 6.5b) has a distinct phase reversal signature, and drape over the sand bar is also very evident in this stack. However, the apparent delay in the Mississippian event that is clear on both the full-offset and far-offset stacks (Figures 6.5a and 6.5c) does not appear in the near-offset stack (Figure 6.5b). This is interpreted to be due to changes in interference pattern because of changes in apparent time thickness as a function of offset. In the far-offset stack, the anomaly appears to be very broad and lower-frequency, without showing any overlying drape nor clear reversal character.

To explain the differences between the various stacks in Figure 6.5, an analysis was taken to investigate the possibility that the differences are caused by a lateral change in Poisson's ratio. Since low-velocity gas-saturated sands have relatively low Poisson's ratio, they often show up as amplitude anomalies when the corresponding seismic data are displayed in some offset-dependent format such as CDP gather panels (Ostrander, 1984).

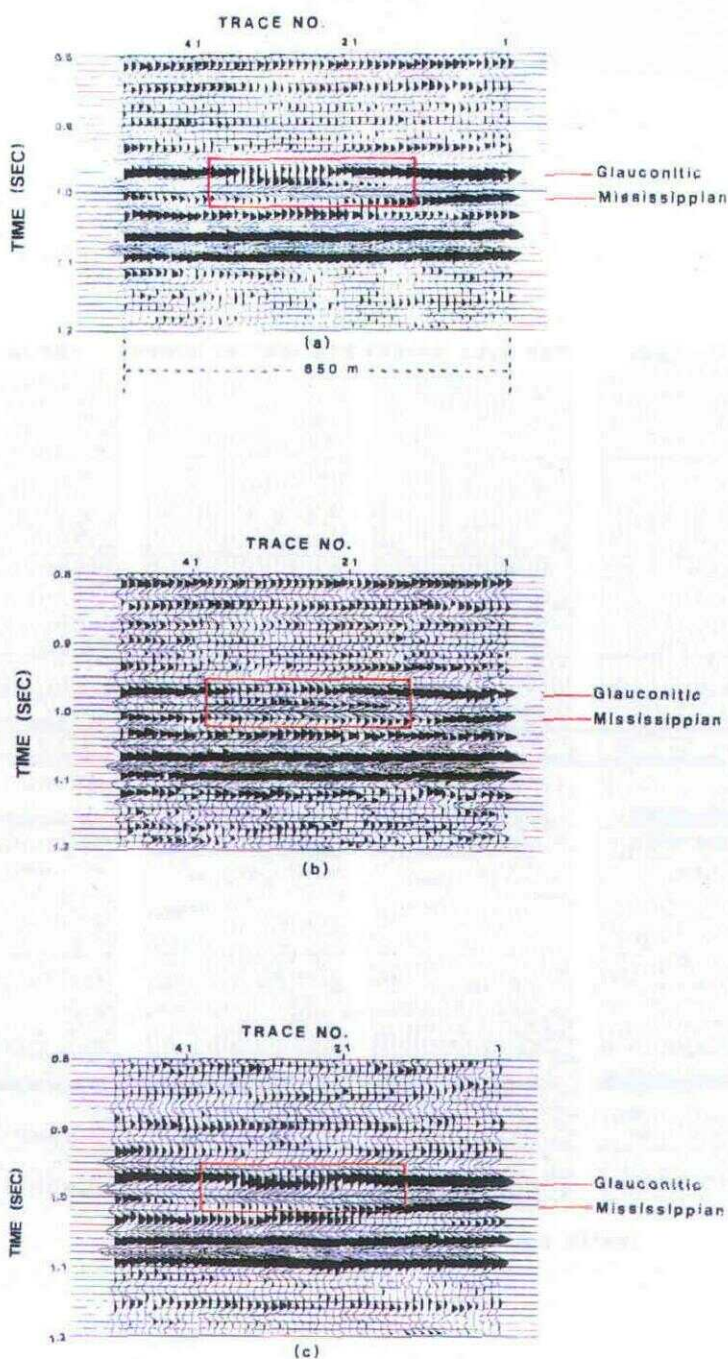


Figure 6.5 (a) Full-offset stack (21-fold) of seismic anomaly with normal polarity (P -wave velocity increases correspond to peaks). The offset covers a distance of 0 - 1600 m. (b) Near-offset stack (8-fold) of seismic anomaly with normal polarity. The offset covers a distance of 0 - 1050 m. (c) Far-offset stack (8-fold) of seismic anomaly with normal polarity. The offset covers a distance of 1050 - 1600 m.

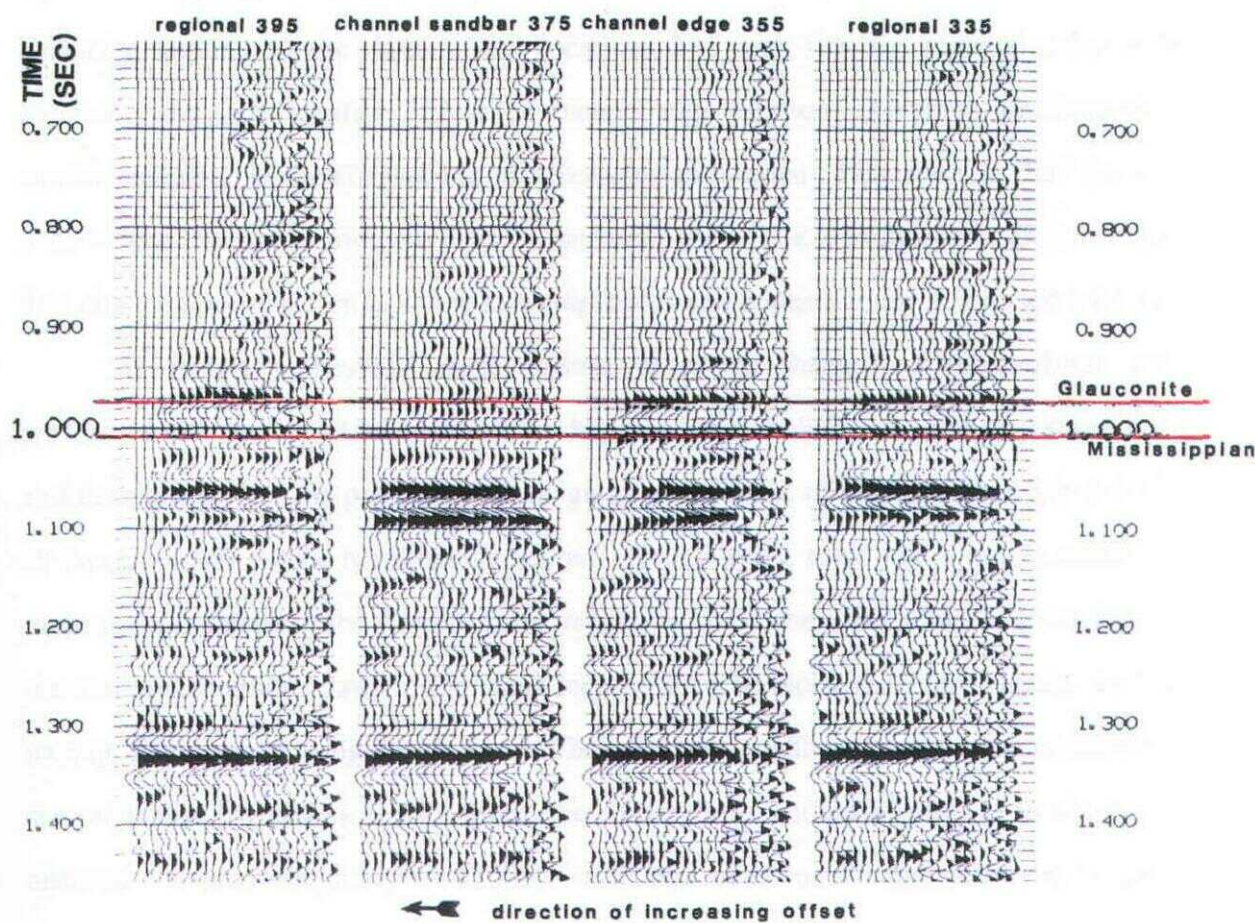


Figure 6.6 Ostrander gather, summing over 6 CDP locations and three-offset range with no trace-balancing.

Figure 6.6 shows the Ostrander gather (Ostrander, 1984) for four CDP locations along the seismic template line. To obtain the gather, six CDP panels across each location are summed with a range of three offsets for each output trace, so that each trace on the Ostrander gather in Figure 6.6 is the sum of eighteen traces. This effectively smears the reflections over six CDP locations (62.5 m) for an offset range of 75 m. However, the signal-to-noise ratio is enhanced by a factor of four. Note that there has been no trace balancing applied to the data. CDP locations 335 and 395 are regional off-channel locations, and CDP location 355 is the channel-edge location. All three locations show similar character at the Glauconitic to Mississippian interval. However, at CDP location 375, where the gas-bearing sand bar is situated, there is a significantly different result. The Glauconitic reflection has very low amplitudes and appears to have reversed polarity.

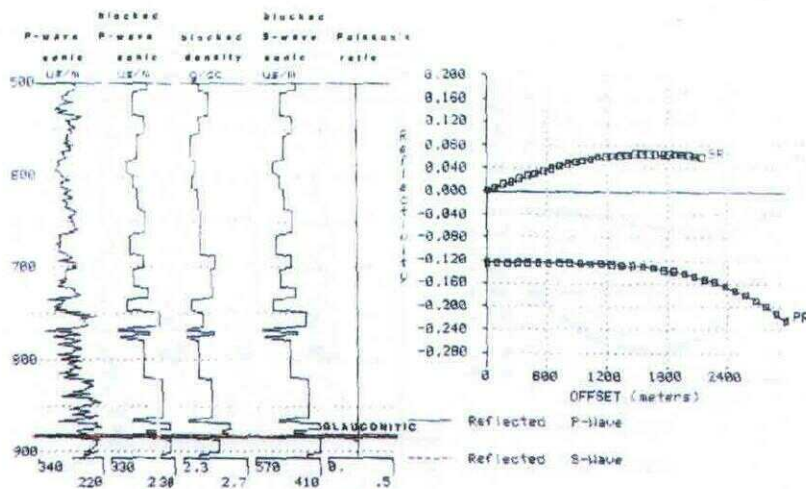
To better understand these seismic character changes, AVO analyses were performed using an industrial software package. In this analysis, one inputs the sonic log and density log, and the program will assign an initial value of 0.25 for Poisson's ratio for all layers, which can be modified as desired. If an *S*-wave sonic log is not available, the program will calculate the *S*-wave sonic responses using the input *P*-wave sonic log and the assumed Poisson's ratio. The input logs have to be blocked to form layers, and ray tracing is performed using Snell's Law. The reflection coefficients of the layers' interfaces are calculated by solving the Zoeppritz equations for specified offsets up to the critical distance. A peak frequency of 31 Hz, which was observed on the seismic data, and a maximum offset of 3000 m were used in all the AVO synthetic gathers. For each well chosen for AVO analysis, two synthetic gathers were generated. The first is an NMO-corrected synthetic gather, where ray tracing is first performed, and then NMO correction is applied; the second is a pseudo-zero-offset synthetic gather. In this gather, for each trace location, the Ricker zero-phase wavelet is convolved with the zero-offset reflectivity time series, but with offset-dependent amplitudes calculated from the Zoeppritz equations.

This allows investigation of AVO effects, as predicted by the Zoeppritz equations, without the interference of offset-dependent thin-bed tuning and NMO stretch.

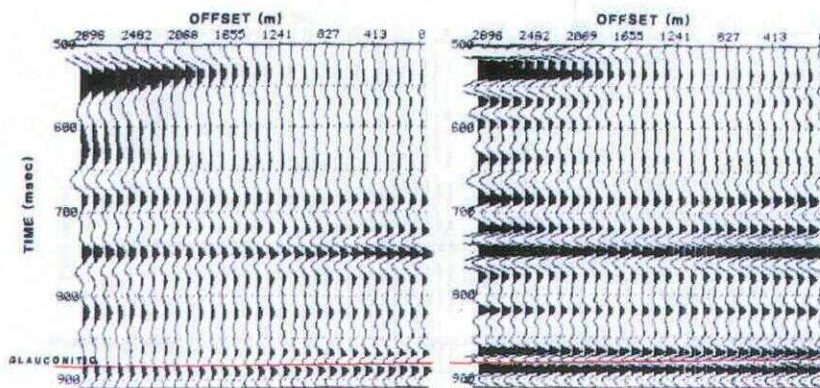
The wells chosen for AVO analysis are labelled B, C and F in Figure 6.2; well B is a Glauconitic channel gas well; well C is a Glauconitic channel shale well (also a gas well from another formation), and well F is a Glauconitic regional well. All three wells have *P*-wave sonic logs and density logs only. Well B has lithologies similar to those of the subject well E, but since well E does not have a sonic log, the thicknesses of the two lithological units in the Glauconitic Member in well B were modified to the corresponding thicknesses as in well E. Figure 6.7 shows the results of the AVO modelling on this modified sonic log with the Poisson's ratio equal to 0.1 for the gas-bearing channel facies and 0.25 elsewhere. These values are often associated with gas sands (0.1) and nonporous sands (0.25) as discussed by Domenico (1976, 1977, 1984). The *P*-wave reflection coefficients at the top of the channel facies are negative because of the low-velocity porous sands and do not change appreciably for offsets less than 2000 m. The corresponding NMO-corrected synthetic seismogram (Figure 6.7b) shows some noticeable amplitude changes at an offset of 1800 m or larger. NMO-stretch effects are observable beyond about 2400 m. In comparison, the pseudo zero-offset seismogram (Figure 6.7c) reveals hardly any amplitude changes.

Figures 6.8a, 6.8b, and 6.8c are the models for well C, which encountered channel-fill silty shale. The *P*-wave reflection coefficients (Figure 6.8a) for the top of Glauconitic Member are positive and start to change significantly only for offsets greater than 2400 m. Both the NMO-corrected synthetic seismogram (Figure 6.8b) and the pseudo zero-offset synthetic seismogram (Figure 6.8c) reveal insignificant amplitude changes as a function of offset.

Figures 6.9a, 6.9b, 6.9c are the models for F, which is a Glauconitic regional well. The *P*-wave reflection coefficients (Figure 6.9a) show a similarity to those from well C.



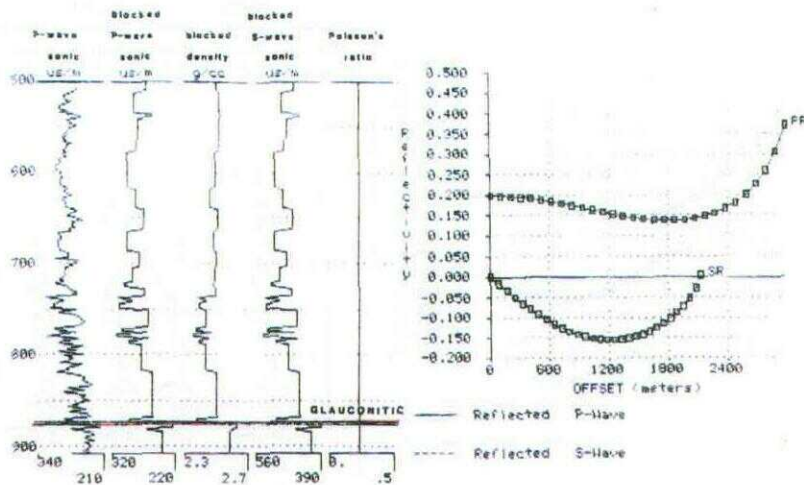
(a)



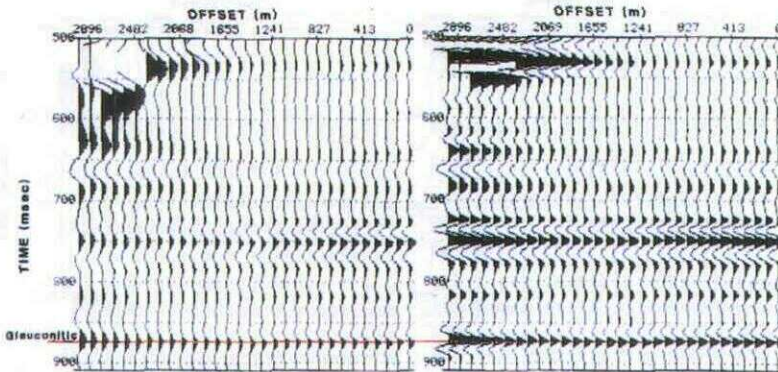
(b)

(c)

Figure 6.7 (a) Reflection coefficients versus offsets for the Glauconitic Member in modified well B. The left-hand side shows the logs from the well with the Poisson's ratio equal to 0.1 for the Glauconitic Member and 0.25 for all other formations. (b) NMO-corrected synthetic seismogram, and (c) pseudo-zero-offset synthetic seismogram for well B.



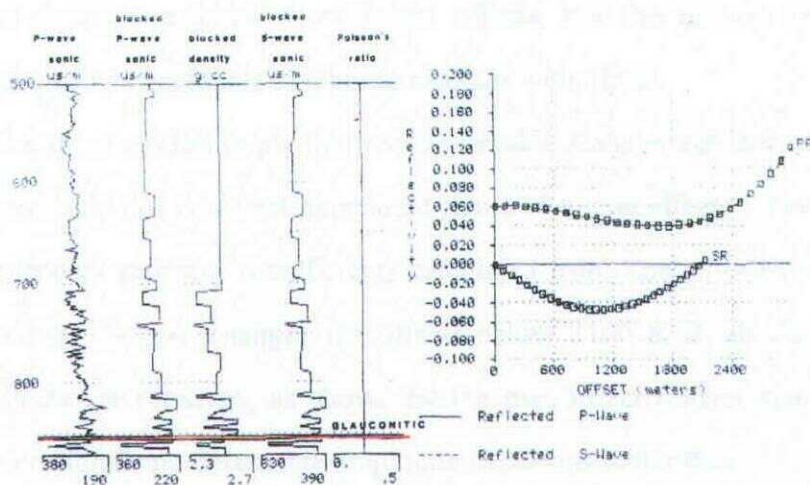
(a)



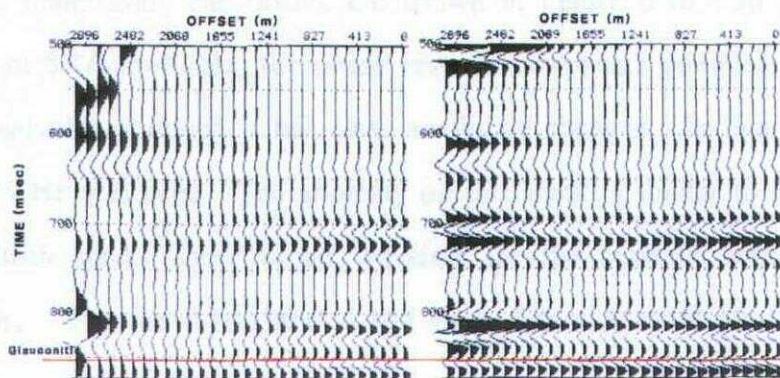
(b)

(c)

Figure 6.8 (a) Reflection coefficients versus offsets for the Glauconitic Member in the channel shale well C. The left-hand side shows the logs from the well with the Poisson's ratio equal to 0.25 for all formations. (b) NMO-corrected synthetic seismogram, and (c) pseudo-zero-offset synthetic seismogram for well C.



(a)



(b)

(c)

Figure 6.9 (a) Reflection coefficients versus offsets for the Glauconitic Member in the regional well F. The left-hand side shows the logs from the well with the Poisson's ratio equal to 0.25 for all formations. (b) NMO-corrected synthetic seismogram, and (c) pseudo-zero-offset synthetic seismogram for well F.

The two synthetic seismograms (Figures 6.9b and 6.9c) show similar results to those of Figures 6.7b and 6.7c. The NMO-corrected synthetic seismograms show some significant amplitude changes at 1800 m or larger offsets, but the pseudo zero-offset synthetic seismogram shows negligible amplitude changes with offset.

The three models imply that any observable AVO effects for offsets of 2100 m or less are probably due to offset-dependent thin-bed tuning effects. The magnitudes of the offset-dependent reflection coefficients calculated from Zoeppritz equations do not show any significant *P*-wave changes for offsets below 2100 m in all cases. Once thin-bed tuning effects are removed, as shown by the pseudo-zero-offset synthetic seismograms, there are no significant detectable amplitude variations with offset.

Since the near-offset stack (Figure 6.5b) appears to have a higher frequency content than the far-offset stack (Figure 6.5c), a filter panel analysis of the near-offset stack was undertaken; the results are shown in Figure 6.10. In Figure 6.10a, for a bandpass of 8/16-35/40 Hz, the phase reversal disappears completely, and the drape is barely observable although it has clear amplitude changes. In Figure 6.10b, a filter of 8/16-40/45 Hz was used. The anomaly on this stack is similar to that in the far-offset stack. Both stacks show broad wavelets for the anomaly with apparently similar bandwidths. Figures 6.10c and 6.10d have filters 8/16-45/50 Hz and 8/16-50/55, respectively. They indicate that when frequencies higher than 45 Hz are present in the data, the near-offset stack starts to develop the distinct character for the anomaly. The results imply that the differences in the anomaly as it appears in the near-offset and far-offset stacks can be partly attributed to a lower frequency content of data in the far-offset stack.

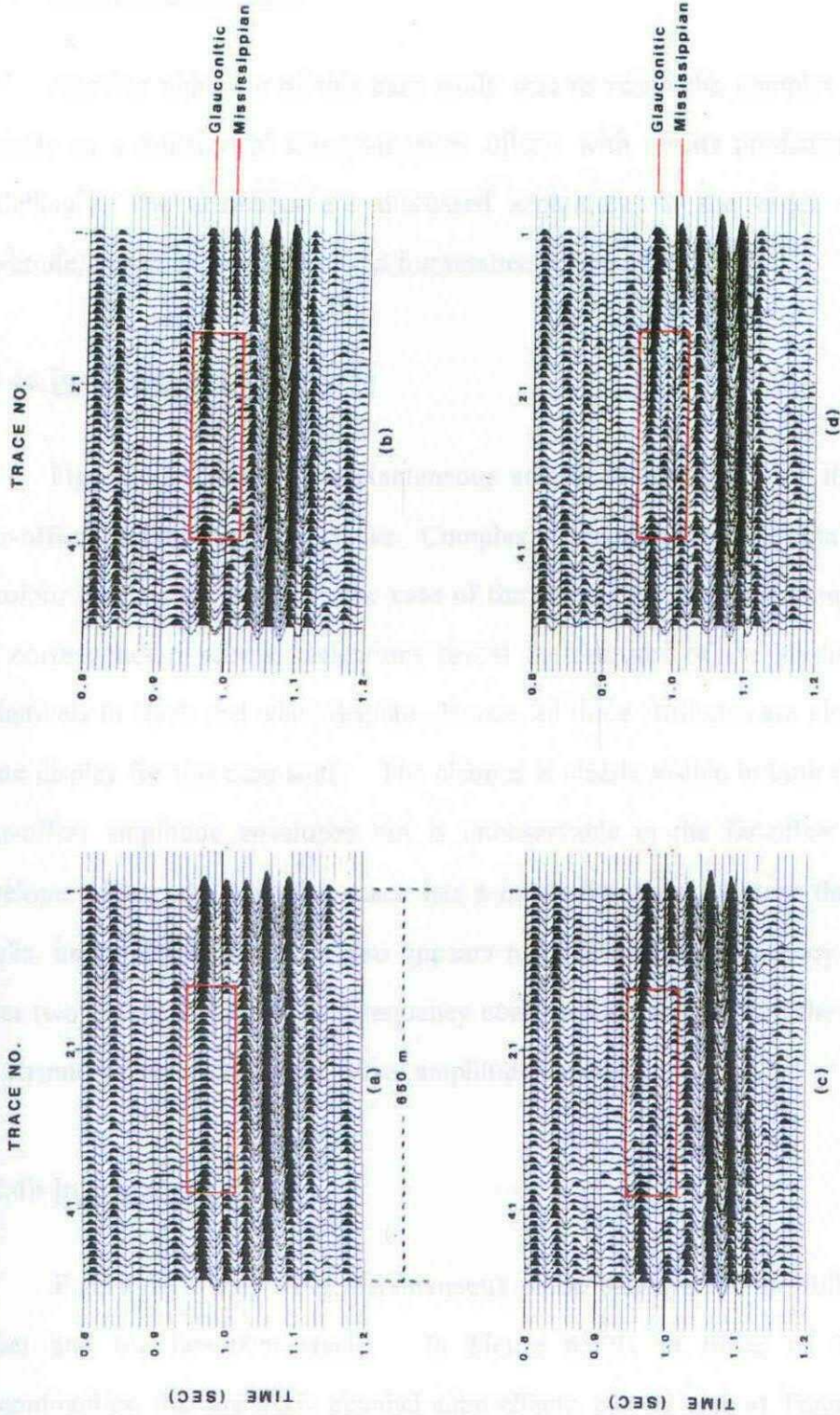


Figure 6.10 Near-offset stack (0 - 1050 m) with a band-pass filter of (a) 8-16/35-40 Hz and, (b) 8-16/40-45 Hz, (c) 8-16/45-50 Hz, and (d) 8-16/50-55 Hz.

6.2.4 Complex attributes

Another objective of this case study was to relate the complex attributes of the anomaly as a function of source-receiver offsets with results predicted from numerical modelling. The attributes are discussed separately, in the order of instantaneous amplitude, instantaneous phase, and instantaneous frequency.

6.2.4a Instantaneous amplitude

Figure 6.11 show the instantaneous amplitude envelopes for the full-offset, the near-offset, and the far-offset stacks. Complex attributes of seismic data are often plotted in colour displays, however, in the case of the studied sandbar, the complex attributes of the corresponding seismic reflections reveal the features of the studied sandbar more definitively in black and white display. Hence, all three attributes are plotted in black and white display for this case study. The channel is clearly visible in both the full-offset and near-offset amplitude envelopes but is unobservable in the far-offset stack amplitude envelope. Since the far-offset stack has a lower frequency content than the other two stacks, its amplitude envelope also appears to have a lower frequency content than the other two envelopes: the lower frequency content may have caused the disappearance of the channel signature in the far-offset amplitude envelope.

6.2.4b Instantaneous phase

Figure 6.12 shows the instantaneous phase displays for the full-offset, the near-offset and the far-offset stacks. In Figure 6.12b, at times of 0.98 to 1.0 ms, discontinuities, that are likely channel-edge effects, can be seen at Trace 18 and between Traces 61 and 81. They are interpreted as effects of laterally accreted sands that are often

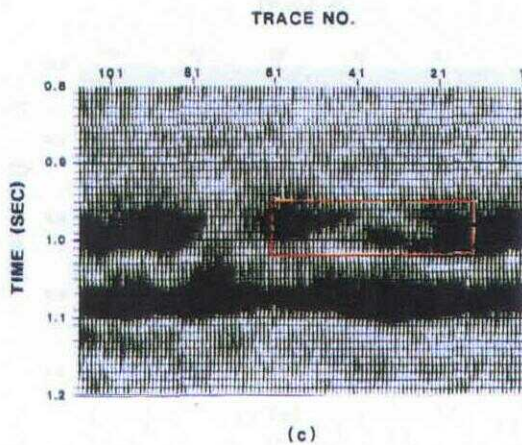
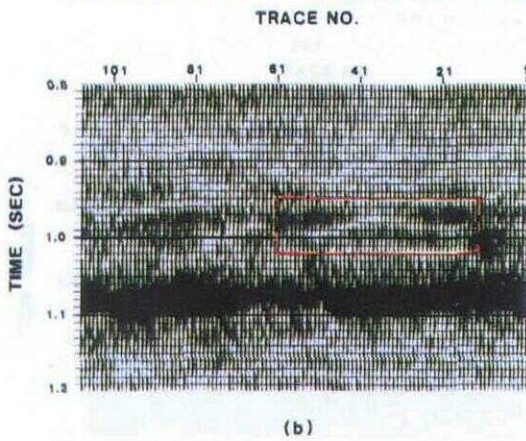
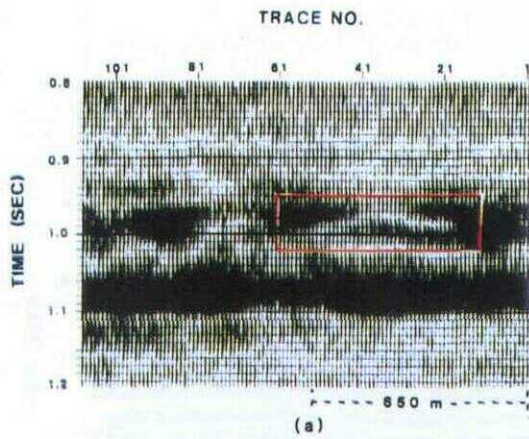


Figure 6.11 The instantaneous amplitude plot of the sandbar anomaly for the (a) full-offset stack (0 - 1600 m), (b) near-offset stack (0 - 1050 m), and (c) mid-offset stack (1050 - 1600 m).

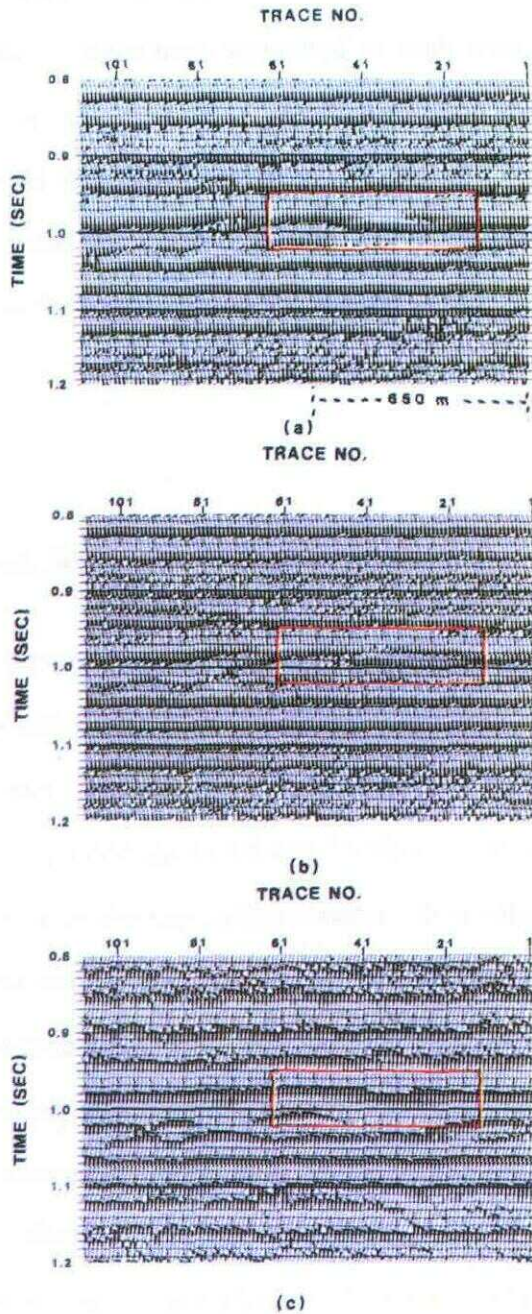


Figure 6.12 The instantaneous phase plot of the sandbar anomaly for the (a) full-offset stack (0 - 1600 m), (b) near-offset stack (0 - 1050 m), and (c) mid-offset stack (1050 - 1600 m).

associated with channel edges. However, the channel anomaly is not detectable in the far-offset instantaneous phase plot (Figure 6.12c), nor are there any channel-edge effects visible. The event at about 1.020 s between Traces 48 and 68 on the far-offset phase plot (Figure 6.12c) appears to have been truncated at both ends and exhibits some overlying drape. However, the corresponding event in the near-offset phase plot is rather continuous. This event is probably related to reflections from the Mississippian surface which occurs 30 ms after the channel event. Given the differences in the Mississippian reflection character in the near-offset range and far-offset range stacked sections (Figures 6.5b and 6.5c), it is not surprising that the corresponding instantaneous phase plots also exhibit differences.

6.2.4c Instantaneous frequency

Figure 6.13 shows the instantaneous frequency plots for the full-offset, the near-offset, and the mid-offset stacks, respectively. For this attribute, only the near-offset instantaneous frequency plot (Figure 6.13b) shows the sandbar anomaly unequivocally, with a dipping event between traces 19 and 50 about 0.98 s. This dipping event appears to outline the structure of the top of the sandbar. It is virtually absent on the other two frequency plots. This implies that, among the three attributes, the instantaneous frequency is the best tool to outline the sandbar anomaly. This is probably true whenever a thin bed is involved. Robertson and Nogami (1984) reported that as a bed thins to a quarter period, there is an anomalous increase in instantaneous frequency, which remains high as the bed continues to thin. This agrees with Widess's (1983) conclusion that when the bed thins to $1/8$ of the predominant wavelength, the wavelet shape will assume the shape of its derivative and remain constant until the thickness approaches zero, while its amplitude will also decrease to zero. As mentioned earlier, the sandbar under study is only 8-m thick and

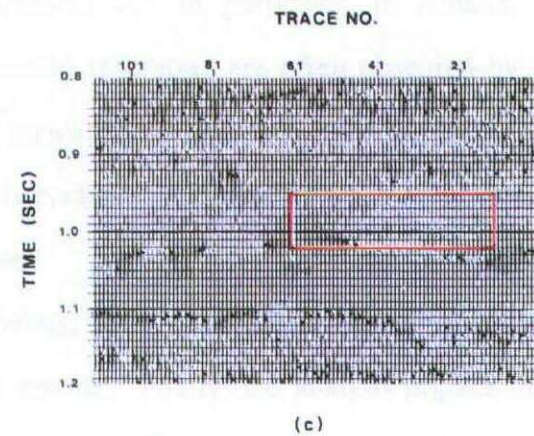
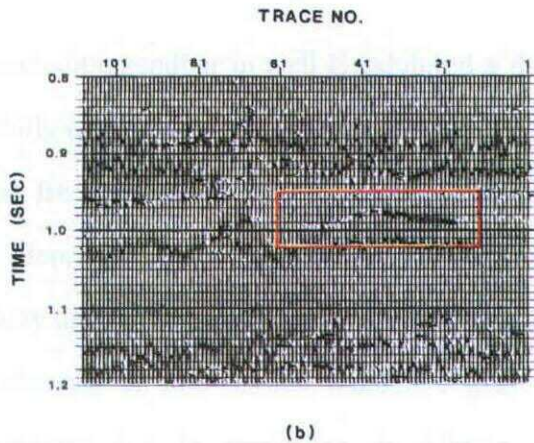
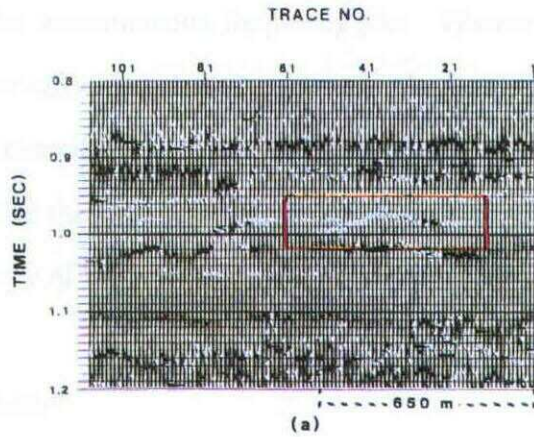


Figure 6.13 The instantaneous frequency plot of the sandbar anomaly for the (a) full-offset stack (0 - 1600 m), (b) near-offset stack (0 - 1050 m), and (c) mid-offset stack (1050 - 1600 m).

is below tuning thickness (assuming a peak frequency of 40 Hz and a Glauconitic sand velocity of 3700 m/s, which gives a tuning thickness of 23 m). Hence, it should be detectable in the instantaneous frequency plot. However, the gas-sand anomaly appears only in the near-offset stack instantaneous plot, not in the other two frequency plots. Obviously, the instantaneous frequency attribute is very sensitive to the frequency content of the data. Note that the "low-frequency shadow" reported by Taner *et al.* (1979) is not observable on any of the instantaneous frequency plots.

6.2.5 Discussion

The Glauconitic sandbar in well E exhibited a detectable anomaly on conventional seismic data. Although the channel section is 40-m thick, only 8 m of it are gas-bearing. Assuming a peak frequency of 40 Hz and a sand velocity of 3700 m/s, the tuning thickness is about 23 m. Hence, the gas-bearing zone is well below tuning thickness. This, in turn, means that to fully understand the amplitude behaviour of the anomaly, the effect of tuning on amplitude changes at non-normal incidence must be taken into consideration, as discussed in Chapter 5. In particular, in Alberta, the AVO effects of many thin hydrocarbon-bearing reservoirs are often obscured by their tuning effects. Although in Chapter 5, this conclusion is also drawn for the four types of reflectivities which are only single-layer, it is evidently also true for multi-layer reflectivities, as shown in this channel sandbar example.

Nevertheless, the AVO analysis performed on the three wells are still informative in a qualitative manner. Firstly, the analysis implies that for the Glauconitic Member in southern Alberta, AVO effects due to a lateral change of lithology can be observed only for offsets greater than 2500 m. For the subject seismic line, the largest effective offset is 1600 m, with any data from larger offsets being muted at the Glauconitic reflection times

in order to mute first break energy. Hence, one could not observe any conclusive evidence for any anomalous AVO effects as a result of a lateral change in the Poisson's ratio of the gas-bearing sand between the near-offset stack and the far-offset stack, notwithstanding the presence of other character differences.

Secondly, the AVO analysis clearly indicates that, for the Glauconitic Member in the study area, offset-dependent thin-bed tuning effects dominate any AVO effect attributed to lateral changes in Poisson's ratio. This agrees with the results for Types I, II, and IIA reflectivities, particularly for 1 m and 5 m thicknesses (Figures 5.2a, 5.4a, and 5.5a). Furthermore, NMO-stretch effects for far-offset traces are evident on all the synthetic seismograms. This also makes any AVO effects due to lateral changes of lithology more difficult to observe on large offset traces since it lowers the apparent frequency of those traces. The differences of the anomaly between the near-offset stack and the far-offset stack are probably largely due to lower frequency content in the far-offset stack.

In Chapters 4 and 5, it is concluded that complex attributes are good pattern recognition tools. The complex attributes for the subject sandbar is a good example. The complex attributes for the three offset stacks indicate that the channel can be recognized clearly on data where a frequency of 45 Hz or higher is present. The instantaneous phase (Figures 6.12a and 6.12b) outlines clearly the lateral discontinuities at the channel edge for the near-offset stack. The instantaneous frequency (Figure 6.13b) is even more remarkable in its ability to delineate the sandbar. This agrees with the important conclusion about complex attributes in Chapters 4 and 5: that the instantaneous frequency is probably the most effective tool among the three attributes to delineate subtle thin-bed anomalies that are often difficult to detect on conventional stack display. Furthermore, the differences between the instantaneous phase and frequency plots for the near-offset and far-offset stacks suggest that the attributes are very sensitive to the frequency content of

the seismic data. Thus, it would be a very useful exercise to study how the apparent frequency content of the attributes relate to the frequency of the corresponding seismic data.

6.3 Sheet sand example

The seismic data chosen for the second case study is from central Alberta where sands of the Triassic Halfway Formation are good oil and gas producers. In this area the Halfway sands behave as a single layer and the data quality is excellent, thus offering an opportunity to test the conclusions drawn in Chapters 2 through 4 for the one-layer case, using actual field seismic data.

6.3.1 Geological background

Figure 6.14 shows an informal stratigraphic column in the subject area. The Halfway Formation is overlain by the predominantly dolomitic Charlie Lake Formation and underlain by the shaly Doig Formation. In this area, the Halfway Formation was deposited initially as a blanket sand, and was then faulted, with linear horsts and grabens trending predominantly in a northwest-southeast direction. Subsequent to faulting, the Halfway Formation experienced regional erosion with the result that the sands in the horst blocks were eroded away, whereas the sands in the grabens were mostly preserved. Following the erosion, a blanket of impermeable shale was deposited. Consequently, the majority of the hydrocarbons in the Halfway Formation across this area are trapped within the grabens where the sands are permeable and porous with the overlying shales serving as seals. These traps are mostly oil-prone but are often accompanied by significant gas caps. Figure 6.15 shows a plan view of seismic lines, the trend of a graben, and the locations of wells A, B, and C.

Figure 6.16 shows the synthetic seismogram generated from a sonic log for well A. The source wavelet for the seismogram is a 35 Hz Ricker wavelet, but the Halfway reflection in the seismogram resembles a 90°-phase wavelet. As discussed in Chapter 2, this implies that the Halfway Formation behaves as a Type I reflectivity, with its thickness below $(1/8)\lambda_d$. In well A, the *P*-wave velocity of sands of the Halfway Formation is approximately 4150 m/s. Thus, the $(1/8)\lambda_d$ value is approximately 11.6 m for a 35 Hz source wavelet. The thickness of the Halfway Formation in well A is 5.7 m, and is thus well below the $(1/8)\lambda_d$ value.

Early Jurassic	Nordeg
Late Triassic	Baldonnel
	Charlie Lake
Middle Triassic	Halfway
	Doig
Early Triassic	Montney

Figure 6.14 Informal stratigraphic column for the study area (Kohrs and Norman, 1988).

6.3.2 Geophysical background

Lines 1 and 3 were acquired in March, 1985. Three seconds of data were recorded at 2 ms sampling rate with a MDS-10 recording system. A recording filter of 0-125 Hz was applied together with a notch filter at 60 Hz. Each shot was recorded with dynamite in a 3-hole pattern, with 1 kg in each hole at a depth of 9 m. The shot point spacing was 100 m and the geophone group spacing was 25 m, with 9 phones for each group spread over 25 m; L-28 14 Hz geophones were used. The spread configuration was 1500-25-X-25-1500 m with 120 traces/shot. Resulting multiplicity was 15-fold. Line 2 was recorded in January, 1988, using parameters similar to lines 1 and 3 except that the geophone group interval was increased to 30 m, and smaller charge sizes (0.5 kg) were used.

The processing of these three lines followed a standard processing sequence, and consisted of demultiplexing, gain application, geophone and instrument phase compensation, spiking deconvolution, weathering and surface consistent statics, velocity analysis and NMO correction, mute and trim statics, stacking, bandpass filtering and scaling, and finite difference migration. The parameters chosen are quite typical of parameters chosen for Western Canada. For example, the bandpass filter was 8/12 - 90/110 Hz, the deconvolution operator was 80 ms in length, and the migration velocity was 90% of the stacking velocity.

6.3.3 Amplitude analysis

Figures 6.17a, 6.18a, and 6.19a show portions of processed seismic data from lines 1, 2, and 3, respectively with the Halfway event highlighted in red, and the synthetic seismograms for wells A, B, and C spliced in at their drilling locations. A panel of traces from each line with a time window of 50 ms, centred at the troughs representing the Halfway reflections were selected for amplitude study. The absolute maximum amplitudes of the troughs representing the Halfway reflections were picked for all traces within the panels and are plotted in Figure 6.20. Since these three lines are not all of the same vintages, these maximum amplitudes have been normalized with respect to another line (line 4) which intersects with all three lines (Figure 6.15). The corresponding thicknesses as indicated by the vertical axes on the right-hand-side of the graphs in Figure 6.20 are calculated by multiplying the maximum amplitudes with conversion factors equal to the thickness of the Halfway sands in the three wells divided by the maximum amplitudes of the traces at which the wells were drilled. The trace numbers in Figures 6.17, 6.18, and 6.19 correspond to the trace numbers in Figure 6.20, respectively. Figure 6.20 indicates that wells A and C were not drilled at the locations where the amplitudes are the highest,

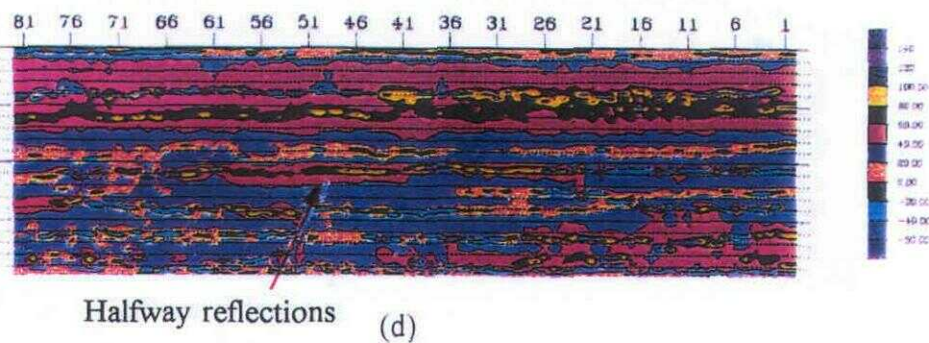
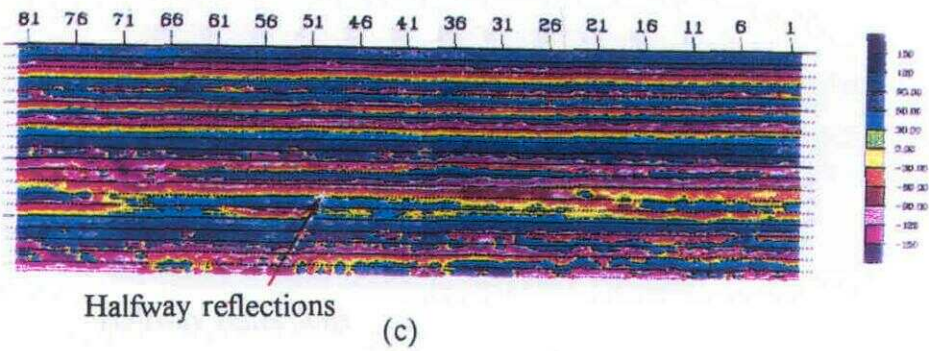
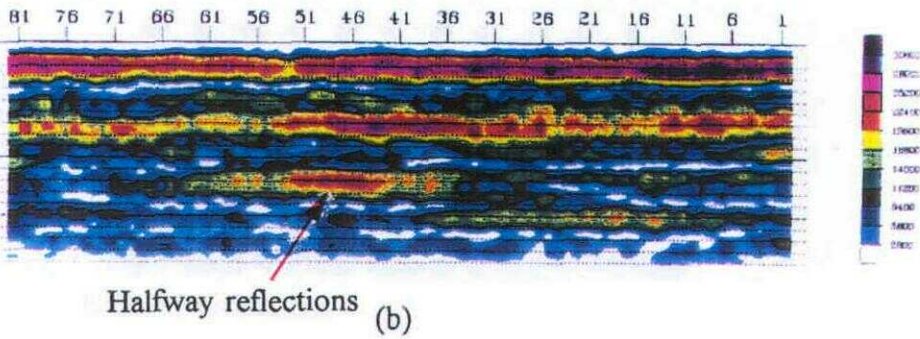
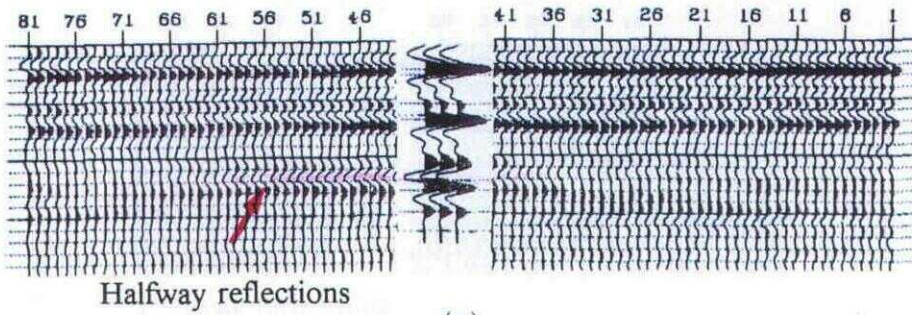


Figure 6.17 Seismic displays for line 1: (a) conventional display; (b) instantaneous amplitude; (c) instantaneous phase; (d) instantaneous frequency. Timing lines are at 10-ms intervals.

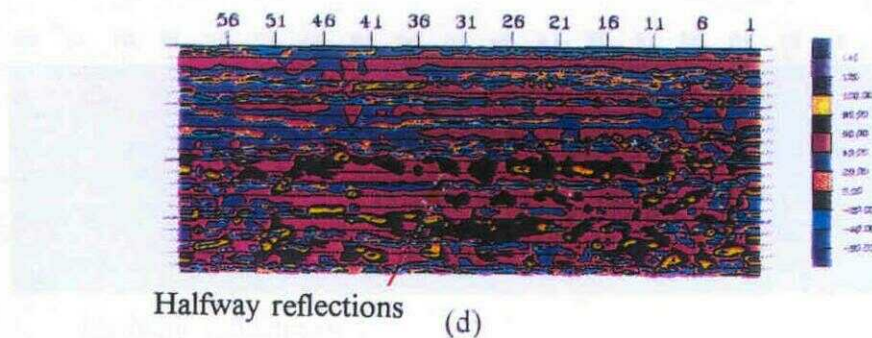
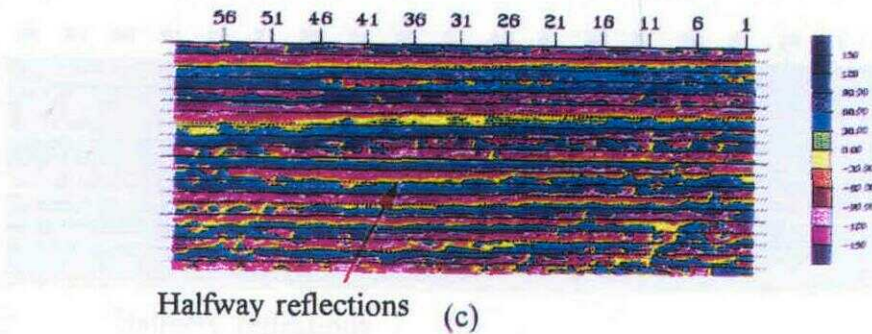
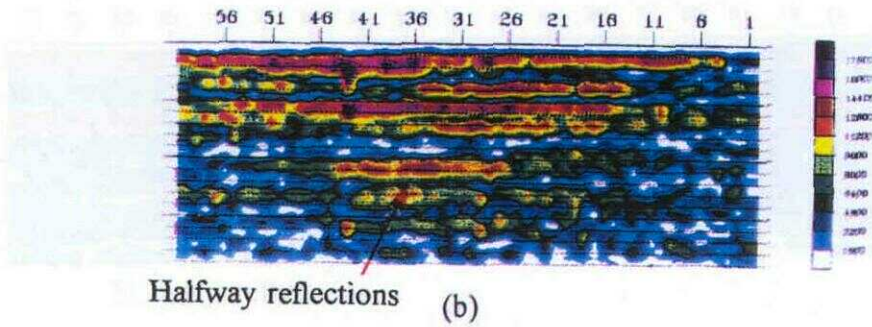
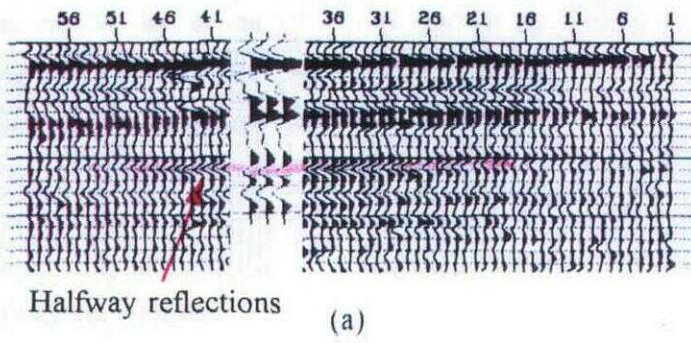
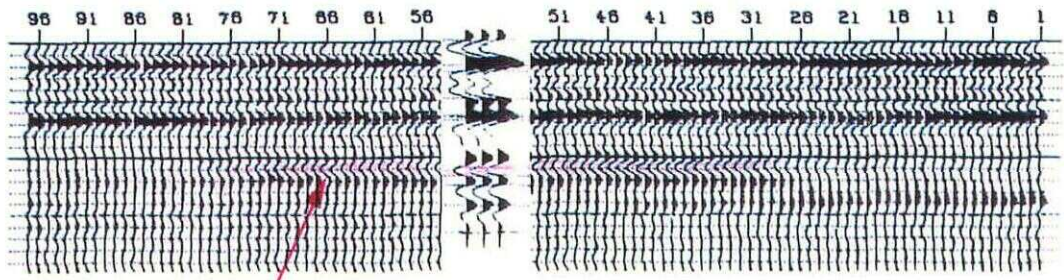
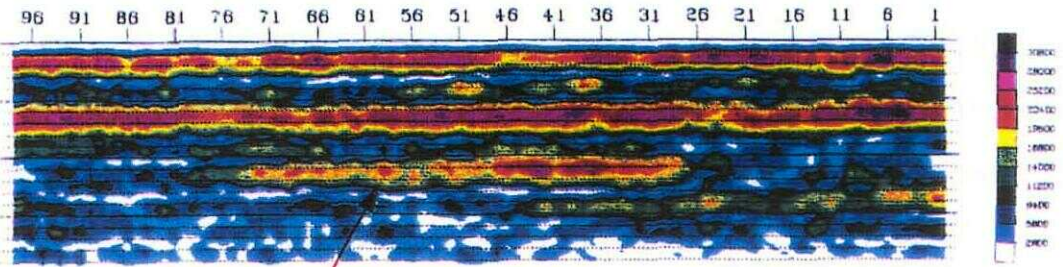


Figure 6.18 Seismic displays for line 2: (a) conventional display; (b) instantaneous amplitude; (c) instantaneous phase; (d) instantaneous frequency. Timing lines are at 10-ms intervals.



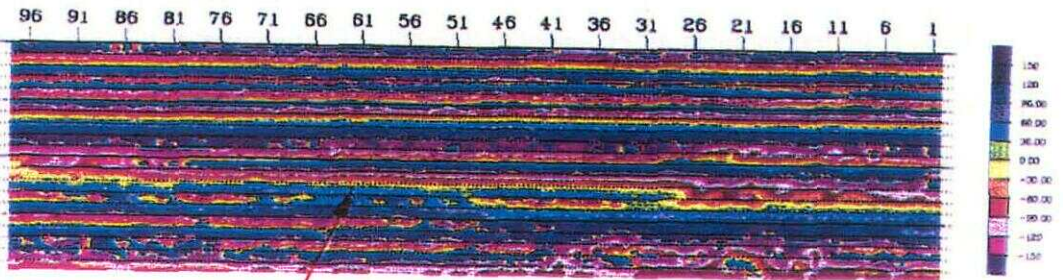
Halfway reflections

(a)



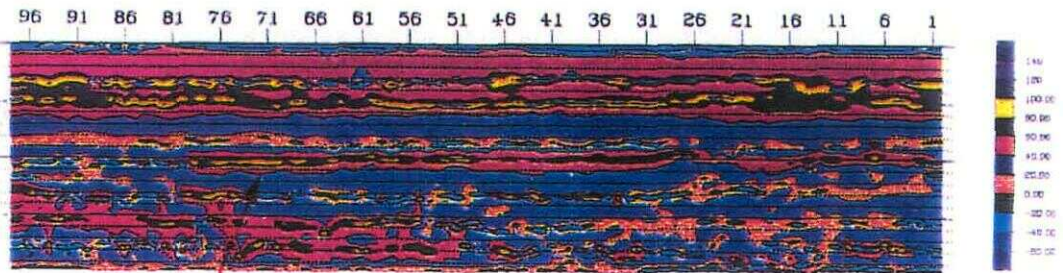
Halfway reflections

(b)



Halfway reflections

(c)



Halfway reflections

(d)

Figure 6.19 Seismic displays for line 3. (a) conventional display; (b) instantaneous amplitude; (c) instantaneous phase; (d) instantaneous frequency. Timing lines are at 10-ms intervals.

i.e. not at the thickest portion of the sands. That is probably due to the fact that most drilling locations are still chosen on a visual basis rather than on a quantitative basis.

As indicated by the sonic log data shown in Figure 6.16, the velocity of the Halfway sand is approximately 4150 m/s. The peak frequencies of the Halfway reflections on seismic data are approximately 35 Hz (Figure 6.24). This gives a predominant wavelength of about 91 m, and a value of 11.4 m for $(1/8)\lambda_p$. The acoustic impedance of the Halfway sand is about 10,500 kg/(sec-m²) and that of the overlying Charlie Lake and the underlying Doig formations are about 16,000 kg/(sec-m²). Therefore, the reflection coefficients for the Halfway sand top and bottom are approximately -0.2075 and +0.2075. Thus, using these parameters and equation (2.3) with $A_i = 750$ (this value of A_i is chosen so that the data from wells A, B, and C will lie as closely as possible to the resulting straight line in Figure 6.21), a set of maximum amplitudes versus thickness are obtained, and are plotted in Figure 6.21. Since this case can be represented by Type I reflectivity, the resulting plot will be a straight line for thicknesses below 11.4 m. Plotted also in the same figure are the maximum amplitude values for the Halfway reflections where the traces tie with the wells. Figure 6.21 shows that these amplitudes from seismic data agree very well with results predicted by modelling. If the modelling results in Figure 6.21 had been used as a guide to determine the thicknesses of the sands at which the amplitudes are maximum in Figures 6.20a to 6.20c, thicker pay would have probably been encountered than the ones in wells A and C.

6.3.4 Frequency interpretation

Figure 6.22 shows the results of the peak frequency analysis of the Halfway Formation event for the three seismic lines. The peak frequencies were obtained with the same narrow time gates (50 ms) as used for amplitude study in the previous section.

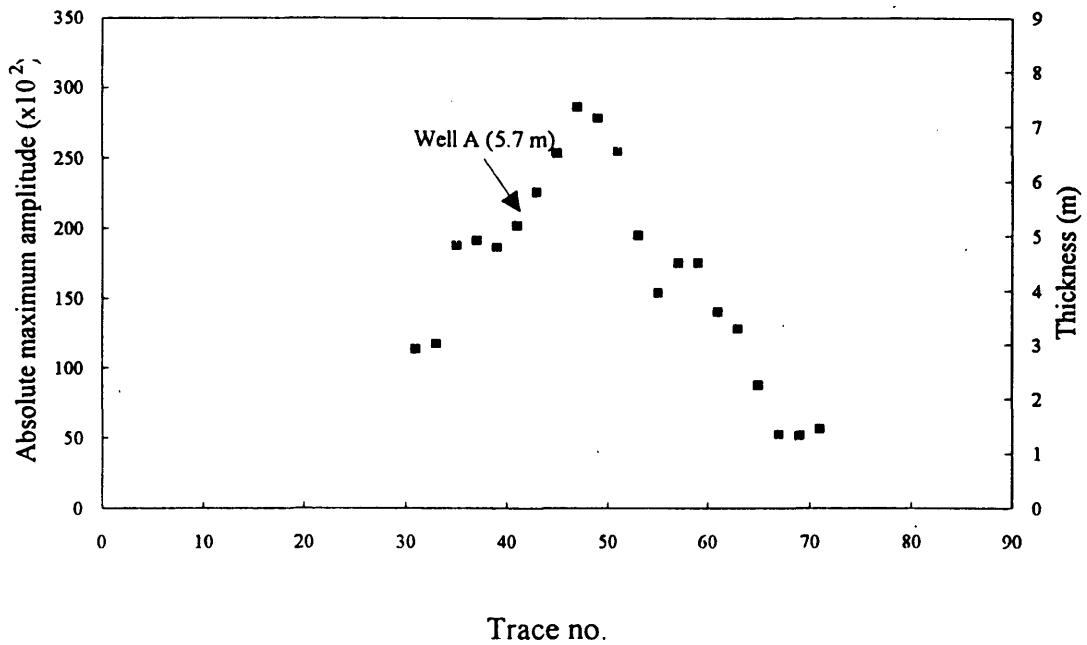


Figure 6.20a Absolute maximum amplitudes for the Halfway Formation event for line 1.

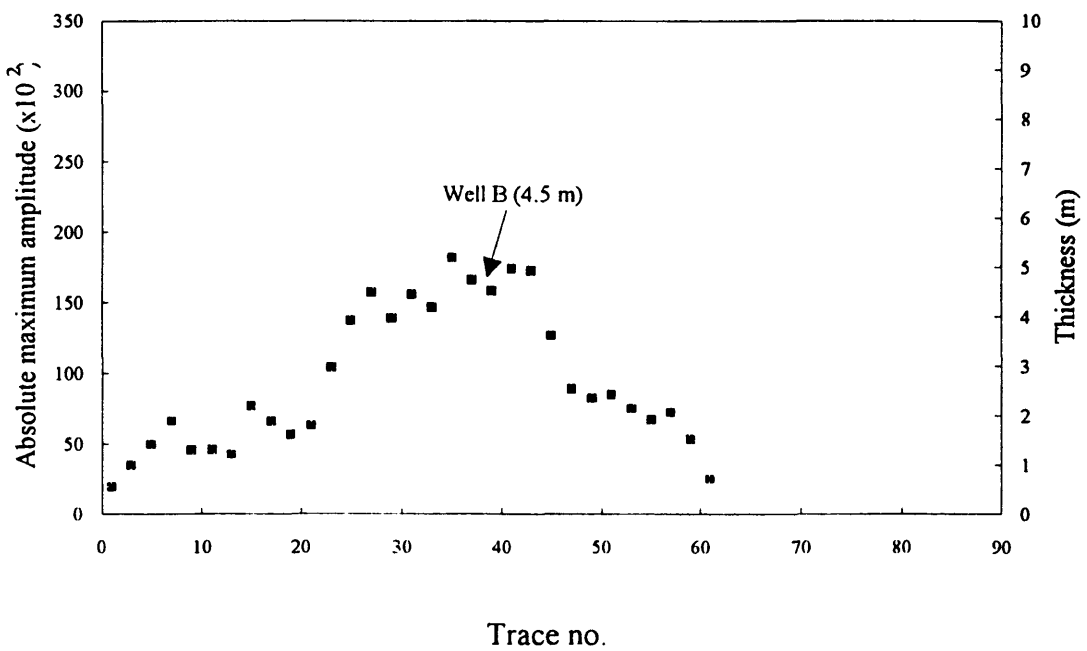


Figure 6.20b Absolute maximum amplitudes for the Halfway Formation event for line 2.

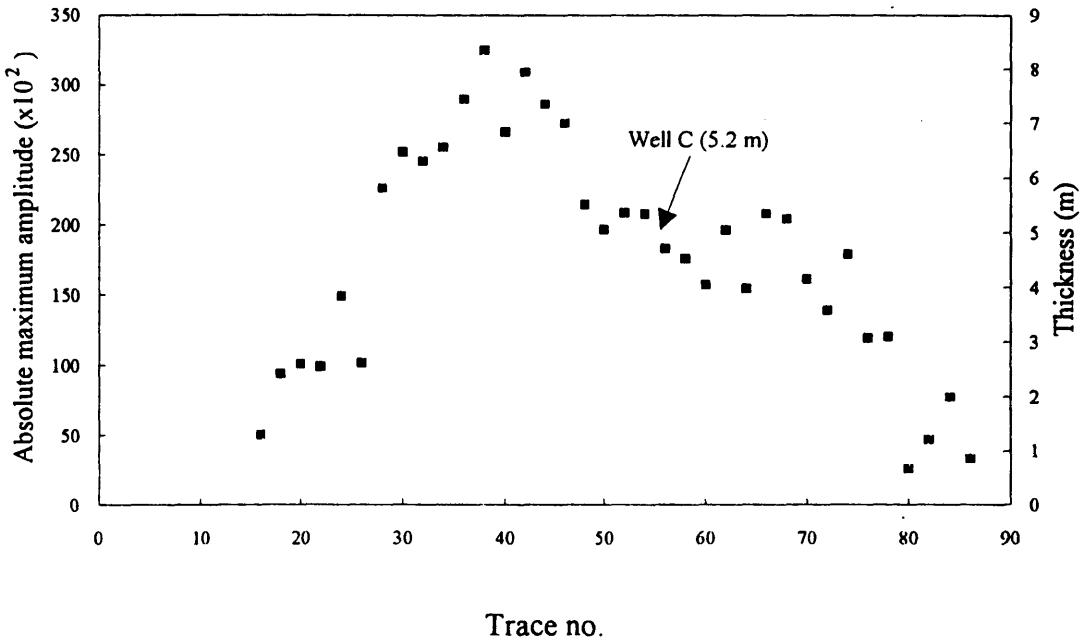


Figure 6.20c Absolute maximum amplitudes for the Halfway Formation event for line 3.

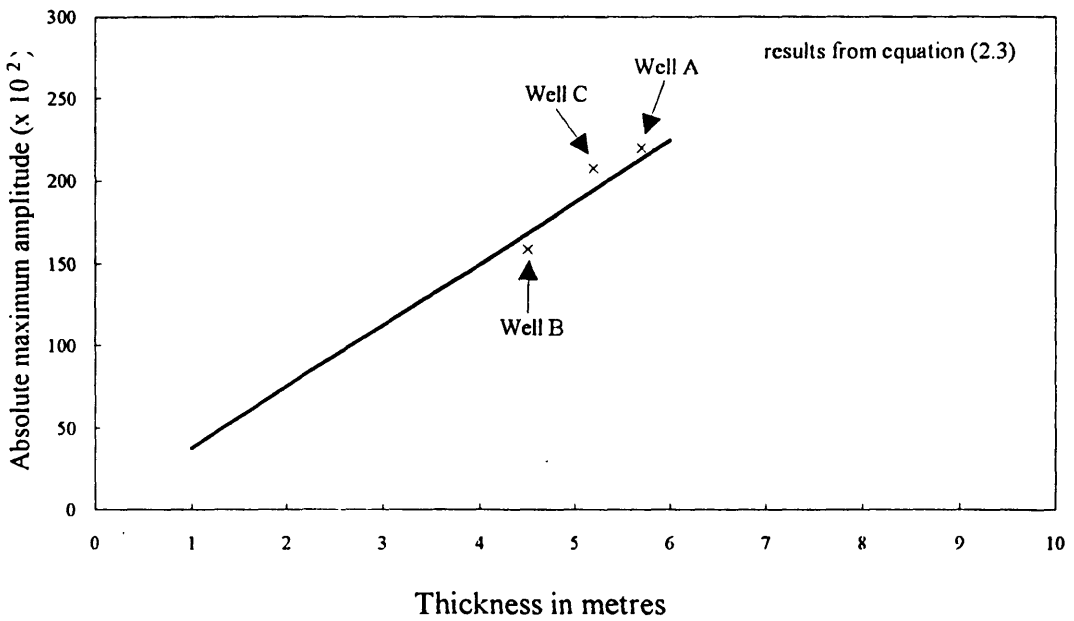


Figure 6.21 Absolute maximum amplitudes for the Halfway reflections as a function of the thickness. Maximum amplitudes corresponding to wells A, B, and C are also plotted.

Figure 6.22 indicates that the results for the peak frequency analysis are more erratic than the amplitude study. For a thin bed that can be represented by Type I reflectivity, theoretical prediction and modelling results (Figure 3.3) show that the peak frequency should decrease slowly with increasing thickness. The amplitude results shown in Figure 6.20 indicate that the Halfway Formation along the graben trend has a non-uniform thickness, with the thickest part lying close to traces 51, 38, and 46 for lines 1, 2, and 3, respectively. If the first ten traces and the last ten traces are ignored for each line, to avoid diffraction effects from the graben edges, then the frequency results show minima at traces 56, 35 and 50 for lines 1 and 2 and 3, respectively. These locations of frequency minima agree fairly well with the corresponding maximum amplitude locations.

Figure 6.23 shows three amplitude spectra of three traces from Line 4 at the locations where it intersects lines 1, 2, and 3. The time window for the spectral analysis was 50 ms centred at the Halfway reflection. The peak frequencies in these spectra are approximately 35 Hz. Using a 35 Hz Ricker wavelet as the source wavelet, a velocity of 4150 m/s for the Halfway Formation, and values of -0.2075 and 0.2075 for the reflection coefficients at the boundary of the Halfway sands, a set of theoretical peak frequencies versus thickness are obtained and these results are plotted in Figure 6.24. These theoretical frequencies decrease only fractionally over the thickness range in Figure 6.24, and hence appear to lie in a straight line. Plotted also are the normalized peak frequencies of the traces where the three wells were drilled. Figure 6.24 shows that, using a 35 Hz Ricker wavelet as the source wavelet, the normalized peak frequencies for the three wells are all within ± 5 Hz of the theoretical values. However, there is one inconsistency among the normalized peak frequencies for the three wells. The thickness of the Halfway normalized peak frequency for well B (37.3 Hz). However, Figure 6.24 shows that the Formation in well C (5.2 m) is slightly larger than that in well B (4.5 m); hence, the normalized peak frequency for well C (42.9 Hz) should be slightly less or equal to the

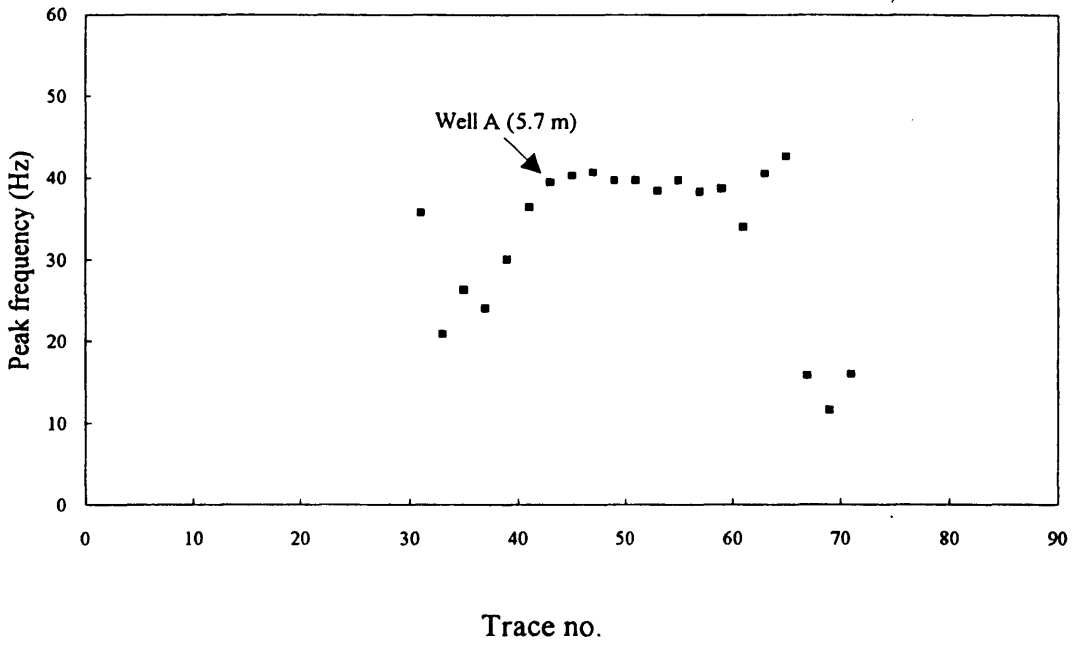


Figure 6.22a Peak frequencies for the Halfway Formation event for line 1.

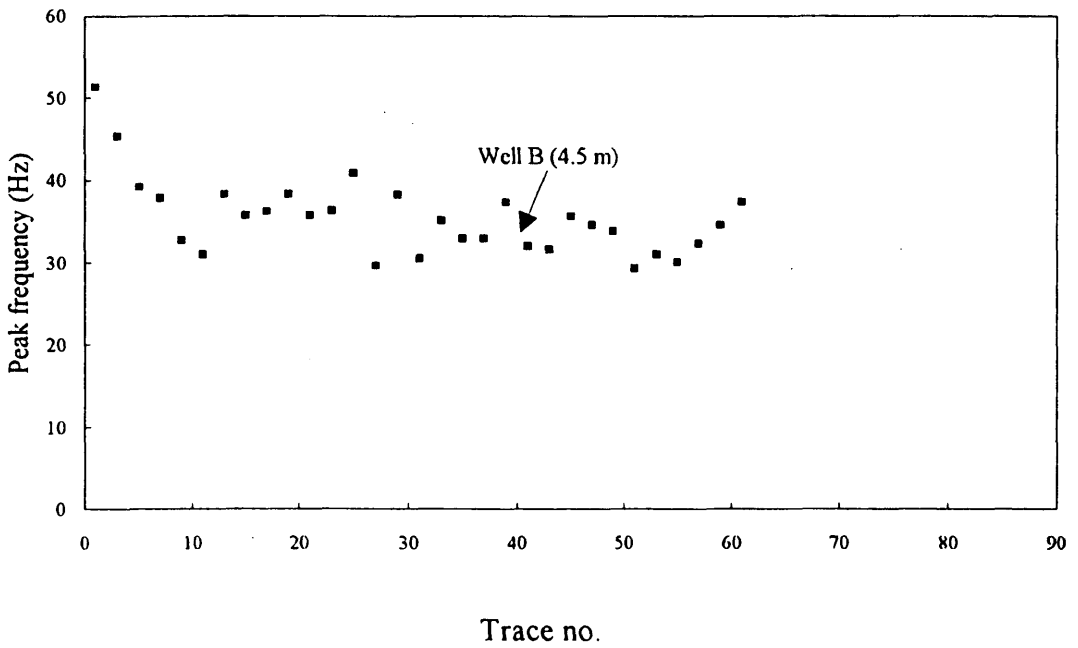


Figure 6.22b Peak frequencies for the Halfway Formation event for line 2.

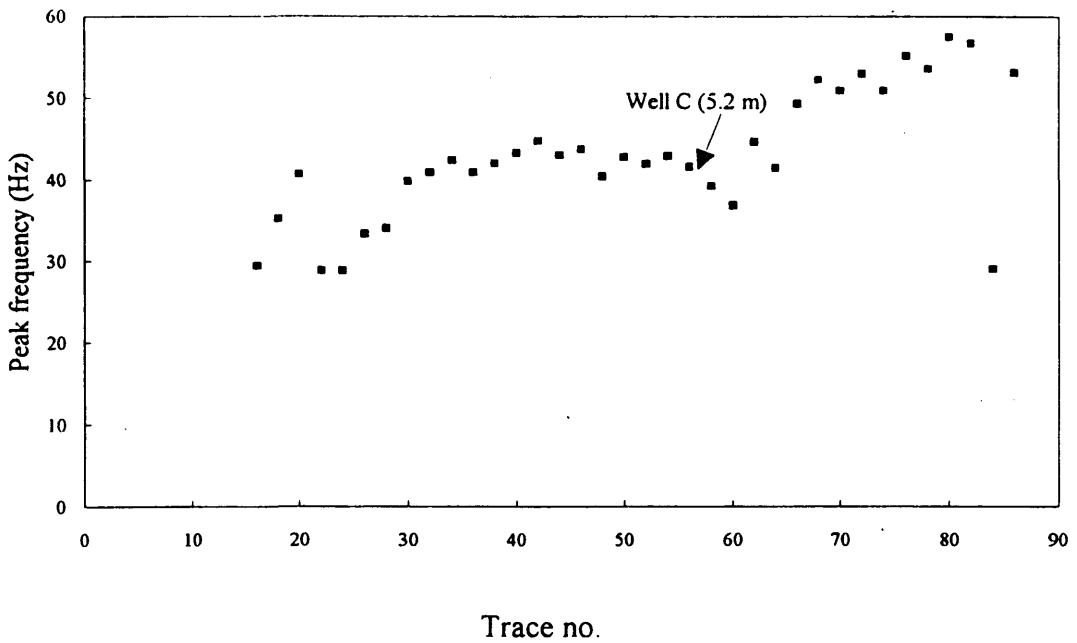
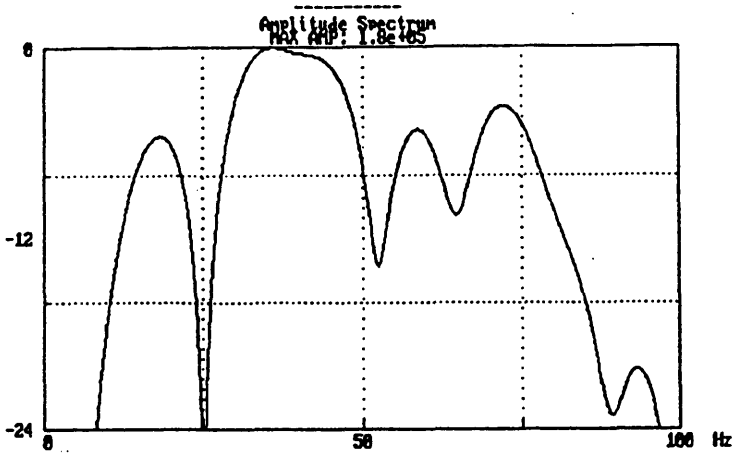


Figure 6.22c Peak frequencies for the Halfway Formation event for line 3.

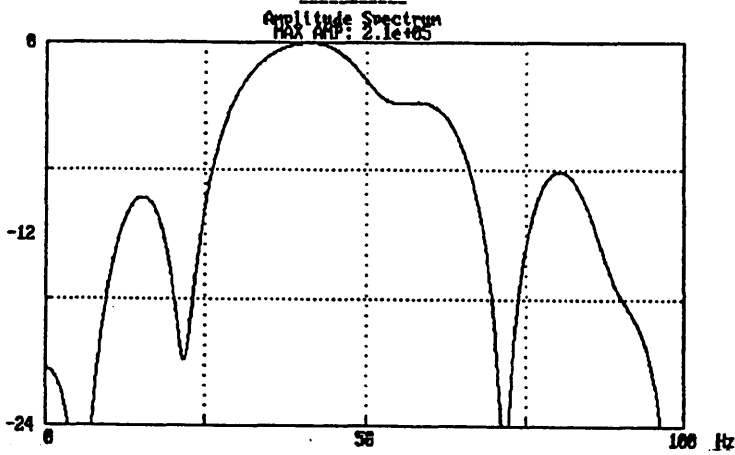
normalized peak frequency for well C is actually higher than that of well B. More interpretation case studies, preferably data with several tying wells, on the use of peak frequency are needed before its behaviour and limitations can be fully understood.

6.3.5 Complex attributes

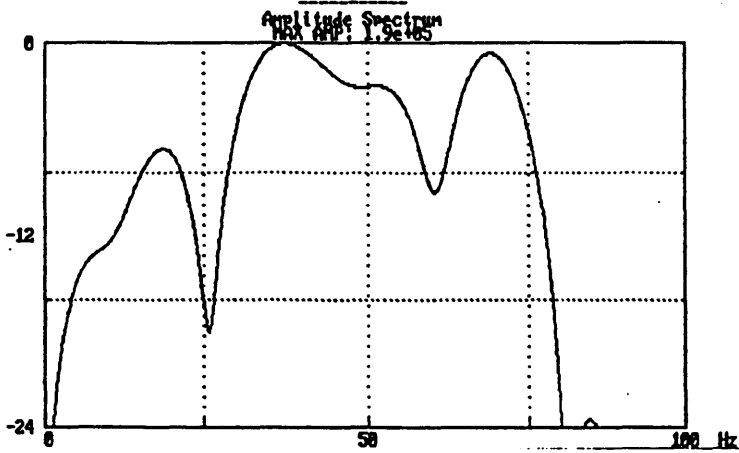
Figures 6.17b, 6.18b, and 6.19b show the instantaneous amplitudes for lines 1, 2, and 3, respectively. The Halfway reflections exhibit amplitude tuning for all three lines, shown in red-purple colours in the figures. The corresponding instantaneous phase plots are shown in Figures 6.17c, 6.18c, and 6.19c. For lines 1 and 3, the Halfway reflections appear as phase discontinuities. However, for line 2, the phase discontinuities that correspond to the spatial limits of the Halfway reflections are not visually clear. Conversely, the corresponding instantaneous frequency plots in Figures 6.17d, 6.18d, and 6.19d show the frequency-tuning effect clearly for all three lines, as shown in black and



(a)



(b)



(c)

Figure 6.23 Three frequency spectra for the Halfway reflections on line 4 at three seismic line intersections: (a) intersection with line 1, (b) intersection with line 2 and, (c) intersection with line 3. The amplitude is measured in db down.

yellow colours. This agrees with modelling results in that the instantaneous frequency is more sensitive and hence more useful in delineating lateral discontinuities than is instantaneous phase. Furthermore, an examination of the numerical values of the instantaneous frequencies for the three lines where the Halfway reflections lie indicates that there are no negative frequencies, although there are large positive values, caused by the frequency tuning effect. Such frequency tuning indirectly indicates the presence of a thin bed. By contrast, the Halfway reflections in the conventional displays in Figures 6.17a, 6.18a, and 6.19a only indicate the presence of the Halfway Formation without a clear indication to its thickness.

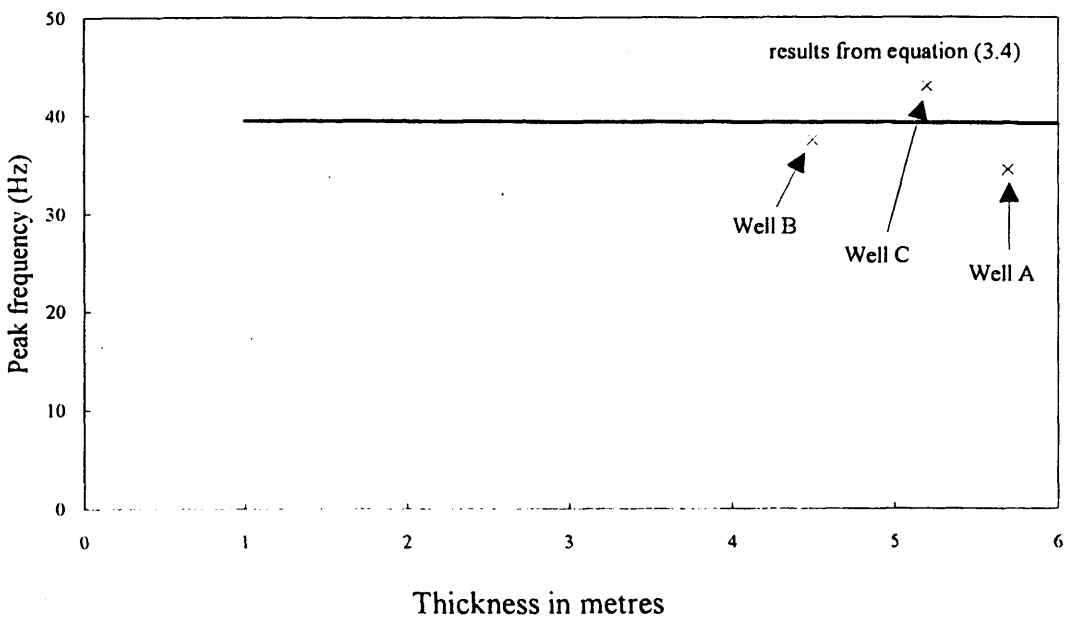


Figure 6.24 Peak frequencies for the Halfway reflections as a function of thickness. Peak frequencies corresponding to wells A, B, and C are also plotted.

6.3.6 Discussion

The case study for the Halfway sands is an evaluation of how one set of real seismic data can be assessed with respect to the thin-bed properties developed in Chapters 2, 3, and 4. To fully evaluate the validity of many of the conclusions developed in these three chapters, it would be preferable to have one or more sets of real data for each of the four reflectivities. Nevertheless, the study of one set of data gives some indication of the potential usefulness of applying some of these conclusions for seismic interpretation of thin geological formations.

The amplitude analysis using the real data agrees well with the modelling results, as indicated in Figure 6.21. Thus, if further exploration is undertaken along the same graben trend or along another graben trend in the same area, the seismic amplitudes of the Halfway reflections can be used as a guide to drill for the thickest sand, assuming that there is no significant lateral change in the lithology of the sands within the graben. If the maximum amplitudes of these reflections are plotted versus trace locations, the trace location with the maximum amplitude is likely to be the location where the sand thickness, and hence the hydrocarbon pay thickness, is the greatest.

The peak frequency results are less indicative. While they agree with the peak frequency property of a Type I reflectivity in a general manner, the inconsistency between the thicknesses and frequencies of wells B and C as discussed in section 6.3.4 indicates that a drilling location cannot be decided based on the peak frequency alone. Since the peak frequency has not been used extensively for interpretation, the results from one set of data are hardly conclusive. Just as amplitude is affected by many factors such as absorption and anisotropy, frequency is affected by factors such as dispersion and absorption. More case studies should be done on the use of peak frequency in order to fully understand its merits and pitfalls in seismic interpretation.

The complex attributes are useful in that the instantaneous amplitude and the instantaneous frequency both show tuning effects, which indicate the Halfway event represents a composite reflection from a thin bed. The instantaneous phase is also useful, although it is slightly less sensitive than the instantaneous frequency. In general, for qualitative interpretation, colour plots often are good visual aids, and complex attributes plotted in colours are good examples.

Chapter 7 - Dissertation summary

7.1 Summary

The study of the properties of a thin layer embedded in an homogeneous medium shows that the maximum amplitudes of seismic reflections from the layer as a function of the layer thickness is linear for thicknesses less than or equal to $(1/8)\lambda_d$ only for Type I reflectivity sequence. For Types II, III, and IV reflectivity sequences, the functional relationship between the maximum amplitudes and the layer thicknesses is quadratic. This is also true of the two-layer reflectivity sequences of Types V, VI, and VII. The well-established tuning thickness of $(1/4)\lambda_d$ for Type I reflectivity sequence is also valid for Types II, III, and IV, but is not valid for the two-layer reflectivity sequences.

Thus, in general, the theories which have been developed for Type I reflectivity in published literature on thin-bed interpretation may not be applicable to seismic reflections unless they are reflections from geological sequences that can be represented by Type I reflectivity. Since, in reality, very few geological sequences truly resemble Type I reflectivity, the conclusions of linearity of amplitude versus thickness for thin layers whose thicknesses are less than the $(1/8)\lambda_d$ value and of tuning at $(1/4)\lambda_d$ thickness should be applied with caution. For multi-layer seismic reflections, the results can be complicated, as illustrated by the amplitude results of Type VI reflectivity. Under such circumstances, modelling should be performed whenever there is sufficient geological information, and the results should be studied quantitatively to establish any functional relationship.

In the peak frequency study, equations that give exact values of peak frequencies of the reflected composite wavelets as a function of bed thickness were developed for both one-layer and two-layer models. These equations can always be used in forward modelling, and the modelled results can be compared to the peak frequencies of real

seismic data. Parameters such as bed thickness or the reflection coefficients can be varied until a match is attained between the modelled frequencies and the real data frequencies.

More importantly, the frequency analyses, both normal-incident and offset-dependent, indicate that the peak frequency can be a useful tool for interpreting seismic reflections from thin beds. For example, frequency tuning can be indicative of the presence of a geological sequence whose reflection coefficients have alternating polarities, as illustrated by both Types III and VI reflectivity sequences. There are other possible situations where frequency tuning could occur, for example the peak frequencies for Type IA reflectivity in the offset-dependent analysis. Since peak frequency has not been used extensively in seismic interpretation, more research is definitely needed in order to understand more completely its usefulness and pitfalls in seismic interpretation.

It has been shown qualitatively in many papers that anomalous AVO effects due to a lateral change of the Poisson's ratio can be strongly affected by offset-dependent tuning effects for thin layers. The offset-dependent analysis in Chapter 5 not only confirms this conclusion, but shows the effect quantitatively for four models. The numerical results indicate that for some geological sequences such as ones that can be represented by Types I and II reflectivity sequences, the offset-dependent tuning effects completely overwhelms the anomalous AVO effects if the layer thickness is very thin. Therefore, in seismic interpretation of data from thin geological formations, the offset-dependent tuning effects must be taken into account before any meaningful conclusions concerning AVO effects can be drawn.

The complex attribute analysis for the various models show that they are effective pattern-recognition tools for studying subtle waveform changes. Both amplitude and frequency tuning effects are outlined clearly by the attribute displays. In particular, the instantaneous frequency shows subtle interference patterns that are difficult to detect on conventional seismic displays.

7.2 Future research

For future research, the effects of multiples on amplitude responses should be investigated for both the normal-incidence and offset-dependent models. More studies on the use of peak frequency, both theories and case histories, should be conducted to fully develop the potential use of this wavelet attribute in seismic interpretation. In particular, frequency tuning effects should be investigated further as to how and when they occur. For complex attributes, research should be directed towards linking the qualitative observations to the geological changes.

REFERENCES

- Ackroyd, M.H., 1970, Instantaneous spectra and instantaneous frequency: Proc. Inst. of Electr. and Electron. Eng. **58**, 141.
- Aki, K.I., and Richards, P.G., 1980, Quantitative seismology, **1**: W. H. Freeman and Company.
- Allen, J.L., and Peddy, C.P., 1993, Some AVO failures and what we have learned: The Leading Edge, **12**, 162-167.
- Almoghrabi, H., and Lange, J., 1986, Layers and Bright Spots: Geophysics: **51**, 699-709.
- _____, 1988, Lithology discrimination for thin layers using wavelet signal parameters: Geophysics **53**, 1512-1519.
- Anderson, N., Hills, L.V., Cederwall, D.A., 1989, Geophysical Atlas of Western Canadian Hydrocarbon Pools: Canadian Society of Exploration Geophysicists and Canadian Society of Petroleum Geologists..
- Backus, M.M., 1992, On sensitivity, detectability, and ambiguity: How useful is AVO analysis? Joint SEG/EAGE summer research workshop abstracts, 178-188.
- Barnes, A.E., 1991, Instantaneous frequency and amplitude at the envelope peak of a constant-phase wavelet, Geophysics, **56** 1058-1060.
- _____, 1993, When the concepts of spectral frequency and instantaneous frequency converge: The Leading Edge, **12**, 1020-1023.
- Berkout, A.J., 1984, Seismic Resolution: Handbook of Geophysical Exploration, Section I., **12**, chap.II.
- Bodine, J.H., 1986, Waveform analysis with seismic attributes: Oil and Gas J. **84**, 59-63.
- Bortfeld, R., 1961, Approximation to the reflection and transmission coefficients of plane longitudinal and transverse waves: Geophys. Prosp., **9**, 485-503.

- Bracewell, R., 1965, The Fourier transform and its application: New York, McGraw-Hill Book Co. Inc., 267-272
- Burnett, R.C., 1990, Seismic amplitude anomalies and AVO analyses at Mestena Grande Field, Jim Hogg Co., Texas: *Geophysics* **55**, 1015-1025.
- de Voogd, N., and den Rooijen, H., 1983, Thin-layer response and spectral bandwidth: *Geophysics* **48**, 12-18.
- Domenico, S.N., 1976, Effect of brine-gas mixture on velocity in unconsolidated sand reservoir: *Geophysics* **41**, 882-894.
- _____, 1977, Elastic properties of unconsolidated porous sand reservoirs: *Geophysics* **42**, 1339-1368.
- _____, 1984, Rock lithology and porosity determination from shear and compressional wave velocity: *Geophysics* **49**, 1137-1406.
- Eaton, D.W.S., 1989, The free surface effect: implications for amplitude-versus-offset inversion: *J. Can. Soc. Expl. Geophys.* **25**, 97-103
- Energy Resources Conservation Board, 1978, Table of formations, Alberta: Calgary Energy Resources Conservation Board.
- Ensley, R.A., 1984, Comparison of *P*- and *S*-wave seismic data: A new method for detecting gas reservoirs: *Geophysics* **49**, 1420-1431.
- Farnbach, J.S., 1975, The complex envelope in seismic signal analysis: *Bulletin of the Seismological Society of America* **65**, 951-962.
- Gabor, D., 1946, Theory of communication, part I: *J. Inst. Electr. Eng.* **93**, 429-421.
- Gardner, G.H.F., Gardner, L.W., and Gregory, A.R., 1974, Formation velocity and density-the diagnostic basis for stratigraphic traps: *Geophysics* **39**, 770-780.
- Glaister, R.P., 1959, Lower Cretaceous of southern Alberta and adjoining areas: *Bull. Am. Assn. Petr. Geol.* **43**, 590-640.

- Gochioco, L.M., 1991, Tuning effect and interference reflections from thin beds and coal seams, *Geophysics* **56**, 1288-1294.
- Hampson, D., 1991, AVO inversion, theory and practice: *The Leading Edge*, **10**, No. 6, 39-42.
- Hopkins, J.C., Hermanson, S.W. and Lawton, D.C., 1982, Morphology of channels and channel-sand bodies in the Glauconitic sandstone member (Upper Mannville), Little Bow area, Alberta: *Bull. Can. Petr. Geol.* **30**, 274-285.
- Jain, S., 1985, Some techniques of enhancing seismic reflection data for stratigraphic interpretation: *J. Can. Soc. Expl. Geophys.* **21**, 15-29
- _____, 1987, Amplitude-vs-offset analysis: a review with reference to application in western Canada: *J. Can. Soc. Expl. Geophys.* **23**, 27-36.
- Juhlin, C., and Young, R., 1993, Implications of thin layers for amplitude variation with offset (AVO) studies: *Geophysics*, **58**, 1200-1204.
- Kallweit, R.S. and Wood, L.C., 1982, The limits of resolution of zero-phase wavelets: *Geophysics* **47**, 1035-1046.
- Kim, K.Y., Wrolstad, K.H., and Aminzadeh, F., 1993, Effects of tranverse isotropy on P-wave AVO for gas sands: *Geophysics*, **58**, 883-888.
- Knapp, R.W., 1990, Vertical resolution of thick beds, thin beds, and thin-bed cyclothem: *Geophysics* **55**, 1184-1191.
- Knott, C.G., 1899, Reflexion and refraction of elastic waves, with seismological applications: *Phil. Mag.*, 5th ser. **48**, 64-97.
- Koefoed, O., 1955, On the effect of Poisson's ratio of rock strata on the reflection coefficients of plane waves: *Geophys. Prosp.* **3**, 381-387.
- _____, and de Voogd, N., 1980, The linear properties of thin layers, with an application to synthetic seismograms over coal seams: *Geophysics* **45**, 1254-1268.

- Kohrs, B.M., and Norman, D.K. 1988, Western Atlas International stratigraphic correlation chart of petroleum producing areas of Canada and northern United States.
- Masters, J.A., 1984, Lower Cretaceous oil and gas in Western Canada: *Am. Assn. Petr. Geol., Mem.* **38**, 1-34.
- Mazzotti, A., 1991, Amplitude, phase, and frequency versus offset applications: *Geophys. Prosp.* **39**, 863-886.
- McCormack, M.D., Dunbar, J.A., Sharp, W.W., 1984, A case study of stratigraphic interpretation using shear and compressional seismic data: *Geophysics*, **49**, 509-520.
- Meckel, L.D., Jr., and Nath, A.K., 1977, Geological considerations for stratigraphic modelling and interpretation: *Am. Assn. Petr. Geol., Mem.* **26**, 417-438.
- Meissner, R., and Meixner, E., 1969, Deformation of seismic wavelets by thin layers and layered boundaries: *Geophys. Prosp.*, **17**, 1-27.
- Muskat, M., and Meres, M.W., 1940, Reflection and transmission coefficients, for plane waves in elastic media: *Geophysics*, **5**, 115-155.
- Neff, D.B., 1990, Incremental pay thickness modelling of hydrocarbon reservoirs: *Geophysics*, **55**, 556-566.
- _____, 1993, Amplitude map analysis using forward modelling in sandstone and carbonate reservoirs: *Geophysics*, **58**, 1428-1441.
- Neidell, N.S., 1986, Amplitude variation with offset: *The Leading Edge* **3**, 47-51.
- _____, and Poggiagliolmi, E., 1977, Stratigraphic modelling and interpretation-Geophysical principals and techniques: *Am. Assn. Petr. Geol., Mem.* **26**, 389-416.
- Ostrander, W.J., 1984, Plane-wave reflection coefficients for gas sands at nonnormal angles of incidence: *Geophysics* **49**, 344-352.

- Poley, D.F., Lawton, D.C., and Blasco, S.M., 1985, Amplitude-offset relationships over shallow velocity inversions: *J. Can. Soc. Expl. Geophys.* **21**, 30-39.
- Rene, R.M., Fitter, J.L., Forsyth, P.M., Kim, K.Y., Murray, D.J., Walters, J.K., and Westerman, J.D., 1986: Multicomponent seismic studies using complex trace analysis: *Geophysics*, **51**, 1235-1251.
- Ricker, N., 1940, The form and nature of seismic waves and the structure of seismograms: *Geophysics*, **5**, 348-366.
- _____, 1953, Wavelet contraction, wavelet expansion, and the control of seismic resolution: *Geophysics* **18**, 769-792.
- Robertson, J.D., and Fisher, D.A., 1988, Complex seismic trace attributes: The Leading Edge **7**, 22-26.
- _____, and Nogami, H.H., 1984, Complex seismic trace analysis of thin beds: *Geophysics* **49**, 344-352.
- Rutherford, S.R., and Williams, R.H., 1989, Amplitude-versus-offset variations in gas sands: *Geophysics* **54**, 680-688.
- Saha, J.G., 1987, Relationship between Fourier and instantaneous frequency: 57th SEG meeting, New Orleans, Expanded Abstract, 591-594.
- Scheuer, T.E., and Oldenburg, D.W., 1988, Local phase velocity from complex seismic data: *Geophysics* **53**, 1503-1511.
- Shuey, R.T., 1985, A simplification of the Zoeppritz equations: *Geophysics*, **50**, 609-614.
- Simmons, J. Jr., Backus, M.M., 1993, Amplitude-versus-offset modeling and the locally converted shear wave: 63rd SEG meeting, Washington, D.C., Expanded Abstract, 738-741.
- Swan, H.W., 1991, Amplitude-versus-offset measurement errors in a finely layered medium: *Geophysics*, **56**, 41-49.

- Taner, M.T., and Sheriff, R.E., 1977, Applications of amplitude, frequency and other attributes to stratigraphic and hydrocarbon determination: Am. Assn. Petr. Geol., Mem. 26, 301-327.
- _____, Koehler, F., and Sheriff, R.E., 1979, Complex seismic trace analysis: Geophysics 44, 1041-1063.
- Tatham, R. H., 1982, V_p/V_s and lithology: Geophysics, 47, 336-344.
- Telford, W.M., Geldart, L.P., Sheriff, R.E., and Keys, D.A., 1976, Applied Geophysics, Cambridge University Press.
- Wallace, R., 1991, Correct use of the Hilbert Transform for complex attributes: Veritas Seismic Ltd. Internal Report
- White, R.E., 1991, Properties of instantaneous seismic attributes: The Leading Edge 10, No. 7, 26-32
- Widess, M.B., 1973, How thin is a thin bed?: Geophysics 38, 1176-1180.
- Wren, A.E., 1984, Seismic techniques in Cardium exploration: J. Can. Soc. Expl. Geophys. 20, 55-59.
- Xu, Y., Gardner, G.H.F., and McDonald, J.A., 1993, Some effects of velocity variation on AVO and its interpretation: Geophysics 58, 1297-1300
- Yilmaz, O., 1987, Seismic data processing: SEG, 484-486.
- Yu, G., 1985, Offset-amplitude variation and controlled-amplitude processing: Geophysics, 50, 2697-2708.
- Zoeppritz, K., 1919, Erdbebenwellen VIII B, Über Reflexion and Durchgang seismischer Wellen durch Unstetigkeitsflächen: Gottinger Nachr. I, 66-84.

Appendix A

Table 2.2a Comparison of modelling data with Ricker and sinusoidal approximations for Type I reflectivity at 18-Hz peak frequency ($\lambda_d = 130.26$ m).

Thickness		Absolute Maximum Amplitude (Input = 1000)					
		Zero-Phase Input Wavelet			90°-Phase Input Wavelet		
b (m)	$(b/\lambda_d) \times 10^{-2}$	Ricker (R)	Modelling (M)	$\frac{R-M}{M} \times 100$	Sinusoidal (S)	Modelling (M)	$\frac{R-M}{M} \times 100$
0	0.00	0.00	0.00	0.00	0.00	0.00	0.00
1	0.77	15.01	16.00	-6.60	19.99	19.92	0.35
3	2.30	45.03	43.28	3.89	59.97	59.56	0.68
5	3.83	75.05	74.60	0.60	99.94	100.09	-0.15
7	5.37	105.07	102.85	2.11	139.92	138.10	1.30
9	6.91	135.09	130.01	3.76	179.90	181.53	-0.91
11	8.44	165.11	155.80	5.64	219.88	217.54	1.06
13	9.98	195.13	179.96	7.77	259.86	251.26	3.31
15	11.52	225.15	203.90	9.44	299.83	284.66	5.06
17	13.05	255.17	222.52	12.80	339.81	310.62	8.59
19	14.59	-	241.87	-	-	337.53	-
21	16.12	-	257.41	-	-	359.08	-
23	17.66	-	270.53	-	-	377.14	-
25	19.19	-	281.17	-	-	391.67	-
27	20.73	-	289.89	-	-	403.29	-
29	22.26	-	295.11	-	-	409.94	-
31	23.80	-	298.50	-	-	413.74	-
33	25.33	-	299.67	-	-	414.02	-
35	26.87	-	298.75	-	-	411.24	-
37	28.40	-	295.67	-	-	404.66	-

Table 2.2b Comparison of modelling data with Ricker and sinusoidal approximations for Type I reflectivity at 31-Hz peak frequency ($\lambda_d = 75.63$ m).

Thickness		Absolute Maximum Amplitude (Input = 1000)					
		Zero-Phase Input Wavelet			90°-Phase Input Wavelet		
b (m)	$(b/\lambda_d) \times 10^{-2}$	Ricker (R)	Modelling (M)	$\frac{R-M}{M} \times 100$	Sinusoidal (S)	Modelling (M)	$\frac{R-M}{M} \times 100$
0	0.00	0.00	0.00	0.00	0.00	0.00	0.00
1	1.32	25.82	27.53	-6.62	34.43	35.66	-3.57
3	3.97	77.46	73.98	4.49	103.28	103.40	-0.12
5	6.61	129.11	125.57	2.74	172.14	175.50	-1.95
7	9.26	180.74	169.43	6.26	240.99	236.80	1.74
9	11.90	232.39	208.11	10.40	309.85	290.76	6.16
11	14.54	-	240.58	-	-	336.00	-
13	17.19	-	266.16	-	-	371.34	-
15	19.83	-	285.57	-	-	397.72	-
17	22.48	-	295.51	-	-	410.48	-
19	25.12	-	298.82	-	-	414.15	-
21	27.77	-	297.06	-	-	407.41	-
23	30.41	-	289.38	-	-	391.81	-

Table 2.2c Comparison of modelling data with Ricker and sinusoidal approximations for Type I reflectivity at 50-Hz peak frequency ($\lambda_d = 46.89$ m).

Thickness		Absolute Maximum Amplitude (Input = 1000)					
		Zero-Phase Input Wavelet			90°-Phase Input Wavelet		
b (m)	$(b/\lambda_d) \times 10^{-2}$	Ricker (R)	Modelling (M)	$\frac{R-M}{M} \times 100$	Sinusoidal (S)	Modelling (M)	$\frac{R-M}{M} \times 100$
0	0.00	0.00	0.00	0.00	0.00	0.00	0.00
1	2.13	41.65	44.29	-6.34	55.53	57.50	-3.55
3	6.40	124.94	117.16	6.22	166.59	163.74	1.71
5	10.67	208.24	191.62	7.98	277.65	267.77	3.56
7	14.93	-	245.40	-	-	342.70	-
9	19.19	-	281.08	-	-	391.69	-
11	23.46	-	297.93	-	-	413.23	-
13	27.72	-	297.44	-	-	408.09	-
15	31.99	-	282.08	-	-	377.05	-

Table 2.3a Comparison of modelling data with Ricker and sinusoidal approximations for Type II reflectivity at 18-Hz peak frequency ($\lambda_d = 152.14$ m).

Thickness		Absolute Maximum Amplitude (Input = 1000)				
b (m)	$(b/\lambda_d) \times 10^{-2}$	Modelling (M)	Ricker (R)	$\frac{R-M}{M} \times 100$	Sinusoidal (S)	$\frac{R-M}{M} \times 100$
0	0.00	209.40	209.40	0.00	209.40	0.00
1	0.66	209.22	209.24	0.01	209.22	0.00
3	1.97	207.95	207.97	0.01	204.79	-0.01
5	3.29	205.49	205.44	-0.02	204.94	-0.27
7	4.60	201.45	201.63	-0.01	200.65	-0.40
9	5.92	197.06	196.56	-0.25	194.94	-1.09
11	7.23	190.59	190.22	-0.19	187.79	-1.49
13	8.54	183.57	182.62	-0.52	179.22	-2.43
15	9.86	175.59	173.74	-1.06	169.22	-3.76
17	11.17	165.87	163.60	-1.39	157.79	-5.12
19	12.49	156.11	152.19	-2.58	144.94	-7.71
21	13.80	145.64	139.51	-4.39	130.65	-11.47
23	15.12	134.52	125.56	-7.14	-	-
25	16.43	121.85	110.35	-10.42	-	-
27	17.75	110.89	-	-	-	-
29	19.06	97.40	-	-	-	-
31	20.38	83.66	-	-	-	-
33	21.69	72.12	-	-	-	-
35	23.01	62.28	-	-	-	-
37	24.32	58.67	-	-	-	-
39	25.63	58.03	-	-	-	-
41	26.95	59.48	-	-	-	-
43	28.26	61.96	-	-	-	-

Table 2.3b Comparison of modelling data with Ricker and sinusoidal approximations for Type II reflectivity at 31-Hz peak frequency ($\lambda_d = 88.34$ m).

Thickness		Absolute Maximum Amplitude (Input = 1000)				
b (m)	$(b/\lambda_d) \times 10^{-2}$	Modelling (M)	Ricker (R)	$\frac{R-M}{M} \times 100$	Sinusoidal (S)	$\frac{R-M}{M} \times 100$
0	0.00	209.40	209.40	0.00	209.40	0.00
1	1.13	208.87	208.93	0.03	208.87	0.00
3	3.40	205.11	205.17	0.03	204.63	-0.23
5	5.66	197.90	197.65	-0.13	196.16	-0.89
7	7.92	186.31	186.37	-0.02	183.45	-1.56
9	10.19	173.95	171.33	-1.53	166.50	-4.47
11	12.45	156.31	152.52	-2.48	145.31	-7.57
13	14.72	137.90	129.96	-6.11	119.89	-15.02
15	16.98	117.87	103.64	-13.73	-	-
17	19.24	94.74	-	-	-	-
19	21.51	72.95	-	-	-	-
21	23.77	59.78	-	-	-	-
23	26.04	58.22	-	-	-	-
25	28.30	62.17	-	-	-	-

Table 2.3c Comparison of modelling data with Ricker and sinusoidal approximations for Type II reflectivity at 50-Hz peak frequency ($\lambda_d = 54.77$ m).

Thickness		Absolute Maximum Amplitude (Input = 1000)				
b (m)	$(b/\lambda_d) \times 10^{-2}$	Modelling (M)	Ricker (R)	$\frac{R-M}{M} \times 100$	Sinusoidal (S)	$\frac{R-M}{M} \times 100$
0	0.00	209.40	209.40	0.00	209.40	0.00
1	1.83	208.01	208.22	0.10	208.02	0.00
3	5.48	198.33	198.79	0.23	197.00	-0.68
5	9.13	180.22	179.91	-0.17	174.95	-3.01
7	12.78	152.27	151.61	-0.44	141.88	-7.32
9	16.43	124.12	113.87	-9.00	97.79	-26.92
11	20.08	86.86	66.69	-	-	-
13	23.74	59.91	-	-	-	-
15	27.39	59.77	-	-	-	-
17	31.04	68.98	-	-	-	-

Table 2.4 Comparison of modelling data with Ricker and sinusoidal approximations for Type III reflectivity at 31-Hz peak frequency ($\lambda_d = 75.63$ m).

Thickness		Absolute Maximum Amplitude (Input = 1000)					
		Zero-Phase Input Wavelet			90°-Phase Input Wavelet		
h (m)	$(b/\lambda_d) \times 10^{-2}$	Ricker (R)	Modelling (M)	$\frac{R-M}{M} \times 100$	Sinusoidal (S)	Modelling (M)	$\frac{R-M}{M} \times 100$
0	0.00	70.10	70.10	0.00	70.10	70.10	0.00
1	1.32	73.10	75.45	-3.21	75.49	76.16	-0.89
3	3.97	93.74	102.63	-9.48	109.44	111.82	-2.17
5	6.61	125.28	135.62	-8.25	156.71	158.30	-1.01
7	9.26	161.56	166.45	-3.03	208.53	201.06	3.58
9	11.90	200.14	198.39	-0.87	262.34	246.39	6.08
11	14.54	240.07	223.31	-6.98	317.28	281.95	11.11
13	17.19	-	242.93	-	-	310.00	-
15	19.83	-	257.75	-	-	330.99	-
17	22.48	-	265.67	-	-	341.68	-
19	25.12	-	268.36	-	-	344.07	-
21	27.77	-	266.76	-	-	339.38	-
23	30.41	-	260.98	-	-	326.37	-

Table 2.5 Comparison of modelling data with Ricker and sinusoidal approximations for Type IV reflectivity at 31-Hz peak frequency ($\lambda_d = 83.20$ m).

Thickness		Absolute Maximum Amplitude (Input = 1000)				
h (m)	$(b/\lambda_d) \times 10^{-2}$	Modelling (M)	Ricker (R)	$\frac{R-M}{M} \times 100$	Sinusoidal (S)	$\frac{R-M}{M} \times 100$
0	0.00	209.00	209.00	0.00	209.00	0.00
1	1.20	208.59	208.53	-0.03	208.51	-0.04
3	3.61	205.14	204.81	-0.16	204.65	-0.24
5	6.01	198.42	197.42	-0.51	197.04	-0.70
7	8.41	188.82	186.51	-1.24	185.96	-1.54
9	10.82	177.99	172.35	-3.27	171.92	-3.53
11	13.22	163.67	155.42	-5.31	155.89	-4.99
13	15.63	151.33	-	-	-	-
15	18.03	139.15	-	-	-	-
17	20.43	129.29	-	-	-	-
19	22.84	124.51	-	-	-	-
21	25.24	122.79	-	-	-	-
23	27.64	123.80	-	-	-	-
25	30.04	126.48	-	-	-	-

Table 2.7a Comparison of modelling data with the sinusoidal and pseudo-Ricker approximations for Type V reflectivity with a 2-m underlying thin layer ($\lambda_{d_1} = 75.63$ m, $\lambda_{d_2} = 94.29$ m).

Wedge Thickness	Total Thickness	Absolute Maximum Amplitude (Input = 1000)					
		Zero-Phase Input Wavelet			90°-Phase Input Wavelet		
$(b/\lambda_{d_1}) \times 10^{-2}$	$(2/\lambda_{d_2} + b/\lambda_{d_1}) \times 10^{-2}$	Pseudo Ricker (R)	Modelling (M)	$\frac{R-M}{M} \times 100$	Sinusoidal (S)	Modelling (M)	$\frac{R-M}{M} \times 100$
0	2.12	14.43	14.23	1.41	19.25	19.88	-3.17
1	3.44	40.32	39.52	2.02	53.73	55.21	-2.68
3	6.09	94.65	90.11	5.04	125.11	126.90	-1.42
5	8.73	156.87	134.68	16.48	204.14	189.15	7.92
7	11.38	231.35	180.70	28.03	295.36	253.34	16.59
9	14.02	-	217.00	-	-	303.96	-
11	16.66	-	249.92	-	-	349.63	-
13	19.31	-	272.01	-	-	379.91	-
15	21.95	-	288.35	-	-	401.82	-
17	24.60	-	297.89	-	-	413.65	-
19	27.24	-	299.91	-	-	414.11	-
21	29.89	-	296.22	-	-	405.43	-
23	32.53	-	286.90	-	-	386.61	-

Table 2.7b Comparison of modelling data with the sinusoidal and pseudo-Ricker approximations for Type V reflectivity with a 4-m underlying thin layer ($\lambda_{d_1} = 75.63$ m, $\lambda_{d_2} = 94.29$ m).

Wedge Thickness	Total Thickness	Absolute Maximum Amplitude (Input = 1000)					
		Zero-Phase Input Wavelet			90°-Phase Input Wavelet		
$(b/\lambda_{d_1}) \times 10^{-2}$	$(a/\lambda_{d_2} + b/\lambda_{d_1}) \times 10^{-2}$	Pseudo Ricker (R)	Modelling (M)	$\frac{R-M}{M} \times 100$	Sinusoidal (S)	Modelling (M)	$\frac{R-M}{M} \times 100$
0	4.24	28.87	28.42	1.58	38.49	39.73	-3.12
1	5.56	54.87	54.11	1.40	73.11	76.58	-4.53
3	8.21	107.50	102.57	4.81	142.86	144.18	-0.92
5	10.85	167.75	144.56	16.04	219.95	202.68	8.52
7	13.50	240.24	188.75	27.28	309.08	264.14	17.01
9	16.14	-	223.97	-	-	312.96	-
11	18.78	-	254.67	-	-	355.24	-
13	21.43	-	274.52	-	-	382.19	-
15	24.07	-	289.13	-	-	401.33	-
17	26.72	-	297.03	-	-	410.34	-
19	29.36	-	297.65	-	-	408.35	-
21	32.01	-	293.24	-	-	398.35	-
23	34.65	-	283.33	-	-	377.97	-

Table 2.7c Comparison of modelling data with the sinusoidal and pseudo-Ricker approximations for Type V reflectivity with a 6-m underlying thin layer ($\lambda_{d_1} = 75.63$ m, $\lambda_{d_2} = 94.29$ m).

Wedge Thickness	Total Thickness	Absolute Maximum Amplitude (Input = 1000)					
		Zero-Phase Input Wavelet			90°-Phase Input Wavelet		
$(b/\lambda_{d_1}) \times 10^{-2}$	$(a/\lambda_{d_2} + b/\lambda_{d_1}) \times 10^{-2}$	Pseudo Ricker (R)	Modelling (Δf)	$\frac{R - \Delta f}{\Delta f} \times 100$	Sinusoidal (S)	Modelling (M)	$\frac{R - M}{M} \times 100$
0	6.36	43.30	42.52	1.83	57.73	59.43	2.86
1	7.68	70.91	65.65	8.01	93.93	92.63	1.40
3	10.33	120.84	112.31	7.60	161.09	157.49	2.29
5	12.97	178.20	153.31	16.24	235.36	214.28	9.84
7	15.62	247.85	195.24	26.95	321.62	272.20	18.16
9	18.26	-	228.09	-	-	317.48	-
11	20.90	-	256.82	-	-	356.61	-
13	23.55	-	275.11	-	-	380.72	-
15	26.19	-	288.12	-	-	397.16	-
17	28.84	-	294.90	-	-	404.34	-
19	31.48	-	294.66	-	-	400.62	-
21	34.13	-	289.37	-	-	388.41	-
23	36.77	-	279.25	-	-	367.01	-

Table 2.7d Comparison of modelling data with the sinusoidal and pseudo-Ricker approximations for Type V reflectivity with a 8-m underlying thin layer ($\lambda_{d_1} = 75.63$ m, $\lambda_{d_2} = 94.29$ m).

Wedge Thickness	Total Thickness	Absolute Maximum Amplitude (Input = 1000)					
		Zero-Phase Input Wavelet			90°-Phase Input Wavelet		
$(b/\lambda_{d_1}) \times 10^{-2}$	$(8/\lambda_{d_2} + b/\lambda_{d_1}) \times 10^{-2}$	Pseudo Ricker (R)	Modelling (Δf)	$\frac{R-M}{M} \times 100$	Sinusoidal (S)	Modelling (M)	$\frac{R-M}{M} \times 100$
0	8.48	57.73	54.51	5.91	76.98	76.19	1.04
1	9.80	89.40	76.97	16.15	117.10	108.31	8.04
3	12.45	135.68	121.04	12.10	180.74	169.15	6.85
5	15.09	189.10	159.20	18.78	251.24	221.60	13.38
7	17.74	254.92	198.99	28.10	333.69	276.01	20.90
9	20.38	-	230.30	-	-	318.44	-
11	23.02	-	257.09	-	-	354.25	-
13	25.67	-	273.99	-	-	376.15	-
15	28.31	-	285.88	-	-	390.51	-
17	30.96	-	291.53	-	-	395.22	-
19	33.60	-	290.75	-	-	390.19	-
21	36.25	-	285.66	-	-	378.25	-
23	38.89	-	275.69	-	-	356.54	-

Table 2.7e Comparison of modelling data with the sinusoidal and pseudo-Ricker approximations for Type V reflectivity with a 10-m underlying thin layer ($\lambda_{d_1} = 75.63$ m, $\lambda_{d_2} = 94.29$ m).

Wedge Thickness	Total Thickness	Absolute Maximum Amplitude (Input = 1000)						
		Zero-Phase Input Wavelet		90°-Phase Input Wavelet		90°-Phase Input Wavelet		
$(b/\lambda_{d_1}) \times 10^{-2}$	$(10/\lambda_{d_2} + b/\lambda_{d_1}) \times 10^{-2}$	Pseudo Ricker (R)	Modelling (M)	$\frac{R-M}{M} \times 100$	Modelling (M)	Sinusoidal (S)	Modelling (M)	$\frac{R-M}{M} \times 100$
0	10.61	72.17	65.51	9.23	91.55	96.22	91.55	4.85
1	11.93	111.06	85.85	22.70	120.53	143.42	120.53	15.96
3	14.58	153.00	127.12	16.92	176.87	202.78	176.87	12.78
5	17.22	201.46	163.45	23.25	226.00	268.53	226.00	18.82
7	19.87	262.31	200.92	30.55	276.36	346.15	276.36	25.25
9	22.51	-	230.45	-	315.95	-	315.95	-
11	25.15	-	255.75	-	349.02	-	349.02	-
13	27.80	-	271.37	-	368.19	-	368.19	-
15	30.44	-	282.44	-	380.87	-	380.87	-
17	33.09	-	287.96	-	385.43	-	385.43	-
19	35.73	-	287.03	-	379.85	-	379.85	-
21	38.38	-	281.71	-	366.75	-	366.75	-
23	41.02	-	272.17	-	345.42	-	345.42	-

Table 2.8a Comparison of modelling data with the sinusoidal and pseudo-Ricker approximations for Type VI reflectivity with a 2-m underlying thin layer ($\lambda_{d_1} = 75.63$ m, $\lambda_{d_2} = 94.29$ m).

Wedge Thickness	Total Thickness	Absolute Maximum Amplitude (Input = 1000)					
		Zero-Phase Input Wavelet			90°-Phase Input Wavelet		
$(b/\lambda_{d_1}) \times 10^{-2}$	$(2/\lambda_{d_2} + b/\lambda_{d_1}) \times 10^{-2}$	Pseudo Ricker (R)	Modelling (M)	$\frac{R-M}{M} \times 100$	Sinusoidal (S)	Modelling (M)	$\frac{R-M}{M} \times 100$
0	2.12	15.61	15.38 (t)	1.50	20.81	21.49 (p)	-3.16
1	3.44	8.59	8.45 (t)	1.65	11.32	11.69 (p)	-3.17
3	6.09	10.79	10.27 (p)	5.06	13.10	13.80 (t)	-5.07
5	8.73	29.49	24.58 (p)	19.98	36.65	33.92 (t)	8.05
7	11.38	52.38	39.54 (p)	32.47	64.51	54.66 (t)	18.02
9	14.02	-	52.15 (p)	-	-	71.93 (t)	-
11	16.66	-	63.88 (p)	-	-	88.04 (t)	-
13	19.31	-	73.71 (p)	-	-	101.43 (t)	-
15	21.95	-	81.50 (p)	-	-	112.24 (t)	-
17	24.60	-	86.62 (p)	-	-	118.92 (t)	-
19	27.24	-	90.34 (p)	-	-	123.03 (t)	-
21	29.89	-	90.81 (p)	-	-	123.52 (t)	-
23	32.53	-	89.90 (p)	-	-	121.08 (t)	-
25	35.18	-	87.56 (p)	-	-	115.40 (t)	-
27	37.82	-	83.99 (p)	-	-	107.70 (t)	-

Table 2.8b Comparison of modelling data with the sinusoidal and pseudo-Ricker approximations for Type VI reflectivity with a 4-m underlying thin layer ($\lambda_{d_1} = 75.63$ m, $\lambda_{d_2} = 94.29$ m).

Wedge Thickness	Total Thickness	Absolute Maximum Amplitude (Input = 1000)					
		Zero-Phase Input Wavelet			90°-Phase Input Wavelet		
b (m)	$(a/\lambda_{d_2} + b/\lambda_{d_1}) \times 10^{-2}$	Pseudo Ricker (R)	Modelling (M)	$\frac{R-M}{M} \times 100$	Sinusoidal (S)	Modelling (M)	$\frac{R-M}{M} \times 100$
0	0.00	31.21	30.45 (t)	2.50	41.61	42.55 (p)	-2.21
1	1.32	25.81	25.03 (t)	3.12	33.68	34.74 (p)	-3.05
3	3.97	18.20	16.96 (p)	7.31	21.53	21.39 (p)	0.65
5	6.61	28.17	25.02 (p)	12.59	32.09	30.13 (t)	6.51
7	9.26	49.62	40.41 (p)	22.79	57.90	51.09 (t)	13.33
9	11.90	-	54.62 (p)	-	-	70.57 (t)	-
11	14.54	-	67.99 (p)	-	-	88.83 (t)	-
13	17.19	-	79.68 (p)	-	-	104.44 (t)	-
15	19.83	-	89.75 (p)	-	-	117.71 (t)	-
17	22.48	-	96.60 (p)	-	-	126.47 (t)	-
19	25.12	-	101.01 (p)	-	-	131.65 (t)	-
21	27.77	-	103.09 (p)	-	-	133.34 (t)	-
23	30.41	-	103.06 (p)	-	-	131.74 (t)	-
25	33.06	-	101.00 (p)	-	-	126.94 (t)	-
27	35.70	-	97.78 (p)	-	-	119.45 (t)	-

Table 2.8c Comparison of modelling data with the sinusoidal and pseudo-Ricker approximations for Type VI reflectivity with a 6-m underlying thin layer ($\lambda_{d_1} = 75.63$ m, $\lambda_{d_2} = 94.29$ m).

Wedge Thickness	Total Thickness	Absolute Maximum Amplitude (Input = 1000)					
		Zero-Phase Input Wavelet			90°-Phase Input Wavelet		
$(b/\lambda_{d_1}) \times 10^{-2}$	$(c/\lambda_{d_2} + b/\lambda_{d_1}) \times 10^{-2}$	Pseudo Ricker (R)	Modelling (M)	$\frac{R-M}{M} \times 100$	Simusoidal (S)	Modelling (M)	$\frac{R-M}{M} \times 100$
0	6.36	46.82	44.89 (t)	4.30	62.42	62.74 (p)	-0.51
1	7.68	45.27	39.81 (t)	13.71	58.26	55.43 (p)	5.11
3	10.33	37.35	31.76 (p)	17.60	45.62	42.52 (p)	7.29
5	12.97	41.00	36.57 (p)	12.11	46.78	44.92 (p)	4.14
7	15.62	57.60	50.37 (p)	14.35	65.08	56.35 (t)	15.49
9	18.26	-	65.52 (p)	-	-	76.87 (t)	-
11	20.90	-	79.73 (p)	-	-	96.25 (t)	-
13	23.55	-	92.34 (p)	-	-	113.17 (t)	-
15	26.19	-	102.09 (p)	-	-	126.75 (t)	-
17	28.84	-	109.73 (p)	-	-	136.45 (t)	-
19	31.48	-	116.22 (p)	-	-	143.48 (t)	-
21	34.13	-	117.62 (p)	-	-	145.61 (t)	-
23	36.77	-	119.03 (p)	-	-	144.18 (t)	-
25	35.18	-	116.23 (p)	-	-	139.52 (t)	-
27	37.82	-	113.09 (p)	-	-	130.90 (t)	-

Table 2.8d Comparison of modelling data with the sinusoidal and pseudo-Ricker approximations for Type VI reflectivity with a 8-m underlying thin layer ($\lambda_{d_1} = 75.63$ m, $\lambda_{d_2} = 94.29$ m).

Wedge Thickness	Total Thickness	Absolute Maximum Amplitude (Input = 1000)					
		Zero-Phase Input Wavelet			90°-Phase Input Wavelet		
h (m)	$(8/\lambda_{d_2} + h/\lambda_{d_1}) \times 10^{-2}$	Pseudo Ricker (R)	Modelling (A)	$\frac{R-M}{M} \times 100$	Sinusoidal (S)	Modelling (M)	$\frac{R-M}{M} \times 100$
0	0.00	62.42	58.44 (t)	6.81	83.23	81.67 (p)	1.56
1	1.32	67.74	53.79 (t)	25.93	85.84	75.00 (p)	14.45
3	3.97	60.59	47.10 (p)	28.64	74.07	63.85 (p)	16.00
5	6.61	62.42	53.24 (p)	17.24	72.67	66.28 (p)	9.64
7	9.26	75.32	64.57 (p)	16.65	85.26	73.23 (p)	16.43
9	11.90	-	79.18 (p)	-	-	86.48 (t)	-
11	14.54	-	93.57 (p)	-	-	106.23 (t)	-
13	17.19	-	107.98 (p)	-	-	124.76 (t)	-
15	19.83	-	117.95 (p)	-	-	138.73 (t)	-
17	22.48	-	125.85 (p)	-	-	148.78 (t)	-
19	25.12	-	131.01 (p)	-	-	154.80 (t)	-
21	27.77	-	133.54 (p)	-	-	156.86 (t)	-
23	30.41	-	134.29 (p)	-	-	155.15 (t)	-
25	33.06	-	131.44 (p)	-	-	150.51 (t)	-
27	35.70	-	128.21 (p)	-	-	141.49 (t)	-

Table 2.8e Comparison of modelling data with the sinusoidal and pseudo-Ricker approximations for Type VI reflectivity with a 10-m underlying thin layer ($\lambda_{d_1} = 75.63$ m, $\lambda_{d_2} = 94.29$ m).

Wedge Thickness	Total Thickness	Absolute Maximum Amplitude (Input = 1000)					
		Zero-Phase Input Wavelet			90°-Phase Input Wavelet		
b (m)	$(10/\lambda_{d_2} + b/\lambda_{d_1}) \times 10^{-2}$	Pseudo Ricker (R)	Modelling (M)	$\frac{R-M}{M} \times 100$	Sinusoidal (S)	Modelling (M)	$\frac{R-M}{M} \times 100$
0	0.00	78.03	70.83 (t)	10.17	104.03	98.97 (p)	5.11
1	1.32	93.76	66.69 (t)	40.59	117.06	93.06 (p)	25.79
3	3.97	87.57	61.78 (p)	41.74	106.82	84.12 (p)	26.99
5	6.61	89.15	68.56 (p)	30.03	104.65	87.47 (p)	19.64
7	9.26	100.19	79.92 (p)	25.36	114.47	94.15 (p)	21.58
9	11.90	-	95.40 (p)	-	136.22	104.68 (p)	-
11	14.54	-	109.82 (p)	-	-	118.27 (t)	-
13	17.19	-	122.77 (p)	-	-	135.63 (t)	-
15	19.83	-	132.69 (p)	-	-	150.33 (t)	-
17	22.48	-	140.46 (p)	-	-	159.93 (t)	-
19	25.12	-	146.81 (p)	-	-	166.50 (t)	-
21	27.77	-	149.06 (p)	-	-	167.37 (t)	-
23	30.41	-	148.95 (p)	-	-	165.92 (t)	-
25	33.06	-	146.72 (p)	-	-	160.38 (t)	-
27	35.70	-	142.29 (p)	-	-	150.92 (t)	-

Table 2.9a Comparison of modelling data with the sinusoidal and pseudo-Ricker approximations for Type VII reflectivity with a 2-m underlying thin layer ($\lambda_{d_1} = 83.20$ m, $\lambda_{d_2} = 94.29$ m).

Wedge Thickness	Total Thickness	Absolute Maximum Amplitude (Input = 1000)						
		Zero-Phase Input Wavelet			90°-Phase Input Wavelet			
b (m)	$(\frac{b}{\lambda_{d_1}}) \times 10^{-2}$	$(\frac{2}{\lambda_{d_2}} + \frac{b}{\lambda_{d_1}}) \times 10^{-2}$	Pseudo Ricker (R)	Modelling (M)	$\frac{R-M}{M} \times 100$	Sinusoidal (S)	Modelling (M)	$\frac{R-M}{M} \times 100$
0	0.00	2.12	207.75	207.89	-0.07	207.62	207.88	-0.13
1	1.20	3.32	207.16	207.45	-0.14	206.91	207.44	-0.26
3	3.61	5.73	202.28	202.65	-0.18	201.37	202.84	-0.72
5	6.01	8.13	193.51	194.93	-0.73	192.08	195.67	-1.83
7	8.41	10.53	181.06	184.44	-1.83	179.44	186.50	-3.79
9	10.82	12.94	165.38	170.88	-3.22	164.32	175.39	-6.31
11	13.22	15.34	147.32	158.11	-6.82	148.35	165.86	-10.56
13	15.63	17.75	128.62	145.03	-11.31	134.56	156.81	-14.19
15	18.03	20.15	112.72	134.07	-15.92	127.92	149.68	-14.54
17	20.43	22.55	-	126.65	-	-	144.70	-
19	22.84	24.96	-	122.95	-	-	141.73	-
21	25.24	27.36	-	122.76	-	-	140.63	-
23	27.64	29.76	-	124.55	-	-	140.36	-
25	30.05	32.14	-	127.93	-	-	140.86	-
27	32.45	34.57	-	131.19	-	-	141.44	-

Table 2.9b Comparison of modelling data with the sinusoidal and pseudo-Ricker approximations for Type VII reflectivity with a 4-m underlying thin layer ($\lambda_{d1} = 83.20$ m, $\lambda_{d2} = 94.29$ m).

b (m)	Wedge Thickness $(b/\lambda_{d1}) \times 10^{-2}$	Total Thickness $(a/\lambda_{d2} + b/\lambda_{d1}) \times 10^{-2}$	Absolute Maximum Amplitude (Input = 1000)					
			Zero-Phase Input Wavelet		90°-Phase Input Wavelet			
			Pseudo Ricker (R)	Modelling (M)	$\frac{R-M}{M} \times 100$	Sinusoidal (S)	Modelling (M)	$\frac{R-M}{M} \times 100$
0	0.00	4.24	203.12	203.38	-0.13	202.61	203.24	-0.31
1	1.20	5.44	201.41	202.18	-0.38	201.13	202.02	-0.44
3	3.61	7.85	195.55	196.05	-0.26	193.86	196.10	-1.14
5	6.01	10.25	185.78	187.00	-0.65	182.76	187.74	-2.65
7	8.41	12.65	172.22	176.54	-2.45	168.13	178.85	-5.99
9	10.82	15.06	155.24	162.45	-4.44	150.70	167.62	-10.10
11	13.22	17.46	135.62	148.93	-8.94	132.07	157.83	-16.32
13	15.63	19.87	115.05	136.48	-15.70	115.55	149.58	-22.75
15	18.03	22.27	97.33	126.82	-23.38	107.23	143.48	-25.26
17	20.43	24.67	-	121.37	-	-	139.80	-
19	22.84	27.08	-	119.08	-	-	137.59	-
21	25.24	29.48	-	119.74	-	-	136.78	-
23	27.64	31.88	-	122.22	-	-	136.90	-
25	30.05	34.29	-	125.93	-	-	137.64	-
27	32.45	36.69	-	129.30	-	-	138.49	-

Table 2.9c Comparison of modelling data with the sinusoidal and pseudo-Ricker approximations for Type VII reflectivity with a 6-m underlying thin layer ($\lambda_{d_1} = 83.20$ m, $\lambda_{d_2} = 94.29$ m).

Wedge Thickness		Total Thickness $(a/\lambda_{d_2} + b/\lambda_{d_1}) \times 10^{-2}$	Absolute Maximum Amplitude (Input = 1000)					
b (m)	$(b/\lambda_{d_1}) \times 10^{-2}$		Zero-Phase Input Wavelet			90°-Phase Input Wavelet		
			Pseudo Ricker (R)	Modelling (Mf)	$\frac{R-M}{M} \times 100$	Sinusoidal (S)	Modelling (M)	$\frac{R-M}{M} \times 100$
0	0.00	6.36	195.42	196.63	-0.62	194.31	196.19	-0.96
1	1.20	7.56	192.32	194.81	-1.28	192.41	194.30	-0.97
3	3.61	9.97	185.42	187.59	-1.16	183.29	187.28	-2.13
5	6.01	12.37	174.59	177.52	-1.65	170.29	177.97	-4.32
7	8.41	14.77	159.90	165.53	-3.40	153.60	167.81	-8.47
9	10.82	17.18	141.62	151.09	-6.27	133.79	156.69	-14.61
11	13.22	19.58	120.46	138.84	-13.24	112.42	148.54	-24.32
13	15.63	21.99	93.21	127.13	-26.68	98.11	141.17	-30.50
15	18.03	24.39	-	118.75	-	-	136.04	-
17	20.43	26.79	-	113.91	-	-	132.44	-
19	22.84	29.20	-	113.04	-	-	131.00	-
21	25.24	31.60	-	114.63	-	-	130.73	-
23	27.64	34.00	-	118.13	-	-	131.78	-
25	30.05	36.41	-	122.03	-	-	132.67	-
27	32.45	38.81	-	124.87	-	-	132.97	-

Table 2.9d Comparison of modelling data with the sinusoidal and pseudo-Ricker approximations for Type VII reflectivity with a 8-m underlying thin layer ($\lambda_{d_1} = 83.20$ m, $\lambda_{d_2} = 94.29$ m).

Wedge Thickness	Total Thickness	Absolute Maximum Amplitude (Input = 1000)					
		Zero-Phase Input Wavelet			90°-Phase Input Wavelet		
$(b/\lambda_{d_1}) \times 10^{-2}$	$(8/\lambda_{d_2} + b/\lambda_{d_1}) \times 10^{-2}$	Pseudo Ricker (R)	Modelling (Λ_f)	$\frac{R-M}{M} \times 100$	Sinusoidal (S)	Modelling (M)	$\frac{R-M}{M} \times 100$
0	8.48	184.74	186.58	-0.99	182.86	185.47	-1.41
1	9.68	180.24	184.17	-2.13	181.40	182.91	-0.83
3	12.09	172.18	175.95	-2.14	170.24	174.82	-2.62
5	14.49	160.20	164.99	-2.90	155.20	164.66	-5.75
7	16.89	144.30	153.76	-6.15	136.27	155.63	-12.44
9	19.30	124.64	139.17	-10.44	113.87	144.84	-21.38
11	21.70	101.83	126.10	-19.25	89.37	136.40	-34.48
13	24.11	-	115.29	-	-	130.13	-
15	26.51	-	108.38	-	-	126.12	-
17	28.91	-	105.73	-	-	124.14	-
19	31.32	-	105.97	-	-	123.34	-
21	33.72	-	108.26	-	-	123.48	-
23	36.12	-	111.59	-	-	124.15	-
25	38.53	-	115.57	-	-	125.16	-
27	40.93	-	118.83	-	-	126.07	-

Table 2.9e Comparison of modelling data with the sinusoidal and pseudo-Ricker approximations for Type VII reflectivity with a 10-m underlying thin layer ($\lambda_{d_1} = 83.20$ m, $\lambda_{d_2} = 94.29$ m).

Wedge Thickness	Total Thickness	Absolute Maximum Amplitude (Input = 1000)					
		Zero-Phase Input Wavelet			90°-Phase Input Wavelet		
b (m)	$(b/\lambda_{d_1}) \times 10^{-2}$	Pseudo Ricker (R)	Modelling (M)	$\frac{R-M}{M} \times 100$	Sinusoidal (S)	Modelling (M)	$\frac{R-M}{M} \times 100$
0	0.00	171.16	175.41	-2.42	168.48	173.26	-2.76
1	1.20	165.84	171.32	-3.20	169.30	168.73	0.34
3	3.61	156.43	163.65	-4.41	155.87	161.24	3.18
5	6.01	143.16	152.14	-5.90	138.59	150.51	-7.92
7	8.41	125.92	139.41	-9.68	117.27	140.18	-16.34
9	10.82	104.75	124.76	-16.03	91.98	130.01	-29.25
11	13.22	80.02	112.00	-28.55	63.58	122.61	-48.14
13	15.63	-	103.34	-	-	118.76	-
15	18.03	-	97.76	-	-	115.79	-
17	20.43	-	95.32	-	-	113.54	-
19	22.84	-	96.62	-	-	113.37	-
21	25.24	-	99.52	-	-	113.87	-
23	27.64	-	103.93	-	-	115.66	-
25	30.05	-	107.89	-	-	116.72	-
27	32.45	-	110.15	-	-	116.70	-

Table 3.1 Theoretical and modelling peak frequency values for Type I reflectivity.

Thickness <i>b</i> (metres)	$f_0 = 18\text{Hz}, \lambda_d = 130.26\text{m}$		$f_0 = 31\text{Hz}, \lambda_d = 75.63\text{m}$		$f_0 = 50\text{Hz}, \lambda_d = 46.89\text{m}$				
	$(b/\lambda_d) \times 10^{-2}$	Theoretical	Modelling	$(b/\lambda_d) \times 10^{-2}$	Theoretical	Modelling	$(b/\lambda_d) \times 10^{-2}$	Theoretical	Modelling
1	0.77	22.0	21.9	1.32	38.0	37.9	2.13	61.2	60.8
3	2.30	22.0	21.9	3.97	37.9	37.7	6.40	60.8	60.6
5	3.83	22.0	21.8	6.61	37.7	37.4	10.67	59.9	59.6
7	5.37	21.9	21.8	9.26	37.3	37.2	14.93	58.6	58.3
9	6.91	21.8	21.8	11.90	36.9	36.8	19.19	57.0	56.4
11	8.44	21.7	21.5	14.54	36.4	36.2	23.46	55.0	54.7
13	9.98	21.6	21.5	17.19	35.9	35.5	27.72	52.7	52.6
15	11.52	21.5	21.3	19.83	35.1	34.9	31.99	50.6	50.5
17	13.05	21.3	21.2	22.48	34.4	34.3	-	-	-
19	14.59	21.2	20.9	25.12	33.5	33.4	-	-	-
21	16.12	21.0	20.9	27.77	32.6	32.5	-	-	-
23	17.66	20.7	20.5	30.41	31.5	31.6	-	-	-
25	19.19	20.5	20.3	-	-	-	-	-	-
27	20.73	20.3	20.1	-	-	-	-	-	-
29	22.26	20.0	19.8	-	-	-	-	-	-
31	23.80	19.7	19.7	-	-	-	-	-	-
33	25.33	19.4	19.4	-	-	-	-	-	-
35	26.87	19.1	19.1	-	-	-	-	-	-
37	28.40	18.8	18.8	-	-	-	-	-	-
$f_p = \sqrt{\frac{3}{2}} f_0$		22.0			38.0			61.2	

Table 3.3 Theoretical, modelling, and thin-bed peak frequency values for Type III reflectivity.

Thickness <i>b</i> (metres)	$f_0 = 31\text{Hz}, \lambda_d = 75.63\text{m}$			
	$(b/\lambda_d) \times 10^{-2}$	Theoretical	Modelling	Thin-Bed
1	1.32	31.7	31.7	31.7
2	2.64	33.2	33.1	33.9
3	3.97	34.7	34.7	37.6
4	5.28	35.6	35.4	42.7
5	6.61	36.1	35.9	49.3
7	9.26	36.4	36.4	-
9	11.90	36.4	36.2	-
11	14.54	36.1	35.9	-
13	17.19	35.6	35.5	-
15	19.83	35.0	34.9	-
17	22.48	34.3	34.2	-
19	25.12	33.5	33.2	-
21	27.77	32.7	32.4	-
23	30.41	31.9	31.5	-

Table 3.4 Theoretical, modelling, and thin-bed peak frequency values for Type IV reflectivity.

Thickness <i>b</i> (metres)	$f_0 = 31\text{Hz}, \lambda_d = 83.20\text{m}$			
	$(b/\lambda_d) \times 10^{-2}$	Theoretical	Modelling	Thin-Bed
1	1.20	31.0	31.0	31.0
3	3.61	30.8	30.5	30.8
5	6.01	30.5	30.2	30.5
7	8.41	30.0	29.8	30.0
9	10.82	29.4	29.4	29.3
11	13.22	28.7	28.2	28.5
13	15.63	27.9	27.6	27.4
15	18.03	26.9	26.9	26.3
17	20.43	26.0	25.7	24.9
19	22.84	25.1	24.9	23.4
21	25.24	24.3	23.8	21.7
23	27.64	23.5	23.0	20.0
25	30.04	22.7	22.5	18.3

Table 3.5 Peak frequency comparisons for Types V, VI, and VII reflectivities. λ_d is 75.63 m for Types V and VI, and is 83.2 m for Type VII.

Thickness <i>b</i> (metres)	$(b/\lambda_d) \times 10^{-2}$		Peak Frequency (Hz) Type V Underlying Layer = 2m		Peak Frequency (Hz) Type VI Underlying Layer = 4 m		Peak Frequency (Hz) Type VII Underlying Layer = 6 m	
	Type V, Type VI	Type VII	Theoretical	Modelling	Theoretical	Modelling	Theoretical	Modelling
0	0.00	0.00	37.9	37.9	37.8	37.7	30.3	30.3
1	1.32	1.20	37.9	37.9	38.1	38.0	30.2	30.2
3	3.97	3.61	37.8	37.7	42.2	42.1	29.9	29.8
5	6.61	6.01	37.5	37.5	43.2	43.1	29.3	29.3
7	9.26	8.41	37.2	37.1	41.6	41.6	28.7	28.7
9	11.90	10.82	36.8	36.7	40.5	40.5	27.9	27.8
11	14.54	13.22	36.2	36.1	39.7	39.7	27.1	27.0
13	17.19	15.63	35.6	35.5	38.9	38.8	26.2	26.1
15	19.83	18.03	37.9	34.9	38.1	38.0	25.2	25.2
17	22.48	20.43	34.1	34.1	37.2	37.2	24.3	24.3
19	25.12	22.84	33.3	33.3	36.4	36.3	23.4	23.4
21	27.77	25.24	32.4	32.4	35.4	35.4	22.6	22.5
23	30.41	27.64	31.5	31.4	34.5	34.4	21.8	21.8
25	-	30.05	-	-	-	-	21.1	21.0

Table 3.6 Peak frequency values for Type V reflectivity.

Wedge Thickness b (metres)	$(b/\lambda_d) \times 10^{-2}$	Peak Frequency (Hz) for Underlying Layer Thickness			
		0 m	2 m	6 m	10 m
0	0.00	-	37.9	37.2	36.2
1	1.32	38.0	37.9	37.2	36.2
3	3.97	37.9	37.8	37.0	35.7
5	6.61	37.7	37.5	36.7	35.3
7	9.26	37.3	37.2	36.3	34.9
9	11.90	36.9	36.8	35.8	34.5
11	14.54	36.4	36.2	35.3	33.9
13	17.19	35.9	35.6	34.6	33.3
15	19.83	35.1	34.9	33.9	32.7
17	22.48	34.4	34.1	33.1	31.9
19	25.12	33.5	33.3	32.3	31.1
21	27.77	32.6	32.4	31.4	30.3
23	30.41	31.5	31.5	30.5	29.4

Table 3.7 Peak frequency values for Type VI reflectivity.

Thickness b (metres)	$(b/\lambda_d) \times 10^{-2}$	Peak Frequency for Underlying Layer Thickness			
		0 m	2 m	6 m	10 m
0	0.00	-	37.9	37.7	37.1
1	1.32	38.0	38.3	37.9	37.4
3	3.97	37.8	41.2	40.1	38.8
5	6.61	37.6	39.2	42.9	40.8
7	9.26	37.3	38.6	42.8	41.8
9	11.90	36.9	38.1	42.0	41.7
11	14.54	36.4	37.6	41.1	41.3
13	17.19	35.8	37.0	40.2	40.6
15	19.83	35.1	36.4	39.3	39.8
17	22.48	34.4	35.6	38.4	39.0
19	25.12	33.6	34.8	37.5	38.1
21	27.77	32.7	33.9	36.5	37.1
23	30.41	31.8	33.0	35.5	36.1

Table 3.8 Peak frequency values for Type VII reflectivity.

Thickness b (metres)	$(b/\lambda_d) \times 10^{-2}$	Peak Frequency for Underlying Layer Thickness			
		0 m	2 m	6 m	10 m
0	0.00	-	30.9	30.3	29.2
1	1.20	31.0	30.9	30.2	29.0
3	3.61	30.8	30.6	29.9	28.5
5	6.01	30.5	30.2	29.3	27.9
7	8.41	30.0	29.7	28.7	27.3
9	10.82	29.4	29.0	27.9	26.4
11	13.22	28.6	28.2	27.1	25.5
13	15.63	27.8	27.4	26.2	24.6
15	18.03	26.9	26.5	25.2	23.7
17	20.43	25.9	25.5	24.3	22.9
19	22.84	25.0	24.6	23.4	22.0
21	25.24	24.1	23.7	22.6	21.2
23	27.64	23.2	22.8	21.8	20.5
25	30.05	22.4	22.1	21.1	19.8

Appendix C

Table 5.2a Percentage change in maximum absolute amplitude of *P*-wave for Type I reflectivity as σ changes from 0.3 to 0.1 for the thin layer. Positive and negative signs represent amplitude increases and decreases respectively.

Incidence Angle θ_i	% Change in Maximum Absolute Amplitude				
	Single Interface	Thin-bed Thickness			
		1 m	5 m	9 m	13 m
0	61.6	148.1	97.6	85.0	73.4
5.71	62.4	120.0	97.2	87.9	74.3
11.31	64.7	159.2	106.2	91.6	77.9
16.70	68.7	164.4	108.7	94.8	83.0
21.80	74.0	182.1	116.2	105.2	89.8
26.57	80.5	197.1	135.3	115.0	98.6
30.97	87.8	220.7	148.5	127.0	109.5
34.99	95.0	248.0	156.5	139.2	119.0
38.66	101.6	263.6	170.3	154.0	128.3
41.99	106.7	280.0	190.9	164.5	137.7
45.00	109.8	284.2	197.6	173.9	143.7
47.73	110.7	300.0	204.0	180.3	148.4
50.19	109.5	326.7	222.0	181.0	149.2

Table 5.2b Percentage change in maximum absolute amplitude of *PS*-wave for Type I reflectivity as σ changes from 0.3 to 0.1 for the thin layer. Positive and negative signs represent amplitude increases and decreases respectively.

Incidence Angle θ_i	% Change in Maximum Absolute Amplitude				
	Single Interface	Thin-bed Thickness			
		1 m	5 m	9 m	13 m
0	0	0	0	0	0
7.44	19.7	36.4	28.3	23.7	20.1
14.72	20.3	33.3	27.7	25.2	20.8
21.71	21.4	44.2	29.4	26.1	21.9
28.29	22.8	46.7	32.3	28.2	23.6
34.35	24.7	50.8	33.7	30.2	25.7
39.87	27.0	54.8	35.7	32.9	28.3
44.81	29.6	58.3	41.6	36.4	31.6
49.18	32.5	72.0	45.7	40.0	35.1

Table 5.3a Percentage change in maximum absolute amplitude of *P*-wave for Type IA reflectivity as σ changes from 0.3 to 0.1 for the thin layer. Positive and negative signs represent amplitude increases and decreases respectively.

Incidence Angle θ_i	% Change in Maximum Absolute Amplitude				
	Single Interface	Thin-bed Thickness			
		1 m	5 m	9 m	13 m
0	-65.2	-63.0	-56.9	-58.0	-59.2
5.71	-66.6	-65.2	-58.4	-59.7	-60.7
11.31	-71.1	-61.1	-62.4	-63.0	-64.9
16.70	-78.8	-72.5	-69.2	-70.3	-71.8
21.80	-89.7	-72.7	-79.6	-80.6	-81.7
26.57	-96.6	-76.7	-91.7	-92.7	-91.4
30.97	-82.1	-77.8	-88.1	-87.2	-84.2
34.99	-70.3	-78.6	-75.5	-73.4	-70.6
38.66	-65.3	-75.8	-67.0	-64.2	-61.1
41.99	-68.8	-86.9	-68.3	-62.4	-59.2

Table 5.3b Percentage change in maximum absolute amplitude of *PS*-wave for Type IA reflectivity as σ changes from 0.3 to 0.1 for the thin layer. Positive and negative signs represent amplitude increases and decreases respectively.

Incidence Angle θ_i	% Change in Maximum Absolute Amplitude				
	Single Interface	Thin-bed Thickness			
		1 m	5 m	9 m	13 m
0	0	0	0	0	0
7.44	-1.3	0	4.4	1.8	0.7
14.72	-0.1	3.6	5.0	3.9	1.1
21.71	2.6	5.6	6.9	4.5	3.2
28.29	8.3	11.4	10.3	11.4	7.8
34.35	22.1	18.2	22.5	19.7	15.5
39.87	75.1	43.4	38.9	32.8	30.3

Table 5.4a Percentage change in maximum absolute amplitude of *P*-wave for Type II reflectivity as σ changes from 0.3 to 0.1 for the thin layer. Positive and negative signs represent amplitude increases and decreases respectively.

Incidence Angle θ_i	% Change in Maximum Absolute Amplitude				
	Single Interface	Thin-bed Thickness			
		1 m	5 m	9 m	13 m
0	-61.9	-1.2	11.2	38.7	86.9
5.71	-59.4	-1.0	11.6	40.0	89.2
11.31	-51.9	-1.0	12.5	42.8	92.0
16.70	-39.1	-1.1	15.2	48.7	99.6
21.80	-21.5	-1.2	17.9	55.6	108.7
26.57	0.4	-2.0	19.9	60.7	117.9
30.97	24.1	-2.7	21.9	64.3	121.9
34.99	45.6	-4.0	19.5	61.6	115.8
38.66	60.6	-6.4	14.3	51.0	97.0

Table 5.4b Percentage change in maximum absolute amplitude of *PS*-wave for Type II reflectivity as σ changes from 0.3 to 0.1 for the thin layer. Positive and negative signs represent amplitude increases and decreases respectively.

Incidence Angle θ_i	% Change in Maximum Absolute Amplitude				
	Single Interface	Thin-bed Thickness			
		1 m	5 m	9 m	13 m
0	0	0	0	0	0
7.44	-23.0	-1.8	-3.0	-5.4	16.7
14.72	-22.9	-2.0	-4.3	-6.5	11.1
21.71	-22.5	-2.3	-4.2	-7.7	5.5
28.29	-21.7	-2.5	-4.6	-10.3	-6.2
34.35	-19.9	-2.7	-5.4	-14.4	-24.4
39.87	-16.1	-2.9	-8.4	-23.1	-35.7

Table 5.5a Percentage change in maximum absolute amplitude of *P*-wave for Type IIA reflectivity as σ changes from 0.3 to 0.1 for the thin layer. Positive and negative signs represent amplitude increases and decreases respectively.

Incidence Angle θ_i	% Change in Maximum Absolute Amplitude				
	Single Interface	Thin-bed Thickness			
		1 m	5 m	9 m	13 m
0	134.5	0	12.2	39.0	86.5
5.71	136.4	0.2	12.7	40.8	87.8
11.31	141.9	0.3	13.6	42.3	89.7
16.70	151.1	0.3	15.0	45.5	93.9
21.80	163.4	0.6	17.2	50.2	100.1
26.57	178.3	0.7	20.2	56.0	107.1
30.97	194.3	1.2	23.1	63.1	115.0
34.99	209.3	1.8	26.1	68.8	122.5
38.66	221.3	2.0	31.0	76.9	130.9
41.99	228.5	2.1	33.0	80.0	136.5
45.00	230.0	2.3	36.2	84.9	139.1
47.73	226.1	3.0	38.3	86.9	136.2
50.19	218.0	3.6	37.2	84.9	135.1

Table 5.5b Percentage change in maximum absolute amplitude of *PS*-wave for Type IIA reflectivity as σ changes from 0.3 to 0.1 for the thin layer. Positive and negative signs represent amplitude increases and decreases respectively.

Incidence Angle θ_i	% Change in Maximum Absolute Amplitude				
	Single Interface	Thin-bed Thickness			
		1 m	5 m	9 m	13 m
0	0	0	0	0	0
7.44	41.1	0	0	6.8	57.1
14.72	42.5	-0.5	-0.5	6.5	56.3
21.71	44.6	-0.4	0	5.2	50.4
28.29	47.9	-0.6	0	5.3	47.8
34.35	52.4	-0.6	0	4.9	44.4
39.87	58.1	-0.9	-0.3	5.3	42.9
44.81	65.2	-0.6	-1.0	5.4	39.6
49.18	73.8	-0.9	0.3	5.1	34.2

Table 5.6a Peak frequencies of reflected P -wave for Type I reflectivity as a function of the incident angle.

θ_1 (deg)	f_p (Hz) (1 m)		f_p (Hz) (5 m)		f_p (Hz) (9 m)		f_p (Hz) (13 m)	
	$\sigma = 0.1$	$\sigma = 0.3$	$\sigma = 0.1$	$\sigma = 0.3$	$\sigma = 0.1$	$\sigma = 0.3$	$\sigma = 0.1$	$\sigma = 0.3$
0.00	36.0	37.4	37.4	37.6	36.3	36.9	34.7	35.8
5.71	36.0	37.6	37.4	37.6	36.3	36.9	34.7	35.8
11.31	36.0	37.5	37.4	37.6	36.4	37.0	34.7	36.0
16.70	36.0	37.6	37.4	37.7	36.5	37.0	34.8	36.1
21.80	36.0	37.7	37.4	37.7	36.5	37.1	35.0	36.3
26.57	36.0	37.6	37.4	37.7	36.6	37.3	35.1	36.5
30.97	35.9	37.7	37.4	37.7	36.6	37.5	35.2	36.8
34.99	35.9	37.7	37.5	37.9	36.7	37.7	35.4	37.1
38.66	35.8	37.7	37.5	37.9	36.8	37.8	35.5	37.3
41.99	35.7	37.7	37.5	38.0	36.8	38.0	35.7	37.7
45.00	35.6	37.7	37.5	38.0	36.8	38.2	35.7	37.9
47.73	35.5	37.6	37.5	38.1	36.9	38.3	35.8	38.1
50.19	34.8	37.1	37.5	38.1	36.9	38.3	35.9	38.2

Table 5.6b Peak frequencies of reflected PS -wave for Type I reflectivity as a function of the incident angle.

θ_1 (deg)	f_p (Hz) (1 m)		f_p (Hz) (5 m)		f_p (Hz) (9 m)		f_p (Hz) (13 m)	
	$\sigma = 0.1$	$\sigma = 0.3$	$\sigma = 0.1$	$\sigma = 0.3$	$\sigma = 0.1$	$\sigma = 0.3$	$\sigma = 0.1$	$\sigma = 0.3$
0.00	0.0	0.0	0.0	0.0	0.0	0.0	0.0	0.0
7.44	37.0	37.7	37.1	37.2	35.3	35.5	32.8	33.3
14.72	37.1	37.7	37.1	37.2	35.4	35.6	32.9	33.3
21.71	37.1	37.7	37.1	37.2	35.4	35.7	33.0	33.4
28.29	37.0	37.7	37.1	37.3	35.5	35.7	33.0	33.6
34.35	37.0	37.7	37.2	37.3	35.5	35.7	33.2	33.7
39.87	37.0	37.7	37.2	37.3	35.6	35.8	33.3	33.7
44.81	36.9	37.7	37.2	37.3	35.7	35.9	33.4	33.9
49.18	36.5	37.7	37.2	37.3	35.8	36.0	33.6	34.1

Table 5.7a Peak frequencies of reflected *P*-wave for Type IA reflectivity as a function of the incident angle.

θ_i (deg)	f_p (Hz) (1 m)		f_p (Hz) (5 m)		f_p (Hz) (9 m)		f_p (Hz) (13 m)	
	$\sigma=0.1$	$\sigma=0.3$	$\sigma=0.1$	$\sigma=0.3$	$\sigma=0.1$	$\sigma=0.3$	$\sigma=0.1$	$\sigma=0.3$
0.00	37.9	37.2	37.7	37.7	37.1	37.4	36.2	36.9
5.71	37.9	37.3	37.7	37.7	37.1	37.4	36.2	36.8
11.31	37.9	37.0	37.7	37.7	37.0	37.4	36.1	36.8
16.70	37.4	37.4	37.6	37.7	36.9	37.4	35.8	36.8
21.80	35.5	37.4	37.3	37.7	36.6	37.3	35.4	36.7
26.57	31.5	37.3	33.4	37.7	39.2	37.3	41.8	36.8
30.97	31.7	36.8	37.3	37.7	42.6	37.4	42.6	36.8
34.99	33.9	36.0	38.2	37.7	39.4	37.4	40.1	36.8
38.66	37.6	33.8	38.2	37.3	38.5	37.3	38.9	36.9
41.99	38.2	32.0	38.1	35.4	38.2	36.5	38.4	36.5

Table 5.7b Peak frequencies of the reflected *PS*-wave for the IA reflectivity as a function of the incident angle.

θ_i (deg)	f_p (Hz) (1 m)		f_p (Hz) (5 m)		f_p (Hz) (9 m)		f_p (Hz) (13 m)	
	$\sigma=0.1$	$\sigma=0.3$	$\sigma=0.1$	$\sigma=0.3$	$\sigma=0.1$	$\sigma=0.3$	$\sigma=0.1$	$\sigma=0.3$
0.00	0.0	0.0	0.0	0.0	0.0	0.0	0.0	0.0
7.44	37.7	37.4	37.6	37.6	36.8	39.1	35.6	36.2
14.72	37.8	37.4	37.6	37.7	36.9	37.1	35.7	36.3
21.71	37.7	37.7	37.6	37.7	36.9	37.1	35.8	36.3
28.29	37.8	37.6	37.7	37.7	36.9	37.3	36.0	36.4
34.35	37.7	37.7	37.7	37.7	37.0	37.3	36.1	36.5
39.87	37.8	37.7	37.6	37.7	37.1	37.2	36.1	36.5

Table 5.8a Peak frequencies of the reflected P -wave for Type II reflectivity as a function of the incident angle.

θ_1 (deg)	f_p (Hz) (1 m)		f_p (Hz) (5 m)		f_p (Hz) (9 m)		f_p (Hz) (13 m)	
	$\sigma = 0.1$	$\sigma = 0.3$	$\sigma = 0.1$	$\sigma = 0.3$	$\sigma = 0.1$	$\sigma = 0.3$	$\sigma = 0.1$	$\sigma = 0.3$
0.00	31.0	31.0	31.8	30.5	32.6	29.2	32.9	27.3
5.71	31.1	31.0	31.8	30.5	32.7	29.2	33.0	27.3
11.31	31.1	31.0	31.9	30.5	33.0	29.3	33.3	27.5
16.70	31.1	31.0	32.2	30.5	33.3	29.2	33.6	27.6
21.80	31.1	31.0	32.4	30.5	33.8	29.4	34.0	27.8
26.57	31.1	31.0	32.8	30.5	34.3	29.5	34.3	27.9
30.97	31.1	31.0	33.1	30.6	34.6	29.6	34.6	28.3
34.99	31.1	31.0	33.1	30.6	34.7	29.8	34.8	28.6
38.66	31.1	31.0	32.9	30.7	34.6	30.1	34.9	29.9

Table 5.8b Peak frequencies of the reflected PS -wave for Type II reflectivity as a function of the incident angle.

θ_1 (deg)	f_p (Hz) (1 m)		f_p (Hz) (5 m)		f_p (Hz) (9 m)		f_p (Hz) (13 m)	
	$\sigma = 0.1$	$\sigma = 0.3$	$\sigma = 0.1$	$\sigma = 0.3$	$\sigma = 0.1$	$\sigma = 0.3$	$\sigma = 0.1$	$\sigma = 0.3$
0.00	0.0	0.0	0.0	0.0	0.0	0.0	0.0	0.0
7.44	31.0	31.0	29.7	29.9	27.1	27.5	23.6	24.3
14.72	31.0	31.0	29.7	29.9	27.1	27.6	23.6	24.4
21.71	31.0	31.0	29.7	29.9	27.1	27.6	23.7	24.7
28.29	31.0	31.0	29.8	30.0	27.1	27.9	23.9	25.5
34.35	31.0	31.1	29.8	30.1	27.2	28.2	23.7	25.3
39.87	31.0	31.0	29.6	30.2	26.7	28.4	23.2	25.9

Table 5.9a Peak frequencies of the reflected *P*-wave for Type IIA reflectivity as a function of the incident angle.

θ_1 (deg)	f_p (Hz) (1 m)		f_p (Hz) (5 m)		f_p (Hz) (9 m)		f_p (Hz) (13 m)	
	$\sigma = 0.1$	$\sigma = 0.3$	$\sigma = 0.1$	$\sigma = 0.3$	$\sigma = 0.1$	$\sigma = 0.3$	$\sigma = 0.1$	$\sigma = 0.3$
0.00	31.0	31.0	31.6	30.5	32.5	29.2	32.9	27.3
5.71	31.0	31.0	31.7	30.5	32.7	29.1	32.9	27.3
11.31	31.0	31.0	31.9	30.4	32.8	29.2	33.1	27.3
16.70	31.1	31.0	32.0	30.5	33.2	29.4	33.4	27.4
21.80	31.1	31.0	32.3	30.5	33.5	29.5	33.7	27.6
26.57	31.1	31.0	32.6	30.6	33.9	29.6	34.0	27.8
30.97	31.1	31.0	32.9	30.6	34.3	29.7	34.3	28.1
34.99	31.1	31.0	33.2	30.7	34.6	29.9	34.5	28.4
38.66	31.2	31.0	33.5	30.7	34.9	30.0	34.8	28.7
41.99	31.2	31.0	33.7	30.8	35.1	30.2	34.9	28.9
45.00	31.2	31.0	33.9	30.8	35.3	30.3	35.0	29.2
47.73	31.2	31.0	34.1	30.9	35.4	30.4	35.1	29.5
50.19	31.2	31.0	34.0	30.9	35.4	30.6	35.2	29.8

Table 5.9b Peak frequencies of the reflected *PS*-wave for Type IIA reflectivity as a function of the incident angle.

θ_1 (deg)	f_p (Hz) (1 m)		f_p (Hz) (5 m)		f_p (Hz) (9 m)		f_p (Hz) (13 m)	
	$\sigma = 0.1$	$\sigma = 0.3$	$\sigma = 0.1$	$\sigma = 0.3$	$\sigma = 0.1$	$\sigma = 0.3$	$\sigma = 0.1$	$\sigma = 0.3$
0.00	0.0	0.0	0.0	0.0	0.0	0.0	0.0	0.0
7.44	31.0	31.0	29.8	29.8	27.4	27.2	24.8	23.9
14.72	31.0	31.0	29.8	29.8	27.6	27.3	24.8	24.1
21.71	31.0	31.0	29.9	29.9	27.7	27.5	25.0	24.3
28.29	31.0	31.0	29.9	29.9	27.8	27.6	25.2	24.5
34.35	31.0	31.0	30.0	29.9	27.9	27.7	25.5	24.7
39.87	31.0	31.0	30.0	30.0	28.0	27.8	25.7	24.9
44.81	31.0	31.0	30.0	30.0	28.2	27.9	26.1	25.1
49.18	31.0	31.0	30.2	30.2	28.4	28.1	26.3	25.5

Table 5.10a Amplitude comparison between primary reflections only and primary reflections plus locally-converted shear waves for Type I reflectivity.

σ_1	<i>P</i> -wave %	<i>P</i> -wave (primaries only) %	σ_1	<i>PS</i> -wave %	<i>PS</i> -wave (primaries only) %
0.00	97.6	97.6	0.00	0.0	0.0
5.71	97.2	97.2	7.44	28.3	26.9
11.31	106.2	106.1	14.72	27.7	27.7
16.70	108.7	106.7	21.71	29.4	29.1
21.80	116.2	104.0	28.29	32.3	32.3
26.57	135.3	108.4	34.35	33.1	33.1
30.97	148.5	107.4	39.87	35.7	35.5
34.99	156.5	102.6	44.81	41.6	40.8
38.66	170.3	103.5	49.18	45.7	44.5
41.99	190.9	108.2			
45.00	197.6	109.4			
47.73	204.0	109.1			
50.19	222.0	113.0			

Table 5.10b Amplitude comparison between primary reflections only and primary reflections plus locally-converted shear waves for Type IA reflectivity.

σ_1	<i>P</i> -wave %	<i>P</i> -wave (primaries only) %	σ_1	<i>PS</i> -wave %	<i>PS</i> -wave (primaries only) %
0.00	-56.9	-56.9	0.00	0.0	0.0
5.71	-58.4	-59.0	7.44	4.4	-4.3
11.31	-62.4	-63.0	14.72	5.0	-5.5
16.70	-69.2	-69.0	21.71	6.9	-7.7
21.80	-79.6	-66.4	28.29	10.3	-10.1
26.57	-91.7	-49.6	34.35	22.5	2.8
30.97	-88.1	-33.9	39.87	38.9	19.2
34.99	-75.5	-25.8			
38.66	-67.0	-27.1			
41.99	-68.3	-41.6			

Table 5.10c Amplitude comparison between primary reflections only and primary reflections plus locally-converted shear waves for Type II reflectivity.

σ_1	<i>P</i> -wave %	<i>P</i> -wave (primaries only) %	σ_1	<i>PS</i> -wave %	<i>PS</i> -wave (primaries only) %
0.00	11.2	11.2	0.00	0.0	0.0
5.71	11.6	11.7	7.44	-3.0	5.6
11.31	12.5	9.6	14.72	-4.3	4.5
16.70	15.2	14.0	21.71	-4.2	5.5
21.80	17.9	16.1	28.29	-4.6	6.8
26.57	19.9	17.5	34.35	-5.4	9.7
30.97	21.9	18.7	39.87	-8.4	15.4
34.99	19.5	16.3			
38.66	14.3	11.6			

Table 5.10d Amplitude comparison between primary reflections only and primary reflections plus locally-converted shear waves for Type IIA reflectivity.

σ_1	<i>P</i> -wave %	<i>P</i> -wave (primaries only) %	σ_1	<i>PS</i> -wave %	<i>PS</i> -wave (primaries only) %
0.00	12.2	12.2	0.00	0.0	0.0
5.71	12.7	12.4	7.44	0.0	7.6
11.31	13.6	13.2	14.72	-0.5	8.1
16.70	15.0	13.6	21.71	0.0	8.5
21.80	17.2	15.5	28.29	0.0	9.1
26.57	20.2	17.5	34.35	0.0	10.7
30.97	23.1	18.9	39.87	-0.3	11.2
34.99	26.1	20.9	44.81	-1.0	12.2
38.66	31.0	23.1	49.19	0.3	13.9
41.99	33.0	24.9			
45.00	36.2	26.2			
47.73	38.3	27.0			
40.19	37.2	27.1			

Table 5.11a Peak frequency comparison between primary reflections only and primary reflections plus locally-converted shear waves for Type I reflectivity.

σ_1	<i>P</i> -wave				σ_1	<i>PS</i> -wave			
	($\sigma = 0.1$)Hz	($\sigma = 0.3$)Hz	($\sigma = 0.1$)Hz	($\sigma = 0.3$)Hz		($\sigma = 0.1$)Hz	($\sigma = 0.3$)Hz	($\sigma = 0.1$)Hz	($\sigma = 0.3$)Hz
0.00	37.4	37.6	37.4	37.6	0.00	0.0	0.0	0.0	0.0
5.71	37.4	37.6	37.4	37.6	7.44	37.1	37.2	36.0	36.6
11.31	37.4	37.6	37.4	37.7	14.72	37.1	37.2	36.1	36.7
16.70	37.4	37.7	37.4	37.7	21.71	37.1	37.2	36.2	36.7
21.80	37.4	37.7	37.5	37.7	28.29	37.1	37.3	36.2	36.7
26.57	37.4	37.7	37.5	37.6	34.35	37.2	37.3	36.2	36.7
30.97	37.4	37.7	37.5	37.5	39.87	37.2	37.3	36.1	36.7
34.99	37.5	37.9	37.5	37.4	44.81	37.2	37.3	36.0	36.7
38.66	37.5	37.9	37.5	37.2	49.18	37.2	37.3	36.0	36.7
41.99	37.5	38.0	37.5	37.0					
45.00	37.5	38.0	37.5	37.1					
47.73	37.5	38.1	37.5	36.9					
50.19	37.5	38.1	37.5	36.8					

Table 5.11b Peak frequency comparison between primary reflections only and primary reflections plus locally-converted shear waves for Type IA reflectivity.

σ_1	<i>P</i> -wave				σ_1	<i>PS</i> -wave			
	($\sigma = 0.1$)Hz	($\sigma = 0.3$)Hz	($\sigma = 0.1$)Hz	($\sigma = 0.3$)Hz		($\sigma = 0.1$)Hz	($\sigma = 0.3$)Hz	($\sigma = 0.1$)Hz	($\sigma = 0.3$)Hz
0.00	37.7	37.7	37.7	37.8	0.00	0.0	0.0	0.0	0.0
5.71	37.7	37.7	37.7	37.7	7.11	37.6	37.6	37.3	37.0
11.31	37.7	37.7	37.4	37.7	14.72	37.6	37.7	37.4	37.0
16.70	37.6	37.7	34.6	37.3	21.71	37.6	37.7	37.5	37.1
21.80	37.3	37.7	30.6	36.7	28.29	37.7	37.7	37.7	37.2
26.57	33.4	37.7	31.3	35.3	34.35	37.7	37.7	37.5	37.0
30.97	37.3	37.7	32.7	34.2	39.87	37.6	37.7	36.3	35.2
34.99	38.2	37.7	33.7	33.5					
38.66	38.2	37.3	34.3	32.9					
41.99	38.1	35.4	35.2	32.2					

Table 5.11c Peak frequency comparison between primary reflections only and primary reflections plus locally-converted shear waves for Type II reflectivity.

σ_1	<i>P</i> -wave				σ_1	<i>PS</i> -wave			
	($\sigma = 0.1$)Hz	($\sigma = 0.3$)Hz	($\sigma = 0.1$)Hz	($\sigma = 0.3$)Hz		($\sigma = 0.1$)Hz	($\sigma = 0.3$)Hz	($\sigma = 0.1$)Hz	($\sigma = 0.3$)Hz
0.00	31.8	30.5	31.8	30.5	0.00	0.0	0.0	0.0	0.0
5.71	31.8	30.5	31.8	30.5	7.44	29.7	29.9	29.8	29.9
11.31	31.9	30.5	31.9	30.5	14.72	29.7	29.9	29.8	29.9
16.70	32.2	30.5	32.2	30.5	21.71	29.7	29.9	29.8	29.9
21.80	32.4	30.5	32.5	30.5	28.29	29.8	30.0	29.9	30.0
26.57	32.8	30.5	32.9	30.6	34.35	29.8	30.1	30.0	30.1
30.97	33.1	30.6	33.3	30.7	39.87	29.6	30.2	30.0	30.3
34.99	33.1	30.6	33.3	30.7					
38.66	32.9	30.7	33.3	30.8					

Table 5.11d Peak frequency comparison between primary reflections only and primary reflections plus locally-converted shear waves for Type IIA reflectivity.

σ_1	<i>P</i> -wave				σ_1	<i>PS</i> -wave			
	($\sigma = 0.1$)Hz	($\sigma = 0.3$)Hz	($\sigma = 0.1$)Hz	($\sigma = 0.3$)Hz		($\sigma = 0.1$)Hz	($\sigma = 0.3$)Hz	($\sigma = 0.1$)Hz	($\sigma = 0.3$)Hz
0.00	31.6	30.5	31.7	30.5	0.00	0.0	0.0	0.0	0.0
5.71	31.7	30.5	31.7	30.4	7.44	29.8	29.8	29.9	29.9
11.31	31.9	30.4	31.8	30.4	14.72	29.8	29.8	29.9	29.8
16.70	32.0	30.5	31.9	30.5	21.71	29.9	29.9	30.0	29.9
21.80	32.3	30.5	32.3	30.5	28.29	29.9	29.9	30.0	30.0
26.57	32.6	30.6	32.4	30.5	34.35	30.0	29.9	30.0	30.0
30.97	32.9	30.6	32.6	30.5	39.87	30.0	30.0	30.1	30.0
34.99	33.2	30.7	32.8	30.6	44.81	30.0	30.0	30.1	30.1
38.66	33.5	30.7	33.1	30.6	49.18	30.2	30.2	30.2	30.2
41.99	33.7	30.8	33.2	30.7					
45.00	33.9	30.8	33.4	30.6					
47.73	34.1	30.9	33.5	30.7					
50.19	34.0	30.9	33.5	30.7					